



**HAL**  
open science

# Etude expérimentale des propriétés mécaniques et de la microstructure des sédiments contenant des hydrates de méthane

Thi Xiu Le

► **To cite this version:**

Thi Xiu Le. Etude expérimentale des propriétés mécaniques et de la microstructure des sédiments contenant des hydrates de méthane. Matériaux. Université Paris-Est, 2019. Français. NNT : 2019PESC1039 . tel-02884782v1

**HAL Id: tel-02884782**

**<https://pastel.hal.science/tel-02884782v1>**

Submitted on 30 Jun 2020 (v1), last revised 30 Jun 2020 (v2)

**HAL** is a multi-disciplinary open access archive for the deposit and dissemination of scientific research documents, whether they are published or not. The documents may come from teaching and research institutions in France or abroad, or from public or private research centers.

L'archive ouverte pluridisciplinaire **HAL**, est destinée au dépôt et à la diffusion de documents scientifiques de niveau recherche, publiés ou non, émanant des établissements d'enseignement et de recherche français ou étrangers, des laboratoires publics ou privés.

# Thèse

soumise pour l'obtention du grade de  
**Docteur de l'Université Paris-Est**  
Ecole Doctorale Sciences, Ingénierie et Environnement (SIE)

par

**Thi Xiu LE**

---

## **Experimental study on the mechanical properties and the microstructure of methane hydrate-bearing sandy sediments**

---

Spécialité : *Géotechnique*

This PhD thesis is realized at Geotechnical group, the Navier Laboratory  
Ecole des Ponts ParisTech

---

This PhD thesis is funded by the French National Research Agency, which is part of the  
project HYDRE “Mechanical behavior of gas-hydrate-bearing sediments”  
–ANR-15-CE06-0008

Soutenue le 6 décembre 2019 devant un jury composé de :

---

Prof. Gioacchino Viggiani	Université Grenoble Alpes	Rapporteur
Dr. Nabil Sultan	Ifremer	Rapporteur
Prof. Ana Cameirao	Ecole des Mines de Saint-Etienne	Examinatrice
Prof. Daniel Broseta	Université de Pau et des pays de l'Adour	Examineur
Dr. Anthony Delahaye	Irstea	Examineur
Dr. Patrick Aimedieu	CNRS	Examineur
Dr. Michel Bornert	Ecole des Ponts ParisTech	Examineur
Dr. Anh Minh Tang	Ecole des Ponts ParisTech	Directeur de thèse



# Remerciements

La première personne à qui je voudrais exprimer mes sincères remerciements est mon directeur de thèse, M. Anh Minh Tang. Je le remercie d'avoir eu confiance en moi pour réaliser ce travail. Je le remercie pour toutes ses excellentes idées proposées au cours de ces trois années, pour sa disponibilité et aussi pour nos discussions très intéressantes. Je le remercie également pour tous ses encouragements pendant toutes ces trois années.

Je remercie M. Stéphane Rodts qui était mon encadrant de thèse mais qui n'est plus avec nous. Il m'a appris non seulement l'Imagerie par Résonance Magnétique mais aussi la façon de bien réfléchir, et de bien planifier avant de commencer un travail.

Je remercie ensuite M. Michel Bornert, mon encadrant de thèse. Tout ce que je connais sur la Microtomographie aux rayons X est grâce à lui. Je le remercie également pour toutes ses excellentes idées, ses commentaires très pertinents et nos discussions scientifiques très intéressantes.

Je remercie également Patrick Aïmedieu, mon encadrant de thèse. Je le remercie bien de m'avoir soutenue pendant des moments difficiles lors de la mise en place de nouveaux dispositifs expérimentaux au Tomo. Je le remercie aussi pour sa gentillesse et pour nos discussions intéressantes.

J'adresse un grand remerciement à Baptiste Chabot pour tous ses supports techniques pendant toute la réalisation de cette thèse qui porte sur une thématique totalement nouvelle dans notre laboratoire. Je le remercie aussi de m'avoir bien encouragée surtout pendant des moments difficiles.

J'exprime mon sincère remerciement à Ross Brown avec qui j'ai fait les observations au microscope optique. Il m'a aussi aidée pour interpréter des résultats de ma thèse.

Je remercie Andrew King qui nous a bien guidés pendant toute la campagne au Synchrotron Soleil.

Je remercie grandement tous les membres du jury : M. Gioacchino Viggiani, M. Nabil Sultan, les deux rapporteurs, pour leur commentaires très constructifs et encourageants ; Mme. Ana Cameirao, M. Daniel Broseta et surtout M. Anthony Delahaye, monsieur le président pour nos discussions très intéressantes afin de mieux mettre en valeur notre travail dans de futurs articles.

Je remercie également tous les membres de l'équipe technique surtout Marine Lemaire, Emmanuel De Laure, David Hautemayou, et Jaime Gil Roca pour leur support technique.

Je remercie aussi Dyhia Atig qui m'a aidée à préparer des échantillons pour les observations au microscope optique ; Hannelore Derluyn pour nos discussions qui étaient très utiles pour interpréter mes résultats.

Je remercie sincèrement tous mes collègues au laboratoire notamment les amis de Master

avec qui j'ai passé ces trois/quatre années inoubliables. Je remercie également tous mes amis vietnamiens qui sont toujours disponibles quand j'ai besoin, et avec qui je passe de supers moments.

Finalement, je remercie mes parents du fond de mon cœur pour leur soutien pour toujours.

# Abstract

Methane hydrates (MHs), being solid ice-like compounds of methane gas and water, form naturally at high pressure and low temperature in marine or permafrost settings. They are being considered as an alternative energy resource (mainly methane hydrate-bearing sands, MHBS) but also a source of geo-hazards and climate change (MHs in both coarse and fine sediments). Knowledge of physical/mechanical properties of sediments containing MHs, depending considerably on methane hydrate morphologies and distribution at the pore scale (pore habits), is of major importance to be able to minimize the environmental impacts of future exploitation of methane gas from MHBS. Much of the existing experimental work consists in laboratory tests on synthetic samples due to challenges to get cored intact methane hydrate-bearing sediment samples. Various methods have been proposed for methane hydrate formation in sandy sediments to mimic natural MHBS, but without much success. The main objectives of this thesis are to investigate the morphologies and pore habits of MHs formed in synthetic MHBS, considered as model materials for real MHBS, at various scales and to study the effects of these parameters as well as of MH saturation on the mechanical properties of MHBS in order to propose a new MH formation method and to verify the validity of existing idealized models used to describe MH pore habits.

Two methods of MH formation, modified from two methods existing in the literature, have been first proposed to create MHs in sandy sediments at different pore habits. At the macroscopic scale, MH pore habits have been indirectly assessed via comparisons between measured ultrasonic wave velocities, and calculated ones based on rock physic models. The effects of MHs formed following the two proposed methods (at different MH saturations) on the mechanical properties of MHBS were investigated by triaxial tests instrumented with ultrasonic transducers. Furthermore, Magnetic Resonance Imaging (MRI) has been used to investigate the kinetics of MH formation, the MH distribution at the sample scale. A temperature cycle under undrained conditions was supposed to not only complete MH redistribution in the pore space after the water saturation of the sample but also to make MHs distributed more homogeneously in the sample. To create synthetic MHBS that better mimic natural sediments to investigate their mechanical behaviors, MH formation following the excess-gas method, followed by a water saturation could be used at MH saturations smaller than 40 % whereas at higher MH saturations, a temperature cycle should be added.

At the grain scale, MH morphologies and pore habits in sandy sediments were observed by laboratory X-Ray Computed Tomography (XRCT, at Navier laboratory, Ecole des Ponts ParisTech) and Synchrotron XRCT (SXRCT, at the Psiche beamline of Synchrotron SOLEIL). This has been a challenging task because not only of the need of special experimental setups (including both high pressure and low temperature controls) but also of the poor XRCT/SXRCT image contrast between methane hydrate and water. Specific experimental setups and scan conditions have been developed for pore-scale investigations of MH growth and MH morphologies in sandy sediments by using XRCT, and SXRCT. Observations (at a better spatial and temporal resolution) via Optical Microscopy (in cooperation with the University of Pau) have finally been used to confirm diverse MH morphologies in sandy sediments. Comparisons between observed MH morphologies, pore

habits and existing idealized models are discussed. Methane hydrate formation in sandy sediments is found to be an unstable and complex process. Different types of MH morphologies and more complex pore habits could co-exist.

Besides, an original method has been developed for an accurate determination of volumetric fractions of three-phase media from XRCT images. The method has been applied to determine methane hydrate saturation of MHBS under excess-gas conditions.

*Keywords:*

Methane hydrates, sandy sediments, formation, dissociation, morphologies, pore habits, mechanical properties, X-Ray Computed Tomography, Synchrotron XRCT, optical microscopy, triaxial tests, rock physic model.

# Résumé

Les hydrates de méthane (MHs), composés de méthane et d'eau, se forment naturellement à haute pression et faible température dans les sédiments marins ou les pergélisols. Ils sont actuellement considérés comme une potentielle ressource énergétique (principalement les MHs dans les sédiments sableux) mais aussi une source de risques géologiques et un facteur du changement climatique (MHs dans les sédiments grossiers et fins). La connaissance de leurs propriétés mécaniques/physiques, qui changent considérablement avec la morphologie et la distribution des hydrates dans les pores, est très importante pour minimiser les impacts environnementaux liés aux futures exploitations du gaz de méthane à partir des sédiments sableux contenant des MHs (MHBS). La plupart des études expérimentales concernent MHBS synthétiques à cause des difficultés pour récupérer des échantillons intacts. Différentes méthodes ont été proposées pour former MHs dans les sédiments au laboratoire pour reproduire des sédiments naturels, mais sans grand succès. Cette thèse a pour objectif d'évaluer la morphologie, et la distribution des MHs dans des MHBS synthétiques, considérés comme des matériaux modèles pour les vrais MHBS, à différentes échelles et d'étudier les effets de ces paramètres ainsi que de la teneur en hydrate sur les propriétés mécaniques des MHBS afin de proposer une nouvelle méthode de formation d'hydrates et aussi de valider les modèles existants utilisés pour décrire la distribution des hydrates à l'échelle de grain.

Deux méthodes de formation d'hydrates dans les sédiments sableux ont été proposées. Au niveau macroscopique, la distribution des hydrates au niveau des pores a été évaluée en se basant sur la vitesse de propagation d'onde de compression mesurée et calculée à partir des modèles théoriques existants. Des essais triaxiaux instrumentés avec des transducteurs à ultrasons ont été utilisés pour étudier l'influence des MHs à différentes teneurs en hydrate sur les propriétés mécaniques des MHBS. Par ailleurs, l'Imagerie par Résonance Magnétique a été utilisée pour étudier la cinétique de formation/dissociation d'hydrates ainsi que la distribution des hydrates le long d'un échantillon. Les résultats montrent qu'un cycle de température en conditions non drainées complète la redistribution des hydrates dans les pores après la saturation en eau de l'échantillon à une teneur en hydrate plus grande que 40 %. La distribution des hydrates sur l'ensemble de l'échantillon devient plus homogène avec la saturation en eau suivie par un cycle de température.

A l'échelle du grain, la tomographie aux rayons X de laboratoire (XRCT, au laboratoire Navier, Ecole des Ponts ParisTech) et Synchrotron XRCT (SXRCT, ligne Psiché, Synchrotron SOLEIL) ont été utilisées pour observer la morphologie et la distribution des MHs au niveau des pores des sédiments sableux. Ce travail n'a pas été facile car il a nécessité des dispositifs expérimentaux complexes, pour maintenir la haute pression et la faible température, mais aussi en raison du faible contraste entre MHs et l'eau sur les images de XRCT, et SXRCT. Des dispositifs spécifiques ont été développés pour étudier la formation d'hydrates, la morphologie et la distribution dans l'espace poral entre les grains des MHs par XRCT, et SXRCT. Des observations au Microscope Optique (en coopération avec l'Université de Pau et des Pays de l'Adour) ont également été faites pour confirmer diverses morphologies de MHs dans les sédiments sableux. Les morphologies et distributions d'hydrates observées sont comparées avec les modèles existants. Les observations montrent que la formation des MHs dans les sédiments sableux est un processus instable



et complexe. Différentes morphologies et plus complexe distributions des MHs au niveau des pores peuvent coexister.

Par ailleurs, une nouvelle méthode a été développée pour déterminer plus précisément les fractions volumiques d'un milieu triphasique à partir des images XRCT. Cette méthode a été appliquée pour déterminer la teneur en hydrate des MHBS à l'état gaz saturé.

*Mots-clés :*

Hydrates de méthane, sable, formation, dissociation, morphologies, distribution, tomographie aux rayons X de laboratoire, Synchrotron, microscope optique, essais triaxiaux, propriétés mécaniques, modèle de mécanique des roches.

# Contents

<b>List of Table</b>	<b>xiii</b>
<b>List of Figures</b>	<b>xiv</b>
<b>1 Introduction</b>	<b>1</b>
1.1 Context	1
1.1.1 Methane hydrates: an energy resource	3
1.1.2 Methane hydrates: geo-hazards	4
1.1.3 Methane hydrates and climate change	5
1.2 Thesis objectives	5
1.3 Thesis structure	7
<b>2 Literature review</b>	<b>9</b>
2.1 Gas hydrate formation and dissociation	9
2.1.1 Gas hydrate formation	9
2.1.2 Gas hydrate dissociation	16
2.2 Physical and mechanical properties	18
2.2.1 Pure gas hydrates	18
2.2.2 Gas hydrate-bearing sediments	19
2.3 Pore-scale observations	34
2.3.1 Pure gas hydrates	34
2.3.2 Gas hydrate-bearing sediments	36
2.4 Conclusions	41
<b>3 Mechanical properties</b>	<b>43</b>
3.1 Introduction	43
3.2 Experimental method	43
3.2.1 Materials	43
3.2.2 Experimental setup	43
3.2.3 Test procedure	44
3.2.4 Test program	49
3.3 Experimental results	49
3.3.1 Isotropic consolidation	49
3.3.2 Methane hydrate formation	50
3.3.3 Compressional wave velocity	56
3.3.4 Triaxial compressive properties	60
3.4 Conclusions	61

<b>4</b>	<b>Kinetics of MH formation and dissociation</b>	<b>65</b>
4.1	Introduction	65
4.2	Experimental method	65
4.2.1	Experimental setup	65
4.2.2	Test procedure	67
4.2.3	Test program	68
4.2.4	Calibration tests	68
4.3	Experimental Results	68
4.3.1	MH formation	68
4.3.2	Water saturation	71
4.3.3	MH dissociation - reformation	74
4.3.4	Depressurization-induced hydrate dissociation	78
4.4	Conclusions	81
<b>5</b>	<b>XRCT MH observation technical developments</b>	<b>83</b>
5.1	Introduction	83
5.2	Part I: Experimental setups for XRCT/SXRCT observations	83
5.2.1	Introduction	83
5.2.2	Optimization of image contrast	84
5.2.3	Experimental setup investigations	88
5.2.4	Discussions and recommendations	97
5.2.5	Conclusions	97
5.3	Part II: Methodology for accurate determination of volume fractions from XRCT images	98
5.3.1	Introduction	98
5.3.2	Method	99
5.3.3	Validations	105
5.3.4	Discussions on accuracy	108
5.3.5	Application to MHBS	111
5.3.6	Conclusions	116
<b>6</b>	<b>MH morphologies and pore habits</b>	<b>119</b>
6.1	Introduction	119
6.2	Experimental method	119
6.2.1	Experimental setups	119
6.2.2	Test procedure	122
6.3	Experimental Results	124
6.3.1	MH growth	124
6.3.2	MH morphologies and pore habits	141
6.4	Conclusions	146
<b>7</b>	<b>Discussions</b>	<b>147</b>
7.1	Introduction	147
7.2	MH formation under excess-gas conditions	147
7.2.1	MH nucleation	147
7.2.2	MH growth	149
7.2.3	MH stabilization	155
7.3	MH morphologies and pore habits under excess-water conditions	157

7.3.1	Water saturation . . . . .	157
7.3.2	Temperature cycle . . . . .	159
7.3.3	MH morphologies and pore habits . . . . .	161
7.4	Mechanical properties of MHBS . . . . .	162
7.5	Conclusions . . . . .	164
<b>8</b>	<b>Conclusions and Perspectives</b>	<b>167</b>
8.1	General conclusions . . . . .	167
8.2	Perspectives . . . . .	169
	<b>References</b>	<b>173</b>



# List of Tables

2.1	Comparison of properties of ice, sI, and sII hydrate crystal structures . . .	19
2.2	Thermal properties of hydrate-bearing sediment components . . . . .	20
2.3	Gas-hydrate constitutive models . . . . .	31
3.1	Test program. . . . .	49
3.2	Parameters used for Dvorkin’s model. . . . .	59
5.1	Effects of threshold choices used for the proposed method on the final results. . . . .	109
5.2	Effects of threshold choices for a global threshold method on the final results . . . . .	111
6.1	Test program of SXRCT and optical microscopy . . . . .	123

# List of Figures

1.1	The MGH structure . . . . .	1
1.2	Phase equilibrium of MHs in marine and permafrost conditions . . . . .	2
1.3	Macroscopic morphologies of natural MHs in Bay of Bengal . . . . .	3
1.4	Locations of sampled and inferred MH occurrences . . . . .	4
1.5	Macroscopic morphologies of natural methane hydrate-bearing sediments	5
1.6	Methane hydrate resource pyramid . . . . .	6
2.1	A diagram showing the components of various types of methane hydrate systems . . . . .	10
2.2	Different types of MH reservoir . . . . .	11
2.3	Pore-scale distribution of gas hydrates and sediment grains . . . . .	12
2.4	Gas uptake profile during MH formation in sediments . . . . .	14
2.5	The influence of pore diameter on thermodynamic equilibrium curve . . . . .	14
2.6	Final MH saturation versus initial water saturation . . . . .	15
2.7	Diagram of proposed methane hydrate production methods . . . . .	17
2.8	Average dissociation rates depending on depressurizing range and rate of pressure drop . . . . .	18
2.9	Thermal conductivity of hydrate-bearing sand and kaolinite . . . . .	20
2.10	Model prediction of Malik 2L-38 . . . . .	24
2.11	Conventional drained triaxial compression test on bonded and dense soil . . . . .	25
2.12	Dependence of stress and volumetric strain on axial strain for four MHBS . . . . .	26
2.13	Effect of gas hydrate saturation . . . . .	26
2.14	Peak strength versus methane hydrate saturation . . . . .	27
2.15	Maximum deviator stress of gas-saturated and water-saturated specimens plotted against MH saturation . . . . .	28
2.16	Stress-strain curves, excess pore pressure with axial strain, and effective stress path . . . . .	29
2.17	Micromechanism of the shear deformation of gas hydrate-bearing sand . . . . .	30
2.18	Simulation results from (T + H) for Class 3 hydrate deposit . . . . .	32
2.19	Isotropically consolidated MHBS dissociated by thermal recovery method . . . . .	33
2.20	$K_0$ consolidated methane hydrate-bearing sediments during the depressurization and shear process . . . . .	33
2.21	Sediment characteristics and physical properties . . . . .	34
2.22	$CO_2$ hydrate morphology depending on sub-cooling temperature, $\Delta T$ . . . . .	35
2.23	Micromodel tests . . . . .	36
2.24	2D gray scale image of natural gas hydrate-bearing sands . . . . .	37
2.25	GH film growth . . . . .	38
2.26	Diagram showing mass migration during hydrate formation . . . . .	40

2.27	Mechanism of the MH formation . . . . .	40
2.28	Schematic of two-step MH growth during the ATR-IR measurement . . . . .	40
3.1	Particle size distribution curve . . . . .	44
3.2	Schematic diagram of the experimental setup . . . . .	45
3.3	Pressure-Temperature control systems . . . . .	46
3.4	Sample preparation . . . . .	47
3.5	<i>P-T</i> conditions during the methane hydrate formation . . . . .	48
3.6	The system to measure methane gas quantity released from MH dissociation. . . . .	48
3.7	Void ratio versus effective stress for all tests. . . . .	51
3.8	Compressional wave velocity versus effective stress for all tests. . . . .	51
3.9	Pore pressure, temperature and volumetric deformation evolution during the MH formation. . . . .	52
3.10	Volumetric deformation evolution during the MH formation at 3MPa of effective stress. . . . .	53
3.11	Compressional wave velocity versus elapsed time during methane hydrate formation in gas-saturated media. . . . .	53
3.12	Compressional wave velocity versus elapsed time during water saturation. . . . .	54
3.13	Pore pressure, temperature and volume of water expelled versus elapsed time during heating path. . . . .	55
3.14	Pore pressure versus cell temperature during dissociation. . . . .	56
3.15	Temperature and volume of injected water versus elapsed time during hydrate reformation. . . . .	57
3.16	Compressional wave velocity during the whole methane hydrate formation of all tests. . . . .	58
3.17	Comparison between experiments and Dvorkin's models (Dvorkin et al., 2000) in gas-saturated media . . . . .	58
3.18	Comparison between experiments and Dvorkin's model in water-saturated media . . . . .	60
3.19	Deviator and volumetric strain versus axial strain . . . . .	62
3.20	Dependence of mechanical properties of sand on methane hydrate saturation for all tests . . . . .	63
3.21	$\sigma'_1/\sigma'_3$ versus $1 - \dot{\epsilon}_v/\dot{\epsilon}_1$ . . . . .	63
4.1	Diagram of the MRI experimental setup. . . . .	66
4.2	The preparation of the sample for MRI observations. . . . .	67
4.3	Reference signal. . . . .	68
4.4	MH formation following the excess-gas method . . . . .	70
4.5	MRI signal versus the sample height in methane gas-saturated media . . . . .	71
4.6	Vertical slices of Test 2 during the MH Formation in gas-saturated media. . . . .	72
4.7	FID Intensity evolution of two tests during the water saturation process. . . . .	72
4.8	Signal versus the sample height for Test 2 during the water saturation process. . . . .	73
4.9	Signal versus the sample height for both tests at the end of the water saturation phase. . . . .	73
4.10	MH dissociation-reformation of Test 1 . . . . .	76
4.11	MH dissociation-reformation of Test 2 . . . . .	77



4.12	Signal versus the sample height at the end of the water saturation, MH dissociation, and MH reformation phases . . . . .	78
4.13	FID Intensity and Remaining MH evolution during the MH dissociation . . . . .	79
4.14	Signal versus the sample height for two tests during the MH dissociation. . . . .	80
5.1	Linear attenuation coefficient ratio between phases versus photon energy. . . . .	85
5.2	XRCT images of unsaturated sand . . . . .	87
5.3	SXRCT images of unsaturated sand . . . . .	87
5.4	Experimental setup principles for XRCT scans of MHBS . . . . .	89
5.5	Experimental setup No. 1 . . . . .	90
5.6	Example of image of an unsuccessful scan due to the cell vibration, obtained by the experimental setup No. 1. . . . .	90
5.7	Example of image of MHBS obtained by the setup No. 1. . . . .	91
5.8	Gray value profiles to determine the ratio of MH/quartz of MHBS in Figure 5.7. . . . .	91
5.9	Experimental setup No. 2 . . . . .	92
5.10	Example of image of MHBS obtained by the setup No. 2. . . . .	93
5.11	Gray value profiles to determine the ratio of MH/quartz of MHBS in Figure 5.10. . . . .	93
5.12	Experimental setup No. 3 . . . . .	94
5.13	Example of XRCT image of MHBS obtained by the setup No. 3. . . . .	95
5.14	Gray value profiles to determine the ratio of MH/quartz of MHBS in Figure 5.13. . . . .	95
5.15	Example of SXRCT image of MHBS obtained by the setup No. 3. . . . .	96
5.16	Gray value profiles to determine the ratio of MH/quartz of MHBS in Figure 5.15. . . . .	96
5.17	Classification of voxels . . . . .	101
5.18	Histogram of the example image shown in Figure 5.17a . . . . .	102
5.19	Histogram of the remaining voxels to pre-determine the water-only voxels. . . . .	103
5.20	Histogram of air-only and grain-only in the original image . . . . .	104
5.21	Histogram of the water-only phase. . . . .	104
5.22	Test with unsaturated glass beads . . . . .	106
5.23	Histogram of the image obtained on unsaturated glass beads. . . . .	107
5.24	Test with an unsaturated sand . . . . .	107
5.25	Effects of threshold choices on the resulting image . . . . .	109
5.26	3D view of the resulting image. Image dimensions . . . . .	110
5.27	Comparison between the proposed method and Otsu's method . . . . .	110
5.28	Histogram of filtered image and threshold choices . . . . .	111
5.29	MHBS under excess-gas conditions: (a) SXRCT image, 1.200 mm x 1.200 mm; (b) its histogram. . . . .	112
5.30	Histograms of the grain-only phase and grain interfaces. . . . .	113
5.31	Histograms of the rest and two fitted Gaussian curves. . . . .	113
5.32	Image obtained after the classification of all voxels into five families . . . . .	114
5.33	Line profile to determine the mean gray values of the methane gas-only and the methane hydrate-only phase . . . . .	115
5.34	Image obtained after the classification of all voxels into six families . . . . .	116

6.1	Schema of the experimental setup showing pressure/temperature controls for SXRCT tests and scan types/positions. . . . .	120
6.2	SXRCT experimental setups . . . . .	121
6.3	Schematic view of experimental setup for optical microscopy tests . . . . .	121
6.4	In-situ optical microscopy experimental setup. . . . .	122
6.5	Scan type and position versus experiment time . . . . .	123
6.6	Test 1, transverse cross-section through Z0_HR: (a) t = 0.5 h; (b) t = 1 h; (c) t = 1.5 h; (d) t = 10.5 h. . . . .	124
6.7	Test 3, transverse cross-section through Z0_HR: (a) t = 0.3 h; (b) t = 0.8 h; (c) t = 2.2 h; (d) t = 4.3 h; (e) t = 6.0 h. . . . .	126
6.8	Test 3, vertical cross-section through Z0_HR: (a) Before temperature decrease; (b) t = 0.3 h. . . . .	127
6.9	Test 3, transverse cross-section through Z0_HR: (a) t = 0.3 h; (b) t = 0.8 h; (c) t = 2.2 h; (d) t = 4.3 h; (e) t = 6.0 h. . . . .	128
6.10	Test 3, vertical cross-section through Z1_HR: (a) t = 1.6 h; (b) t = 6.3 h. . . . .	129
6.11	Test 2, transverse cross-section through Z0_HR: (a) t = 4.3 h; (b) t = 7.7 h; (c) t = 11.2 h; (d) t = 14.6 h; (e) t = 17.6 h; (f) t = 21.3 h. . . . .	130
6.12	Test 2, vertical cross-section through: (a) Z3_HR at t = 18.2 h and Z2_HR at t = 18.0 h; (b) Z1_HR at t = 17.8 h and Z0_HR at t = 17.6 h. . . . .	131
6.13	Test 4, vertical cross-section through Z0_HR: (a) t = 0 h; (b) t = 0.6 h; (c) t = 4.0 h; (d) t = 4.5 h. . . . .	132
6.14	Test 4, vertical cross-section through Z1_HR: (a) t = 3.8 h; (b) t = 4.3 h; (c) t = 8.0 h; (d) t = 12.4 h. . . . .	133
6.15	Test 4, detail transverse cross-section through Z0_HR: (a) t = 0.6 h; (b) t = 2.3 h; (c) t = 4.3 h; (d) t = 6.5 h; (e) t = 10.3 h. . . . .	134
6.16	Test 4, vertical cross-section through Z0_HR: (a) t = 12.2 h; (b) t = 13.4 h; (c) t = 16.3 h. . . . .	135
6.17	Test 4, vertical cross-section through Z1_HR: (a) t = 13.6 h; (b) t = 16.5 h. . . . .	136
6.18	Test 4, vertical cross-section through: (a) Z1_LR, t = 19.5 h; (b) Z0_LR, t = 19.5 h; (c) Z-1_LR, t = 19.2 h. . . . .	138
6.19	Test 4, vertical cross-section through: (a) Z-3_LR, t = 19.0 h; (b) Z-5_LR, t = 18.8 h; (c) Z-7_LR, t = 18.5 h. . . . .	139
6.20	Test 4, vertical cross-section through: (a) Z9_LR, t = 20.5 h; (b) Z7_LR, t = 20.2 h; (c) Z5_LR, t = 20 h; (d) Z3_LR, t = 19.7 h. . . . .	140
6.21	Test 1: a transverse cross-section obtained after the injection of saline water. . . . .	141
6.22	Test 1 and Test 2, MH morphologies and pore habits under excess-gas conditions . . . . .	142
6.23	Test 5: Methane hydrate spike grow on the grain surfaces, observed by optical microscopy. . . . .	143
6.24	Test 5: Different MH morphologies in methane gas and water sides observed by optical microscopy. . . . .	144
6.25	Test 6: Different MH morphologies . . . . .	144
6.26	Test 4, Possible MH morphologies and pore habits in saline water media . . . . .	145
6.27	Test 4, Normalized Histogram of Figure 6.26 (a, b, c). . . . .	146
7.1	Kinetics of the MH formation following the excess-gas method . . . . .	148
7.2	MH layer propagation on a solid surface . . . . .	151

---

7.3	Schematic of the first mechanism of MH formation under gas-excess conditions. . . . .	152
7.4	Schematic of the MH spike formation (Modified from Lei et al., 2019b). . . . .	152
7.5	A new model of MH pore habits under excess-gas conditions (Blue: methane gas; Cyan: MHs; and Red: sand grains). . . . .	157
7.6	MH morphologies and pore habits under excess-gas conditions . . . . .	158
7.7	The effects of the water saturation . . . . .	159
7.8	The effects of temperature cycle . . . . .	160
7.9	An example of MH morphologies and pore habits under excess-water conditions. . . . .	161
7.10	The influence of methane hydrate saturation under excess-gas conditions . . . . .	162
7.11	Dependence of mechanical properties of sand on methane hydrate saturation for all tests . . . . .	163

---

# 1 Introduction

## 1.1 Context

Gas hydrates are solid ice-like compounds of water and gas/liquid. Methane hydrates (MHs), natural gas hydrates, form naturally at high pressure and low temperature. Figure 1.1 shows the structure of MHs: structure I – the most common clathrate structure with methane gas molecules residing within crystal structure of water ( $CH_4 \cdot 5.99H_2O$  (Circone et al., 2005)). They are found worldwide: in an unconventional form (frozen in arctic regions), at shallower marine areas (tens to hundreds of meters, more accessible water depths than conventional oil and gas), and at some locations both within and outside of the permafrost and marine areas that supply conventional fuels (Ruppel, 2007). Figure 1.2 shows the stability conditions of MHs in marine and permafrost settings. The blue lines show in-situ pressure-temperature conditions while the red lines present the MH phase equilibrium curve. MHs are stable when pressure-temperature conditions are inside of the phase equilibrium curve while they are dissociated (releasing methane gas and water) once pressure-temperature conditions are outside of the phase equilibrium curve.

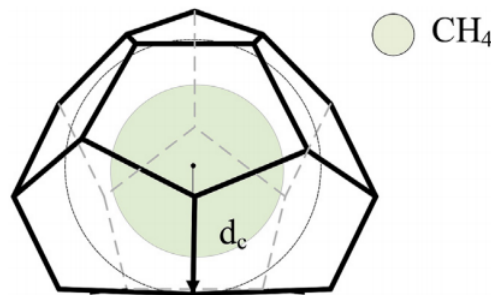


Figure 1.1: The MGH structure,  $S_I$  - dodecahedron, diameter of cavity ( $d_c$ ):  $5.09 \text{ \AA}$  (Malagar et al., 2019).

Methane hydrates can be identified by several methods but using seismic data is the most popular one. *The seismic technique labeled BSR - Bottom Simulating Reflector*, making mechanical waves pass through sea bottom beds and propagate downward, is based on the difference of velocities between sedimentary layers containing MHs and free gas zones (Popenoe et al., 1993). Note that the absence of BSR does not imply that there are no MHs within sediments. *Logging methods* have been widely used for MH exploration because of their accurate parameter determination for methane hydrate-bearing sediments regardless of their high cost (Dallimore et al., 1999). *Drilling to get cores* is the most effective method for recovering and identifying natural gas hydrates, but it is usually used together with other methods like seismic method to constrain where the core is taken.

*X-ray computed tomography, XRCT* gives visual access to the inner structure and macroscopic morphology of methane hydrate bearing-sediment cores (Holland et al., 2008). *<sup>1</sup>H Nuclear magnetic resonance spectroscopy, NMR*, used to investigate the molecular structures and physical properties of substances, is one of the most important means for studying methane hydrate characteristics in natural methane hydrate-bearing sediments (Davidson et al., 1977). We can also infer the presence of methane hydrates from their dissociation impacts on the chemistry of the surrounding sediment (e.g. pore-water salinity) (Ruppel and Kessler, 2017). Locations of sampled and inferred MH occurrences in oceanic sediments of outer continental margins and permafrost regions are shown in Figure 1.4. Most of the recovered MH samples have been obtained during deep coring projects or shallow seabed coring operations while most of the inferred MH occurrences are sites at which bottom simulating reflectors (BSRs) have been observed on available seismic profiles (Collett et al., 2014).

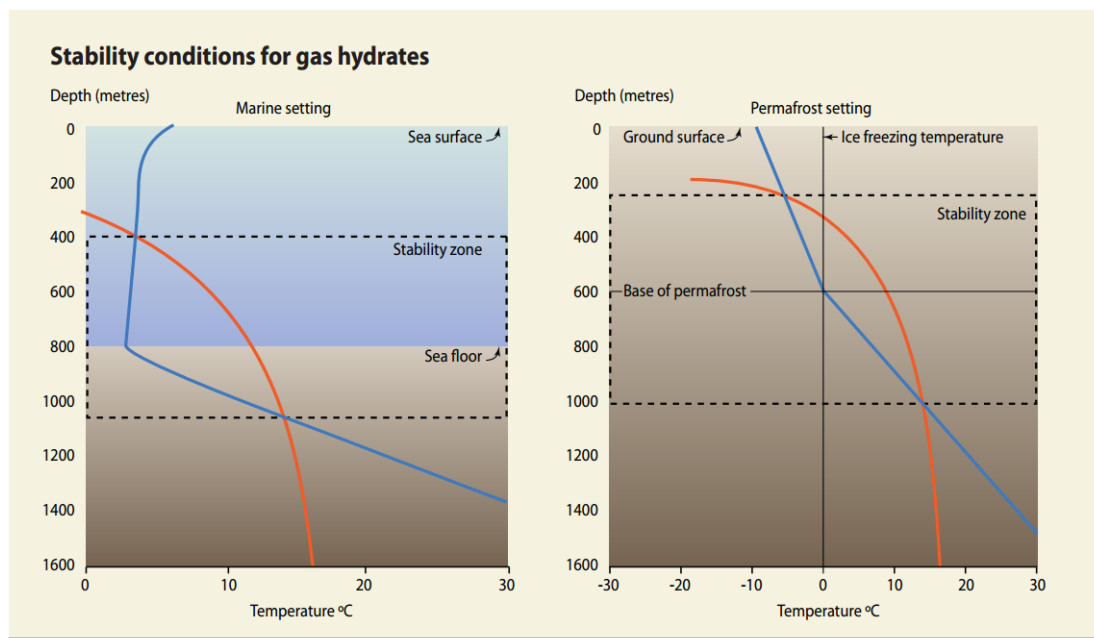


Figure 1.2: Phase equilibrium of MHs in marine and permafrost conditions (Beaudoin et al., 2014).

The way MHs fill or alter the pore space of sediments is quite different depending on formation temperature and pore pressure, gas chemistry, pore-water salinity, availability of gas and water, gas and water migration pathways, and the presence of reservoir rocks and seals (Collett, 2002). Figure 1.5 shows three types of naturally occurring methane hydrates observed: *lenses/veins*, *pore-filling* and *nodules/chunks*. Pore-filling MHs correspond to deep, coarse-grained sediments. Nodules/chunks MHs can be seen when hydrates are allowed to grow by displacing particles in every direction. At intermediate conditions, lens are formed when methane hydrate growth is capillarity controlled but grain displacement is preferentially aligned normal to the local minimum stress (Dai et al., 2012). Recently, based on XRCT, compressional wave velocity and gamma density, macroscopic morphologies of in-situ MHs in the Bay of Bengal were evaluated by Holland et al., 2018 (Figure 1.3). For sandy reservoir sediments, MH saturation reached

65-85 % in the pore space while MHs occupied almost the entire pore space of gravelly sediments. MH saturation was near 10 % in clayey interlayers between reservoir sediments, with no evidence of gas hydrate veins in XRCT images, whereas veins of gas hydrate were visible in X-ray images of clayey non-reservoir sediments.

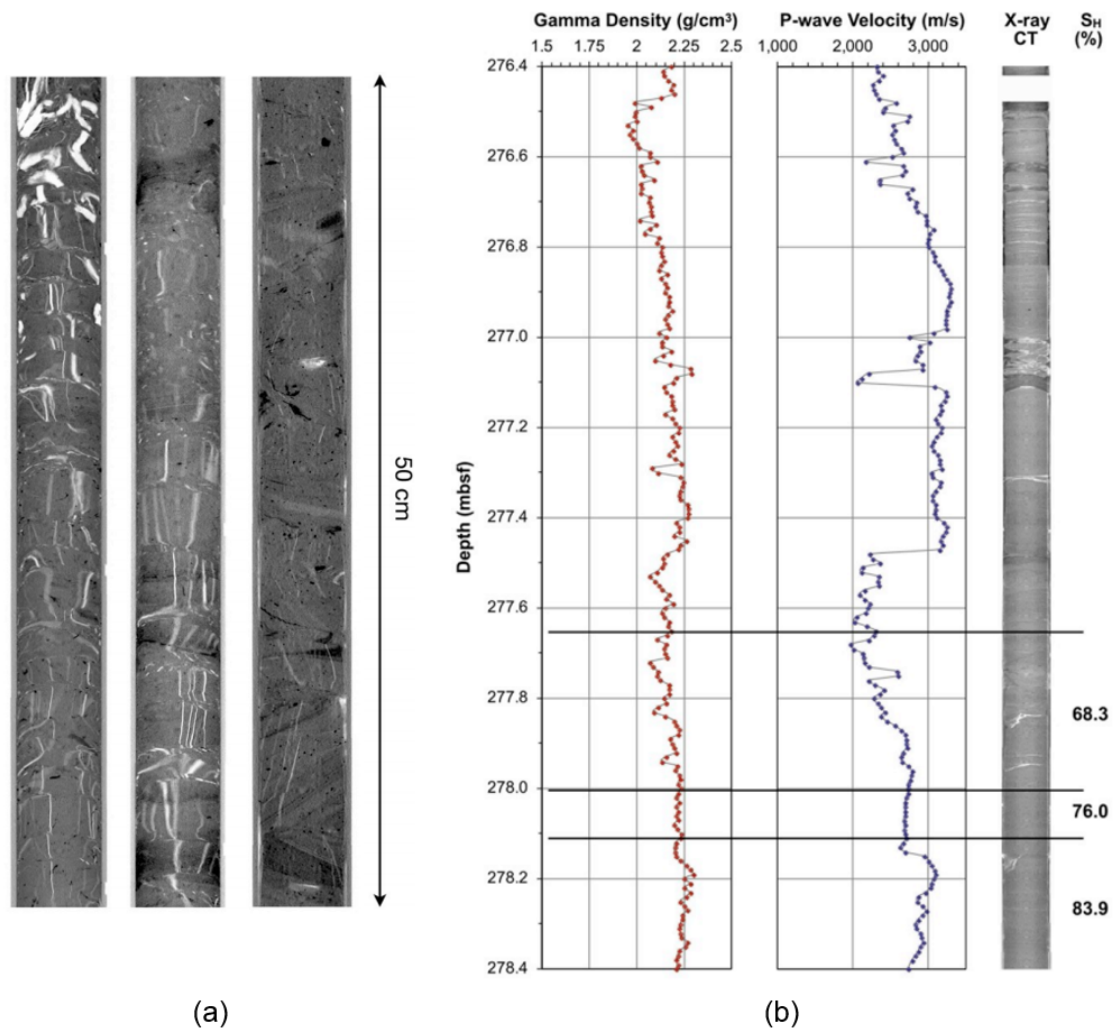


Figure 1.3: Macroscopic morphologies of natural methane hydrate-bearing sediments in the Bay of Bengal: (a) vein MHs in clayey sediments; (b) pore-filling MHs in sandy sediments (Holland et al., 2018).

The study of methane hydrates in sediments has been performed for over forty years, but estimating the role they may play as an energy resource, a source of geologic hazards and lastly a possible agent in climate change, has up to now been limited.

### 1.1.1 Methane hydrates: an energy resource

Geophysical methods (seismic bottom simulating reflector, complex 3D seismic inversion using rock physics and geologic models) are commonly used to estimate the global volume of methane hydrates. Methane-hydrate resource estimates rely on two basic parameters: the porosity and the percentage of the volume occupied by MHs, called methane

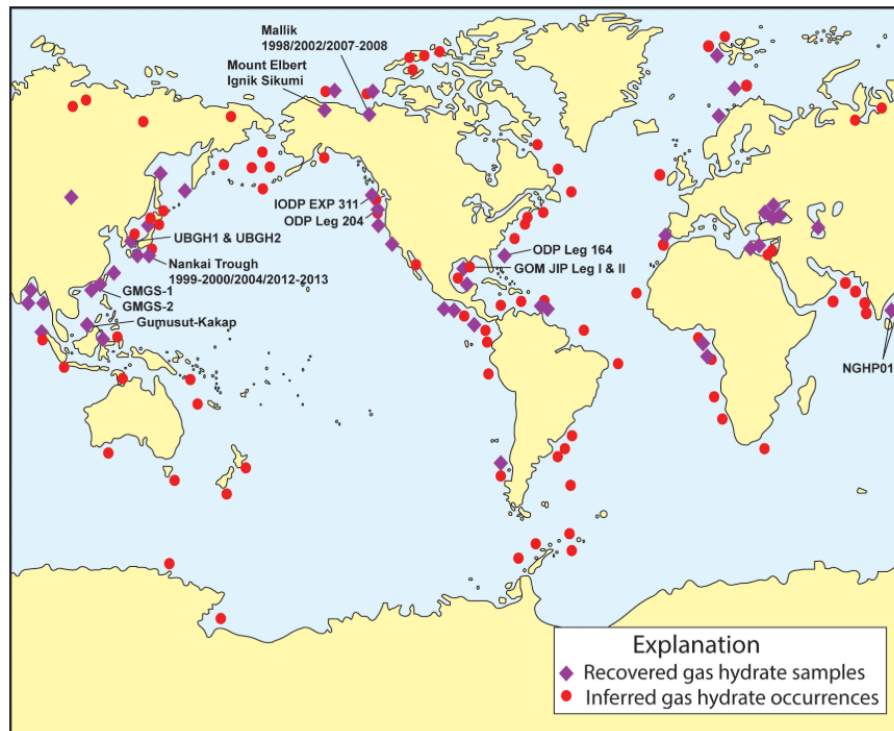


Figure 1.4: Locations of sampled and inferred MH occurrences in oceanic sediment of outer continental margins and permafrost regions (Collett et al., 2014).

hydrate saturation. These estimates, ranging over several orders of magnitude ( $\sim 3100 \text{ Tm}^3$  to  $\sim 7,650,000 \text{ Tm}^3$ ) (Ruppel, 2007), indicate an enormous potential as future energy resource of methane hydrates. Figure 1.6 shows four types of methane hydrate-bearing sediments and their role in the MH resource pyramid. The vast majority (90 %) of methane hydrates is found in fine-grained sediments, as dispersed forms, but hydrate saturation is typically low in that case. The larger pore size and relatively high permeability of sandy sediments facilitate methane hydrate formation as pore-filling with high methane hydrate saturation. That is why methane hydrate-bearing sands (MHBS) have been considered as the actual target for potential methane hydrate exploration within the scope of future methane gas production (Le et al., 2018b).

### 1.1.2 Methane hydrates: geo-hazards

Dissociation of MHs replaces rigid components with free gas and excess water. MH decomposition within surrounding impermeable porous media causes extraordinary pressures, which may significantly reduce the geo-mechanical stability of affected sediments. Slope instability and wide-scale gas venting are the two most important geo-hazards associated with methane hydrate dissociation problems. Human activities like drilling and production through methane hydrate-bearing sediments are considered as operational geo-hazards and cause the same concerns, such as casing collapse, gas leakage outside the conductor casing, and gas blowouts. The geo-hazard aspects of MHs provide an additional constraint on exploiting oceanic methane hydrates as a future energy resource (Collett et al., 2014).

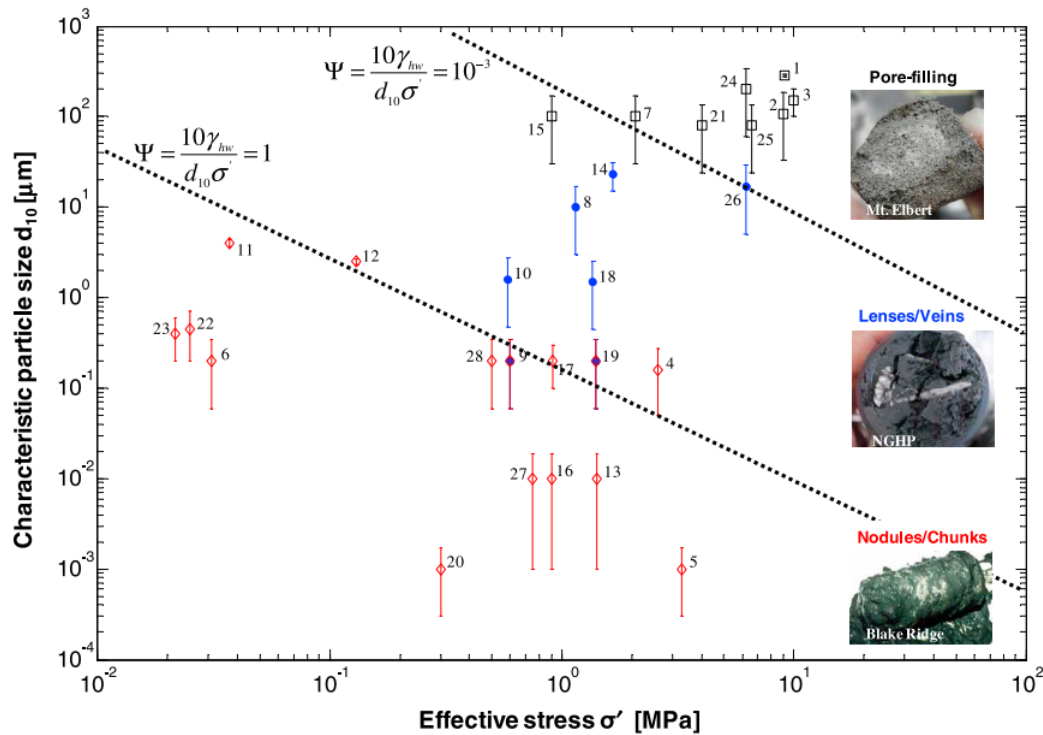


Figure 1.5: Macroscopic morphologies of natural methane hydrate-bearing sediments (Dai et al., 2012).

### 1.1.3 Methane hydrates and climate change

Methane is an important component of the atmosphere. It is an active “green-house” gas that has a global warming potential twenty times greater than an equivalent weight of carbon dioxide when integrated over 100 years. Methane hydrates existing in metastable equilibrium can be affected by changes in pressure and temperature that occur mainly with changes in sea level. An instantaneous release of methane gas from onshore and offshore could have great impacts on the atmospheric composition and thus the global climate. Methane hydrate resources, susceptible to natural destabilization in near term, are surficial or very shallow burials, likely focused on shallower water settings. Actually, for more deeply buried deposits, dissociation beginning at the base of the MH stability zone will need to propagate through thick sediment columns. In addition, the gas pathway to the overlying ocean or atmosphere requires a transfer through the overlying intervals that still lay within the MH stability conditions (Boswell et al., 2011). However, detailed knowledge about how released methane gas reaches atmosphere needs to be clarified as that is a key issue in understanding the connections between methane hydrates as an energy resource and also a potential player in future climate scenarios.

## 1.2 Thesis objectives

This thesis is in the context of **Hydre project**, funded by *French National Research Agency*, which serves to study the mechanical behaviors of methane hydrate-bearing sediments at various scales and via different methods to assess and minimize the environmen-



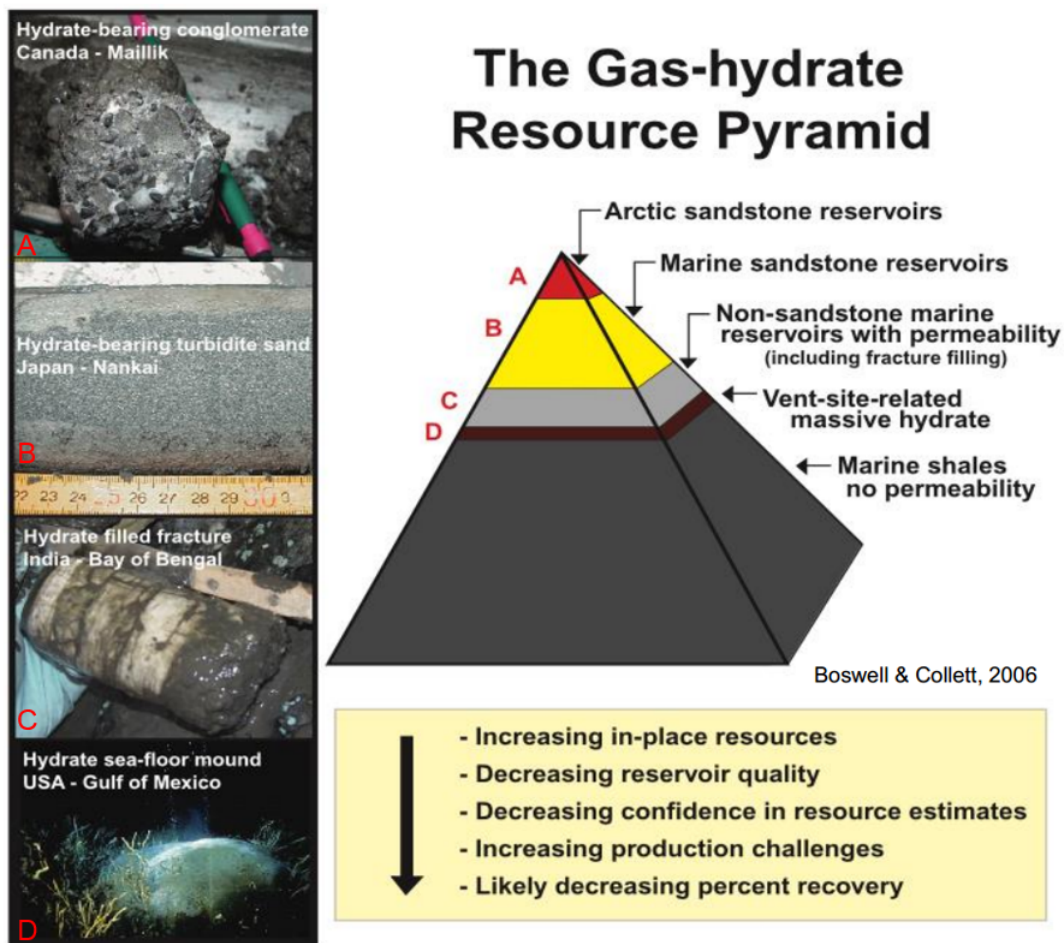


Figure 1.6: Methane hydrate resource pyramid (Collett et al., 2010).

tal impacts of future methane gas exploitation from deep-sea methane hydrate-bearing sediments.

Various studies have been performed in the literature to investigate the mechanical behaviors of methane hydrate-bearing sediments especially MHBS in the scope of methane gas production and environmental effects of methane gas exploration from MHBS. Geologic sampling inevitably disturbs natural sediments and the presence of hydrates adds further difficulties to sampling. With new methods like pressure coring, sample disturbance is reduced but still some are not eliminated as the loss of effective stress during sampling, shear along the soil-core liner interface (Waite et al., 2009). Therefore, almost all experimental works concern laboratory tests on synthetic sediments to investigate the mechanical behaviors of methane hydrate-bearing sandy sediments. Different methods have been proposed in the objective of creating MHs as pore-filling in MHBS. However, different MH pore-scale distributions (pore habits) have been supposed to be created in synthetic MHBS via measured compressional wave velocities and that calculated based on rock physics models (Choi et al., 2014).

The main objectives of this thesis are to investigate the morphologies and pore habits of methane hydrates formed in synthetic MHBS at various scales, via different methods and to study the effects of these parameters as well as of MH saturation on the mechanical properties of MHBS for the final purposes of proposing a MH formation method and verifying the validity of existing idealized models used to describe MH pore habits.

First, it is essential to find an efficient experimental method to recreate synthetic MHBS that better mimic natural MHBS for the study of mechanical properties of MHBS. MHs formed following this method should be verified whether or not they are in the pore space of sandy sediments (pore-filling habit) and how they are distributed (at the macroscopic scale) in the sample. Furthermore, the mechanical properties of formed MHBS with the corresponding MH pore habits need to be investigated. The traditional triaxial cell has been modified to instrument high pressure and low temperature controls (for the MH formation) as well as ultrasonic transducers (to follow the MH formation and to indirectly assess MH pore habits by comparing measured compressional wave velocity with that calculated via rock physics models) for the study of mechanical properties of MHBS. Furthermore, the kinetics of MH formation and dissociation as well as the MH distribution at the sample scale have been investigated by using Magnetic Resonance Imaging (MRI).

Second, few studies have investigated synthetic methane hydrate-bearing sandy sediments at the grain scale as this is really challenging (Lei et al., 2019b). Specific experimental setups and scan conditions have been developed for pore-scale investigations of MH growth, morphologies and pore habits in sandy sediments by using XRCT, and Synchrotron XRCT (SXRCT). These results have been further confirmed via observations at higher image spatial resolution and higher temporal resolution (i.e. by using optical microscopy). Existing idealized models have been verified by comparing with observed MH morphologies, pore habits. Moreover, SXRCT images could have been used to numerically investigate the effects of MH morphologies and pore habits on the mechanical behaviors of MHBS (the works of another PhD thesis in the context of **Hydre project**).

Besides, an alternative method has been developed for an accurate determination of volume fractions of three-phase media from XRCT images in the objective of determining methane hydrate saturation of MHBS from XRCT/SXRCT images.

### 1.3 Thesis structure

After the introduction (**Chapter 1**), literature is reviewed in **Chapter 2**. We first discuss about macroscopic observations (especially via ultrasonic wave velocities and MRI) of existing methods to form/dissociate MHs in synthetic MHBS. After that, physical/mechanical behaviors of natural and synthetic MHBS are presented. Finally, observations of pure gas hydrate formation, gas hydrate formation in sandy sediments at the grain scale (via Optical Microscopy, SXRCT, XRCT) are described.

As described in **Chapter 3**, methane hydrates were created in sandy samples following two methods. The first one corresponds to the creation of MHs in a partial water saturated sample followed by a water saturation phase prior to the mechanical testing.

The second one was similar to the first one but completed with a temperature cycle (as suggested by Choi et al., 2014). The measurement of compressional wave velocity was used to indirectly assess the grain-scale methane hydrate distribution in sediments. Tests were performed at various methane hydrate saturations (0-50 %) to investigate the effects of this parameter on the mechanical properties of MHBS via triaxial tests.

In **Chapter 4**, the kinetics of MH formation after the second method (with a temperature cycle) were followed by means of MRI. Global distribution of MHs in sample was observed. In addition, MH dissociation following the depressurization method, performed at the end of the MH formation was shown.

Experimental setups of triaxial and MRI tests are shown respectively in **Chapter 3** and **Chapter 4**. **Chapter 5** is devoted to discuss about new experimental setups developed for grain-scale investigations of MH growth, morphologies and distributions in the pore space of sandy sediments by using XRCT, and SXRCT. Furthermore, a new method, developed for an accurate determination of volume fractions of three-phase media from XRCT images, is presented and applied to determine methane hydrate saturation of MHBS under excess-gas conditions.

In **Chapter 6**, MH growth, morphologies and pore habits at the grain scale in sandy sediments, observed by SXRCT and optical microscopy, are presented. Mechanisms of MH formation in gas-saturated media are discussed. Furthermore, MH morphologies and pore habits in sandy sediments under excess-gas as well as excess-saline-water conditions are shown.

**Chapter 7** is devoted for the discussions of all aforementioned results (at various scales and via different methods) compared to that found in the literature.

Finally, the conclusions of this work, together with some perspectives, are given in **Chapter 8**.

## 2 Literature review

### 2.1 Gas hydrate formation and dissociation

The formation and dissociation of naturally occurring methane hydrates are governed by heat and mass transfer through sediments and the thermodynamic parameters, the pressure-temperature (P-T) conditions (Clennell et al., 1999; Tohidi et al., 1997). In this section, we first present mechanisms supposed for the MH formation in natural sediments, existing methods to create synthetic methane hydrate-bearing sediments in laboratory and MH pore habits. After that, different methods, used for MH dissociation in the scope of methane gas exploration, are discussed.

#### 2.1.1 Gas hydrate formation

Methane gas entrapped in natural methane hydrate-bearing sediments is mostly the result of biogenic activities (Malagar et al., 2019). Furthermore, in an aqueous system, MH formation/dissociation depends on methane gas solubility in surrounding water. Therefore, the actual base of methane hydrate occurrence is often shallower than that predicted from pressure and temperature considerations alone (Waite et al., 2009). The concept of methane hydrate system in nature comprising of individual factors that contribute to the MH formation (MH pressure-temperature stability conditions, methane gas charge - combination of methane gas source and migration, the presence of suitable host sediments or reservoirs) is shown in Figure 2.1. Depending upon prevailing boundary conditions for the MH formation in sediments, four types of MH reservoirs shown in Figure 2.2 could exist. Class I and II reservoirs are characterized by methane hydrate-bearing sediments with an underlying fluid-zone; methane hydrate-bearing sediments of class III reservoirs are within two impermeable sediment layers, whereas for class IV reservoirs, MHs are dispersed in less permeable sediments without being bounded by any confining strata (Malagar et al., 2019). Furthermore, the formation of various pore habits of MHs in natural sediments (e.g. pore-filling, fractures and nodules) depends on the sediments and their matrix characteristics (Dai et al., 2012).

*In-situ* observations of natural gas hydrate growth, that in the order of geologic time scale, are almost unfeasible due to limited experiment time. Different models have been proposed to describe methane hydrate growth in natural sediments based on available data of methane hydrate pore habits observed in sediments (Tohidi et al., 1997; Clennell et al., 1999). Two mechanisms of natural gas hydrate formation in subsea sediments (methane hydrate formation from dissolved gas or free gas) have been proposed based on a thermodynamic model (Tohidi et al., 1997). The transfer of salts by diffusion is likely to be a controlling factor for natural gas hydrate formation. Based on the Capillary model,

Clennell et al., 1999 suggested that in fine-grained sediments where MH growth rate is modest, blocks of hydrates or diffused hydrates (small nodules or inclusions) could be formed in sediments while interstitial hydrates are favored in coarse sediments where the reactions to form hydrates progresses rapidly. Knowledge of methane hydrate nucleation and growth from aqueous solution is fundamental for understanding of how methane hydrates are formed in natural sediments.

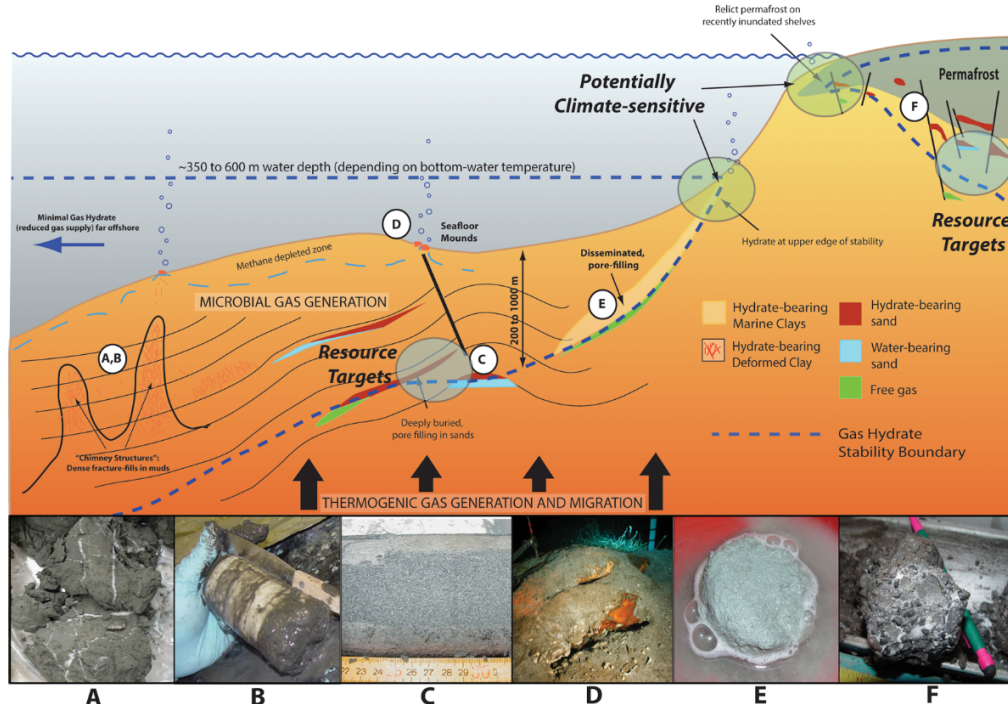


Figure 2.1: A diagram showing the components of various types of methane hydrate systems. Typical methane hydrate reservoir pore habits including (A) networks of hydrate-filled veins; (B) massive hydrate lenses; (C) pore-filling methane hydrate in marine sands; (D) massive sea-floor mounds; (E) pore-filling methane hydrate in marine clays; (F) pore-filling methane hydrate in onshore Arctic sands/conglomerates (Boswell et al., 2014).

Laboratory synthesis of MHs with different pore habits and at different hydrate saturations in sediments formed to mimic natural methane hydrate-bearing sediments is of primary importance for the study of the effects of MHs on the mechanical, geophysical and hydrological properties of sediments.

MH formation in bulk-water, under controlled thermodynamic conditions has been performed to understand the phase transition of water, and methane gas into solid crystals: to characterize the mechanical and physical properties of pure MHs (Natarajan et al., 1994; Sloan Jr and Koh, 2007), to enhance natural gas storage in tanks by converting it into hydrates (Bybee et al., 2009), and to prevent hydrate formation in gas pipelines (Gudmundsson et al., 1995).

The small pore size of fine-grained sediments associated with capillarity and water-mineral interactions hinder gas hydrate nucleation and formation. Therefore, laboratory stud-

ies on gas hydrate formation in fine-grained sediments are limited. Lei et al., 2018 explored different strategies including: the use of a more soluble guest molecule rather than methane; grain-scale gas storage within porous diatoms; ice-to-hydrate transformation (lenses grown in predefined locations); gas injection into water saturated sediments and long-term guest molecule transport. Inherent difficulties in mimicing methane hydrate formation in natural fine-grained sediments within the relatively short time scale available in laboratory experiments were highlighted. More attention should be paid in the future to create MHs in synthetic fine-grained sediments (Lei and Santamarina, 2018). This concerns more geo-hazard and climate change issues of MHs as the extraction of methane gas from fine-grained sediments is not technically feasible (Merey, 2016).

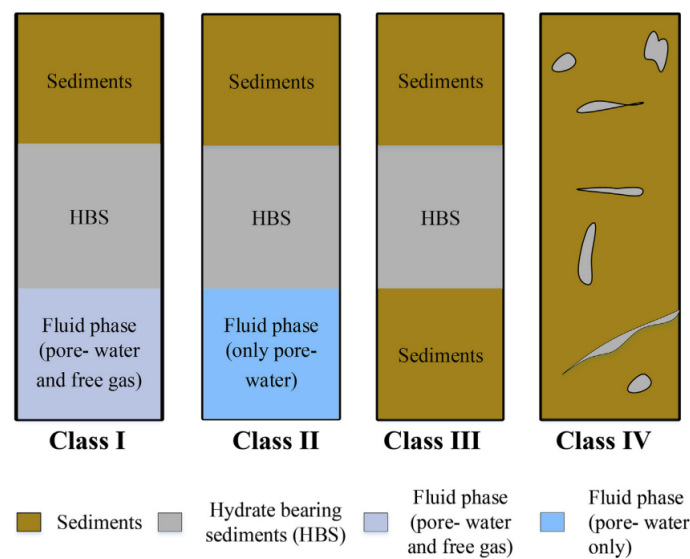


Figure 2.2: Different types of MH reservoir (Malagar et al., 2019).

High intrinsic permeability and thermal conductivity of sandy sediments facilitate MH formation at high saturation and in a non-displaced pore habit (pore-filling) (Lei and Santamarina, 2018; Malagar et al., 2019). This makes also methane gas recovery from MHBS technically feasible and economical (Merey, 2016). Consequently, several laboratory studies have focused on gas hydrate formation in sandy sediments. In the objective of creating MHs as pore-filling in sandy sediments, different methods have been proposed: dissolved gas (Spangenberg et al., 2005), excess-gas (Waite et al., 2004), ice-seeding (Priest et al., 2005), excess-water methods (Priest et al., 2009) and a combination of the excess-gas method, saline water injection with a temperature cycle (Choi et al., 2014). The gas hydrate pore habits in sediments have usually been assessed indirectly by comparing the measured seismic velocities and that calculated via models (Dvorkin and Nur, 1996; Nur et al., 1998; Helgerud et al., 1999; Dvorkin et al., 2000). In the models proposed by Dvorkin et al., 2000, the four pore-scale gas hydrate distributions (pore habits) shown in Figure 2.3, were considered. These models were based on the fact that seismic velocities depend on elastic moduli of the system, which are controlled by the grain-scale arrangements of gas hydrates and sediments. For a given gas hydrate saturation, gas hydrates floating in pore fluid (pore-filling gas hydrates, observed in natural gas hydrate-bearing sand) increase the modulus of the pore fluid (thus the seismic velocities)

and has the smallest impact on the host sediment's elastic properties. On the contrary, gas hydrates forming only at the grain contacts and acting as cementing (cementing - grain contacts) have the greatest impact on elastic properties of sediments and increase the seismic velocity by locking individual grains together. Gas hydrates forming as a part of the sediment frame (load-bearing) are simply accounted as the second mineral in the quartz sand pack while gas hydrates surrounding and cementing sediment grains (cementing - mineral coating) are held together by the effective stress. Their presence increases the granular contact stiffness dramatically by locking grains in place. Details of these models will be given in Section 2.2.

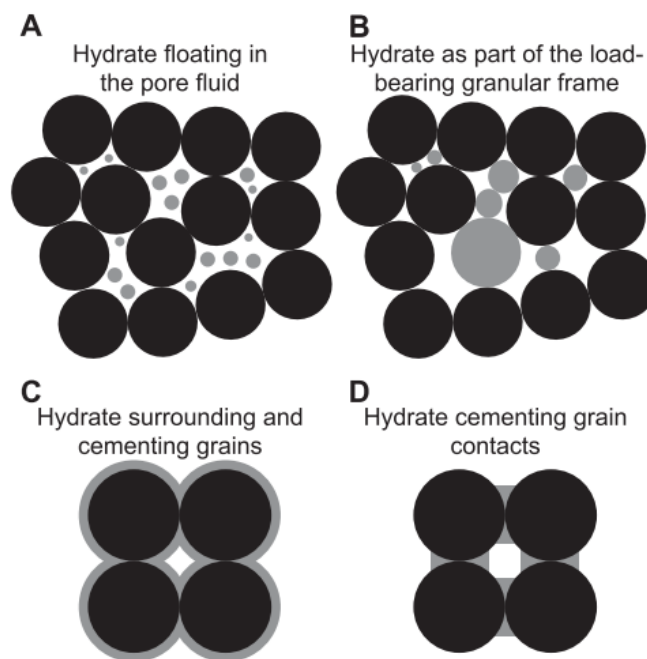


Figure 2.3: Pore-scale distribution of gas hydrates (gray) and sediment grains (black) (Dvorkin et al., 2000).

*The dissolved gas method* (transport of dissolved methane gas into the methane hydrate stability field via fluid migration (Spangenberg et al., 2005)) is considered as a good method to reproduce natural gas hydrate formation in marine sediments (pore-filling MHs) but this method is time-consuming especially at high methane hydrate saturation due to low solubility of methane gas in water. Ultrasonic wave velocities, measured on glass bead sample, were similar when comparing with theoretical predictions and with field data from Malik well (Lee and Collett, 2001) for methane hydrate free and almost methane hydrate saturated samples.

For the *Excess gas - Partial water saturation method* (Waite et al., 2004), MHs are formed either from unsaturated sand or saturated sand by injecting methane gas and decreasing the sample temperature. This method has been widely used as it is fast and easy to control. It was assumed that this method created MHs surrounded and cemented quartz grains (cementing).

The effects of methane hydrate cementation on elastic wave velocities in quartz sand were investigated by Priest et al., 2005. Methane gas was injected into unsaturated frozen sample for MH formation (*Ice-seeding method*). It was suggested that MHs initially cemented grain contacts then infilled the pore space. Similar to the excess-gas method, MH saturation after the ice-seeding method depends on the initial water saturation of the sample.

Priest et al., 2009 proposed the *Excess-water method* consisting of injecting first a predetermined amount of methane gas into a dry sand sample and then injecting water until a predetermined water pressure. MH saturation was restricted by the amount of methane gas. No apparent effects of MHs on velocities were measured until MH saturation was greater than 20 %. In addition, MHs were supposed to be formed at gas bubble/water interfaces and exhibited load-bearing behavior. The maximum MH saturation created was only 40 % and MHs seemed to be formed heterogeneously inside the sample.

Using the excess-water method first to form MHs quickly then combining it with the dissolved gas method to increase MH saturation was supposed to be a promising method (Waite et al., 2011). However, this approach was, in practice, prone to MH clog formation in the inlet and outlet lines.

In the work of Ebinuma et al., 2008, MHs were first formed after the excess-gas method, making ultrasonic wave velocities increased. Subsequent distilled water injection at a constant flow rate into the pore space of the sample to purge excess-methane gas made these velocities decreased.

Choi et al., 2014 proposed a non-cementing MH formation method by combining the excess-gas method with a saline water injection at restricted conditions (P-T conditions outside of the saline water phase stability but inside of the water phase stability) and a temperature cycle (dissociation then reformation of MHs). It was concluded that slow saline water injection was a key process to initiate the formation of non-cementing MHs and the temperature cycle ensured this formation. Compressional wave velocity,  $V_P$  after the MH dissociation was quite high while the sample was not saturated. The MH dissociation was perhaps not finished before the MH reformation, which may result in a small difference of  $V_P$  after the saline water injection and that after the temperature cycle. This method will be modified to use in this PhD thesis.

Based on a synthesis of existing literature, the effects of different parameters (sediments and their matrix characteristics, mineralogy, pore diameter, sediment diameter - mean diameter), specific surface area, initial water saturation, salinity and volume of sample on the MH formation have been discussed by Malagar et al., 2019. Different stages of the MH formation in sediments have been observed and reproduced in Figure 2.4 (MH nucleation - stage I; MH growth: at high formation rate - stage II, at low formation rate - stage III; and steady state - stage IV).

Furthermore, it was observed that the methane gas uptake profile for fine-grained sediments was different from that for coarse sediments. Pore diameter, particle diameter and salinity affect the MH thermodynamic equilibrium conditions, that in turn influence the



driving force for the MH formation. MHs occupy the pore space of the sediment matrix and hence the pore size distribution characteristics influence the MH thermodynamic equilibrium conditions ( $TEC$ ), which in turn affect their formation and dissociation processes (Malagar et al., 2019). Figure 2.5 shows a summary of pore diameter ( $d_p$ ) effects on  $TEC$ .  $TEC$  of MHs was shifted from  $TEC_1$  to  $TEC_6$ , with a decrease in  $d_p$ . The  $TEC_1$  corresponds to bulk water case ( $d_p$  was not defined);  $TEC_2$  corresponds to  $d_p$  of 101.3 nm and ultimately  $TEC_6$  corresponds to  $d_p = 9.2$  nm. That means that the MH phase transition will occur at higher pressure and/or lower temperature with a decrease in  $d_p$ . In addition, MH formation rate depends on the sediment specific surface area.

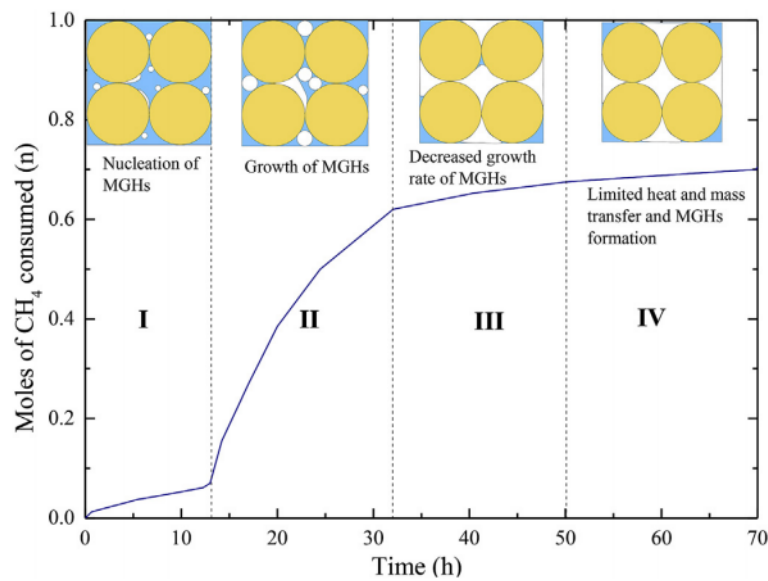


Figure 2.4: Gas uptake profile during MH formation in sediments (Malagar et al., 2019).

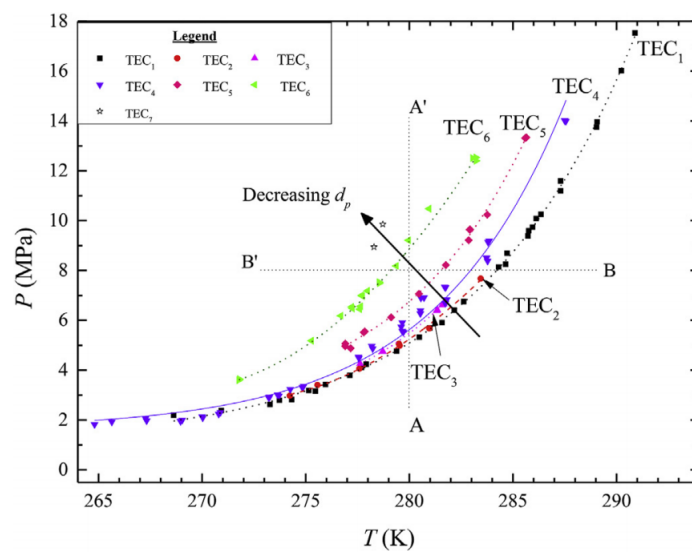


Figure 2.5: The influence of pore diameter ( $d_p$ ) on thermodynamic equilibrium curve ( $TEC$ ) of MHs (Malagar et al., 2019).

Malagar et al., 2019 investigated also the effects of the initial water saturation ( $S_w$ ) on the final MH saturation ( $S_h$ ), as shown in Figure 2.6. It can be seen that in the region (a),  $S_h$  increases with an increase of  $S_w$ . That can be explained by an increase of the amount of water available in the sediment matrix, participating in the MH formation. The maximum  $S_h$  reached for a given thermodynamic condition was in the region (b) where the data points are dispersed ( $S_h$  is in a range of 25-60 %). In the region (c), most likely to be encountered in a marine environment,  $S_h$  decreases with an increase in  $S_w$  due to the decrease of interaction between methane gas and water.

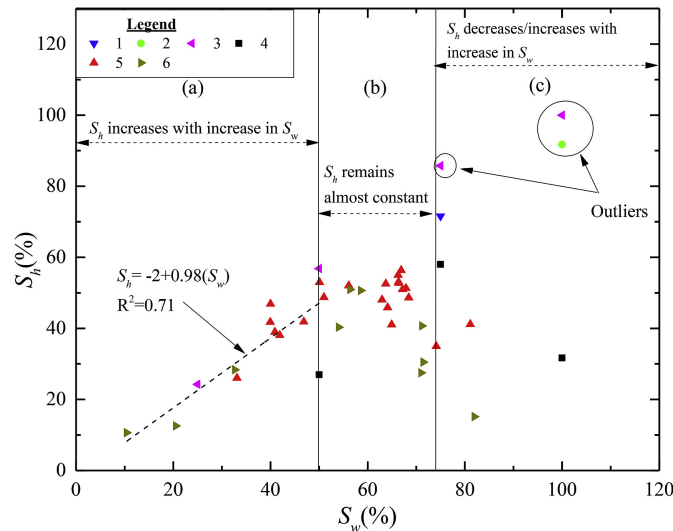


Figure 2.6: Final MH saturation versus initial water saturation of the samples tested in the laboratory (Malagar et al., 2019).

Besides the P-T observations and the elastic wave velocity measurements, which are usually used to study the kinetics and mechanisms of gas hydrate formation and dissociation, *Magnetic Resonance Imaging* is a well-suited mean to quantitatively/qualitatively follow these kinetics. In most MRI studies, glass beads were used to simulate the porous media to investigate Tetrahydrofuran (*THF*), or carbon dioxide ( $CO_2$ ) hydrate formation. Methane hydrate formation (following the dissolved gas or partial water saturation method) was observed via Mean Intensity (*MI*, MRI mean intensity calculated from the images) evolution and 2D images (Zhao et al., 2014; Zhao et al., 2015a). The effects of different sizes of glass beads on MH growth were investigated. In general, MH growth rate increased when the size of the porous media decreased. In addition, three growth stages of methane hydrates formed following the partial water saturation method were observed: the initial-growth, the rapid-growth and the steady stages. In sandstone media, methane hydrate formation and spontaneous conversion of methane hydrates to  $CO_2$  hydrates were studied by mean of *MI* and 3D images (Baldwin et al., 2009; Erslund et al., 2010). As time is needed to take 3D images, spatial distribution of MHs within the specimen during the methane hydrate formation was not measured regularly. The MH formation in an unconsolidated bed of silica with different size ranges was investigated via the *MI* evolution, measured on vertical and horizontal slices (Bagherzadeh et al., 2011). The MH formation was observed non-uniform and occurred at different times and different positions. In addition, by using different water saturations, MH formation was found to be faster at a

lower initial water content.

### 2.1.2 Gas hydrate dissociation

The exploitation of solid methane hydrates (involving controlled dissociation of MHs through perturbations of pressure, temperature, and/or chemical conditions in the reservoirs) probably remains economically and logistically impractical (Collett, 2002). Most methods of methane gas recovery from MHs deal with dissociation or melting in-situ MHs: thermal method, depressurization method and inhibitor injection method (see diagram shown in Figure 2.7). The injection of heated fluids (liquids or steam) is the simplest technique for triggering MH dissociation. It has been shown that methane gas can be produced from MHs at sufficient rates. However, heat loss during the transit and following heat disturbances figure some problems to be resolved. Similarly, the use of methane hydrate inhibitors (e.g. methanol, saline solutions or other thermodynamic inhibitors) has been shown to be technically feasible but the use of large volumes of chemicals such as methanol comes with a high economic and environmental cost. The depressurization technique (lowering pressure in the overlying sediments) was considered as the most economically promising method. However, if it is performed without external heat, MH dissociation is limited in rate and extent because it stops when reservoir pressure reaches the equilibrium conditions.  $CO_2$ - $CH_4$  exchange ( $CO_2$  injection into methane hydrate reservoir to release  $CH_4$ ) is now a potential method. Natural gas hydrate reservoirs could thus be used for simultaneous energy extraction and sequestration of  $CO_2$  waste generated by burning fossil fuel.

Three successful offshore field tests (together with onshore field tests in Malik in 2008), up to now, used the depressurization method. The first offshore methane hydrate production test was conducted by Japan Oil, Gas, and Metals National Corporation (JOGMEC) in the eastern Nankai Trough in 2013. Approximately 120,000 m<sup>3</sup> of methane gas (20,000 m<sup>3</sup>/day) was produced by lowering pressure from 13.5 MPa to 4.5 MPa. The production was interrupted due to an unexpected increase of sand production (Konno et al., 2017). That was followed by the second attempt, made in April to June of 2017, at a nearby location: the first borehole (AT1-P3, continued for 12 days with a stable drawdown of around 7.5 MPa and 41,000 m<sup>3</sup> of methane gas being produced despite intermittent sand-production events) and the second borehole (AT1-P2, followed with a total of 24 days of flow and 222,500 m<sup>3</sup> of methane gas being produced without sand problems, despite limit 5 MPa of drawdown) (Yamamoto et al., 2019). Recently in 2017, the China Geological Survey extracted 309,000 m<sup>3</sup> of methane gas from natural gas hydrate deposits in the Shenhu area with a world record of the longest continuous duration of gas production and maximal gas yield (Li et al., 2018). As production costs are still high, an economically feasible way to exploit gas hydrates on a large scale should be found to commercialize the methane gas production from natural gas hydrate-bearing sediments. Furthermore, various phenomena (e.g. fine migration, pore clogging, sand production, grain crushing and gas-driven fractures in sediments) during gas production causing sediment instability should be studied more carefully.

As it is challenging to study *in-situ* MH dissociation of natural methane hydrate-bearing sediments, most of experimental works concern laboratory tests on synthetic specimens

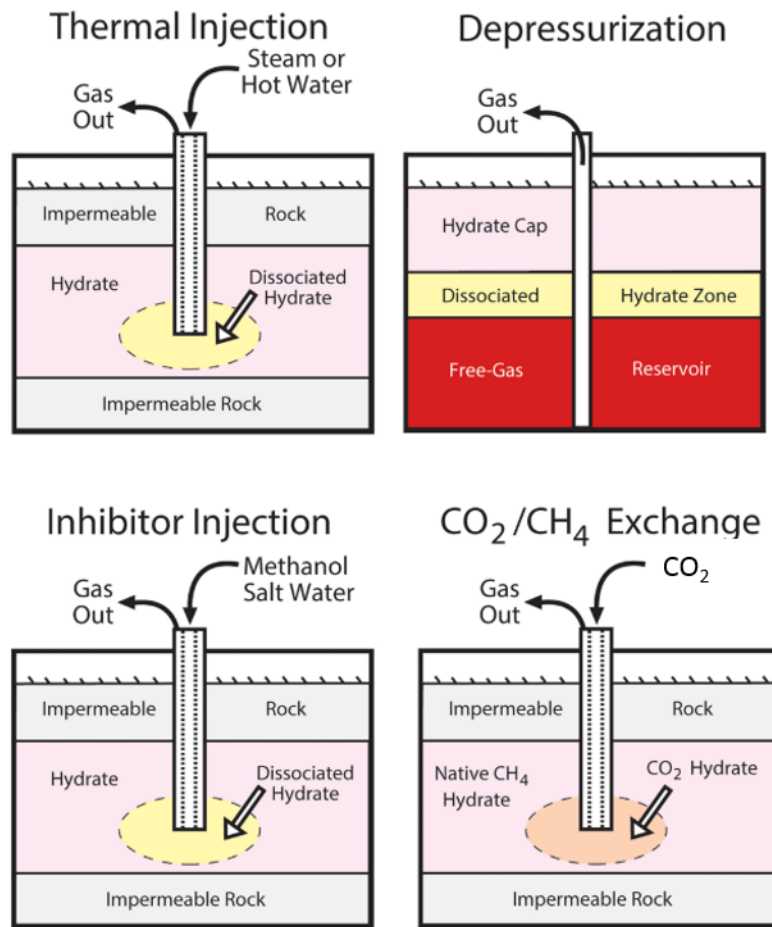


Figure 2.7: Diagram of proposed methane hydrate production methods (Collett et al., 2014).

to investigate methane hydrate dissociation rate, pressure-temperature evolution during MH dissociation (Haligva et al., 2010; Konno et al., 2012; Tonnet and Herri, 2009; Xiong et al., 2012). The experimental reactor dimension is a crucial factor. Actually, a larger reactor better mimics field conditions but it is more difficult to ensure the homogeneity of synthesized specimens in large reaction (Xu and Li, 2015).

The methane hydrate formation, dissociation and reformation in a partially water saturated Ottawa sand at different water saturations were studied by combining measurements of *MI* and elastic velocities (Rydzny, 2014). *MI* profiles along the specimen height after these three procedures (MH formation, dissociation and reformation) show an almost homogeneous distribution of MHs. The consolidation of the unsaturated sand may have induced a more homogeneous water distribution in the sample before the MH formation.

The effects of depressurizing range and rate of pressure drop on MH dissociation rate of methane hydrate-bearing glass beads under excess-gas conditions have been investigated via MRI (Zhang et al., 2016), and are shown in Figure 2.8. The average dissociation rates of Cases 1–3 (at different rates of pressure drop) were 0.01 %/min, 0.25 %/min and 0.23

%/min for depressurizing drops of 0.3 MPa, 0.7 MPa, and 1.1 MPa. The average dissociation rate of Case 1 was the lowest among the three cases (back pressure of 3.0 MPa was very close to the MH equilibrium pressure: 3.3 MPa). However, the average MH dissociation rate of Case 3 was lower than that of Case 2. Low back-pressure led to a large temperature drop, which can cause ice generation and MH reformation during MH dissociation, resulting in a greater heat transfer and slower MH dissociation rate.

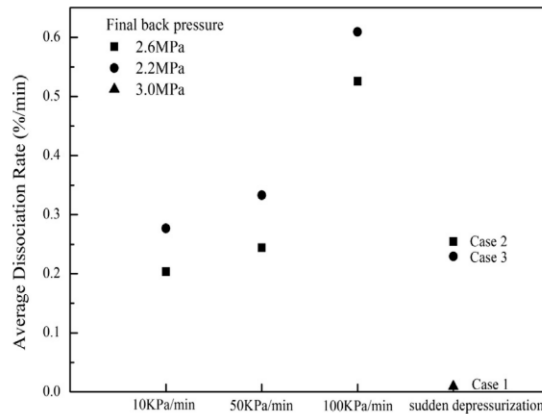


Figure 2.8: Average dissociation rates depending on depressurizing range and rate of pressure drop (Zhang et al., 2016).

## 2.2 Physical and mechanical properties

The knowledge of physical/mechanical properties of natural gas hydrates trapped in sediments is of the importance not only for detecting the presence of these compounds but also for estimating their amount in sediments, to predict how methane hydrate-bearing sediments evolve in response to changes in their surrounding environment, as well as to develop appropriate processes for natural gas exploitation. Furthermore, the presence of methane hydrates in marine sediments dramatically alters some of their physical properties (Gabbitto and Tsouris, 2010). Unfortunately, little is known about the physical properties of natural gas hydrate deposits in nature, making their detection by remote geophysical surveys difficult. In this section, some rare properties of pure gas hydrates are first presented. After that, some properties of gas hydrate-bearing sediments are mentioned.

### 2.2.1 Pure gas hydrates

The crystal structure of formed gas hydrates depends on the size of the guest molecule ( $CH_4$ ,  $C_2H_6$  form  $s_I$  hydrate;  $C_3H_8$  forms  $s_{II}$  hydrate while larger guest molecules such as cyclopentane form  $s_H$  hydrate in presence of methane gas) (Mak and McMullan, 1965). If all the cages of each gas hydrate structure are filled, they have approximate proportion of 85 % of water and 15 % of gas (Sloan, 1998). Therefore, gas hydrates have similar physical properties to those of ice (hexagonal crystal, shown in Table 2.1) except the thermal conductivity and the thermal expansivity (Cox, 1983; Tse, 1994). The thermal conductivity of clathrate hydrates, increasing slightly with an increase in temperature, is

five times lower than that of ice near the melting point and even lower (by a factor  $>20$ ) at a lower temperature (Tse and White, 1988).

Table 2.1: Comparison of properties of ice, sI, and sII hydrate crystal structures (Gabbitto and Tsouris, 2010).

Property	Ice ( $I_h$ )	Structure I	Structure II
Water molecules number	4	46	136
Lattice parameters at 273 K, nm	a = 0.452 c = 0.736	1.20	1.73
Dielectric constant at 273 K	94	~ 58	58
Water diffusion correlation time, $\mu$ s	220	240	25
Water diffusion activation energy, kJ/m	58.1	50	50
Isothermal Young's modulus at 268 K, GPa	9.5	8.4 (est.)	8.2 (est.)
Poisson's ratio	0.33	~ 0.33	~ 0.33
Bulk modulus (272 K)	8.8	5.6	NA
Shear modulus (272 K)	3.9	2.4	NA
Compressional velocity, m/s	3870.1	3778.0	3821.8
Shear velocity, m/s	1949.0	1963.6	2001.1
Velocity ratio (comp./shear)	1.99	1.92	1.91
Linear thermal expn., at 200 K, $10^{-6} K^{-1}$	56	77	52
Adiab.bulk compress, at 273 K, $10^{-11} Pa$	12	14 (est.)	14 (est.)
Heat capacity, $J kg^{-1} K^{-1}$	3800	3300	3600
Thermal conductivity, at 263 K, $W m^{-1} K^{-1}$	2.23	$0.49 \pm 0.02$	$0.51 \pm 0.02$
Refractive index, 638 nm, $-3^\circ C$	1.3082	1.3460	1.350
Density, $kg m^{-3}$	916	912	940

## 2.2.2 Gas hydrate-bearing sediments

The properties of sediments containing gas hydrates are expected to be similar to that containing ice, provided that the morphologies, pore habits and degree of saturation of MHs are similar to those of ice, as the physical properties of bulk hydrates are remarkably close to those of ice. However, unlike ice, hydrates can be ignited and require both low temperature and high pressure to be stable.

### 2.2.2.1 Thermal Conductivity

The material's responses to a heat addition or loss are described by the thermal conductivity (quantifying the efficiency of heat transport),  $\lambda$  ( $W m^{-1} K^{-1}$ ); specific heat (measuring the heat stored in or extracted from a material due to a temperature change),  $c_p$  ( $J kg^{-1} K^{-1}$ ); and thermal diffusivity (measuring the rate at which material changes temperature when subjected to an external heat flux),  $\kappa$  ( $m^2 s^{-1}$ ). We have:

$$\kappa = \frac{\lambda}{\rho c_p} \quad (2.1)$$

where  $\rho$  is volumetric mass of the material ( $kg/m^3$ ). In addition, heat flow in materials undergoing a phase change such as hydrates undergoing formation or dissociation is described by the reaction enthalpy,  $\Delta H$  ( $J mol^{-1}$ ). The thermal properties of the constitutive phases of gas hydrate bearing-sediments are summarized in Table 2.2 where the used references (a-t) were detailed in the work of Waite et al., 2009. Furthermore, Figure 2.9 shows the thermal conductivity for THF-saturated sand and kaolinite specimens before and after hydrate formation found by Cortes et al., 2009. A marked increase in

conductivity at low vertical effective stress in both sand and kaolinite specimens upon hydrate formation at a vertical effective stress of 0.05 MPa was observed.

Table 2.2: Thermal properties of hydrate-bearing sediment components (Waite et al., 2009).

Material	$\lambda(Wm^{-1}K^{-1})$	$\kappa(m^2s^{-1})$	$c_p(Jkg^{-1}K^{-1})$	$\rho(kgm^{-3})$
Air	0.024 <sup>b</sup> (273 K)	$183 \times 10^{-7c}$	1010 <sup>b</sup> (273 K)	1.298 <sup>d</sup> (272 K)
Water	0.56 <sup>e</sup> (273 K)	$1.33 \times 10^{-7c}$	4218 <sup>e</sup> (273K)	999.9 <sup>e</sup> (273 K)
Water	0.58 <sup>e</sup> (283 K)	$1.38 \times 10^{-7c}$	4192 <sup>e</sup> (283 K)	999.7 <sup>e</sup> (283 K)
Ice Ih	2.21 <sup>f</sup> (270K)	$11.7 \times 10^{-7c}$	2052 <sup>g</sup> (270 K)	917 <sup>h</sup> (273 K)
Methane gas	0.0297 <sup>i</sup> (260 K, 1 MPa)	$18.0 \times 10^{-7c}$	2170 <sup>d</sup> (260K)	7.61 <sup>i</sup> (260 K, 1 MPa)
Methane gas	0.099 <sup>i</sup> (260 K, 40 MPa)	$1.6 \times 10^{-7c}$	2170 <sup>d</sup> (260 K)	286 <sup>j</sup> (260 K, 40 MPa)
Methane hydrate, $CH_4.6H_2O$	0.57 <sup>k</sup> (263 K)	$3.35 \times 10^{-7l}$	2170 <sup>d</sup> (260 K)	929 <sup>n</sup> (263 K)
THF + water, $THF.17H_2O$	0.47 <sup>o</sup> (283 K)	$3.12 \times 10^{-7c}$	4080 <sup>p</sup> (282 K)	982 <sup>q</sup> (283 K)
THF hydrate, $THF.17H_2O$	0.5 <sup>f</sup> (261 K)	$2.55 \times 10^{-7f}$	2020 <sup>f</sup> (261 K)	971 <sup>r</sup> (273 K)
THF hydrate, $THF.17H_2O$	0.5 <sup>f</sup> (261 K)	$2.6 \times 10^{-7c}$	1980 <sup>s</sup> (260 K)	971 <sup>r</sup> (273 K)
Quartz	7.7 to 8.4 <sup>t</sup>	$41 \times 10^{-7c}$	730 <sup>b</sup> (273K)	2650 <sup>h</sup>

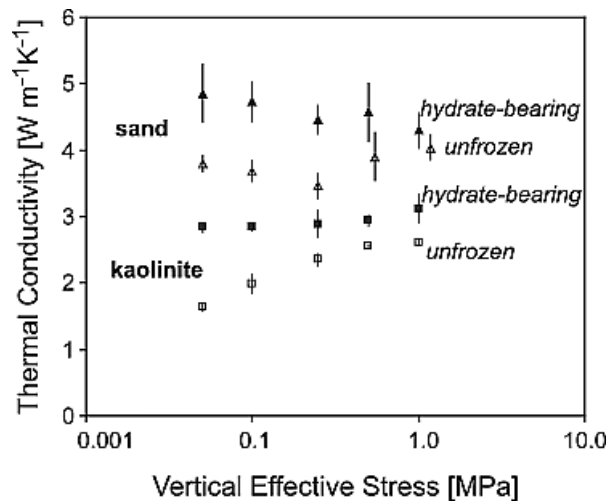


Figure 2.9: Thermal conductivity of hydrate-bearing sand and kaolinite (filled symbols) and saturated, unfrozen sand and kaolinite samples with water + liquid THF as the wetting fluid (open symbols) versus vertical effective stress. (Cortes et al., 2009).

### 2.2.2.2 Permeability and Fluid Migration

Fluid migration through a sedimentary system is controlled by permeability which plays an important role in heat and chemical transfer occurring via fluid migration. In gas hydrate-bearing sediments, permeability affects the dissolved gas and free gas transport as well as the hydrate accumulation, distribution and concentration (Waite et al., 2009). Therefore, permeability can influence the ability to produce methane gas from methane hydrate reservoirs, local perturbation of MH stability field and methane gas flux to the ocean (Moridis and Collett, 2003; Moridis and Reagan, 2007). The dissociation of gas hydrates results in a multi-phase fluid migration through these sediments. That is why it is mandatory to determine the relative permeability of both gaseous and aqueous fluids corresponding to different gas hydrate saturations and gas hydrate pore habits. However, few

reliable permeability measurements are available due to experimental setup challenges to prevent gas hydrate dissociation/dissolution (Minagawa et al., 2008; Kumar et al., 2010; Johnson et al., 2011; Konno et al., 2015).

On the basis of a multi-component, multi-phase, fluid and heat flow model, effects of gas hydrates on permeability of the sample through the reduction of pore size and shape were investigated by Liu and Flemings (2007). Pore-filling gas hydrates reduced the permeability more significantly than cementing - mineral coating gas hydrates. However, gas hydrates at grain contacts (cementing - grain contacts) can block the pore throats and cause a more pronounced permeability reduction (Liu and Flemings, 2007).

Macroscale analyses of single-phase and multi-phase flows in sediments generally assume that the sediments can be represented by an equivalent homogeneous porous medium. However, a proper understanding of conduction properties requires the pore-scale assessment of coexisting multiple phases and of all relevant flow pathways. Some studies have used XRCT to investigate permeability of gas hydrate-bearing sediments at the pore scale (Seol and Kneafsey, 2011; Dai and Seol, 2014).

### 2.2.2.3 Electromagnetic properties

In order to characterize natural gas hydrate-bearing sediments in the field, either electrical conductivity (inverse of resistivity) or permittivity can be used to distinguish between water and methane hydrate or ice (Waite et al., 2009).

Gas hydrates exclude salt in the pore fluid from which it forms, and thus they have high electrical resistivity just as ice. Therefore, sediments containing gas hydrates have a higher resistivity compared to sediments without gas hydrates (Judge, 1982). **The electrical conductivity** of gas hydrate-bearing sediments is dominated by the electrical conductivity of the pore fluid,  $\rho_f$ , scaled by the volume fraction of liquid in pores,  $\phi(1 - S_h - S_g)$  where  $\phi$ : porosity;  $S_h$ : gas hydrate saturation;  $S_g$ : gas saturation. However, the surface conduction (from electrical double layers around mineral surfaces) must be considered in high surface area sediments (Klein and Santamarina, 2003). The relation between electrical properties and hydrate saturation is generally based on Archie's equation whose parameters must be chosen with care (Waite et al., 2009).

Nominal **permittivity** values for components of methane hydrate-bearing sediments in the microwave frequency range are as follows: unfrozen water,  $\kappa_{w'} = 80$  (at 4 °C); gas/air,  $\kappa_{g'} \sim 1$ , most minerals,  $\kappa_{m'} \sim 4-9$  and methane hydrate,  $\kappa_{h'} = 2.5$ . The polarization of an unfrozen water dominates the permittivity of methane hydrate-bearing sediments. However, the permittivity of methane hydrates may be significantly higher at lower frequencies.

Electrical conductivity/permittivity approximations and field data were detailed by Waite et al., 2009. The anisotropy and spatial heterogeneity of sediments, altered by networks of methane hydrate lenses, cause additional difficulties for data interpretations and the selection of proper models.



### 2.2.2.4 Seismic wave velocity and small strain stiffness

Velocity of compressional P waves (producing longitudinal strains with particle motion in the direction of wave propagation) and shear S waves (causing shear strains with particle motion perpendicular to the direction of wave propagation), denoted  $V_P$  and  $V_S$  respectively, are extensively used for mapping methane hydrate occurrences and estimating methane hydrate saturation within those occurrences. The wave velocities are controlled by the sediment's small-strain bulk modulus,  $K_b$ , and shear modulus,  $G$ , according to:

$$V_P = \sqrt{\frac{K_b + \frac{4}{3}G}{\rho_b}} \quad (2.2)$$

$$V_S = \sqrt{\frac{G}{\rho_b}} \quad (2.3)$$

where  $\rho_b$  is the bulk sediment density. However, the increase of velocity with respect to the amount of gas hydrates mainly depends on how gas hydrates occur in the pore space (Waite et al., 2009). The presence of gas hydrates can alter the stiffness of both the pore fluid and the sediment skeleton. Different models have been proposed to quantify the amount of gas/gas hydrates in sediments: *WE* (Lee et al., 1996) (used empirical weighted equations), *TPEM* (Ecker et al., 1998) (used three-phase effective medium theory), *TPB* (Carcione and Tinivella, 2000) (used the three-phase Biot theory), *DEM* (Jakobsen, 2000) (used differential effective medium theory) and the effective medium modeling (Dvorkin et al., 2000).

Dvorkin et al., 2000 modeled first brine saturated sediments as a function of porosity, mineral, fluid moduli and effective stress. Afterward, gas hydrates, considered as pore fluid or sediment frame or cements (grain contacts or mineral coating), were taken into account.

The porosity at which a granular composite ceases to be a suspension and becomes grain supported is called the critical porosity  $\phi_c$ . For a dense random packing of nearly identical spheres,  $\phi_c$  is approximately 0.36-0.40 (Nur et al., 1998). The effective bulk  $K_{HM}$  and shear  $G_{HM}$  moduli of the dry rock frame at  $\phi_c$  are calculated from the Hertz-Mindlin contact theory (Minagawa et al., 2008). For porosity  $\phi < \phi_c$ , the bulk ( $K_{Dry}$ ) and shear ( $G_{Dry}$ ) moduli of the dry frame are calculated via the modified lower Hashin-Shtrikman bound (Dvorkin and Nur, 1996). The modified upper Hashin-Shtrikman bound is used when  $\phi > \phi_c$ .

For **the water saturated sediment baseline model**, the effect of water saturation is modeled by Gassmann's equations (Gassmann, 1951).

For **the gas hydrates as a part of pore fluid model (pore-filling)**, the presence of gas hydrates affects only the elastic modulus of the fluid and the bulk density of the sample. If gas hydrate and water are homogeneously mixed throughout the pore space, the effective bulk modulus of the water/hydrate pore mixture is the Reuss isostress average of the water

and gas hydrate bulk moduli ( $K_f$  and  $K_h$  respectively) (Reuss, 1929):

$$\bar{K}_f = \left( \frac{S_h}{K_h} + \frac{1 - S_h}{K_f} \right)^{-1} \quad (2.4)$$

where  $S_h$  is hydrate saturation and  $\bar{K}_f$  is pore fluid modulus in Gassmann's equations.

For **the gas hydrates as a part of the solid phase model (load-bearing)**, the original dry sediment calculations must be altered to account for the changes in the effective solid phase (mineral plus gas hydrate) moduli and sediment porosity.

The presence of gas hydrates reduces the porosity of the original sediment  $\phi$  down to a new value  $\bar{\phi} = \phi - C_h$ .

The effective mineral moduli for the gas hydrate/sediment solid phase is recalculated by treating hydrates as an additional mineral component with a volume fraction,  $\bar{f}_h$ :

$$\bar{f}_h = \frac{C_h}{1 - \phi + C_h} \quad (2.5)$$

For **the gas hydrates as cement - grain contacts or mineral coating** case, the contact cement theory (Dvorkin et al., 1994) has been used to calculate the effective bulk and shear moduli of dry cemented sphere pack (considered as a dense, random pack of identical elastic spheres):

$$K_{CCT} = \frac{n(1 - \phi_c)}{6} (K_c + \frac{4}{3}G_c)S_n \quad (2.6)$$

$$G_{CCT} = \frac{3}{5}K_{CCT} + \frac{3n(1 - \phi_c)}{20}G_cS_\tau \quad (2.7)$$

where  $K_c$ ,  $G_c$  are the bulk and shear moduli of the cement (gas hydrates);  $n$  is the average number of contacts per grain. The coefficients  $S_n$ ,  $S_\tau$  (solutions of integral equations, see (Dvorkin et al., 2000) for more details) depend on a parameter  $\alpha$  which can be evaluated for the two cement distributions.

For **cementing - grain contacts**:

$$\alpha = 2 \left[ \frac{\phi_c - \bar{\phi}}{3n(1 - \phi_c)} \right]^{0.25} \quad (2.8)$$

For **cementing - mineral coating**:

$$\alpha = \left[ \frac{2(\phi_c - \bar{\phi})}{3(1 - \phi_c)} \right]^{0.5} \quad (2.9)$$

The arrangement "cementing - grain contacts" is much stiffer than that of "cementing - mineral coating". Furthermore, at high cement concentrations, the model is greatly simplified by assuming equidimensional residual porosity. For this reason, only **cementing - grain contacts** is used to model high gas hydrate cement concentration (residual porosity <25 %). Figure 2.10 shows an example of wave velocity increase with an increase of hydrate saturation of the Malik samples (Dai et al., 2004).

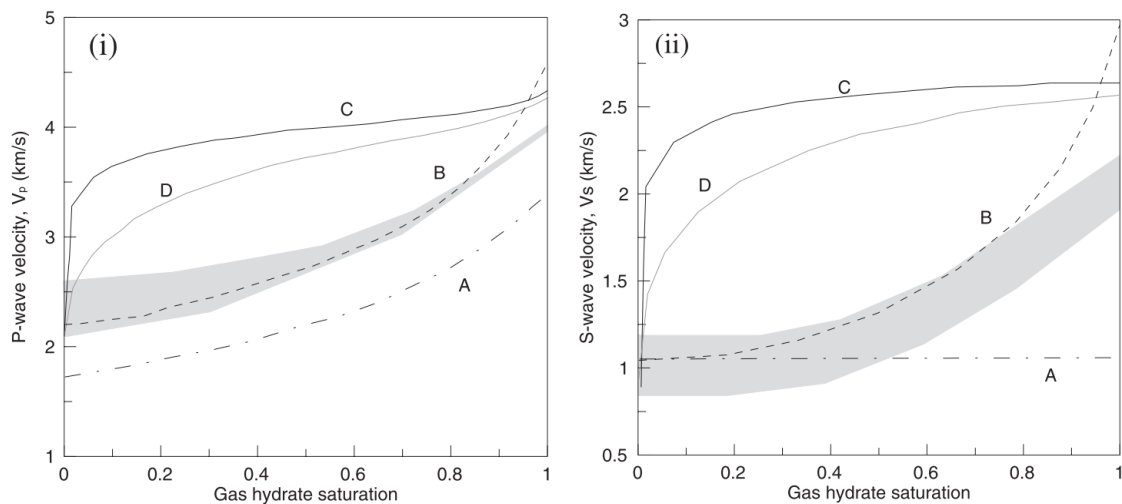


Figure 2.10: Model prediction for (i) P-wave velocity and (ii) S-wave velocity versus methane hydrate saturation in Malik 2L-38: (A) Pore-filling; (B) load-bearing; (C) cementing - grain contacts; (D) cementing - mineral coating (Dai et al., 2004).

### 2.2.2.5 Mechanical properties

#### Effects of gas hydrates on stress-strain behaviors

As gas hydrates in the pore space make the soil “effectively” denser or more bonded, it is usually assumed that gas hydrate-bearing soils behave similarly to bonded and dense soils (Uchida et al., 2012). Figure 2.11 shows the idealized geo-mechanical behaviors of bonded and dense soils. Contact stiffness hence macroscopic tangent stiffness (gradient of deviator stress  $q$  versus deviatoric strain  $\epsilon_d$ ) together with shear resistance (peak strength, represented by the greatest value of  $q$ ) increase with the formation of bonds at grain contacts or interlocking of grains. More dilation is also observed once bonds are increased. However, once the bonds or interlockings are broken due to shearing, the soils exhibit strain softening behavior (the shear resistance is decreased).

Furthermore, triaxial tests also provide prefailure information to determine Young’s modulus,  $E$ ; Poisson’s ratio,  $\mu$  whose values are often reported at 50 % of the failure load,  $E_{50}$  and  $\mu_{50}$ .

The measured stress-strain responses of natural gas hydrate-bearing sandy sediments retrieved from the Nankai Trough as a function of methane hydrate saturation under drained conditions (Masui et al., 2006) are shown in Figure 2.12. The dilation angle,  $\psi$ , can be calculated from the slope of the volumetric strain as shown in Figure 2.12. In general, the peak strength,  $E_{50}$  and the dilation angle increased with an increase in methane hydrate saturation. However, the Poisson’s ratio,  $\mu_{50}$ , varied between 0.10 and 0.19, with no apparent relation with methane hydrate saturation.

Almost all the experimental works concern laboratory tests on synthetic samples because of challenges to get cored-intact methane hydrate-bearing sediment samples. With re-

cent advances in core pressure technology (pressure-core analysis and transfer system - PCATs), temperature and pressure of samples were maintained within methane hydrate stability so that mechanical tests on almost no disturbed Nankai Trough samples could be done. However, improvements are still needed to increase the successful pressuring core ratio and also to well extrude samples into PCATs Triaxial cell (Yamamoto, 2015; Yoneda et al., 2015; Santamarina et al., 2015).

Some data showing the effects of gas hydrate saturation (THF hydrates or MHs) on maximum tangent stiffness, peak strength and dilation angle of synthetic gas hydrate-bearing sandy sediments (in drained conditions) are shown in Figure 2.13 (Uchida et al., 2012). All the samples were tested at an effective confining stress of 1 MPa. These mechanical values at different gas hydrate saturations were normalized by those without gas hydrates. It can be seen that gas hydrate-bearing sands exhibited greater stiffness, strength and dilatancy compared to those of sands without gas hydrates.

Masui et al., 2005a and Ebinuma et al., 2006 prepared synthetic methane hydrate-bearing sandy sediments at different methane hydrate saturations using the excess-gas method and the ice-seeding method. The results showed that the peak strength (maximum deviator stress) increased with an increase in methane hydrate saturation, Figure 2.14. However, the rate of increase was different. It was believed that MHs formed after the excess-gas method created strong contact bonds within sediments while weak contact bonds were created for MHs formed following the ice-seeding method. Note that Ebinuma's data were at 3 MPa of confining pressure (Ebinuma et al., 2005) whereas Masui's data were at 1 MPa (Masui et al., 2005). All test were under drained conditions.

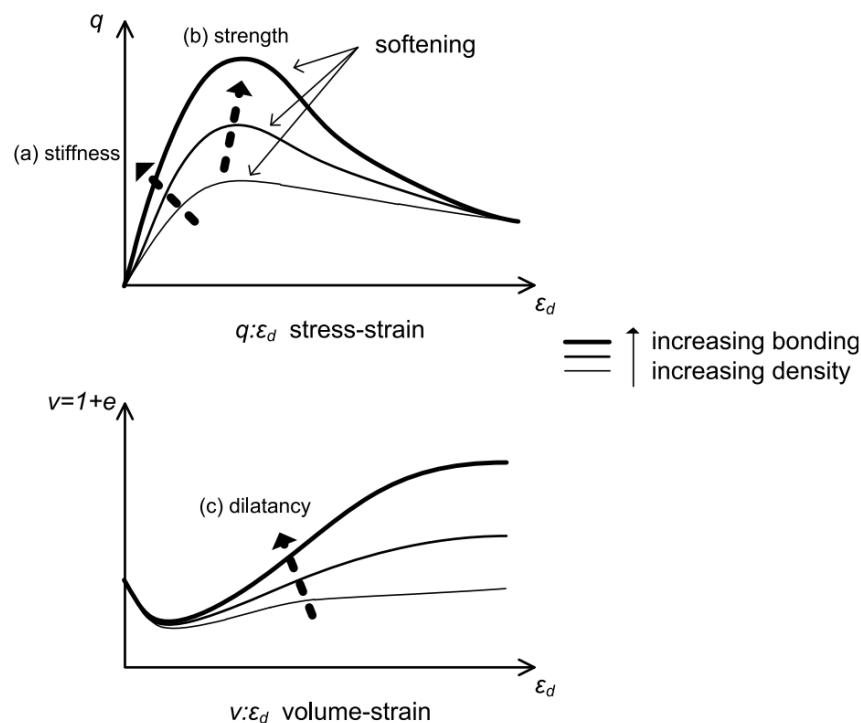


Figure 2.11: Conventional drained triaxial compression test on bonded and dense soil (Uchida et al., 2012).

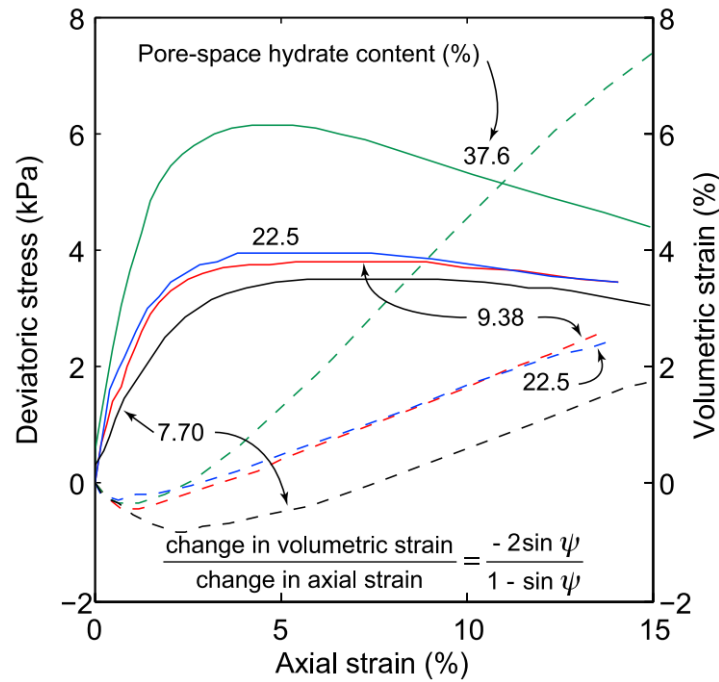


Figure 2.12: Dependence of stress (solid curves) and volumetric strain (dashed curves) on axial strain for four methane hydrate-bearing sands (Masui et al., 2006).

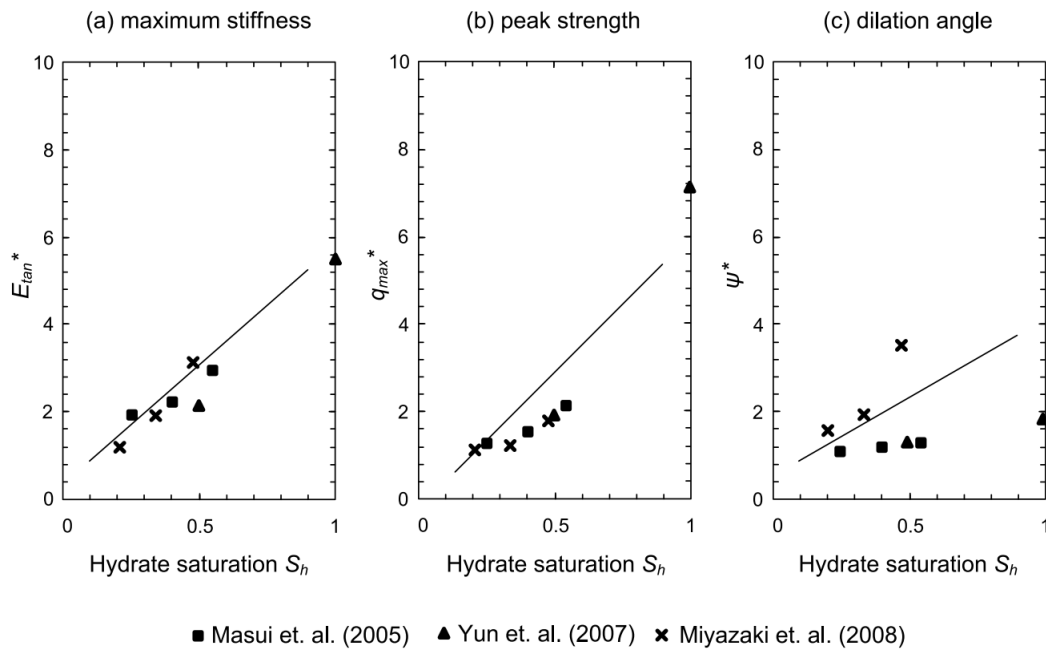


Figure 2.13: Effect of gas hydrate saturation on (a) stiffness, (b) strength and (c) dilatancy (Uchida et al., 2012).

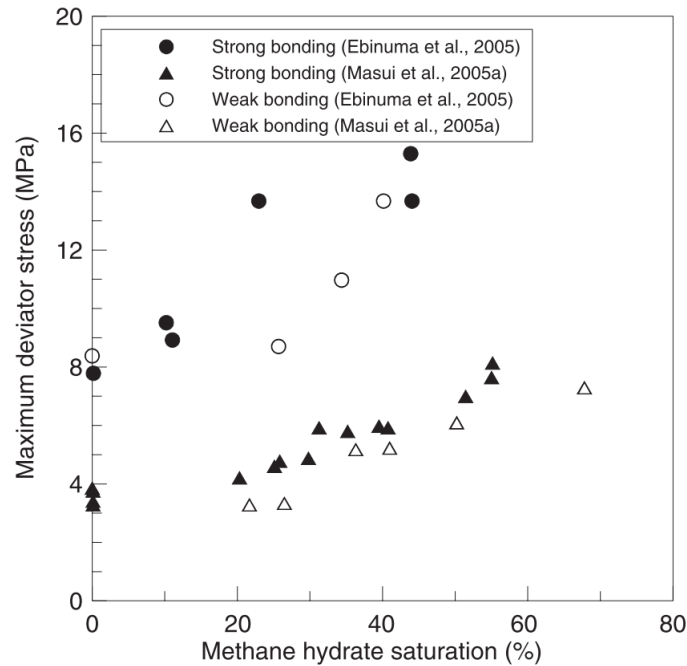


Figure 2.14: Peak strength versus methane hydrate saturation (Soga et al., 2006).

Hyodo et al., 2013 and Miyazaki et al., 2011 formed methane hydrates in sandy sediments under excess-gas conditions (by freezing unsaturated sandy specimens, injecting methane gas and finally increasing temperature for the MH formation) then saturated the media with water (water-saturated media). The experimental results obtained during drained triaxial tests showed higher values of maximum deviator stress, secant Young's modulus, residual deviator stress (deviator stress at high axial strain rate), and dilation angle at a higher methane hydrate saturation. Furthermore, a higher effective confining stress enhanced the frictional force between the particles, and more energy was required to overcome the intergranular frictional force during the shear test (Hyodo et al., 2013). The failure strength, shown in Figure 2.15, of gas-saturated specimens showed a more marked dependency on methane hydrate saturation than that of water-saturated specimens.

Sandy sediments usually deform under drained conditions because of the high permeability of the soils. However, undrained conditions can occur for sandy methane hydrate-bearing sediments in some scenarios (e.g. very rapid drawdown of borehole pressure, limited drainage due to low permeability of surrounding clay layers, a sudden landslide event or earthquake).

The results of undrained triaxial tests of coarse sands recovered from the Mallik 2L-38 permafrost were presented by Winters (2000). The presence of methane hydrates in sediments increased the undrained shear strength dramatically compared to that of specimens without MHs. In addition, methane hydrate-bearing sediments exhibited large negative excess pore pressures, whereas sediments without MHs showed much smaller negative excess pore pressures. That means that the samples with MHs exhibited dilation tendency while the samples without MHs showed rather limited dilation tendency. Congruent trends were observed when compared to those gathered in drained tests: gas

hydrate-bearing sands exhibited a higher dilation tendency than the same sediments without gas hydrates (Winters, 2000).

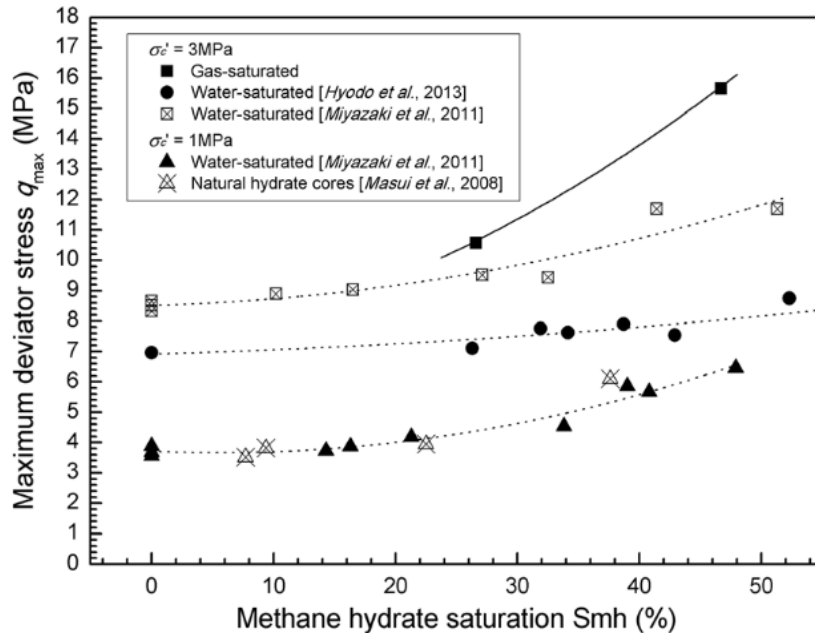


Figure 2.15: Maximum deviator stress of gas-saturated and water-saturated specimens plotted against methane hydrate saturation (Hyodo et al., 2013).

**The effects of fine contents and density** on peak shear strength, stiffness, and deformation behavior of synthetic methane hydrate-bearing sediments were investigated by Hyodo et al., 2017. An increase of fine contents within methane hydrate-bearing sandy sediments significantly enhanced the peak shear strength and promoted a dilation behavior. The formation of MHs in samples with various amounts of fine contents increased the stress ratios at the critical state. Furthermore, it was supposed that an addition of fine particles into coarse sands altered the internal microstructure of sand matrix and the MH formation patterns in the pore space between sand grains and fines particles (Hyodo et al., 2017).

Drained behaviors of **clayey methane hydrate-bearing sediments** are important to assess the long-term deformation behaviors of the sediments. However, limited drained shear data are available, further investigations are needed. Undrained compression tests (axial strain rate: 0.05 %/min) were conducted on methane hydrate-free sediment AT1-C-6P (82-92) and methane hydrate-bearing pressure core clayey silt AT1-C-8P (102-112) with  $S_h = 23$  % (Yoneda et al., 2017). The stress-strain curves, the excess pore water pressure versus axial strain and the effective stress path are shown in Figure 2.16. For AT1-C-8P (102-112), results of the pressure core and the reconstituted sample using the same sediments are quite different. Positive excess pore pressure gradually increased with an increase in axial strain for all tests. Low found strengths were supposed due to the low permeability and existence of gas hydrate (AT1-C-6P (82-92) showed a strength ( $\sim 1$  MPa) at around 5 % of the axial strain while a peak strength of only 0.8 MPa appeared at

an axial strain of 12 % for AT1-C-8P (102-112)).

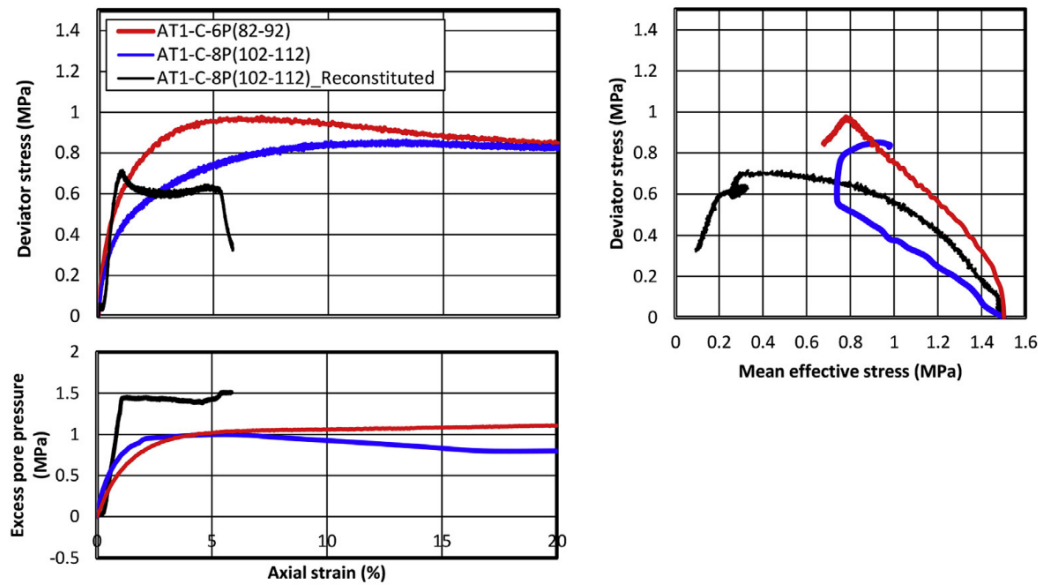


Figure 2.16: Stress-strain curves, excess pore pressure with axial strain, and effective stress path (Yoneda et al., 2017).

Undrained triaxial test data gathered for THF hydrates disseminated in Kaolinite clay and precipitated silt (each silt grain was an agglomerate) were summarized by Yun et al., 2007. Specimens without gas hydrates exhibited a frictional, linear increase of undrained shear strength as the initial effective confining stress increased. However, for high gas hydrate saturation sediments, the undrained shear strength was insensitive to the effective confining stress. The undrained modulus  $E_{50}$  followed a similar trend (Yun et al., 2007).

**The micro-mechanical behaviors of gas hydrate-bearing sediments** have not been well investigated because of experimental setup limitations. The macro and micro behavior of MH-bearing sand subjected to plane strain compressions was investigated experimentally by using both a confining plate and observation windows (Kato et al., 2016). The thickness of shear bands in MHBS was thinner than that in the pure host sand, independently of the confining pressure. Similarly, contractive and dilative behaviors were always observed in the shear band in MHBS without the influence of confining pressure. By using a novel high-pressure microtriaxial testing apparatus, Yoneda et al., 2016 observed triaxial compression of cemented krypton hydrate-bearing sands at submillimeter and micrometer scales via XRCT. Some changes in structure of soil particles which were weakly cemented by gas hydrates and in cluster shape were observed. In the shear band, sediment structure significantly changed due to movement and rotation of soil particles and gas hydrates. Furthermore, with an increase in  $S_h$ , the inclination angle of the shear band (expressed by the Mohr-coulomb failure criteria as  $\theta = \pi/4 + \phi/2$ , where  $\phi$  is the material internal friction) increased while the thickness of the shear band decreased. The micromechanism of the shear deformation of MHBS is shown in Figure 2.17.



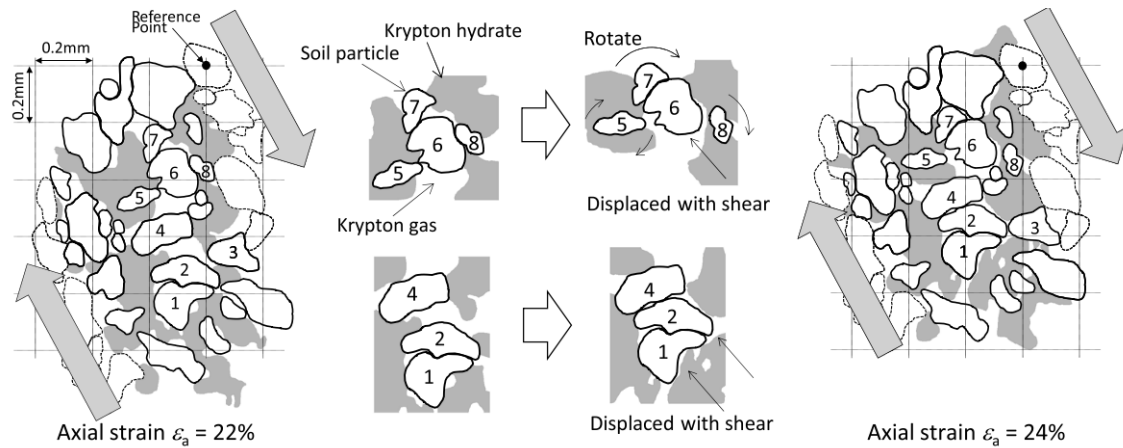


Figure 2.17: Micromechanism of the shear deformation of gas hydrate-bearing sand (Yoneda et al., 2016).

**Several constitutive models for methane hydrate-bearing soils** have been proposed to incorporate the effects of methane hydrates on stress-strain behaviors of soils. Uchida et al., 2012 summarized some methane hydrate constitutive models, as shown in Table 2.3. Most cases used the elastic/perfect plastic Mohr-Coulomb model (stiffness and strength parameters are a function of methane hydrate saturation) (Freij-Ayoub et al., 2007; Rutqvist et al., 2009; Klar et al., 2010). Original/Modified Cam-clay model has been used to take into account volumetric yielding (Kimoto et al., 2010; Sultan and Garziglia, 2011; Uchida et al., 2012). The Methane Hydrate Critical State model proposed by Uchida et al., 2012 can take into account not only the effects of MHs on enhancing stiffness, strength, dilatancy, softening, volumetric yielding but also the degradation of methane hydrate cementing and interlocking by plastic straining. Sanchez et al., 2017 adopted some concepts suggested by Uchida et al., 2012 to deal with specific features of methane hydrate-bearing soils but replaced the Modified Cam-clay model by the Hierarchical Single Surface (HISS) elasto-plastic one (incorporating sub-loading and dilation enhancement concepts). However, the number of inputs for these constitutive models is really important.

**The discrete element method** (DEM, treating soils as an assembly of discrete elements, starting with basic constitutive laws at interparticle contacts) appears to be a powerful numerical modeling approach for investigating mechanical behaviors and strain localizations of sands (Jung et al., 2012; Brugada et al., 2010). Microscopic and macroscopic responses of the particle assembly under different loading conditions can be calculated (Jung et al., 2012). Brugada et al., 2010 studied the effects of methane hydrate saturation (pore-filling) on the stress-strain relationship, the strain volumetric responses and the mechanical properties of sediments by a series of DEM simulations of triaxial tests. The results of the numerical simulations were compared with the laboratory triaxial test data of Masui et al., 2005 performed on sandy methane hydrate-bearing sediments. In addition, a simple bond contact model was proposed to study the effects of methane hydrates (cementing), whose simulations confirm that DEM was a powerful method to investigate methane hydrate-bearing sediments (Jiang et al., 2013). Furthermore, based on results of a series of laboratory tests on the bonded granules idealized by two glued aluminum rods

and the available experimental data of methane hydrate samples, a pressure and temperature dependent bond contact model was proposed (Jiang et al., 2014).

Table 2.3: Gas-hydrate constitutive models (Uchida et al., 2012).

Parameter	Mohr-Coulomb model based			Critical State model based	
	Freij-Ayoub et al. [2007]	Rutqvist and Moridis [2007]	Klar et al. [2010]	Kimoto et al. [2010]	Methane Hydrate Critical State
Stiffness	Yes	Yes	Yes	No	Yes
Strength	Yes	Yes	Yes	Yes	Yes
Dilation	No	No	Yes	Yes	Yes
Softening	explicit	explicit	No	Yes	Yes
Vol. yield	No	No	No	Yes	Yes
Bond deg.	No	No	No	No	Yes

### Effects of methane hydrate dissociation

Methane hydrate dissociation reduces the solid methane hydrate volume, produces methane gas and water, and decreases water salinity. Depending on boundary conditions, these changes produce: variations in the pore fluid pressure and the effective stress and/or changes in the volume occupied by the sediment (Waite et al., 2009). In natural settings, volume contraction typically follows the MH dissociation due to some mechanisms as bulk MH dissociation, disseminated MH dissociation, effective stress increase, mineral migration/removal. Furthermore, the horizontal effective stress decreases during the MH dissociation. As the results, sediments can reach internal shear failure conditions (Shin and Santamarina, 2009). The effects of MH dissociation on shear strength and deformation behaviors of methane hydrate-bearing sediments are of the importance in the context of geo-hazards and energy resource of methane hydrate-bearing sediments.

Fundamental understandings of the MH dissociation kinetics are essential to predict the MH reservoir dissociation process in the objective of selecting appropriate methane hydrate-bearing zones and estimating methane gas production behaviors before the execution of any field tests. Some kinetic models were developed to simulate the production process based on heat/mass transfer and/or intrinsic kinetics of MH decomposition and/or gas-water two-phase flow (Yousif et al., 1991; Hong et al., 2003). Different assumptions were used, their applicability to reservoir-level studies is also limited to particular situations. Various MH reservoir simulators (computational tools taking into account the complex highly-coupled transport equations, the reaction kinetics, the phase transition and the physical/chemical properties of methane hydrate-bearing sediments, for example Hydrosim, MH 21, STOMP-HYD, CMG-STARs, TOUGH + HYDRATE), are being developed (Moridis, 2008; Yamamoto, 2015; Xu and Li, 2015). Figure 2.18 shows an example of numerical simulations using TOUGH + HYDRATE to optimize the production strategy for different types of MH reservoirs. The effects of vertical/horizontal well configuration, reservoir temperature and methane hydrate saturation on methane gas production were investigated. However, further field-scale production tests are needed to improve the accuracy of those numerical predictions.

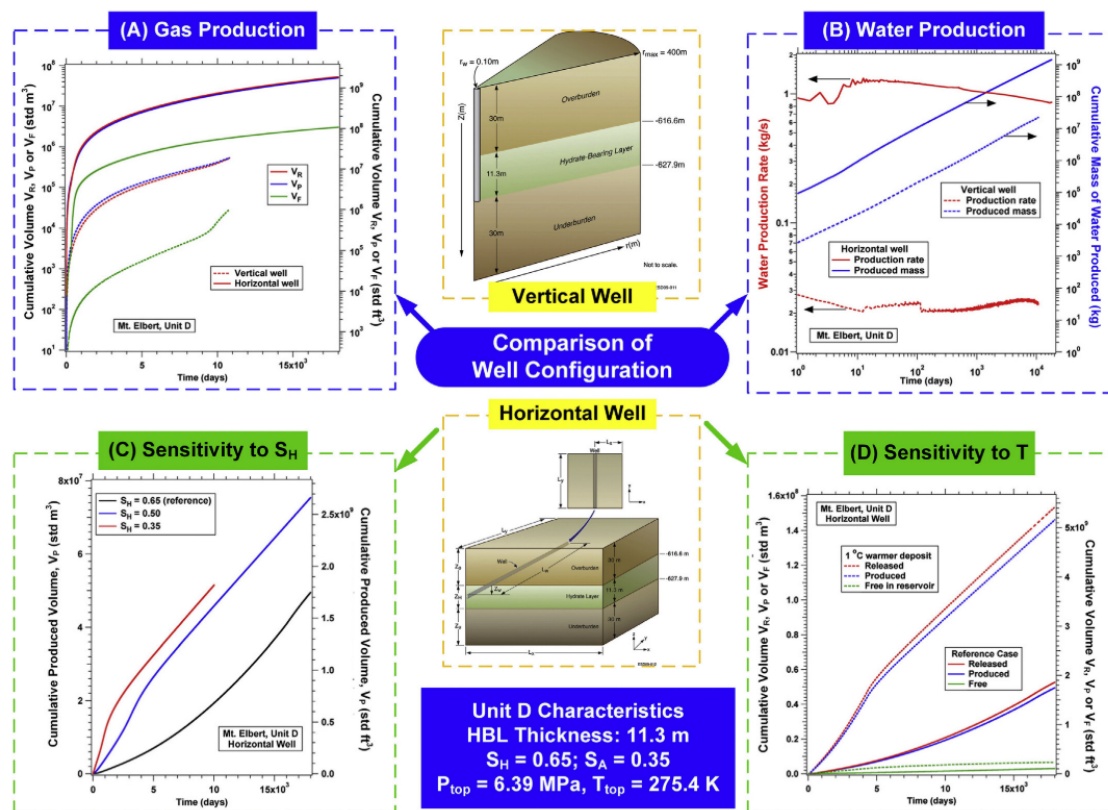


Figure 2.18: Simulation results from  $(T + H)$  for Class 3 hydrate deposit with properties retrieved from Mt. Elbert Gas Hydrate Stratigraphic Test Well, Alaska. Compiled with permission (Moridis et al., 2011).

At the laboratory scale, Hyodo et al., 2013 studied the deformation behaviors of isotropically consolidated MHBS which were dissociated by heating and depressurizing. The MH dissociation by heating caused large axial strains for samples with an initial shear stress and total collapse for samples consolidated in the metastable zone. On the other hand, axial strains were generated by increasing effective stress until a stable equilibrium was reached for the case of MH dissociation following the depressurization method.

The shear strength and deformation behaviors of methane hydrate-bearing sediments during the MH dissociation following the thermal or depressurization method were investigated by Hyodo et al., 2014. Figure 2.19 and Figure 2.20 show the relations of deviator stress, axial strain and volumetric strain of:

- Isotropically consolidated specimens which were dissociated using the thermal recovery method (T-c5-01, T-c5-02, T-c5-03) and pure Toyoura sand (S-c5-01), Figure 2.19;
- $K_0$  (0.4) consolidated specimens during the depressurization, Figure 2.20

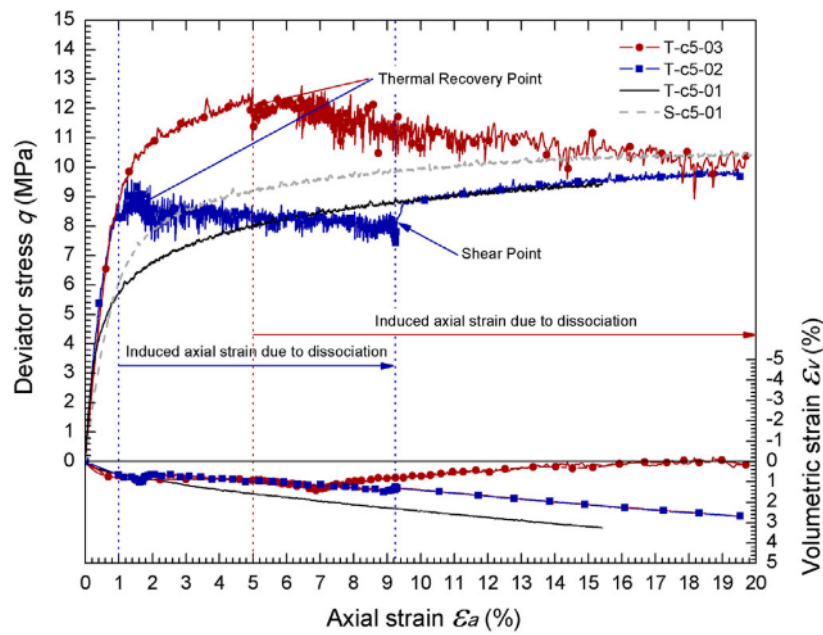


Figure 2.19: Deformation behaviors of isotropically consolidated methane hydrate bearing sediments dissociated by the thermal recovery method (Hyodo et al., 2014).

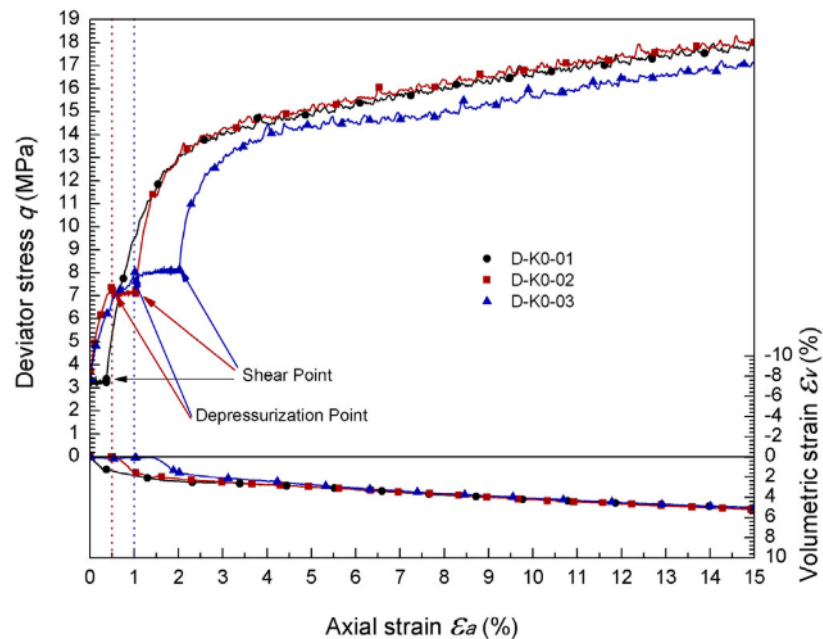


Figure 2.20: Deviator stress, volumetric strain and axial strain relations of the  $K_0$  consolidated methane hydrate-bearing sediments during the depressurization and shear process (Hyodo et al., 2014).

The results indicated that:

- The failure strength of isotropically consolidated methane hydrate-bearing sediments (dissociated completely using the thermal method) was less than that of pure

Toyoura sand. However, the initial stiffness and volumetric strain were higher than that of pure Toyoura sand. The thermal method can cause the failure of methane hydrate-bearing sediments when the axial load was higher than the strength of methane hydrate-bearing sediments after the MH dissociation;

- The depressurization method would not cause collapse of methane hydrate-bearing sediments during the depressurization. However, water pressure recovery would lead to failure when the axial load was higher than the strength of the methane hydrate-bearing sediments after the MH dissociation.

Jung et al., 2011 investigated **the effects of small fraction of fine particles on gas production** from gas hydrate-bearing sediments and on the sediment stability via  $CO_2$  hydrates. It was found that even small fraction of fines can decrease the pore size and the sediment permeability dramatically. Gas hydrate saturation and pore habits changed with fine content. Figure 2.21 summarizes suggested effects of fine contents on gas production from gas hydrate-bearing sediments.

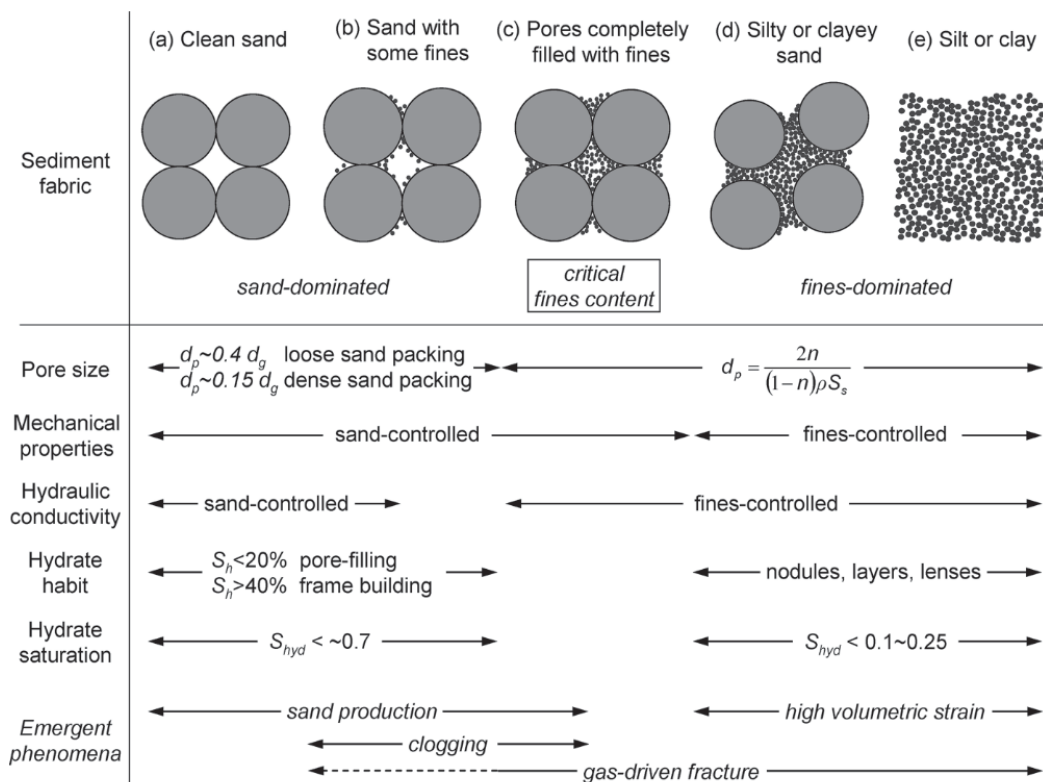


Figure 2.21: Sediment characteristics and physical properties: the relevance of fines and potential phenomena during gas production (Jung et al., 2011).

## 2.3 Pore-scale observations

### 2.3.1 Pure gas hydrates

Optical microscopy has been widely used to follow the kinetics of pure gas hydrate formation and dissociation (Uchida et al., 1999; Beltrán and Servio, 2010). It was found

that the morphology of gas hydrates changes considerably with different pressure and temperature conditions (Ohmura et al., 2005; Servio and Englezos, 2003). Methane and Carbon dioxide hydrates were formed on spherical water droplets at several pressures above the corresponding three-phase hydrate equilibrium pressure (Servio and Englezos, 2003). Water droplets were jagged and exhibited many hair-like crystals extruding from the droplet surfaces at higher pressures while the droplet surfaces were smooth at lower pressures. Furthermore, various morphologies of  $CO_2$  hydrates were observed in water saturated with  $CO_2$  gas (Figure 2.22) as dendrites at high sub-cooling temperatures, thick columns or polyhedral crystals at lower sub-cooling temperatures (Ohmura et al., 2005).

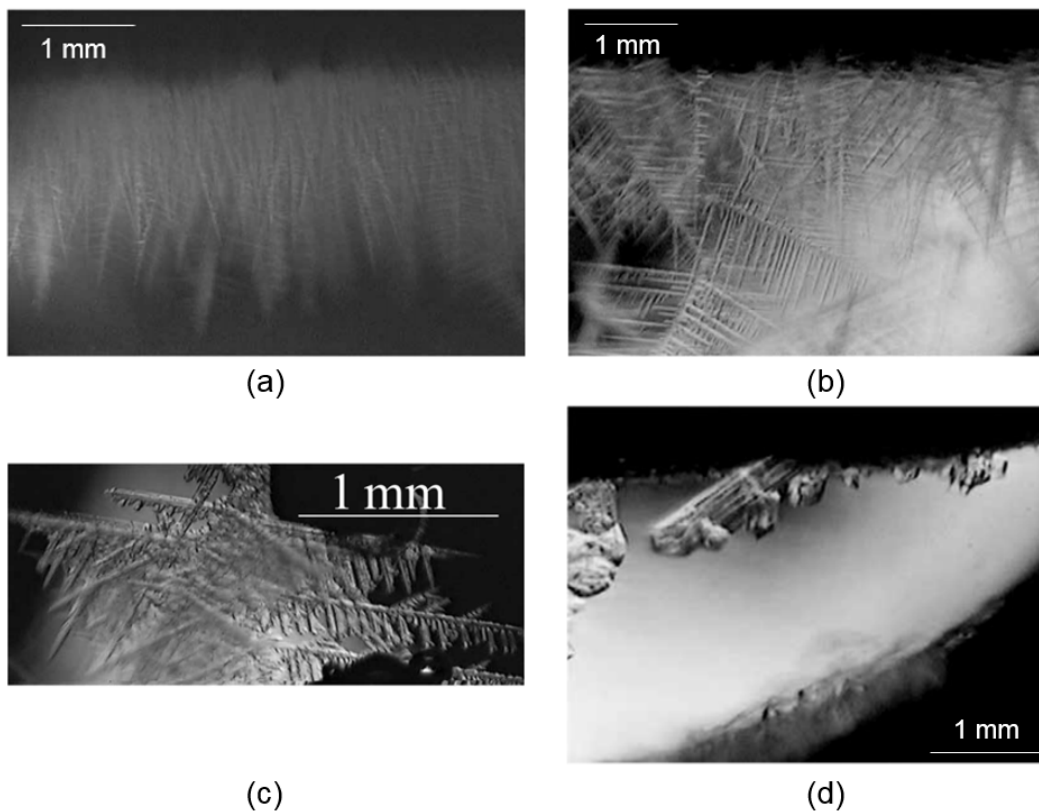


Figure 2.22:  $CO_2$  hydrate morphology depending on sub-cooling temperature,  $\Delta T$ : a,  $\Delta T = 5.8\text{ }^\circ\text{C}$ ; b,  $\Delta T = 3.6\text{ }^\circ\text{C}$ ; c,  $\Delta T = 3.0\text{ }^\circ\text{C}$ ; d,  $\Delta T = 2.3\text{ }^\circ\text{C}$  (Ohmura et al., 2005).

Gas hydrate formation and growth on glass micromodels (i.e., a 2D network of channels and pores) were also observed by means of optical microscopy (Tohidi et al., 2001), Figure 2.23. The micromodel was first flushed with methane gas and distilled water. Afterward, pressure and temperature were set for MH formation ( $-4.0\text{ }^\circ\text{C}$  and 5.5 MPa, no ice presence). The MH formation began after 12 h and then their growth proceeded rapidly. Crystallization began at methane gas/water interfaces by encapsulating methane gas bubbles with a crust of methane hydrates which were then collapsed inward as the methane gas trapped inside was converted to MHs. In some cases, crystallization spread from one to another methane gas bubble via small seed nuclei being forced along by the fluid movement. After crystallization, MHs underwent redistribution over a period of 36 h, although no specific patterns emerged. Generally, MH regions grew in size by the

agglomeration of smaller crystal masses to minimize surface area and energy.

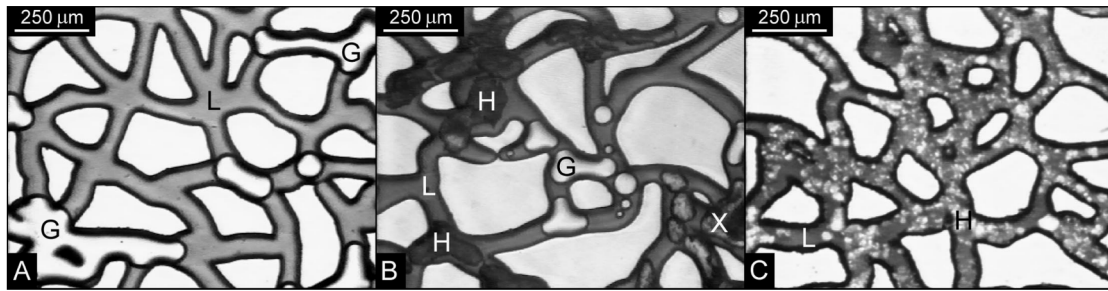


Figure 2.23: Micromodel tests: A, Bubbles of methane gas (G) and liquid (L) prior to MH formation (White areas are grains); B, Newly formed MHs (H), liquid, and gas bubbles during formation (Light gray areas visible within some dark methane hydrate crystals (X) are encapsulated methane gas bubbles, prior to their complete conversion to clathrate); C, MH redistribution after 2 days (MHs are white areas visible against dark zones of liquid) (Tohidi et al., 2001).

### 2.3.2 Gas hydrate-bearing sediments

X-ray computed tomography (XRCT) has been extensively used to investigate the 3D microstructure of gas hydrate-bearing sediments thanks to its high spatial resolution (Jin et al., 2006; Kneafsey et al., 2007; Kneafsey, 2011; Ta et al., 2015; Zhao et al., 2015b). However, this is really challenging to investigate MHs due to not only the need of special experimental setups (both high pressure and low temperature should be maintained during scans) but also to poor image contrast between methane hydrate and water. At an insufficient image spatial resolution, it is impossible to observe directly gas hydrate morphologies and pore habits without using segmentation methods based on gray values. Efforts have been made to improve the image spatial resolution. Furthermore, contrast in a XRCT image is mainly defined by the material attenuation difference, which depends on the material density and the atomic number. Therefore, it is difficult to distinguish methane hydrate from water in a XRCT image. Within high temporal resolution of Synchrotron radiation X-Ray computed tomography (SXRCT), gas hydrate growth and dissociation in sediments at the grain scale were followed. In addition, the spatial resolution of image was improved (Kerkar et al., 2009; Chaouachi et al., 2015; Kerkar et al., 2014; Yang et al., 2016a; Sahoo et al., 2018; Han et al., 2018).

By using traditional segmentation method based on gray values, it was observed that methane hydrates in sandy sediments, formed following the excess-gas method from deionized water, shown in Figure 2.24, were at gas-water interfaces, and floated between sand grains without coating grain surfaces (a water layer was found to envelop grain surfaces) (Jin et al., 2006; Zhao et al., 2015b; Yang et al., 2015). However, image noise, low contrast and partial volume effect can strongly influence the segmentation and the final attributed phases. Morphologies and pore habits of MHs are in questionable.

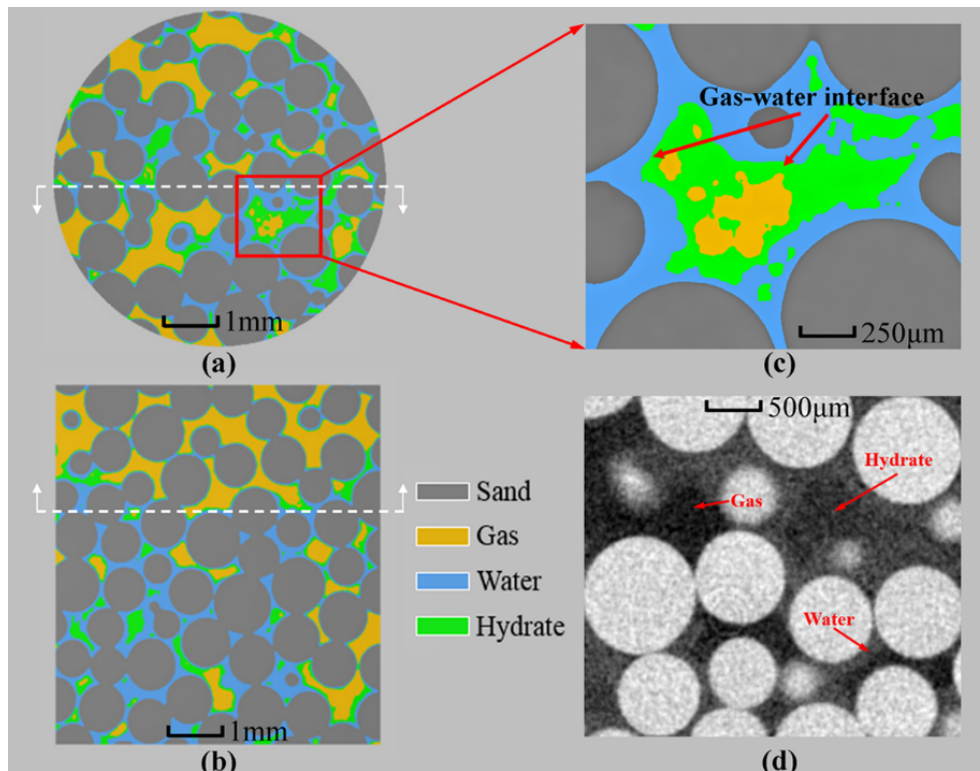


Figure 2.24: Original local gray scale 2D cross section image and segmented image of natural gas hydrate-bearing sands. The component in green represents the methane hydrate phase, which has no contact with the grain surfaces. The water layer in blue was observed to coat the sands (Yang et al., 2015).

To improve XRCT image contrast, Tetrahydrofuran or other types of gas (Carbon dioxide or Xenon) or saline water solutions (Sodium chloride -  $NaCl$ , Barium chloride -  $BaCl_2$ , Potassium iodide -  $KI$ ) have been used (Chaouachi et al., 2015; Kerkar et al., 2009; Kerkar et al., 2014; Ta et al., 2015). Note that the methane hydrate phase boundary depends on salt concentration contained in water (Sloan Jr and Koh, 2007) and salt exclusion during gas hydrate formation can increase salt concentration in the remaining water. Furthermore, morphologies of gas hydrates can depend on the type of used gas.

The nucleation and growth of Xenon hydrate-bearing sediments with submicron voxel resolution were observed by means of SXRCT (Chaouachi et al., 2015). Hydrates were first found at interfaces between juvenile water and xenon gas when the excess-gas method was used. Figure 2.25 shows Xe hydrate growth over time. Micron-sized single crystals were developed over Xe hydrate films (the emerging polyhedral shapes). Some of these accumulated crystals appeared to grow faster than the others. These larger crystals showed an appreciable growth into the gas phase and led to nearly isometric crystal shapes, consistent with a cubic crystal structure. Finally, polyhedral crystals of Xe hydrates around grains and loosely connected aggregates of Xe hydrate crystals in the pore space were found. Thin layers of water were observed to exist between sand grains and hydrates but not when hydrophobic glass-beads were used. Furthermore, experiments with Xe-enriched water showed similar particle arrangements toward the end of the Xe hydrate formation process.



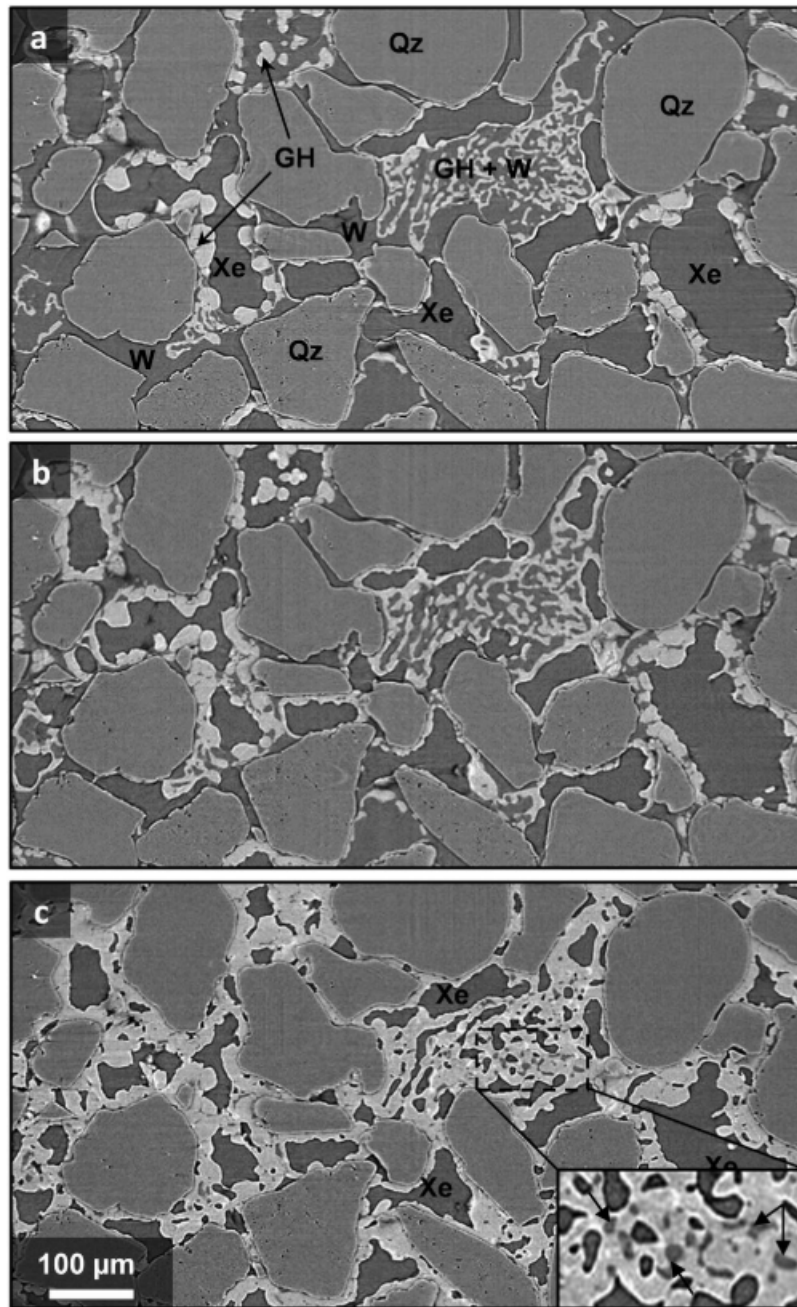


Figure 2.25: Sequence of GH film growth observed by SXRCT when the excess-gas method was used: (a) initial ( $t_R = 4.35$  min); (b) intermediate ( $t_R = 10.2$  min); (c) final ( $t_R = 14.65$  min). The enlarged image shows pockets of remaining water trapped between hydrate crystals probably due to a gas diffusion limitation (Chaouachi et al., 2015).

Chen et al., 2018 observed the Ostwald ripening - changes of Xenon hydrate pore habits and distribution at both the pore and core scales in sediments due to the difference of pressure between gas hydrate and water, termed as “cryogenic suction” via XRCT experiments. Note that Xenon hydrates were formed following the excess-gas method from saline water solution with Sodium Bromide -  $NaBr$ , 10 wt%. Furthermore, water migration during the  $CO_2$  hydrate formation in sediments (consisting of different mass fractions

of sand, clay, and water) was supposed due to cryogenic suction, soil skeleton deformation by capillarity and/or crystallization stress (Lei et al., 2019a). However, the image spatial resolution was low (voxel size bigger than  $10\ \mu\text{m}$ ). The discontinuous water migrations during MH formation in an unsaturated sand (with  $\text{NaBr}$ , 10 wt%) were observed at higher image spatial resolution (about  $2\ \mu\text{m}$ ) and higher temporal resolution by using SXRCT (Nikitin et al., 2019).

In order to mimic natural methane hydrate-bearing sand in saline water saturated media, Kerkar et al., 2014 formed MHs in saline water ( $\text{BaCl}_2$ , 5 wt%) saturated media following the excess-water method. Patchy MH distribution and heterogeneous MH accumulation were observed via SXRCT. However, the image interpretation was based on a standard segmentation method due to low image resolution ( $7.5\ \mu\text{m}$ ), making direct observations of MH morphologies and pore habits impossible.

By using a recent XRCT technique developed by Lei et al., 2018, taking advantages of both attenuation and interference of X-ray waves (phase contrast), methane hydrate pore habits in sandy sediments were investigated by Lei et al., 2019b at high image spatial resolution (about  $2\ \mu\text{m}$ ). Methane hydrates were formed either following the excess-gas method, with deionized water, followed by saline water injections or under excess-saline-water conditions. Some hydrate growth/evolution mechanisms were identified: hydrate growth over sand grain surfaces, hydrate growth via water/brine invasion into methane gas pockets featuring MH shell breakage and MH spikes, extended MH morphology evolution via diffusion of water vapor in excess-gas environments, and dissolved methane gas in excess-water environments. Water migration mechanisms for the MH growth over sand surfaces, proposed by these authors, are shown in Figure 2.26. However, the kinetics of hydrate formation were not fully observed due to limit temporal resolution of XRCT.

Note that together with the aforementioned MH formation mechanisms proposed by Lei et al., 2019b (Figure 2.26a, b), two other mechanisms of the MH formation under excess-gas conditions have been proposed:

- The cementation model for the gas hydrate growth in the capillary water at sand grain contacts (Priest et al., 2009; Pinkert and Grozic, 2014) suggested that films of gas hydrates were first formed quickly at gas/water interfaces. The subsequent gas hydrate formation (from the gas hydrate films toward centers of grain contacts) was slower depending on the gas diffusion through the gas hydrate films and water. The final distribution of gas hydrates should be similar to that of water prior to their creation (as shown in Figure 2.27). Note that in an unsaturated sand, water is restricted to grain surfaces and grain contacts. Observations of water distribution in an unsaturated sand at the pore scale of Crist et al., 2004 revealed that water can be distributed around grains as thin layers (by adsorption) and also at menisci of grain contacts (by capillarity);
- By using attenuated total reflection infrared (ATR-IR) to study the MH formation in porous media, Jin et al., 2012 proposed two steps for the MH growth in gas saturated media (as shown in Figure 2.28). A gas hydrate film was supposed to be first formed at gas-water interface then cracks occurred in the gas hydrate film involving further conversion of water to gas hydrate.

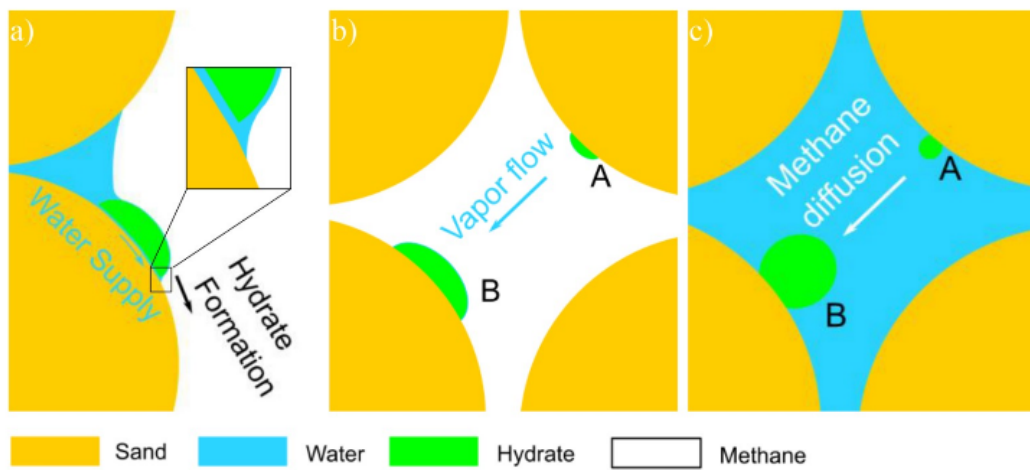


Figure 2.26: Diagram showing mass migration during hydrate formation: (a) Water migration via water film; (b) Water migration via water vapor through gas phase; (c) Methane migration via diffusion of dissolved methane (Lei et al., 2019b).

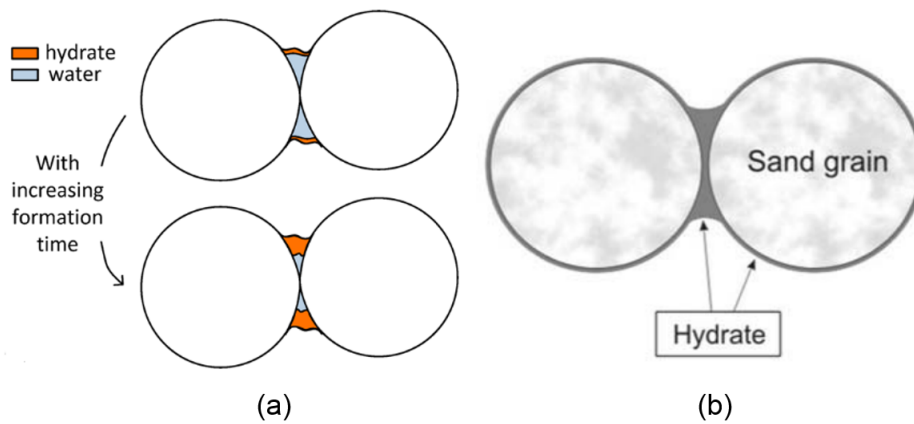


Figure 2.27: (a) Mechanism of the MH formation at grain contacts (Pinkert and Grozic, 2014); (b) MH distribution at the grain scale (Priest et al., 2009).

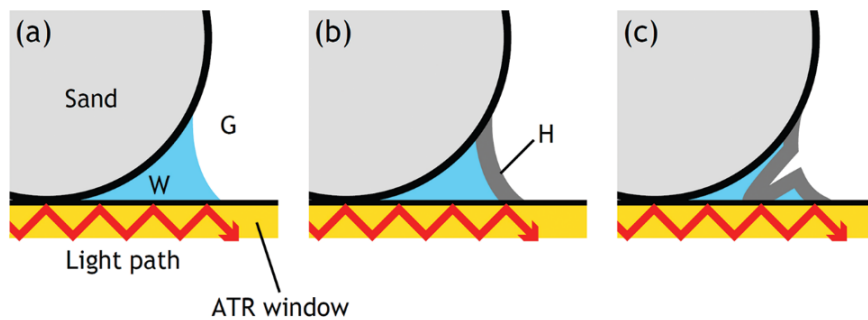


Figure 2.28: Schematic of two-step MH growth during the ATR-IR measurement (Jin et al., 2012).

## 2.4 Conclusions

In this chapter, the importance of finding an efficient experimental method to recreate synthetic MHBS in laboratory for the studies on physical/mechanical properties of MHBS was highlighted. Such properties are important inputs for the studies aiming at optimizing the MH dissociation method as well as minimizing the environmental impacts of future methane gas exploitation via MH dissociation of deep-sea methane hydrate-bearing sediments. Furthermore, results of gas hydrate morphologies and pore habits, formed following various MH formation methods, at various scales and their relevant effects on the mechanical behaviors/properties of gas hydrate-bearing sediments were presented. That shows the necessity of paying more attention to the morphologies and pore habits (at various scales) of MHs formed in synthetic sandy sediments in order to mimic natural gas hydrate-bearing sediments as they affect considerably the physical/mechanical properties of sediments containing methane hydrates. It is evident that studies with methane hydrates - natural gas hydrates need to deal with more complex technical issues (e.g. experimental setups, low image contrast) compared to the cases of other gas hydrates (e.g. *THF*,  $CO_2$ , *Xe*...).



# 3 Mechanical properties

## 3.1 Introduction

In this chapter, we present the results of investigations on methane hydrates created in sandy samples following two methods. The first one corresponds to the creation of methane hydrates in a partial water saturated sample, followed by a water saturation phase prior to the mechanical testing. The second one was similar to the first one, but was completed with a temperature cycle (as suggested by Choi et al., 2014). The measurements of compressional wave velocity and their interpretations through rock physic models (Dvorkin et al., 2000) were used to indirectly assess MH pore habits in sandy sediments. Furthermore, triaxial tests were used to investigate the effects of formed MHs on the mechanical properties of sandy sediments. It should be noted that natural methane hydrate-bearing sandy sediments may have high methane hydrate saturation (up to 80 %). In addition, other researchers (Yun et al., 2007; Yoneda et al., 2017) mentioned that the mechanical properties of gas hydrate-bearing sediments would change exponentially with gas hydrate saturation in a range over 40 - 50 %. However, the methane hydrate pore habits would be more complex at high MH saturation and would need more extensive works. The analysis here is then limited to low and moderate MH saturation (0 - 50 %).

The main findings of this chapter are presented in the publication: T.X. Le, P. Aime-dieu, M. Bornert, C. Baptiste, S. Rodts, A.M. Tang (2019) Effect of temperature cycle on mechanical properties of methane hydrate-bearing sediment. *Soils and Foundations*. doi: 10.1016/j.sandf.2019.02.008.

## 3.2 Experimental method

### 3.2.1 Materials

The soil used for this thesis was Fontainebleau silica sand (NE34). Its mechanical properties are well-documented (Dupla et al., 2007). It consists of poor-graded sub-rounded grains having diameter ranging from 100 to 300 microns (the particle size distribution curve shown in Figure 3.1 was obtained by laser diffraction analysis). Tap water was used in the tests. The standard purity of methane gas used here was 99.995 %.

### 3.2.2 Experimental setup

Figure 3.2 presents a schematic view of the temperature-controlled high-pressure triaxial apparatus. The sample (1), 50 mm in diameter and 100 mm in height, was covered with

a neoprene membrane. A displacement sensor, LVDT (2) was used to monitor the radial strain of the sample, serving to calculate the volumetric strain during the consolidation and MH formation. For the mechanical loading, a confining pressure was applied to the fluid (silicone oil) inside the cell by a volume/pressure controller (3); the deviator stress, applied via the piston (4), was measured by the force transducer (5) installed above the piston. It should be noted that the friction between the cell and the piston (corresponding to approximately 200 kPa of deviator stress) can be measured when the piston is moved down without touching the top baseplate (10). Methane gas was injected via the bottom inlet (6) by a pressure controller, which was connected to a methane gas flowmeter. The top and bottom pore pressure transducers were connected by a T-valve (7). The water pore pressure was controlled by a volume/pressure controller (8). For the temperature control, the cell was immersed in a temperature-controlled bath connected with a cryostat. A thermocouple (9) was placed close to the sample to measure the temperature inside the cell. For measurements of compressional wave velocities, two ultrasonic sensors were installed on the top and bottom baseplates (10) and connected to a wave generator. Figure 3.3 shows the temperature-pressure control systems used. Note that the temperature control system was developed at the beginning of this thesis.

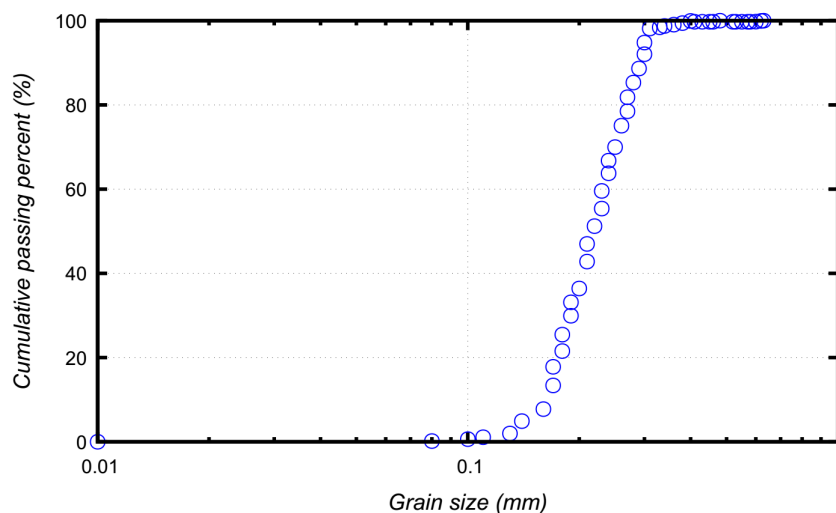


Figure 3.1: Particle size distribution curve (Feia et al., 2015).

### 3.2.3 Test procedure

MHBS samples were prepared by using the following procedure:

- Step 1: Moist sand (having a known moisture content) was compacted by tamping in layers to obtain a void ratio of 0.63 inside the neoprene membrane prior to the assembly of the experimental setup, as shown in Figure 3.4.
- Step 2: The sample was consolidated in drained conditions (state 1 in Figure 3.5). The confining pressure was increased to 25 MPa then decreased to 10 MPa. As the maximal value of confining pressure during the subsequent test was 22 MPa, the consolidation step would ensure that the soil remained in the elastic domain during the remaining steps.

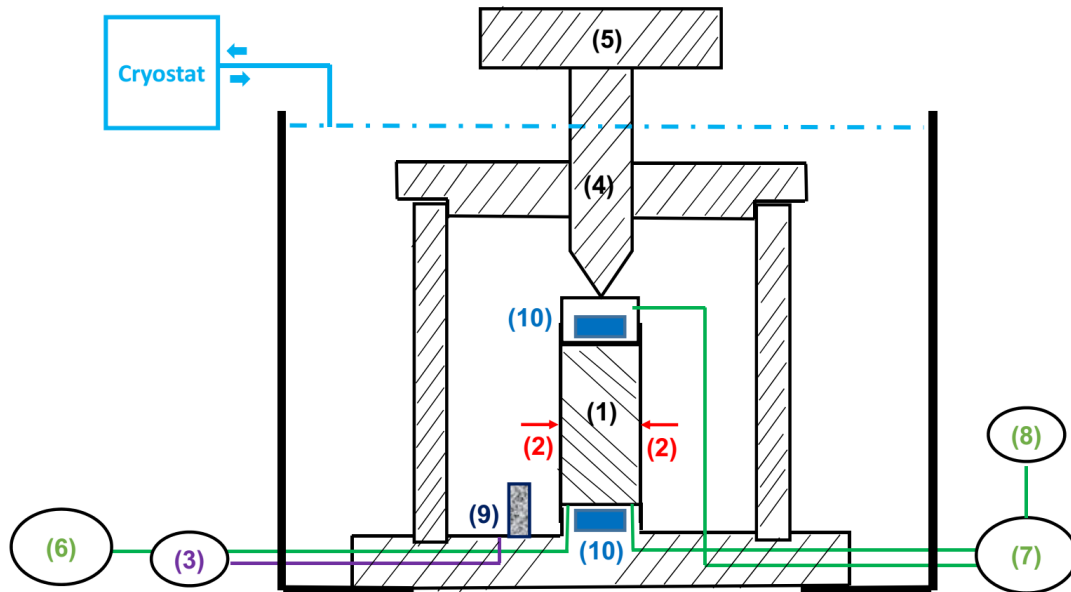
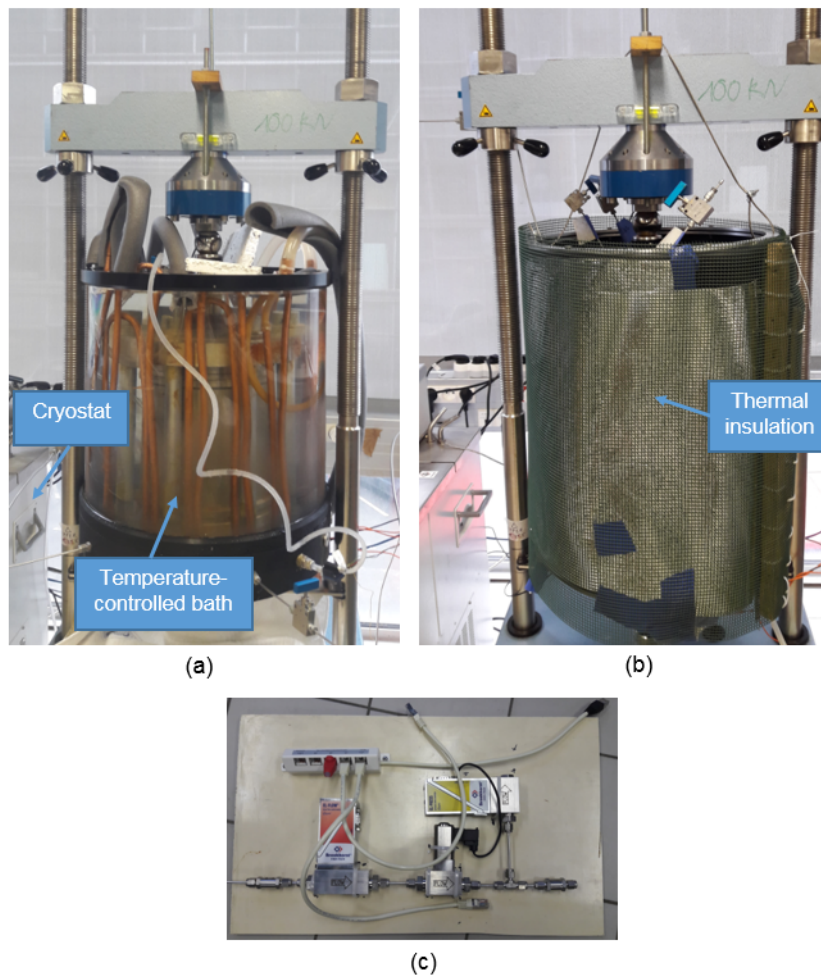


Figure 3.2: Schematic diagram of the experimental setup. (1): sample; (2): displacement sensor; (3): volume/pressure controller to control confining pressure; (4): piston; (5): force transducer; (6): pressure transducer connected to gas flowmeter for methane gas injection; (7): top and bottom pore pressure transducers connected by a T valve; (8): volume/pressure controller to control pore pressure (water pressure); (9): thermocouple; and (10): two ultrasonic sensors connected to a wave generator for measurement of  $V_P$ .

- Step 3: To create methane hydrates inside the sample, the sample temperature was decreased to 3 – 4 °C by setting a cryostat temperature (at about -7 °C) and vacuum was applied to eliminate the pore air in the sample. Afterward, methane gas was injected at 7 MPa during the whole MH formation period (state 2 in Figure 3.5). The MH formation in gas-saturated media was considered complete when the methane gas flow rate became negligible (<0.1 ml/min). At the end of this step, methane hydrate saturation can be estimated from the initial water saturation (an increase in volume of 10 % was considered due to the water-methane hydrate shift). It should be noted that 7 MPa of gas pressure is much higher than the value required to create MHs at a temperature of 3 - 4 °C (see state 2 in Figure 3.5). In addition, preliminary studies have shown that the ultrasonic sensors could correctly measure the compressional wave velocities only in the case of an effective stress higher than 1 MPa (Ebinuma et al., 2008; Rydzy and Batzle, 2010). For this reason, a confining pressure of 10 MPa (corresponding to an effective stress of 3 MPa) was chosen.
- Step 4: To saturate the MHBS sample with water, the T-valve (7) was opened to reach the atmospheric pressure during a short period (about 10 s) to let excess-methane gas (initially under a pressure of 7 MPa) escape from the sample (i.e., the pore pressure decreased to zero) and then this valve was connected to the volume/pressure controller (8) to inject water with a pressure of 7 MPa. This procedure was proposed to let the excess-methane gas in the sample be replaced by water while minimizing the disturbance of methane hydrates that already existed inside the sample by saturating the sample without circulating water.





*Figure 3.3: Pressure-Temperature control systems: (a), image showing the sample temperature control by circulating cooled water (doped with ethylene glycol) in a closed system cryostat-copper coil placed in a water bath surrounding the cell-cryostat; (b), image showing thermal isolation around the water bath; (c), methane gas flowmeter.*

Once these above steps had been completed, two different procedures were used in the objective of creating different MH pore habits:

- For procedure A, a drained triaxial compression test was performed directly after verifying the good saturation of the sample at 22 MPa of confining pressure and 19 MPa of pore pressure by means of Skempton's coefficient.
- For procedure B, a temperature cycle was performed beforehand to modify methane hydrate distribution at the pore scale. For this purpose, the pore pressure and the confining pressure were first decreased from 7 MPa to 4 MPa and from 10 MPa to 7 MPa, respectively. All the drainage valves were then closed and the temperature of the cell was increased to higher than 20 °C. That corresponds to a heating of the sample under undrained conditions in order to progressively dissociate the existing MHs. During this phase, the pore pressure (measured by the pressure transducer) increased progressively because of the heating. A Labview program was made to automatically control the confining pressure (via the volume/pressure controller

(3) in order to maintain the mean effective stress (confining pressure minus pore pressure) at 3 MPa. When the pore pressure reached 19 MPa and the confining pressure reached 22 MPa, the T valve (7) was opened for connection with the volume/pressure controller (8). During this step, the pressure in the volume/pressure controller (8) was maintained at 19 MPa and the volume of water expelled during this heating period was monitored. MHs were supposed to be totally dissociated when the volume of expelled water had stabilized. After this dissociation phase, MHs were then reformed in the sample by decreasing the temperature of the cell to 3-4 °C, while maintaining the pore pressure at 19 MPa (and the confining pressure at 22 MPa). This phase induced an injection of water from the volume/pressure controller (8) to the sample. The methane hydrate reformation phase was considered to be finished when the volume of injected water had stabilized. After the MH reformation, a drained triaxial compression test was performed under an effective confining pressure of 3 MPa as in the case of tests following the procedure A.

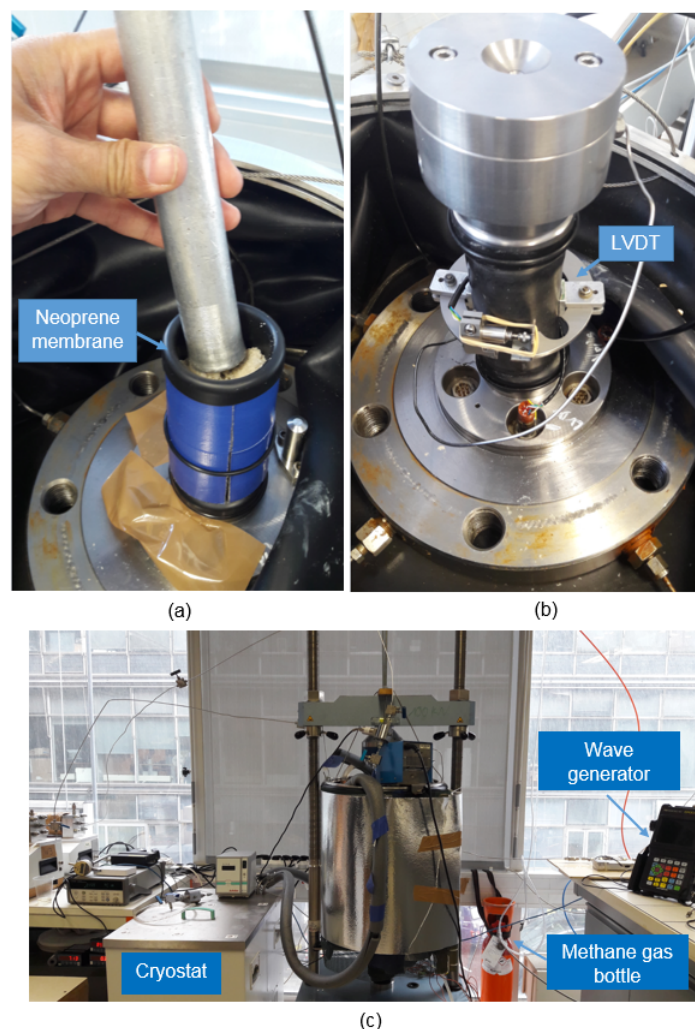


Figure 3.4: Sample preparation: (a), Sand compaction; (b), Thermocouple, LVDT and ultrasonic sensor setup; (c), The whole experimental setup system.

Note that in the pore pressure versus temperature plot (Figure 3.5), the procedure A fol-

lows the path (1)-(2)-(3), while the procedure B follows the path (1)-(2)-(4)-(3). The axial strain rate for all the triaxial compression tests was fixed at 0.1 %/min to ensure the drainage conditions. The final methane hydrate saturation was determined by measuring the volume of methane gas dissociated at the end of the triaxial compression tests by using the system shown in Figure 3.6, composed of both a methane gas/water separator and a methane gas collection system (based on water displacement principle). It is noteworthy that a small quantity of methane gas in excess could still be present in the sample and become MHs at the end of the water saturation or in contrast some MHs could be dissociated during the water saturation.

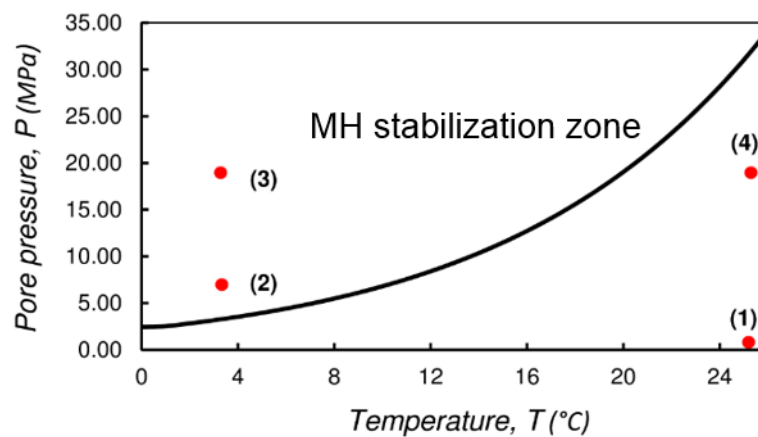


Figure 3.5: *P-T* conditions during the methane hydrate formation. (1): Initial state of the sample (Step 1 and Step 2); (2): *P-T* during MH formation in gas-saturated media (Step 3) and after water saturation (Step 4); (3): Procedure A: *P-T* at the end of water saturation when confining pressure and pore pressure were increased to 22 MPa and 19 MPa, respectively; Procedure B: *P-T* during methane hydrate reformation; (4): *P-T* at the end of methane hydrate dissociation for procedure B tests.

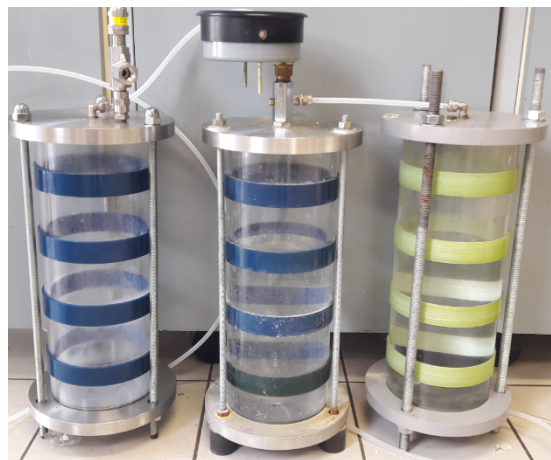


Figure 3.6: The system to measure methane gas quantity released from MH dissociation.

### 3.2.4 Test program

The test program is shown in Table 3.1. Four tests were performed following the procedure A (A1 to A4) and four tests were performed following the procedure B (B1 to B4). Moisture content was imposed prior to the sample preparation. Water saturation was calculated from the imposed moisture content, the void ratio obtained after the sample preparation ( $e = 0.63$ ), and the particle density ( $\rho_s = 2.65 \text{ Mg/m}^3$ ). In addition, a reference test was performed, which consisted of compacting dry sand down to a void ratio of 0.63 in the triaxial cell. After the consolidation step (confining pressure was increased to 25 MPa and then decreased to 10 MPa), the sample was saturated with water at a confining pressure of 10 MPa and a water pressure of 7 MPa. Finally, a triaxial compression phase at 22 MPa of confining pressure and 19 MPa of pore pressure was applied as the other samples. The methane hydrate saturations shown in Table 3.1 were determined at the end of the tests from the volume of methane gas dissociated from the sample.

Table 3.1: Test program.

Test	Moisture content (%)	Water saturation (%)	Hydrate saturation (%)
<i>Reference</i>	0.0	0	0
<i>A1</i>	6.0	25	21
<i>B1</i>	6.0	25	13
<i>A2</i>	8.5	35	31
<i>B2</i>	8.5	35	34
<i>A3</i>	10.0	42	50
<i>B3</i>	10.0	42	41
<i>A4</i>	12.0	50	48
<i>B4</i>	12.0	50	42

## 3.3 Experimental results

### 3.3.1 Isotropic consolidation

Figure 3.7 and Figure 3.8 show the void ratio ( $e$ ) and the compressional wave velocity ( $V_p$ ) versus mean effective stress ( $p'$ ), respectively, during the consolidation step for all the tests (Step 2). The points of the unloading phase correspond to the decrease in confining pressure from 25 MPa to 10 MPa followed by the injection of methane gas at 7 MPa. The compression curves ( $e-p'$  plots) show a decrease in void ratio from 0.63 to 0.58-0.59 during the loading path (up to  $p' = 25$  MPa). During the unloading path, the void ratio increased to 0.60 – 0.61 (when  $p' = 3$  MPa). The effect of the moisture content on the compression behavior was not clear and the small discrepancy in all the results can be then related to the good repeatability of the experimental procedure.

Unlike the compression curves ( $e - p'$  plots), where hysteresis can be observed during the loading/unloading paths, the relationship between  $V_p$  and  $p'$  shows reversible behavior (Figure 3.8). Actually, during the loading path when  $p'$  increased from 1.6 MPa to 25 MPa (the ultrasonic sensors used in this study could not measure  $V_p$  lower than 700

m/s),  $V_p$  increased from 750 – 850 m/s to 1400 – 1500 m/s. During the unloading path when  $p'$  was decreased to 3 MPa,  $V_p$  decreased to 900 – 1000 m/s. The results obtained in the consolidation step confirm that  $V_p$  is strongly dependent on the mean effective stress (Zimmer, 2003), whereas it is independent of the void ratio and moisture content. For instance, when  $p'$  equaled to 3 MPa, the void ratio at the loading path was higher than that at the unloading path, but  $V_p$  obtained following the both paths were similar. This can be explained by the small volumetric strain (3 %). In addition, the results shown in the  $V_p - p'$  plots for all the samples (having various moisture contents) were similar. Actually, the matric suction in sand (few kPa, (Feia et al., 2016)) was much smaller than the mean effective stress. All the subsequent measurements of  $V_p$  were performed at the same mean effective pressure (3 MPa). The discrepancy on  $V_p$  (around  $\pm 50$  m/s) can be attributed to the repeatability of the experimental procedure.

### 3.3.2 Methane hydrate formation

Pore Pressure, Temperature and Volumetric Deformation evolution during the methane hydrate formation are shown in Figure 3.9. Similar tendencies were observed for all the tests. Pore pressure (shown in Figure 3.9(a)) was increased rapidly then maintained at 7 MPa by methane gas injection. Figure 3.9(b) shows a slight sample temperature increase (about 0.1 °C) after methane gas injection due to an exothermic reaction of MH formation. The temperature fluctuations after 10 hours of MH formation were linked to ambient temperature variation. At 10 MPa of confining pressure, pore pressure increase induced an effective stress decrease. That caused a volumetric strain decrease, shown in Figure 3.9(c). Note that the initial volumetric strain here was that after the consolidation. The volumetric strain evolution during the MH formation once the effective stress reached 3 MPa (pore pressure was at 7 MPa) is shown in Figure 3.10. In general, the volumetric deformation decreased from 0.01 to 0.4 h (dilatation) then increased until about 10 hours (contraction) before being stable. These tendencies were independent of initial water saturations.

Figure 3.11 plots  $V_p$  versus elapsed time during the methane hydrate formation (Step 3) in gas-saturated media at 3 MPa of effective stress (the confining pressure and the gas pressure were at 10 MPa and 7 MPa respectively). At the beginning,  $V_p$  was equal to 900 – 1000 m/s, corresponding to  $p' = 3$  MPa.  $V_p$  increased slightly during the firsts minutes and then started to increase quickly. The first period can be identified as the induction time that is necessary time to create the first crystals of methane hydrates (Natarajan et al., 1994). In this study, the induction time was approximately 0.2 h. After the induction time,  $V_p$  increased quickly during the next 10 h to progressively reach the stabilization. The kinetic of  $V_p$  evolution within the elapsed time was generally independent of the initial water saturation. The final value of  $V_p$ , however, depended on the initial water saturation and this dependency will be analyzed later. It should be noted that the flow rate of methane gas injection at the beginning was much higher than the limit of the methane gas flowmeter. For this reason, the total quantity of injected methane gas could not be measured by the flowmeter.

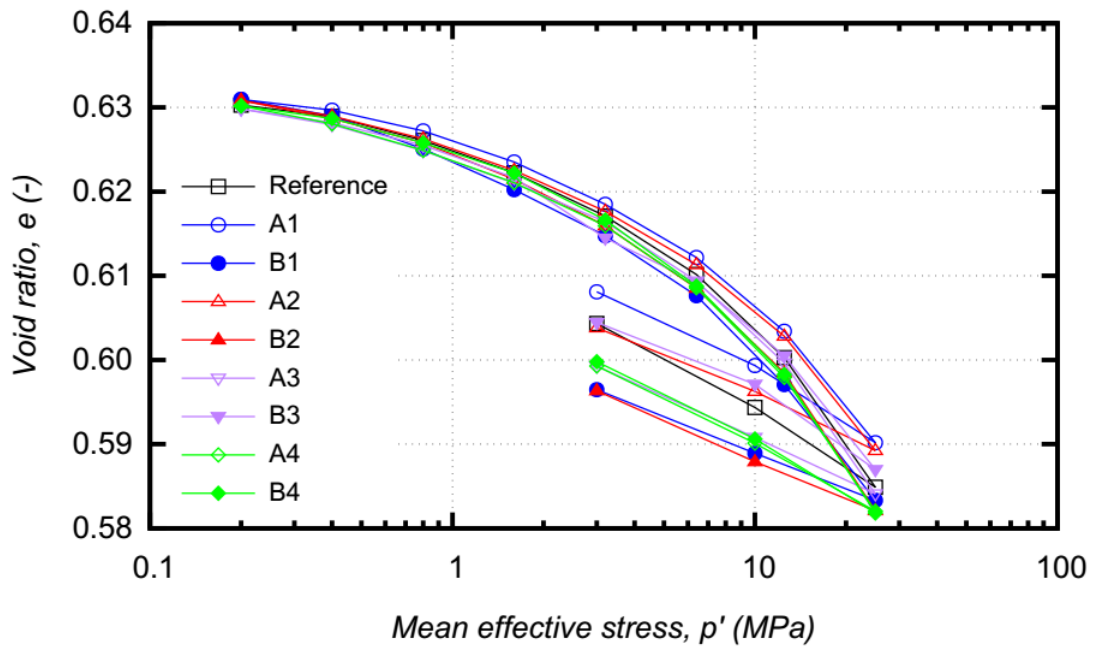


Figure 3.7: Void ratio versus effective stress for all tests.

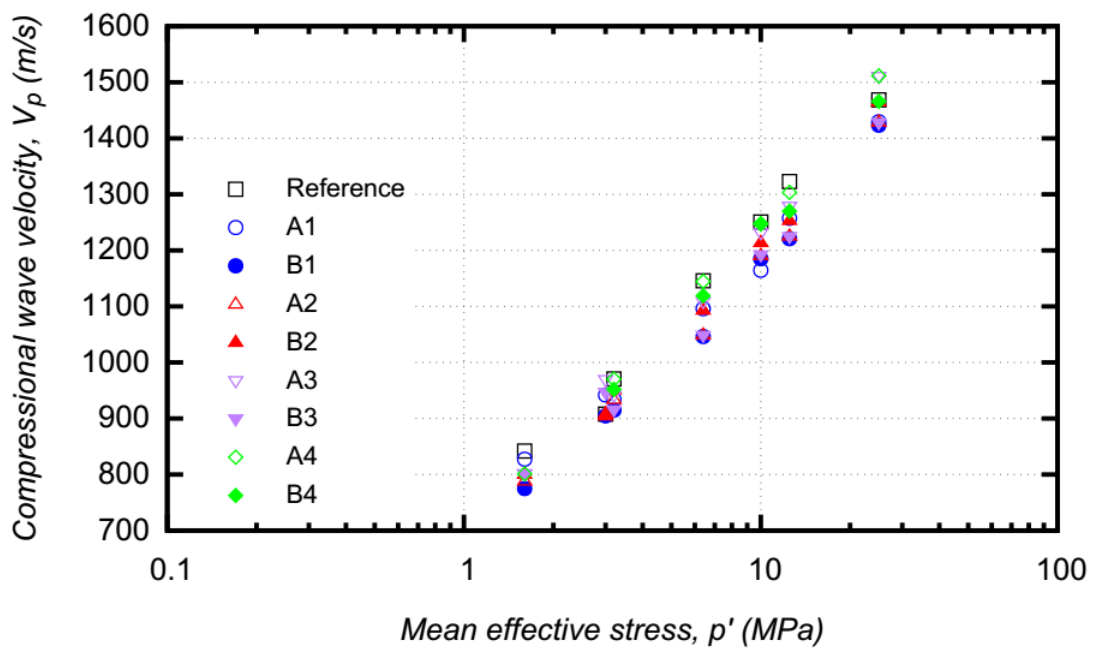


Figure 3.8: Compressional wave velocity versus effective stress for all tests.

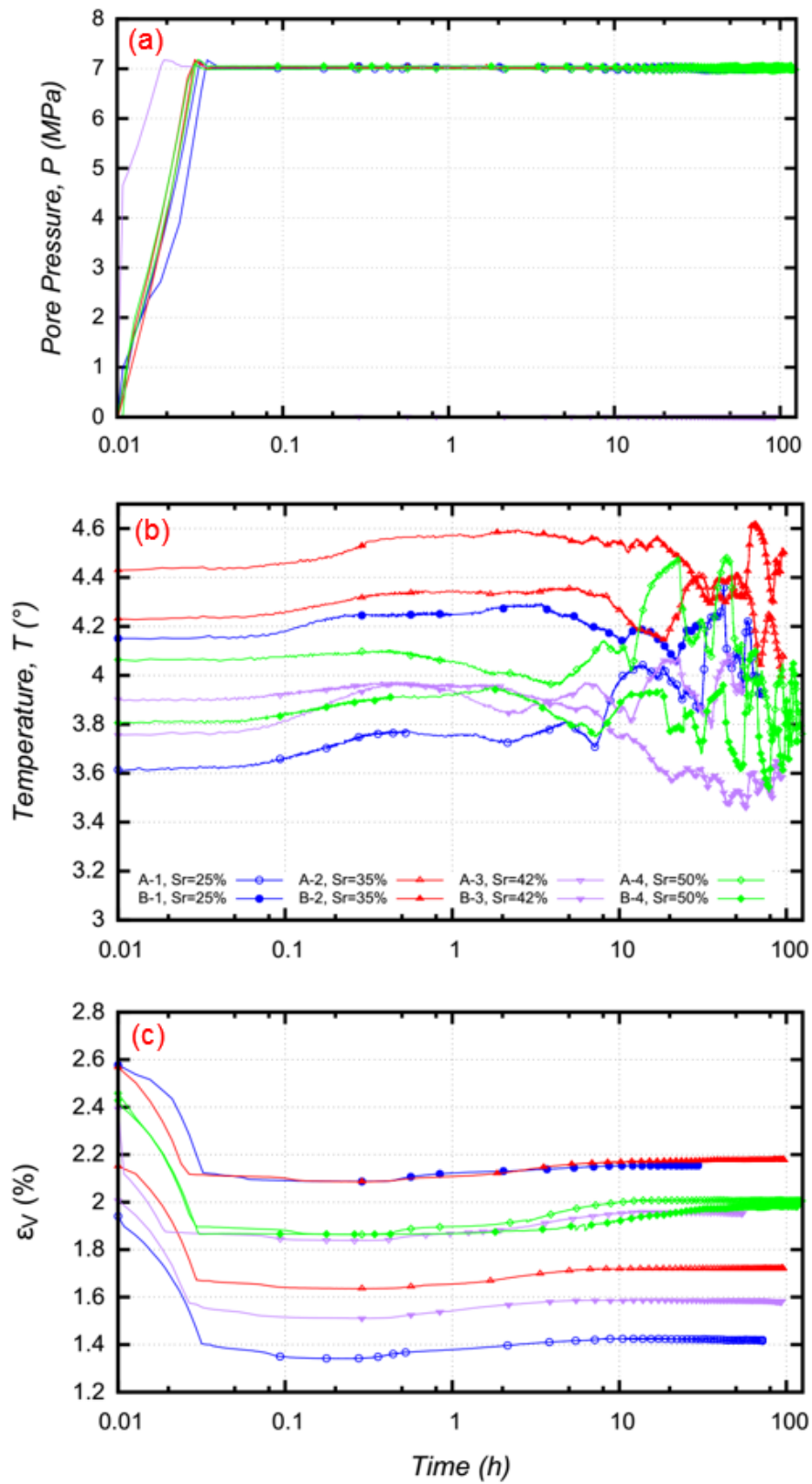


Figure 3.9: Pore pressure, temperature and volumetric deformation evolution during the MH formation.

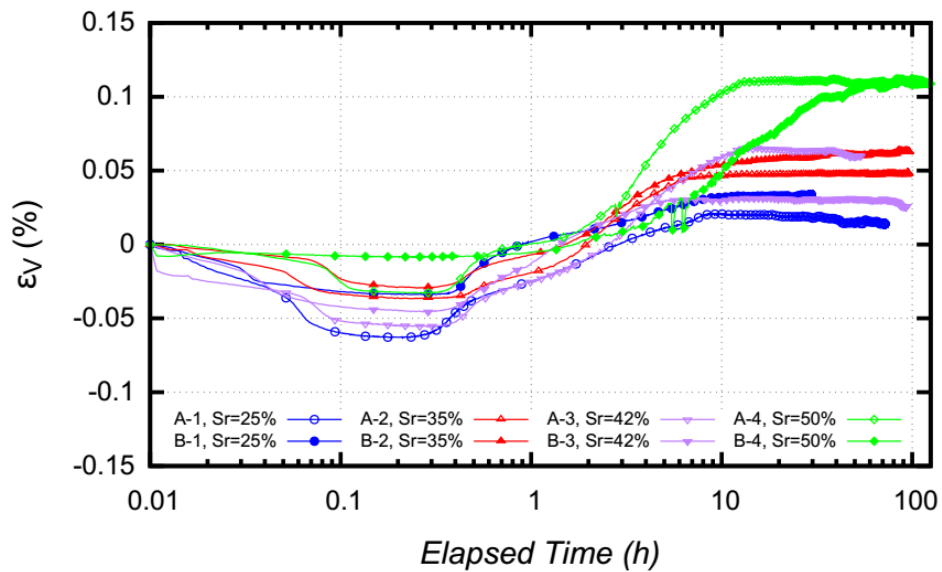


Figure 3.10: Volumetric deformation evolution during the MH formation at 3MPa of effective stress.

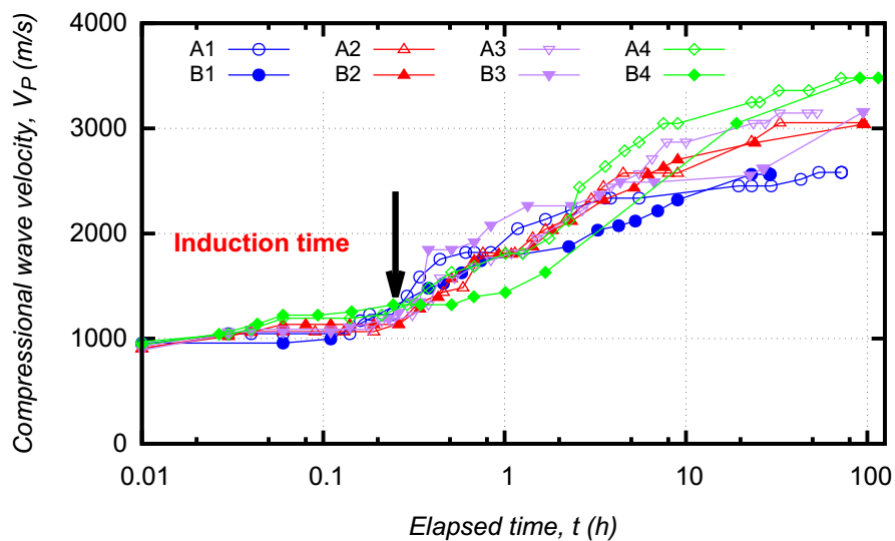


Figure 3.11: Compressional wave velocity versus elapsed time during methane hydrate formation in gas-saturated media.

Figure 3.12 shows  $V_p$  versus elapsed time during the water saturation (Step 4). It should be noted that time zero corresponds to the beginning of the methane gas-water shift. For the reference test,  $V_p$  increased when the sample was saturated with water. In contrast, for all tests with methane hydrates, replacing the excess-methane gas with water decreased  $V_p$ . Furthermore, this process took longer time for higher methane hydrate saturation samples.

As mentioned above, for the tests following the procedure A, triaxial tests were performed after the water saturation (Step 4) at 22 MPa of confining pressure and 19 MPa of



pore pressure, while for the tests following the procedure B, a heating/cooling cycle was applied beforehand to dissociate and recreate methane hydrates inside the sample. The results obtained during the heating path (the procedure B) are shown in Figure 3.13. After decreasing the pore pressure from 7 MPa to 4 MPa, all the inlets were closed. Afterward, the sample was heated under undrained conditions inducing the increase in pore pressure. The pore pressure reached 19 MPa when the temperature of the cell reached 20 °C. As mentioned above, when the pore pressure reached 19 MPa, the volume/pressure controller (8) was connected to the sample to maintain the pore pressure at 19 MPa, while the temperature of the cell continued to be increased. Figure 3.13c plots the volume of water (and/or dissolved methane gas) expelled during this phase. It varied from  $4 \times 10^{-6} m^3$  to  $15 \times 10^{-6} m^3$ , which corresponds to 5 % and 20 %, respectively, of the pore volume. In addition, the samples having higher initial water saturation (higher methane hydrate saturation) showed a higher volume of expelled water.

Figure 3.14 presents pore pressure versus cell temperature during this heating path. The phase diagram (relationship between methane gas pressure and temperature during the MH dissociation) is also plotted (Sloan Jr and Koh, 2007). The results show that during this undrained heating path, the  $P$ - $T$  plots closely follow the phase diagram (due to thermal dilation of water as well as to methane hydrate dissociation), confirming the presence of methane hydrates in the system (Kwon et al., 2008). However, at a given pressure, the cell temperature ( $T$ ) was slightly higher than the corresponding temperature determined by the phase diagram. This can be explained by the partial dissociation of methane hydrates and the continuous heating process (Figure 3.13a) for which the cell temperature was slightly higher than the sample temperature (see also the schematic view of the cell in Figure 3.2). The  $P$ - $T$  plots would be closer to the phase diagram if the heating rate was smaller. As the final state (in term of pore pressure and temperature) was far outside the phase diagram, methane hydrates should be completely dissociated at the end of the heating path.

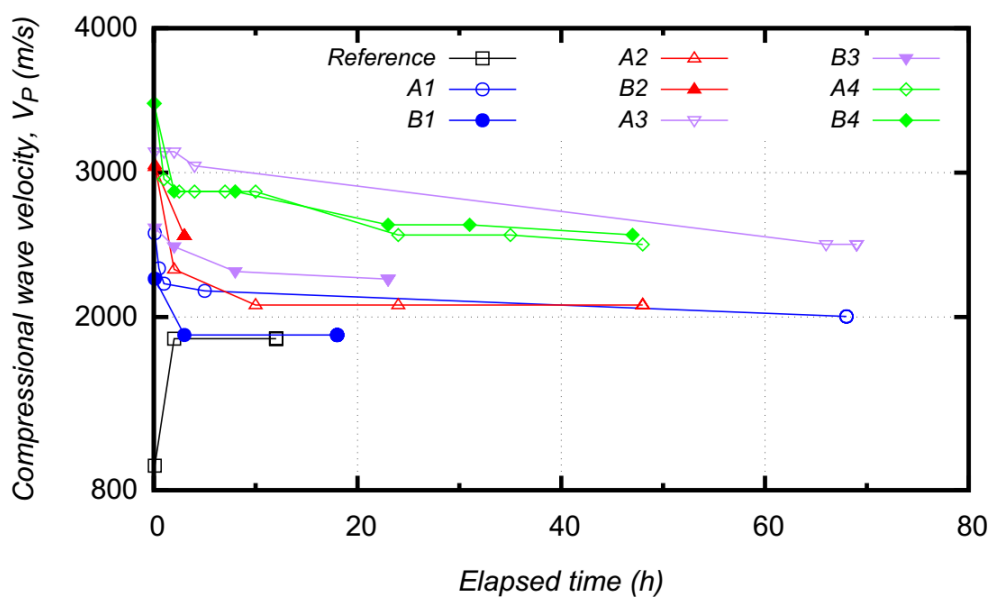


Figure 3.12: Compressional wave velocity versus elapsed time during water saturation.

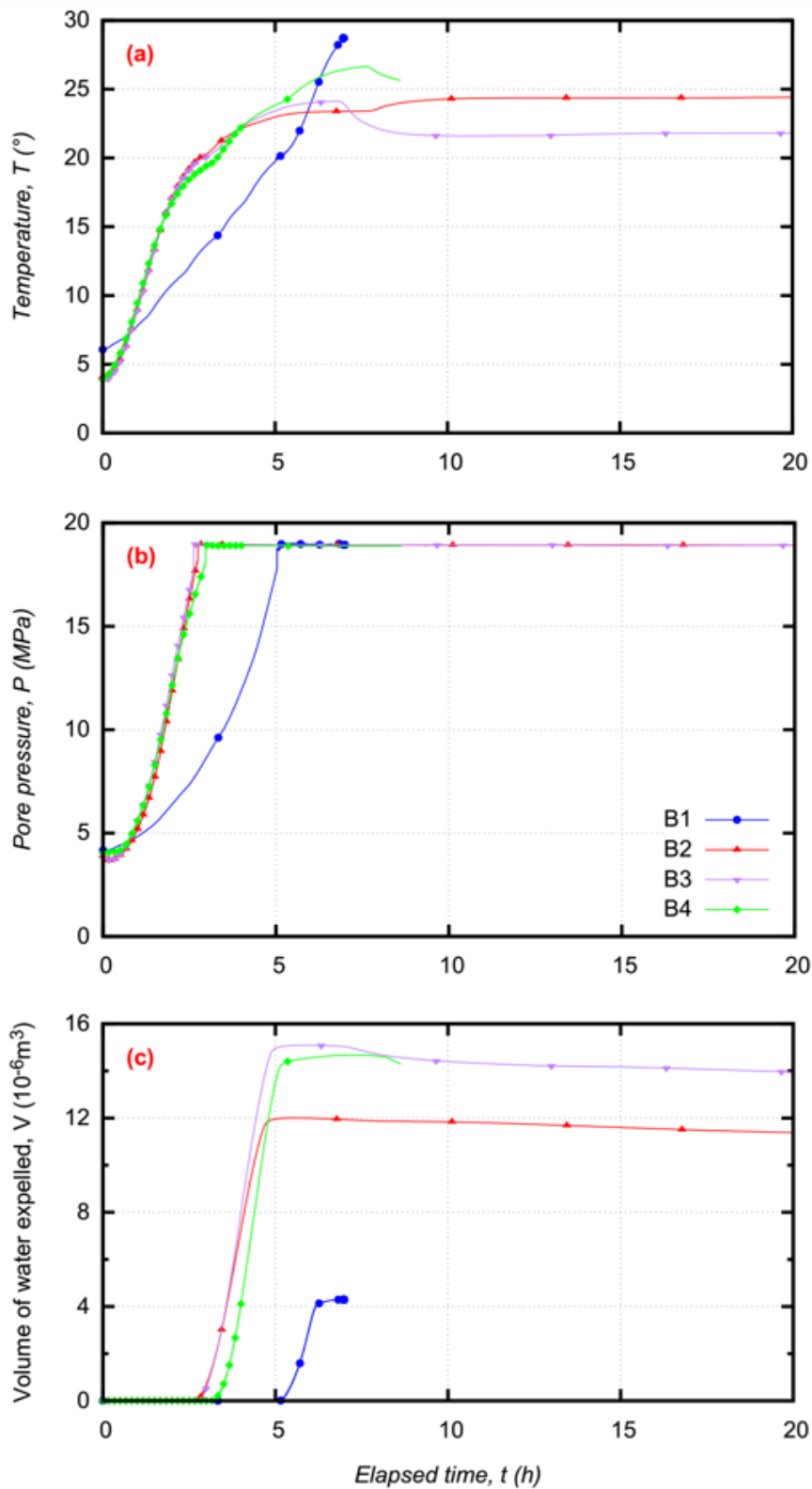


Figure 3.13: Pore pressure, temperature and volume of water expelled versus elapsed time during heating path.

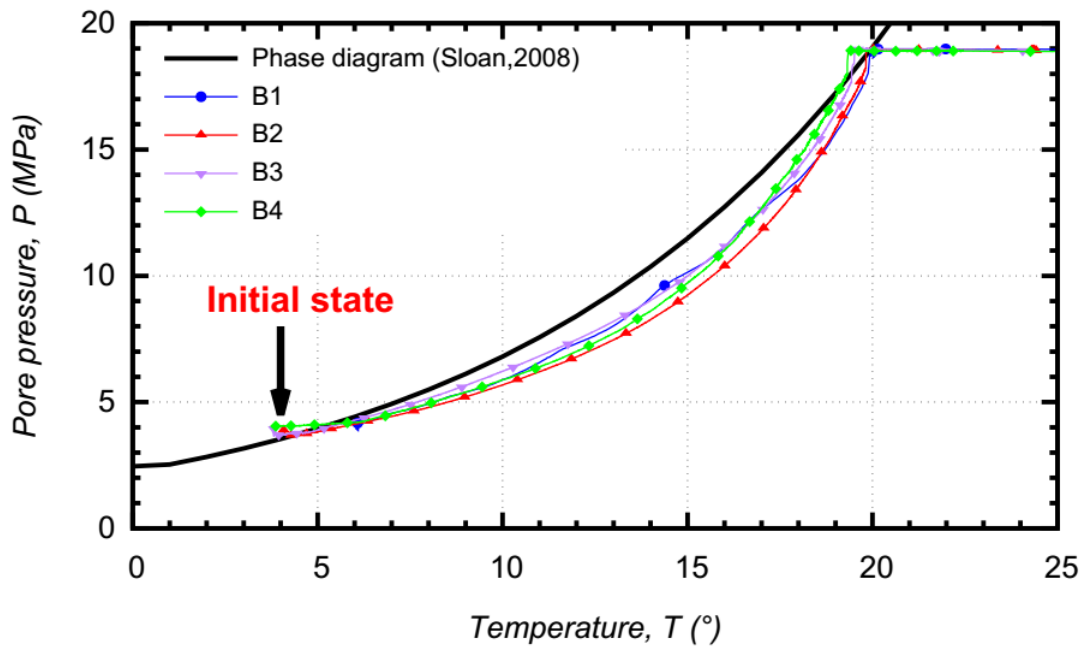


Figure 3.14: Pore pressure versus cell temperature during dissociation.

After this MH dissociation step, to reform methane hydrates, the pore pressure was maintained at 19 MPa, while the cell temperature was decreased to 3 – 4 °C (except for test B2). Figure 3.15 shows the cell temperature and the volume of water injected into the sample versus the elapsed time during this step. Water injection was mainly due to both thermal contraction of water and methane hydrates reformation. Furthermore, except for the case of test B4, the volume of water injected into the sample was similar to that expelled (shown in Figure 3.13c) and reached a stabilization after 100 h. The volume measured in test B4 continued to increase with a constant rate even after 120 h. This was then attributed to a possible leakage in the connection that occurred due to the heating/cooling cycle. For test B2, the temperature was first decreased to 15 °C, MH reformation started and became remarkable after 2 hours (the cell temperature remained constant while the volume of injected water increased abruptly). The temperature was finally set at 3-4 °C like the other tests.

### 3.3.3 Compressional wave velocity

Figure 3.16 shows  $V_p$  at different steps during the methane hydrate formation process for all the tests. After the consolidation (Step 2),  $V_p$  was equal to 900 – 1000 m/s for all the samples, as shown in Figure 3.8 (corresponding to  $p' = 3$  MPa). After the formation of methane hydrates under the gas-saturated state (Step 3),  $V_p$  increased significantly (it was equal to 2500 – 3500 m/s). In addition, samples having similar initial water saturation showed similar  $V_p$ . The subsequent water saturation (Step 4) slightly decreased  $V_p$  of the methane gas-saturated MHBS, while it increased  $V_p$  of the reference sample. These values varied in a range of 1800 – 2600 m/s. After the methane hydrate dissociation phase,  $V_p$  of all four samples following procedure B decreased and approached the corresponding values obtained at the end of the consolidation (Step 2); they varied between 1000 and

1200 m/s. Finally, the re-creation of methane hydrates increased  $V_p$  again to the range obtained before the MH dissociation step (the end of Step 4), between 1800 – 2300 m/s.

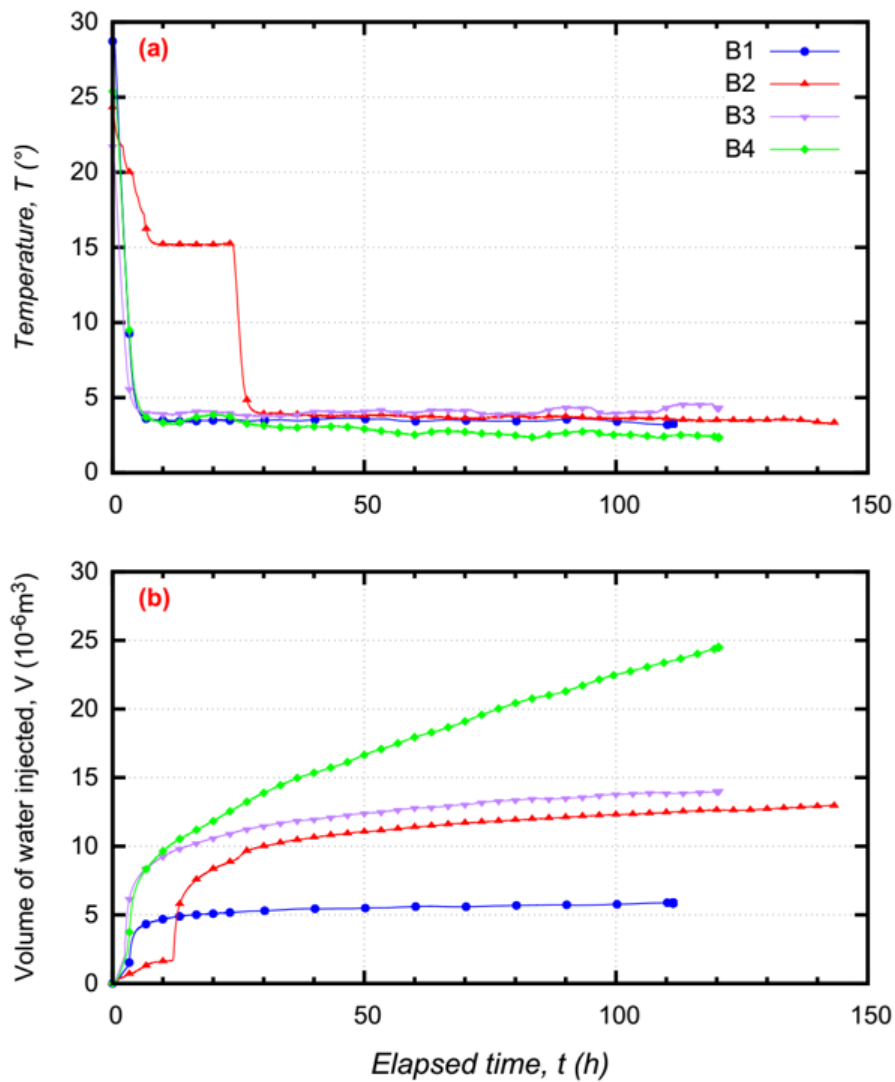


Figure 3.15: Temperature and volume of injected water versus elapsed time during hydrate reformation.

The results obtained at the end of the methane hydrate formation in the methane gas-saturated state (Step 3) are presented in Figure 3.17 where  $V_p$  is plotted versus methane hydrate saturation. The methane hydrate saturation was estimated based on the initial water saturation, all the water was supposed to be used to create methane hydrates. It should be noted that this figure shows the results of eight tests, but the samples with the same moisture content had the same  $V_p$  (as shown in Figure 3.16). That revealed a good repeatability of the experimental procedure. These results showed a clear effect of methane hydrate saturation on  $V_p$ .  $V_p$  was higher at a higher methane hydrate saturation; it increased from 900 – 1000 m/s at the reference state (without methane hydrates) to 3500 m/s at  $S_h = 55\%$ .

In order to assess the methane hydrate distribution at the grain scale in sandy sediments (pore habits), the models proposed by Dvorkin et al., 2000 (see Section 2.2.2.4) were used. To predict the pore habits of MHs in sandy sediments, Dvorkin et al., 2000 proposed two cementing models using two different schemes: (i) methane hydrates are located only at the grain contacts (cementing - grain contacts) and (ii) methane hydrates evenly envelop the grains (cementing - mineral coating). The used parameters are shown in Table 3.2. The results (Figure 3.17) show that the experimental data obtained in the present work correspond to the zone delimited by these two models.

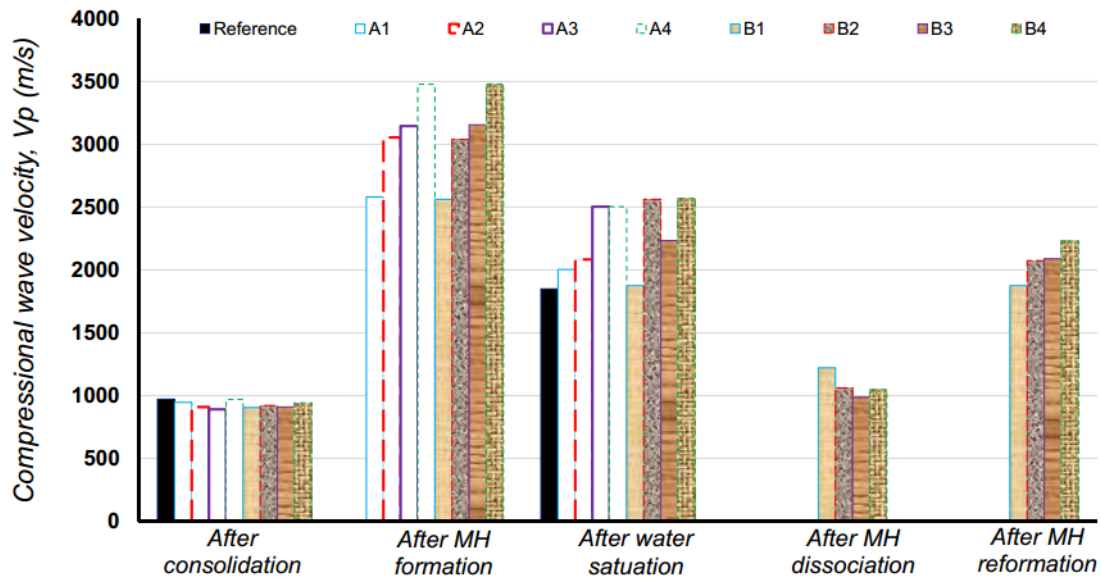


Figure 3.16: Compressional wave velocity during the whole methane hydrate formation of all tests.

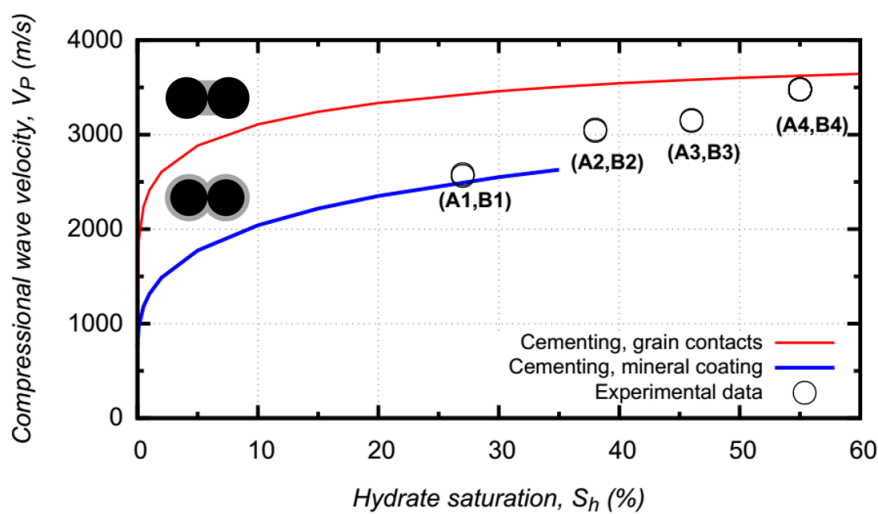


Figure 3.17: Comparison between experiments and Dvorkin's model of compressional wave velocity dependence on methane hydrate saturation in gas-saturated media.

The results corresponding to the water-saturated state are plotted in Figure 3.18. In this figure, the methane hydrate saturation was calculated from the quantity of methane gas dissociated at the end of each test (methane gas dissolved in water was ignored). The data obtained after the methane hydrate reformation, with the temperature cycle (only for the procedure B), are plotted with closed symbols, while the data obtained without the temperature cycle (for the procedure A tests) and before the temperature cycle (for the procedure B tests) are plotted with open symbols. It should be noted that MH saturation was supposed to be constant before and after the temperature cycle for the procedure B tests.  $V_p$  decreased after the temperature cycle in tests B2, B3 and B4, while it remained constant in test B1. Unlike the case of the methane gas-saturated state, the effect of methane hydrate saturation was less significant.  $V_p$  increased from 1850 m/s for the reference case (without methane hydrates) to 2500 m/s for  $S_h = 50\%$ . In addition,  $V_p$  obtained after the water saturation (Step 4) was generally higher than that obtained after the dissociation/recreation cycle at a given methane hydrate saturation.

Table 3.2: Parameters used for Dvorkin's model.

Parameter	Value
<i>Bulk modulus of quartz (GPa)</i>	36.6
<i>Shear modulus of quartz (GPa)</i>	45
<i>Bulk modulus of water (GPa)</i>	2.15
<i>Bulk modulus of air (GPa)</i>	0.01
<i>Porosity (-)</i>	0.387
<i>Density of solid grain (Mg/m<sup>3</sup>)</i>	2.65
<i>Density of water (Mg/m<sup>3</sup>)</i>	1
<i>Density of air (Mg/m<sup>3</sup>)</i>	0
<i>Density of methane hydrate (Mg/m<sup>3</sup>)</i>	0.9
<i>Bulk modulus of hydrate (GPa)</i>	7.9
<i>Shear modulus of hydrate (GPa)</i>	3.3
<i>Critical porosity (-)</i>	0.387
<i>Number of contacts per grain (-)</i>	4.5

In order to assess the pore habits of MHs in water-saturated MHBS, four models proposed by Dvorkin et al., 2000 were used. In addition to the two cementing models presented above, a model considering MHs as a fluid components (pore-filling) and another considering MHs as sediment frame components (load-bearing) were used. The experimental and the models' results plotted in Figure 3.18 show that after the water saturation,  $V_p$  data matched the "load-bearing" model for some cases and were higher than the predicted value for other cases (B2, B4, A3, A4). The higher value of  $V_p$  of test B2 can be explained by a short water saturation time before the temperature cycle (see Figure 3.12). These results suggest that the water saturation modified methane hydrate pore habits; methane hydrates located at the grain contacts or/and around grain surfaces (cementings) would be progressively converted or/and redistributed into the sediment pore space. After the temperature cycle (procedure B), the experimental data corresponded to the pore-filling model, except for test B4 ( $S_h = 42\%$ ), where it was close to the load-bearing model. It can be then expected that the heating/cooling cycle allowed completing the conversion of methane hydrate pore habits into non-cementing type.

### 3.3.4 Triaxial compressive properties

The results obtained from the drained triaxial tests are shown in Figure 3.19 where deviator stress ( $q$ ) and volumetric strain ( $\epsilon_v$ ) are plotted versus axial strain ( $\epsilon_a$ ). It should be noted that all these samples were consolidated at 25 MPa of effective stress prior to being unloaded to 3 MPa. The creation of methane hydrates and triaxial tests were performed at a mean effective stress of 3 MPa. The confining pressure and pore pressure were maintained at 22 MPa and 19 MPa, respectively, via the volume/pressure controller, while the axial strain rate was fixed at 0.1 %/min. The volumetric strain was calculated based on the volume of water entering/being expelled from the sample. The results obtained from all the tests are quite similar:

- The deviator increased almost linearly at the beginning, it reached a peak value at about 2-3 % of axial strain and decreased progressively to reach a residual state;
- The volumetric strain showed a small contraction at the beginning and then decreased significantly (dilatation) prior to reaching the residual state at high axial strain ( $\epsilon_a$  larger than 10%) where  $\epsilon_v$  remained constant;
- There was almost no difference between the results of the two procedures.

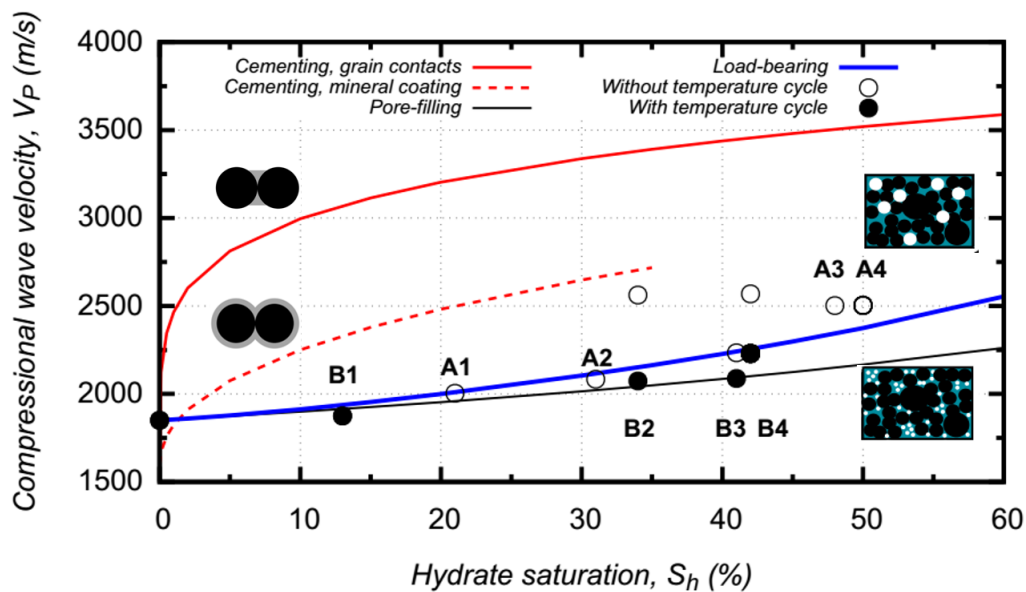


Figure 3.18: Comparison between experiments and Dvorkin's models (Dvorkin et al., 2000) of compressional wave velocity dependence on methane hydrate saturation in water-saturated media.

The triaxial compressive properties, determined from the results shown in Figure 3.19, are plotted in Figure 3.20 versus methane hydrate saturation ( $S_h$ ). The peak strength,  $q_{max}$ , corresponds to the maximal value of the deviator (Figure 3.20a); the residual strength,  $q_{res}$ , corresponds to the deviator at the end of the test (Figure 3.20b). The secant Young's modulus,  $E_{50}$ , corresponds to the secant stiffness at 50 % of the stress difference (Figure 3.20c). The dilation angle,  $\psi$  is determined from the change in volumetric strain with

respect to the change in shear strain by supposing that it is constant between 2 and 4 % of the axial strain (Figure 3.20d). The reference test showed typical results of an over-consolidated sand (softening and dilating behaviors). Furthermore, it was obvious that all these values were higher at a higher methane hydrate saturation but no remarkable difference between the results of the two procedures was observed.

For our triaxial tests, cohesion and friction angle cannot be determined because only one value of effective confining pressure was used. For this reason, the Rowe's stress-dilatancy analysis (Pinkert, 2016) can be appropriate to give more information about the cohesion. Figure 3.21 shows an examination using the approach of Pinkert (2016) of all test results with axial deformations before the peak strength. For triaxial test conditions, the model is given by:

$$\frac{\sigma'_1}{\sigma'_3} = \left( \tan^2\left(\frac{\pi}{4} + \frac{\phi_{cs}}{2}\right) + \frac{2c}{\sigma'_3} \tan\left(\frac{\pi}{4} + \frac{\phi_{cs}}{2}\right) \right) \left(1 - \frac{\dot{\epsilon}_v}{\dot{\epsilon}_1}\right) \quad (3.1)$$

where  $\sigma'_1$  and  $\sigma'_3$  are the major and minor effective stresses, respectively,  $\dot{\epsilon}_v$  and  $\dot{\epsilon}_1$  are the volumetric and major principal strain rates, respectively, and  $\phi_{cs}$  and  $c$  are the critical state friction angle and true cohesion respectively. All the experimental data were close to the values predicted by the model with  $\phi_{cs} = 27^\circ$  and  $c = 0$ , except for tests A3 and A4 with  $c = 0.4$  MPa.

### 3.4 Conclusions

Methane hydrate-bearing sand was created first by pressurizing methane gas (at 7 MPa) into already chilled moistened packed sandy sample (the excess-gas method). Following the MH formation, water was injected into the sample and the remaining gas was simultaneously bled out. The water pressure was then maintained at 19 MPa (22 MPa of confining pressure) until water was no longer injected into the sample. That corresponds to the end of the procedure A to prepare MHBS samples. For the procedure B, a subsequent heating/cooling cycle was applied in order to dissociate methane hydrates completely and then recreate them inside the sample. Measurements of compressional wave velocity were performed along these processes while triaxial compression tests were performed at the end of each procedure. Predictions based on rock physics models were also compared to experimental data to indirectly assess the grain-scale distribution of methane hydrates inside the sediment pore space at each state. The following conclusions can be drawn:

- Pressurizing methane gas into already chilled moistened packed sandy sample increased  $V_p$  significantly;
- Subsequent water saturation decreased  $V_p$ . This process may take several days, depending on the methane hydrate saturation and cannot be completed for high methane hydrate saturation;
- $V_p$  after the water saturation of high methane hydrate saturation samples can be decreased with an additional heating/cooling cycle;



- The effects of methane hydrate saturation on mechanical properties of water-saturated MHBS obtained at the end of both procedures (with and without thermal cycle) were quite similar except the case of high methane hydrate saturation ( $S_h > 40\%$ ).

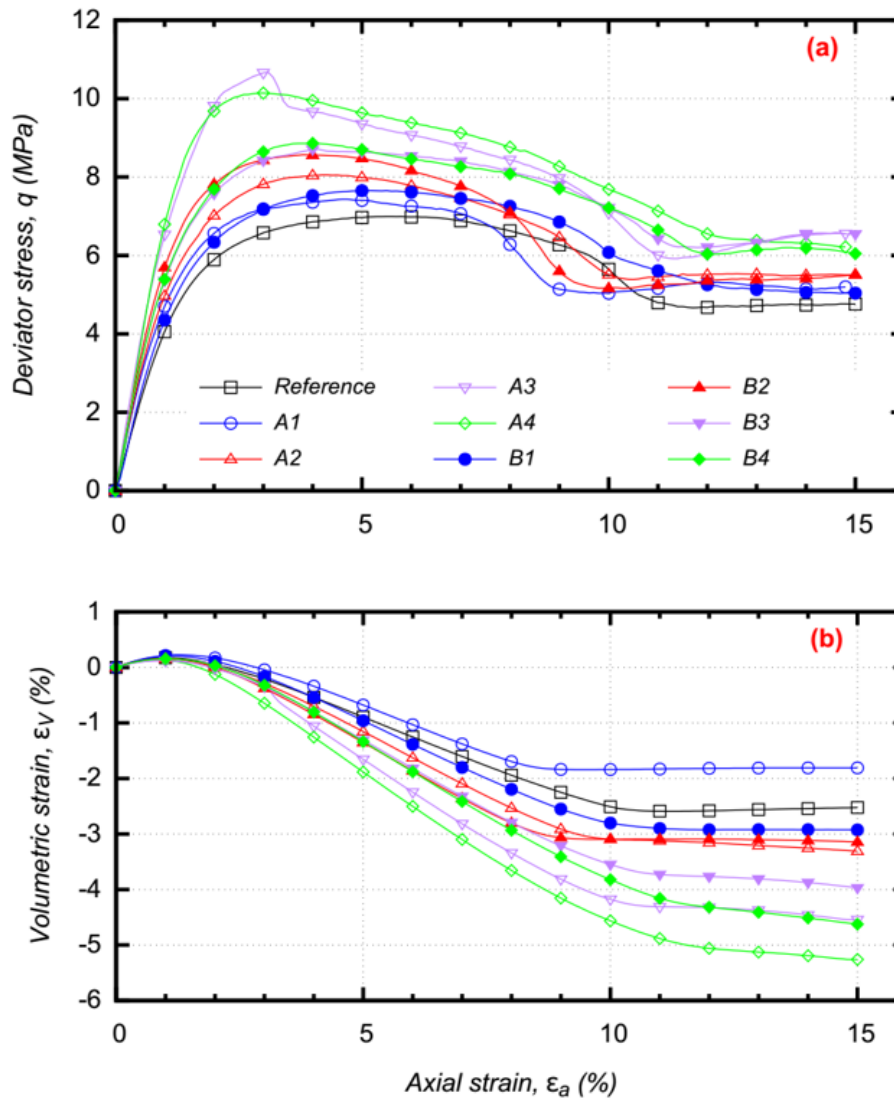


Figure 3.19: Deviator and volumetric strain versus axial strain

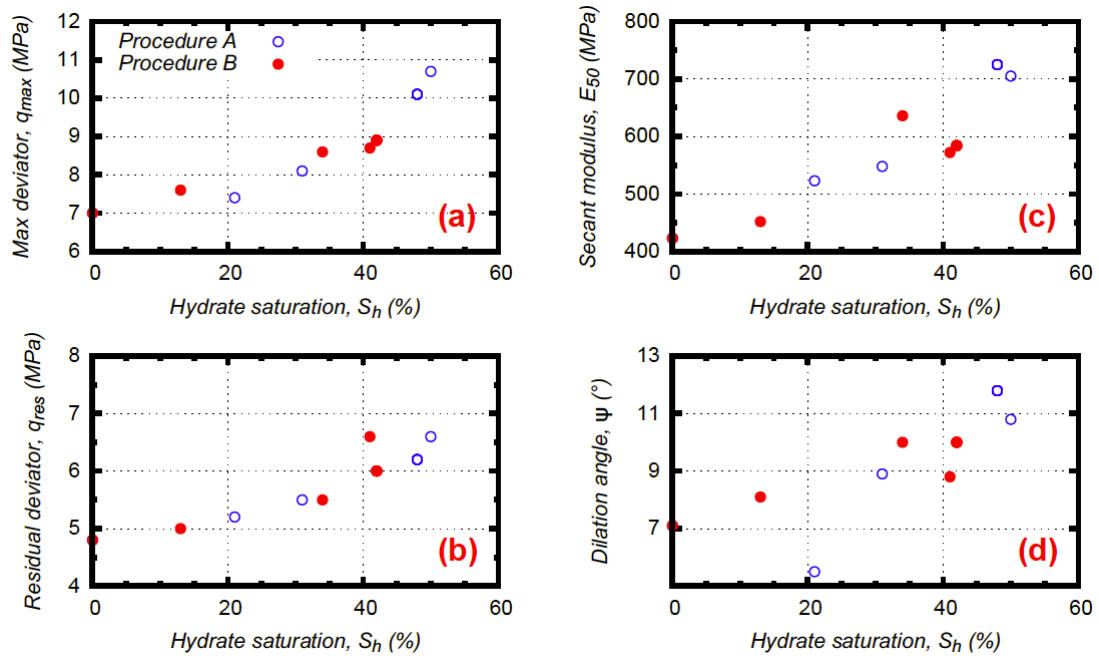


Figure 3.20: Dependence of mechanical properties of sand on methane hydrate saturation for all tests

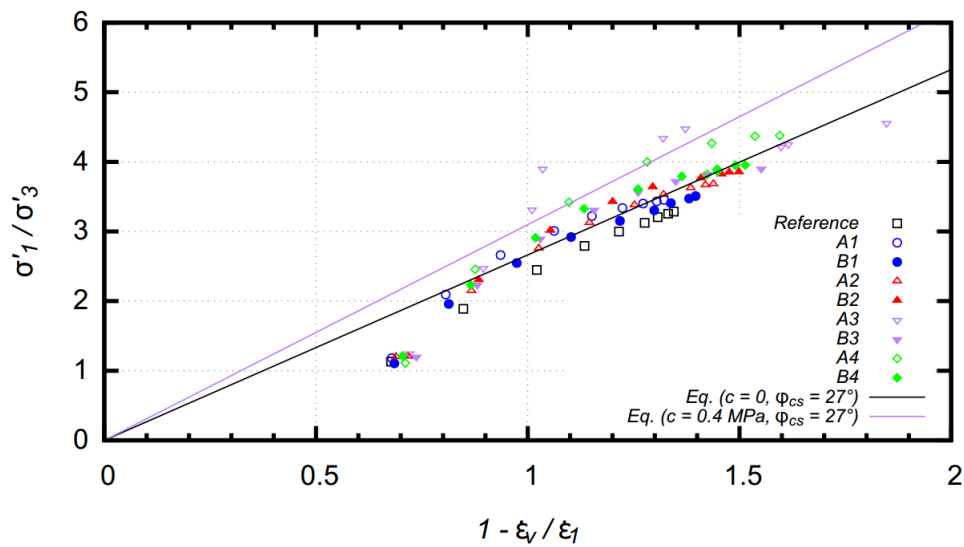


Figure 3.21:  $\sigma'_1/\sigma'_3$  versus  $1 - \epsilon_v/\epsilon_1$



# 4 Kinetics of MH formation and dissociation

## 4.1 Introduction

The kinetics of MH formation following the procedure B (with a temperature cycle) described in chapter 3 were investigated in this chapter in the objective of following the sample homogeneity during the whole MH formation phase by using Magnetic Resonance Imaging (MRI). In addition, MH dissociation after the depressurization method was observed. Methodological efforts were put in getting fast enough measurements to follow the kinetics of MH formation/dissociation during transitory steps.

The results of this chapter are presented in the publication:

T.X. Le, S. Rodts, D. Hautemayou, P. Aïmediou, M. Bornert, C. Baptiste, A.M. Tang (2018) Kinetics of methane hydrate formation and dissociation in sand sediment. *Geomech Energy Environ.* doi: 10.1016/j.gete.2018.09.007.

## 4.2 Experimental method

### 4.2.1 Experimental setup

Schematic views of the experimental setup are presented in Figure 4.1. The sand sample (1), 38 mm in diameter and 76 mm in height, was covered with a neoprene membrane (2). The confining pressure was applied to the sample by a volume/pressure controller (7) using a perfluorinated oil (Galden) as confining fluid (3), chosen due to its low signal intensity in MRI measurements. Methane gas was injected via the bottom inlet (5) by a pressure controller connected to a methane gas flowmeter (10). The top inlet (6) was closed in this study. A second volume/pressure controller (12) was used to control the water pore pressure. The sample temperature was controlled by circulating a perfluorinated oil (Galden), which was connected to a cryostat (8), around the cell (4). The cell was installed in a nuclear magnetic resonance imaging system (13) for observations.

Proton ( $^1H$ ) NMR/MRI measurements are performed with a Bruker 24/80 DBX spectrometer operating at 0.5 T (21 MHz proton frequency) equipped with:

- A birdcage RF coil 200 mm in diameter and height where the whole pressure cell can fit inside;
- A BGA-26 gradient system delivering a maximum gradient strength of 50 mT/m with a rising time of 500  $\mu s$ .

Measurement protocols used in this work rely on the well-established methodologies. They consist of:

- A pulse acquisition sequence, where the overall NMR signal owing to hydrogen was measured after a dead time of  $40 \mu\text{s}$  following the exciting RF pulse. This signal was referred to ‘*FID Intensity*’ signal hereafter;
- A 1D profile imaging based on spin-echo acquisition with a read-out gradient orientated in the vertical direction and an echo time of 4.2 ms, which provided profile measurements with 200 pixels covering a field of view of 200 mm, being large enough to avoid any image aliasing owing to some parts of the external set-up to the observation zone. It provided a space-resolved view of the contribution;
- Furthermore, 2D images (vertical slices) were taken by a combination of spin-echo and gradient-echo acquisition covering a field of 1000 mm (vertical) x 500 mm (horizontal).

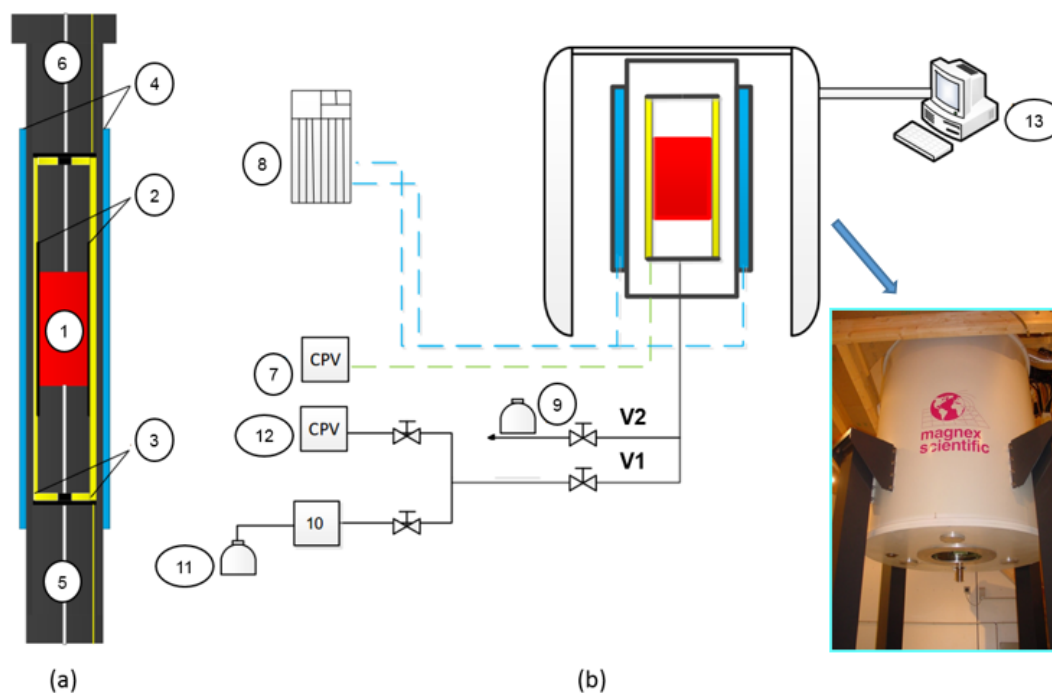


Figure 4.1: Diagram of the MRI experimental setup.

In all kinds of measurements, the signal intensity was expected to be proportional to the amount of hydrogen atoms owing to either liquid (water) or gas (methane) phase. Note that due to the Curie-law for spin polarization, the signal intensity is also inversely proportional to the absolute temperature in  $^{\circ}\text{K}$  of the sample. The dead-time and the echo time were regarded as short enough to neglect bias owing to spin-spin relaxation. On the contrary, methane hydrates and ice contributions were negligible due to their short spin-spin relaxation time. Let us emphasize that *FID Intensities* do not correspond directly to profile intensities, since the integration relationship between them depends on other parameters such as the sample size and the amount of fluid surrounding the sample. Related

data were then presented on independent scales.

If any, the related data processing relied on in-house routines developed under Scilab.

## 4.2.2 Test procedure

Methane hydrate-bearing sandy samples were prepared following the same six steps already described in Section 3.2.3. Similarly, Fontainebleau sand, tap water and methane gas with 99.995 % of purity were used. Note that some magnetic sand grains were eliminated by using a strong magnet to avoid perturbation of MRI measurements.

Furthermore, MH dissociation following the depressurization method (Step 7) was investigated at the end of the MH reformation (Step 6). The confining pressure was maintained at 22 MPa while the valve  $V_2$  was opened to decrease the pore pressure. The volume of methane gas dissociated from the sample was measured by the system (9) shown in Figure 3.6.

Figure 4.2 shows how to prepare the sample outside of the MRI system (Step 1). The steps 3 – 7 were performed in the MRI system and the data were logged automatically during these steps.

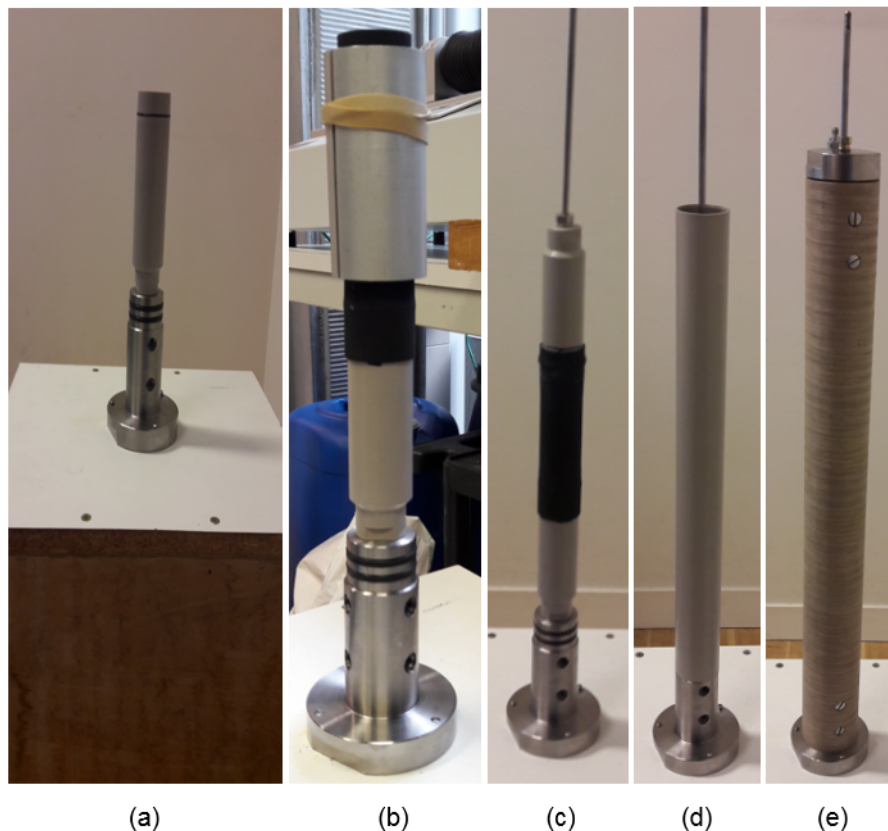


Figure 4.2: The preparation of the sample for MRI observations.

### 4.2.3 Test program

Two tests were performed in this study with the same procedure and the same parameters to ensure the repeatability of the results. The water saturation obtained after the compaction was equal to 25 % (corresponding to a moisture content of 6 %).

### 4.2.4 Calibration tests

Calibration tests were performed at 2 °C on the compacted sample of the first test after the MH dissociation (Step 7). Its density was similar to that of test 2. The sample was saturated with pure phases of various fluids: a, vacuum; b, methane gas at 7 MPa of pressure; c, water at 7 MPa of pressure; and d, water at 19 MPa of pressure. In Figure 4.3, *FID Intensity* obtained for the whole system in each case is plotted. The values corresponding to methane gas at 7 MPa of pressure, water at 7 MPa of pressure, and water at 19 MPa of pressure were then calculated by subtracting that corresponding to the system containing vacuum, in order to remove the spurious signal owing to the pressure cell and the imperfectly perfluorinated oil. In the working conditions of the present study, and as far as the temperature was not modified, the corrected signal was directly proportional to the total amount of hydrogen atoms contained in the fluid molecules. The corrected values of *FID Intensity* are also plotted in the Figure 4.3. The signal of pure methane was significantly smaller than that of water due to different density and chemical composition. In the subsequent sections, the corrected values of *FID Intensity*, i.e. *FID Intensity* measured minus *FID Intensity* obtained from the case (a), are shown.

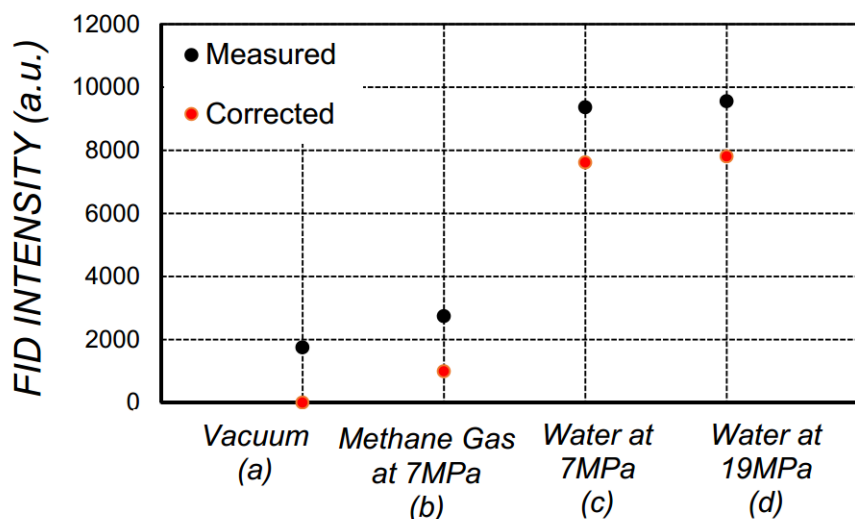


Figure 4.3: Reference signal.

## 4.3 Experimental Results

### 4.3.1 MH formation

The temperature of the cell was first decreased to 2 °C. Vacuum was then applied to eliminate pore air in the sample prior to the injection of methane gas at 7 MPa of pressure

for the MH formation. Figure 4.4 (a) shows the evolution of *FID Intensity* during the MH formation (step 3) for the both tests. When methane gas was injected into the sample, *FID Intensity* increased slightly during the firsts minutes then decreased continuously; the relationship between *FID Intensity* and the logarithm of time during the decrease phase can be correlated with a linear function. After  $t = 40$  h, *FID Intensity* remained constant. The results obtained for the both tests looked similar even if during the first test, the data were not recorded during the firsts minutes. The increase of *FID Intensity* during the firsts minutes can be explained by the accumulation of methane gas inside the sample when methane gas pressure was increased until it reached the target value (7 MPa), see Figure 4.4 (b) where methane gas pressure was plotted versus elapsed time for Test 2 (data for Test 1 were not available). When methane gas pressure exceeded the conditions required to create methane hydrates (3 MPa at 2 °C), MHs started to be created inside the sample. This phenomenon decreased the quantity of water and increased the quantity of methane hydrates. That explains why methane hydrate formation decreased the total *FID Intensity*. Note that the intensity related to methane hydrates was negligible (Baldwin et al., 2009). The following equation was used to estimate methane hydrate saturation ( $S_h$ ):

$$S_h = 1.1 \frac{I_0 + I_m - I}{I_0 + 0.1 \frac{S_{wo}}{1 - S_{wo}} I_m} S_{wo} \times 100\% \quad (4.1)$$

where  $I_o$  was the initial *FID Intensity* of the moist sand sample and  $S_{wo}$  was the initial water saturation ( $S_{wo} = 25$  %). The remaining void space (about 75 % of the total void) contained methane gas (at 7 MPa of pressure when this pressure was reached). For this reason,  $I_m$  - the *FID Intensity* of methane gas (at 7 MPa of pressure) in the sample before the MH formation, equaled to 75 % of the value obtained from the calibration test (case (b) in Figure 4.3):  $I_m = 0.75 \times 1000 = 750$ . This equation was applicable only when the methane gas pressure was 7 MPa. The underlying assumption for this equation was that water reacted locally to form MHs, and that methane gas can go in and out of the sample to occupy the remaining pore space between methane hydrates and the remaining water, owing to the 10 % of volume increase when water was converted to MHs. As a result, during the MH formation, the remaining void containing methane gas was  $(100 - S_{wo} - S_h)$  % of the total void.

Figure 4.4 (c) shows the evolution of the methane hydrate saturation estimated this way for Test 2. MHs could start to be created immediately when the methane gas pressure was higher than 3 MPa. As mentioned before, methane hydrate saturation was only calculated from when the pore pressure reached 7 MPa (at 0.06 h, methane hydrate saturation equaled to 0.3 %). The methane hydrate saturation increased then linearly with the logarithm of time and reached its maximal value after 40 h. Note that after 40 h,  $S_h = 27$  %, that means all water in the sample has been transformed into MHs, and that the remaining MRI signal at the end of the process was that of methane gas.



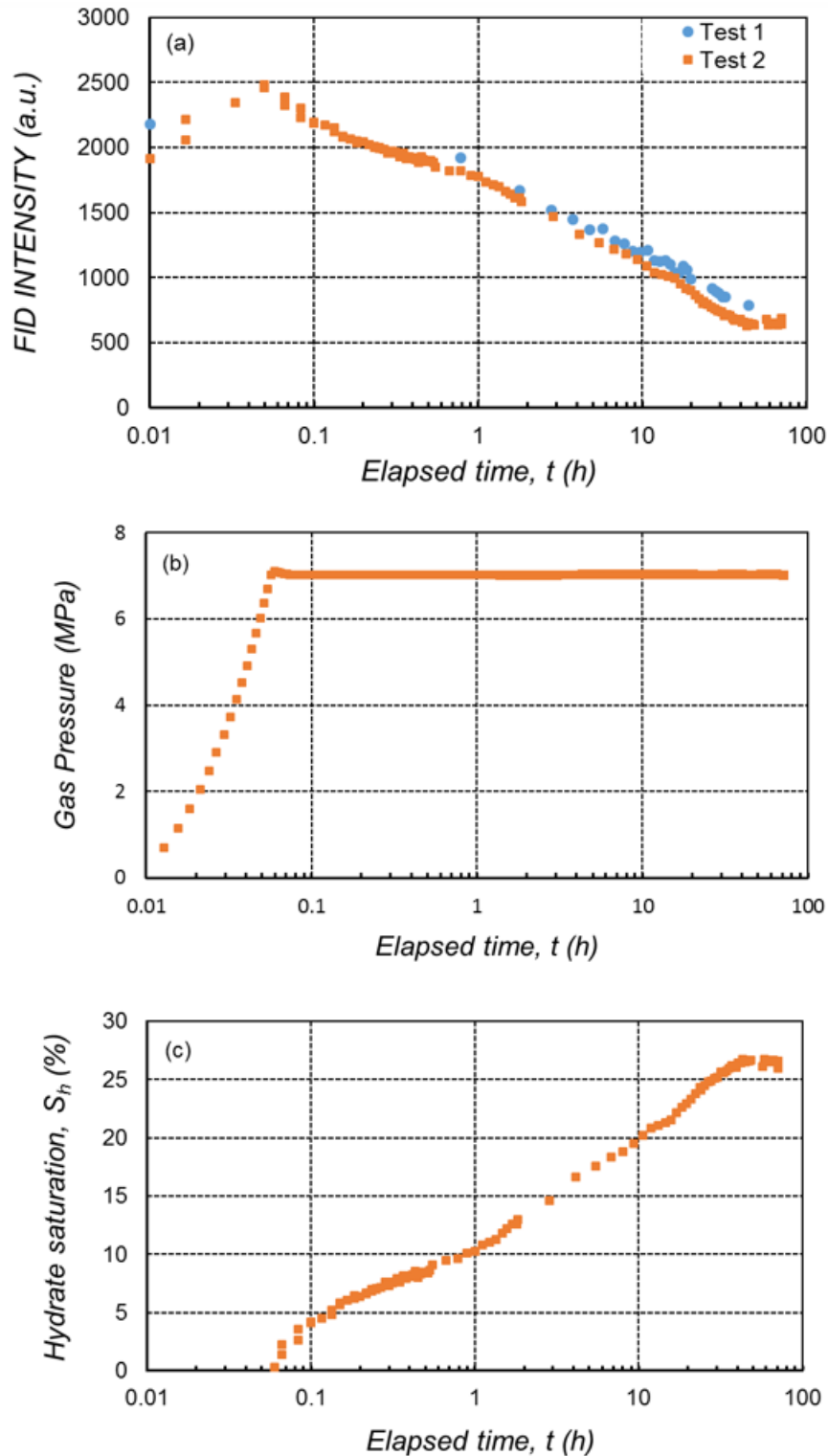


Figure 4.4: (a) FID Intensity evolution of the two tests during the MH Formation in methane gas saturated media; (b) Pore Pressure and (c) Estimated methane hydrate saturation evolution of Test 2.

Figure 4.5 shows the MRI signal (i.e. owing to water and methane gas) versus the sample height ( $Z = 0$  corresponds approximately to the bottom of the sample) for various times.

It can be noted that the signal was generally homogeneous along the sample height. At the beginning ( $t = 0$ ), the sample contained only water and air in the pore space. The observed slight fluctuation of the signal along the sample height might correspond to the compaction procedure (moisture sand tamped by layers of 10 - 20 mm), which induced slight heterogeneity of porosity and water distribution in the sample. When methane gas was injected into the sample, MHs were formed and the water content decreased progressively. That explains why the signal decreased progressively with time. The profile became more homogeneous. The homogeneous formation of MHs in the sample was then confirmed by vertical slices of Test 2 at different times during the MH formation, shown in Figure 4.6, as the brightness was homogeneous in each slice. Note that the brightness of the image was mainly proportional to the actual number of hydrogen nuclei in the liquid water phase in the sample. At the end of the MH formation, the brightness represented methane gas signal in the pore space.

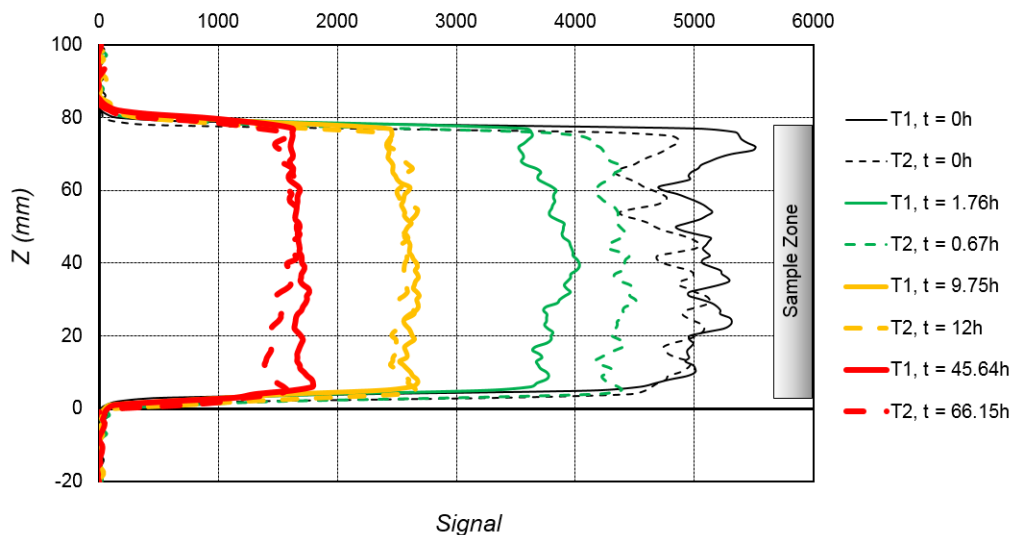


Figure 4.5: MRI signal versus the sample height for the two tests during the MH formation in methane gas-saturated media.

### 4.3.2 Water saturation

Figure 4.7 plots *FID Intensity* during the water saturation (Step 4).  $t = 0$  corresponds to the opening of the valve  $V_2$  to atmosphere during a short period to let all the excess methane gas (initially under a pressure of 7 MPa) escape from the sample (pore pressure decreased to zero). That induced a quick decrease of *FID Intensity* to 0. The valve  $V_2$  was closed before that tap water (at ambient temperature) fixed at 7 MPa of pressure was injected into the sample ( $t = 0.06$  h) via the bottom inlet, connected to the volume/pressure controller (12), shown in Figure 4.1. *FID Intensity* increased quickly and reached the maximal value when water pressure reached 7 MPa. The water injection in Test 1 was slowed down between 0.1 – 0.4 h due to an interruption to inject more water into the volume/pressure controller (12).

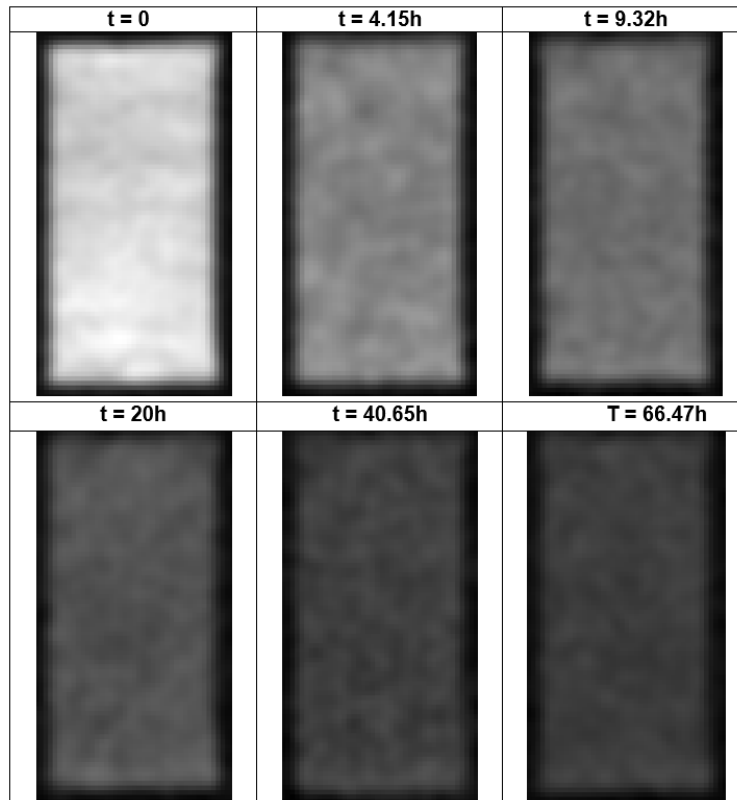


Figure 4.6: Vertical slices of Test 2 during the MH Formation in gas-saturated media.

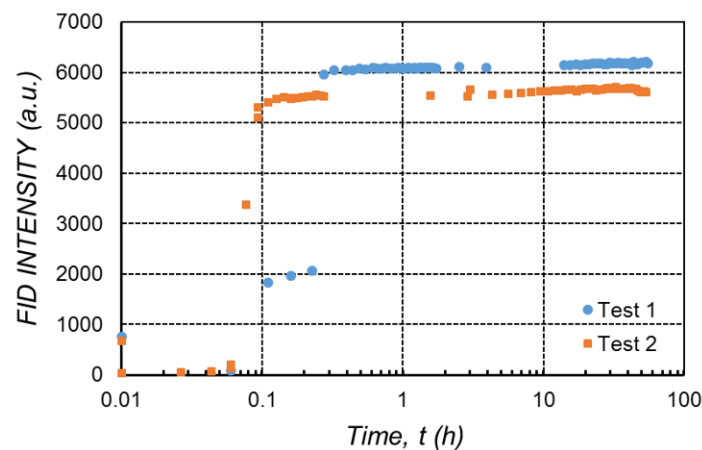


Figure 4.7: FID Intensity evolution of two tests during the water saturation process.

The signal versus the sample height of Test 2 is plotted at various times, Figure 4.8. Profile at 60 s ( $t = 0.047$  h) was measured when methane gas was decreased to the atmospheric pressure. When water was injected from the bottom inlet, signal at the bottom started to increase first ( $t = 0.063$  h). When the water pore pressure reached 7 MPa, the sample can be expected to be fully saturated with water,  $t = 55$  h (methane gas should not exist in these conditions). At this state, higher signal can be observed in the zone close to the bottom of the sample while it was lower in the zone close to the top.

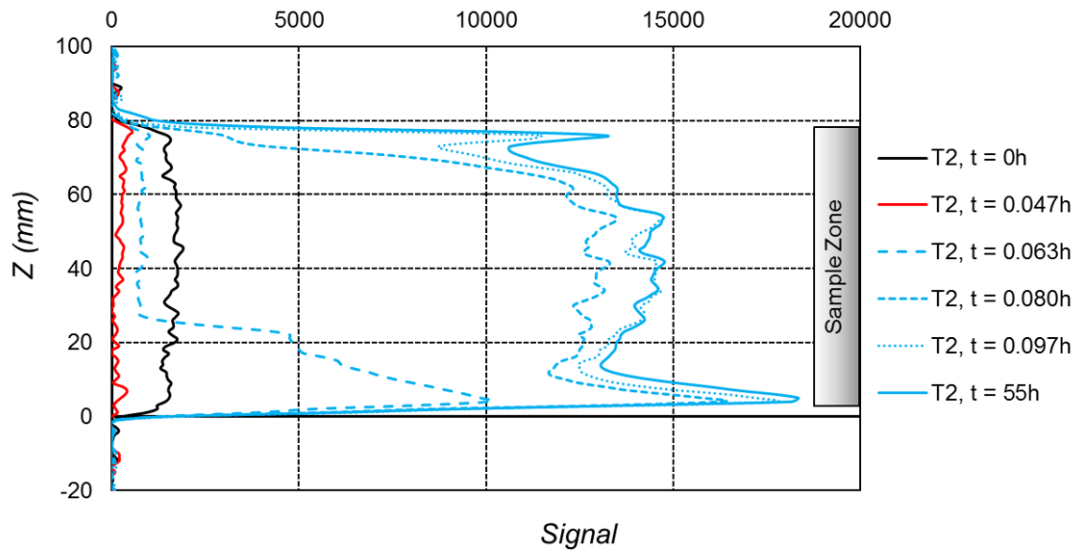


Figure 4.8: Signal versus the sample height for Test 2 during the water saturation process.

Figure 4.9 shows the signal versus the sample height for the both tests at the end of the water saturation step. The results of Test 1 showed also a higher signal close to the bottom but the signal at the top was similar to the remaining part of the sample. The heterogeneity of water distribution along the sample height at the end of this step can be explained by the saturation procedure. Actually, methane gas evacuation and water injection were performed both from the bottom. The methane gas evacuation, even if it was performed quickly, less than one minute, would induce methane hydrate dissociation at the zone close to the bottom. That might explain why in the end, methane hydrate saturation at the bottom was lower (higher signal) than in the other parts of the sample.

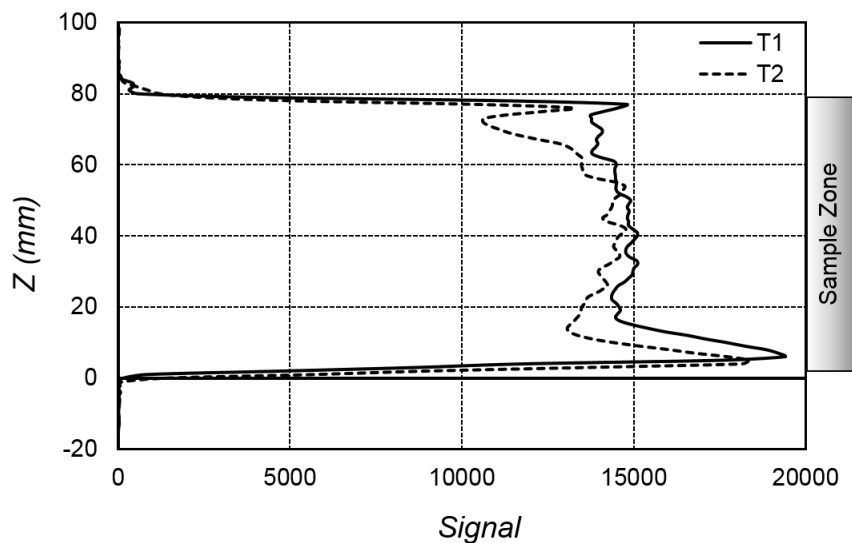


Figure 4.9: Signal versus the sample height for both tests at the end of the water saturation phase.

Based on the intensity of the sample obtained at the end of the water saturation step, methane hydrate saturation estimated for the both tests were 20.5% and 27.5% respectively. MH dissociation at the zone close to the bottom induced eventually a decrease of methane hydrate saturation compared to that after the methane hydrate formation step. However, this decrease was the same for Test 1 and Test 2. When water was injected from the bottom, the remaining gas would accumulate in the zone close to the top of the sample, thus impeding total water saturation. At the end of the water saturation phase, the remaining gas would be transformed into methane hydrates, methane hydrate saturation was then increased. That may be why the methane hydrate saturation in this zone seemed higher than that in the other parts (lower signal) in Figure 4.9.

### 4.3.3 MH dissociation - reformation

A temperature cycle was performed after the water saturation phase. Figure 4.10 shows the pore pressure (a), the cryostat temperature (b) versus elapsed time for Test 1. It should be noted that the sample temperature could not be measured during these tests in the MRI system. However, preliminary tests, performed outside of the MRI system, showed a characteristic time of 20 min for the temperature exchange between the cryostat and the sample. At the beginning of the test, the pore pressure was first decreased to 4 MPa for a faster heating-induced methane hydrate dissociation as methane hydrates were closer to the equilibrium boundary. Afterward, the cryostat temperature was increased from 2 °C to 25 °C with a constant rate. As the heating was performed under undrained conditions (the valves  $V_1$  and  $V_2$  were closed), pore pressure increased according to the heating and stabilized at 14 MPa when the temperature reached 25 °C. After this phase, the valve  $V_1$  was opened to connect the cell to the pressure/volume controller (12) in order to impose a pore pressure of 19 MPa. This pressure was maintained until the end of the cooling-induced hydrate reformation phase (Step 6). At  $t = 7.5$  h, the cell temperature was decreased quickly to 2 °C to recreate MHs.

Figure 4.10 (c) plots *FID Intensity* versus elapsed time during these steps. The data from the beginning to  $t = 1.6$  h were unfortunately not available. From  $t = 1.6$  h, *FID Intensity* decreased as the sample temperature increased. Indeed owing to the Curie law for the spin polarization in the MRI magnet, *FID Intensity* must be here considered to be additionally influenced by temperature, being inversely proportional to its absolute value in Kelvin. For a given fluid content, it then increased when temperature decreased and vice-versa. At  $t = 2.8$  h, *FID Intensity* started to increase when the additional signal of the released water (from the MH dissociation) was higher than the decrease induced by the temperature increase. In the present study, no direct temperature measurement was available inside the sample, and no temperature correction of *FID Intensity* was made. At  $t = 3.6$  h, *FID Intensity* decreased when MHs have been completely dissociated (pore pressure reached 14 MPa) but the sample temperature continued to increase to reach the imposed temperature in cryostat. At  $t = 4.4$  h, increasing pore pressure from 14 MPa to 19 MPa induced an increase in *FID Intensity*. When the cryostat temperature was decreased quickly ( $t = 7.5$  h), the temperature of the sample decreased progressively inducing an increase of *FID Intensity*. At  $t = 8.2$  h, MHs started to be recreated progressively, inducing the decrease of *FID Intensity*. When the MH reformation was completed, *FID Intensity* stabilized.

The results of Test 2 are shown in Figure 4.11. After reducing the pore pressure from 7 MPa to 4 MPa, the cryostat temperature was increased quickly from 2 °C to 20 °C ( $t = 0.1$  h) and then to 25 °C ( $t = 2.1$  h). It was decreased to 2 °C at  $t = 22$  h. Heating under undrained conditions induced an increase of pore pressure from 4 MPa to 15 MPa. The subsequent heating (from 20 °C to 25 °C) did not influence the pore pressure. From  $t = 4.1$  h, the pore pressure was maintained at 19 MPa as the case of Test 1. The results of *FID Intensity* showed phenomena similar to that observed in Test 1:  $t = 0 - 0.6$  h, *FID Intensity* decreased due to the heating;  $t = 0.6 - 1.9$  h, *FID Intensity* increased due to the MH dissociation;  $t = 1.9 - 4$  h, *FID Intensity* decreased due to the heating; from  $t = 4$  h, *FID Intensity* increased due to an increase of pore pressure (from 14 MPa to 19 MPa);  $t = 22$  h, *FID Intensity* increased first due to cooling then decreased due to the MH reformation. More regular *FID Intensity* acquisitions between 2-5 h of Test 2 were not available to reflect better the MH dissociation – reformation.

Figure 4.12 shows the signal versus the sample height for the both tests at the end of the water saturation, MH dissociation, and MH reformation phases. The results showed a slight redistribution of water after the MH dissociation/reformation cycle. At the end of this cycle, water seemed distributed more homogeneously. Min/Mean and Max/Mean profile signal of Test 1 were (0.92; 1.30), (0.93; 1.10) respectively for the water saturation and MH reformation case. Similarly, they were (0.76; 1.32), (0.90; 1.26) for Test 2.

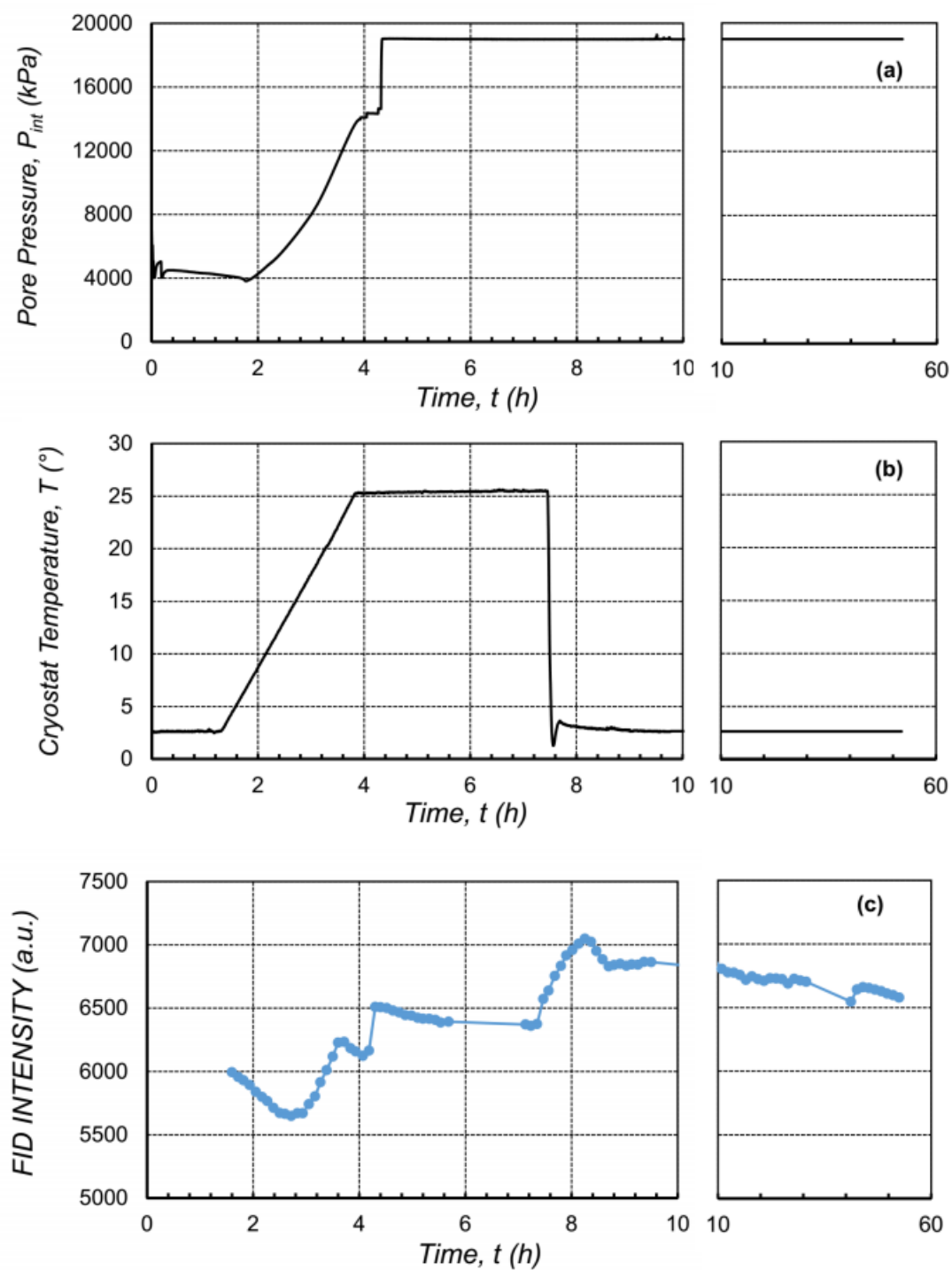


Figure 4.10: (a) Pressure evolution; (b) –Temperature evolution; (c) FID Intensity evolution during the MH dissociation-reformation of Test 1.

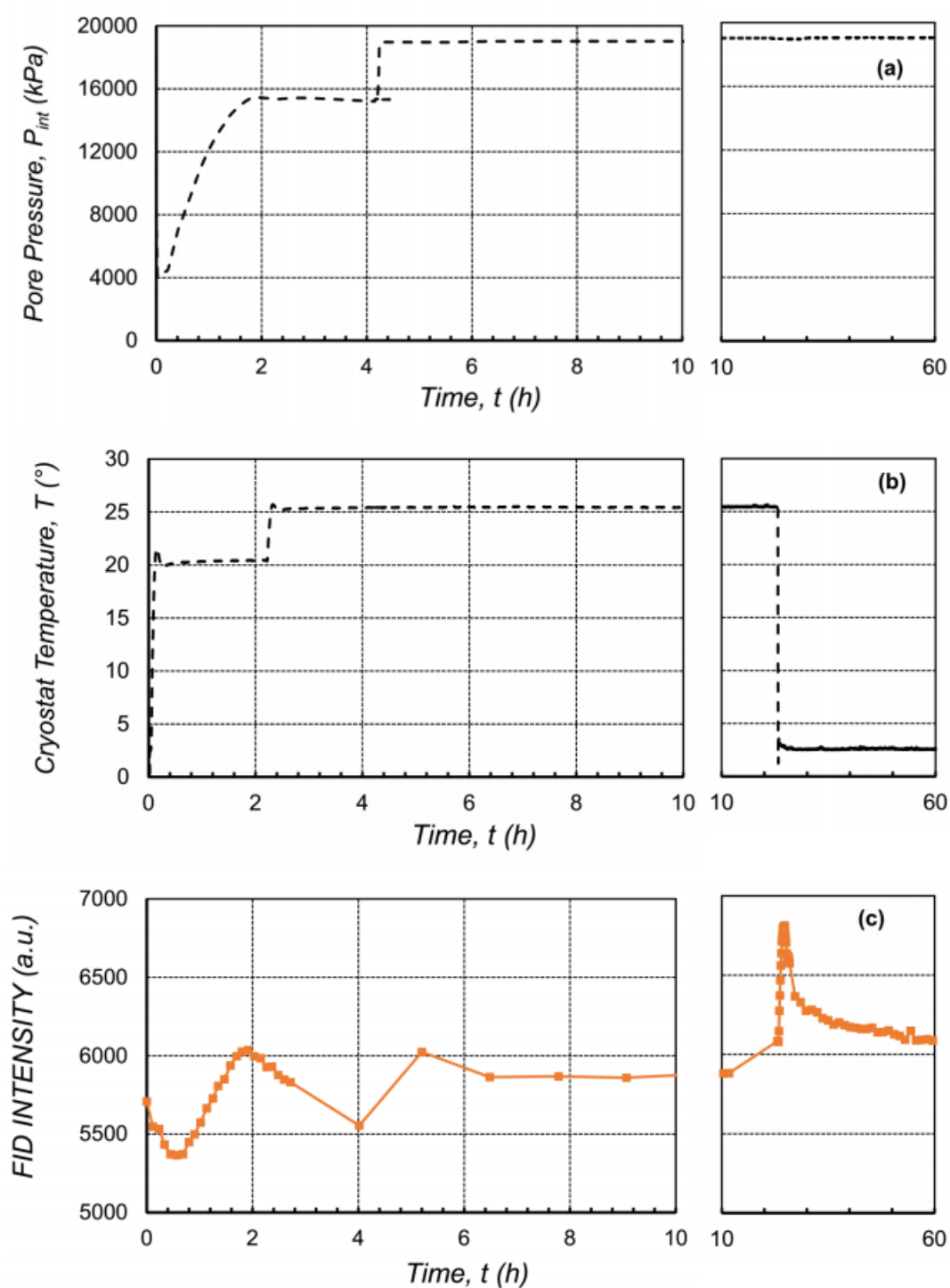


Figure 4.11: (a) Pressure evolution; (b) –Temperature evolution; (c) FID Intensity evolution during the MH dissociation-reformation of Test 2.



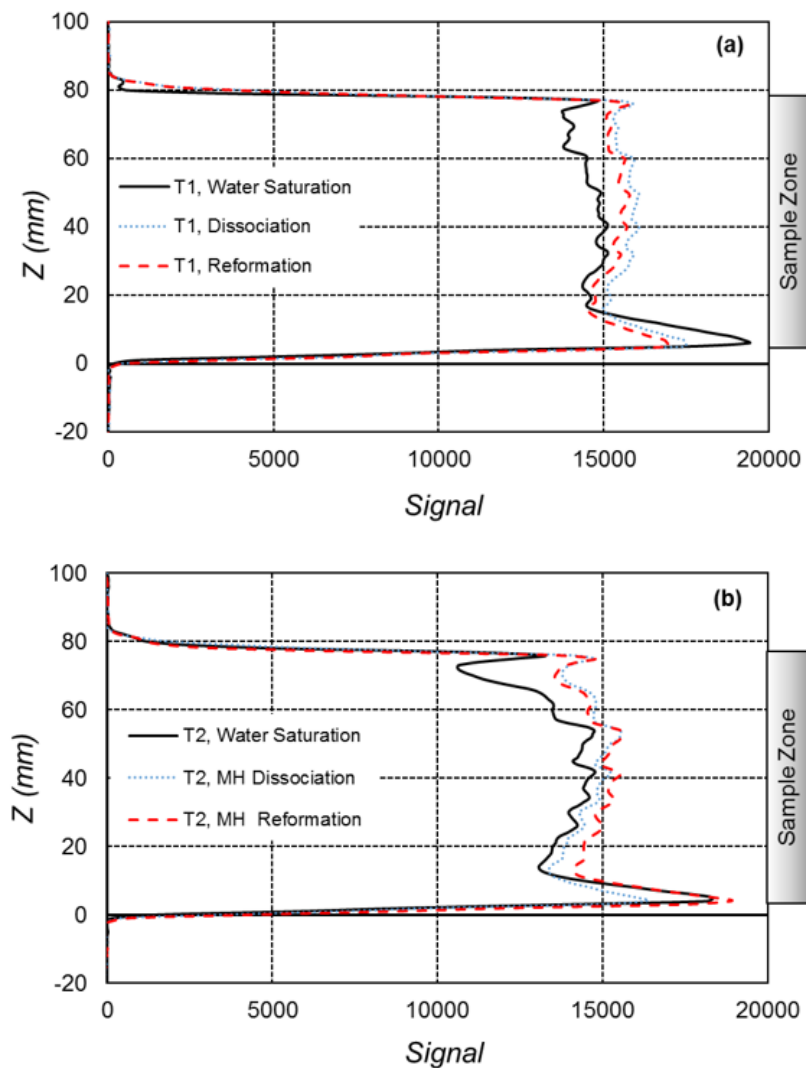


Figure 4.12: Signal versus the sample height at the end of the water saturation, MH dissociation, and MH reformation phases: (a) Test 1; (b) Test 2.

#### 4.3.4 Depressurization-induced hydrate dissociation

To observe the depressurization-induced MH dissociation, pore pressure was first decreased from 19 MPa to 5 MPa while the sample temperature was maintained at 2 °C. Note that these conditions were inside of the MH stable zone. The valve  $V_2$  was then connected to the system (9) while the valve  $V_1$  was closed. That reduced pore pressure directly to the atmospheric pressure. The quantity of dissociated methane gas measured by the system (9) was used to estimate the methane hydrate saturation  $S_h$  remaining in the sample. MRI data were disregarded for such purpose because ice was likely to appear in the sample at this step and impeded the direct interpretation of the signal intensity.

Figure 4.13 shows methane hydrate saturation and *FID Intensity* versus elapsed time during the MH dissociation for Test 1 (a) and Test 2 (b). The results of Test 1 showed a quick decrease of  $S_h$  from 21 % at the beginning to almost zero after 0.2 h. During this period,

*FID Intensity* decreased quickly. Once the MH dissociation was finished, *FID Intensity* increased slowly during the next hour. The results of Test 2 showed similar trends but *FID Intensity* decreased more slowly at the beginning. In fact, in the objective of decelerating the methane hydrate dissociation, for Test 2, valve  $V_2$  was opened partly at the beginning (0 - 0.067 h). However, the MH dissociation was stopped as released methane gas and water were blocked in the sample. Valve  $V_2$  was so opened completely, *FID Intensity* decreased fast afterward. The decrease of *FID Intensity* during the MH dissociation phase can be explained by the expellee of water from the sample by the released methane gas. At the same time, as the MH dissociation is an endothermic process, ice would be formed during this phase. That induced a decrease of *FID Intensity* even when methane hydrates were almost dissociated. In the subsequent phase, ice melting increased the quantity of liquid water in the sample, which explains the increase of *FID Intensity*.

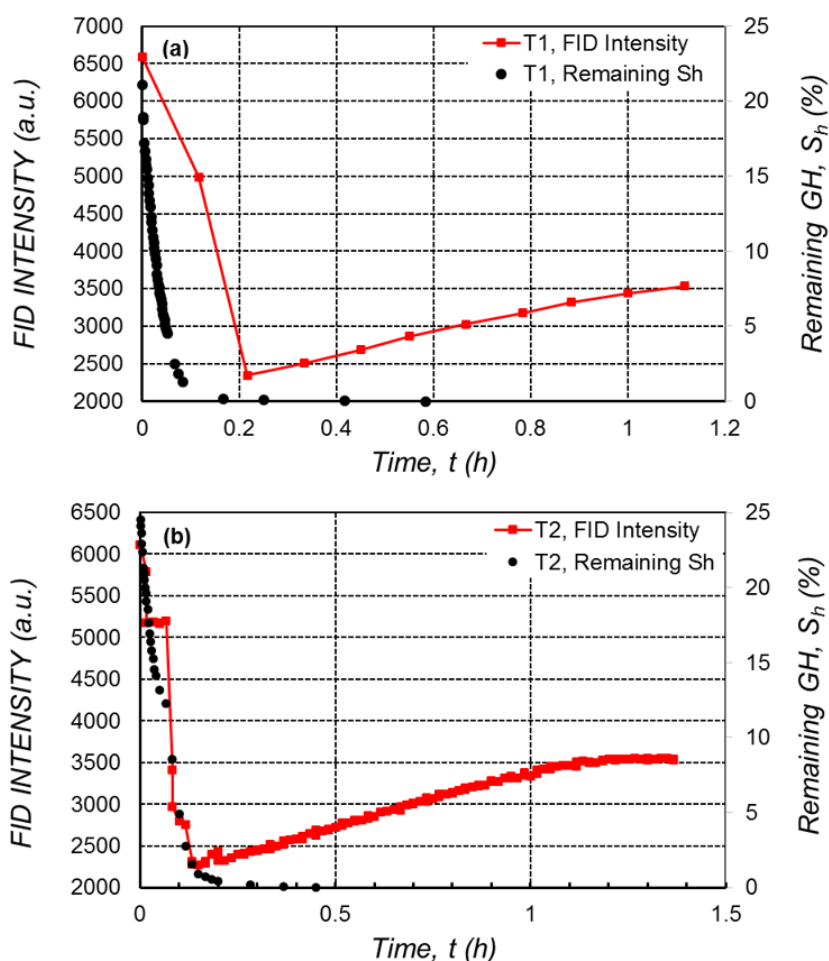


Figure 4.13: *FID Intensity* and Remaining MH evolution during the MH dissociation for (a) Test 1 and (b) Test 2.

The signal versus the sample height is plotted for various times during this step in Figure 4.14. These results confirm the statement above. An ice formation took place only in the zone where methane hydrates were present (i.e. along the whole sample height except the zone close to the bottom). For this reason, signal at this zone increased at the end of the MH dissociation phase (which corresponds to the ice melting) while the signal at the

zone close to the bottom remained constant. Actually, rapid MH dissociation by depressurizing the sediments below the quadruple point of methane hydrates (intersection point of ice-water-vapor-methane hydrate) dropped the sample temperature below the freezing point of water, causing ice formation (Haligva et al., 2010; Konno et al., 2012). Heat of methane hydrate dissociation is  $450 \text{ Jg}^{-1}$  (Garg et al., 2008) while it is  $-342 \text{ Jg}^{-1}$  for the transformation of water at  $2^\circ\text{C}$  to ice. Depending on heat transfer in the temperature control system to compensate the sample temperature decrease due to the MH dissociation, MH reformation and ice formation ratio varied depending also on the kinetics of the MH dissociation. That is why pore pressure was reduced from 19 MPa to 5 MPa before finally being set up at atmospheric pressure for the both tests to better observe the MH dissociation. Fan et al., 2017 investigated the MH dissociation in glass beads (under excess-gas conditions) after the depressurization method. The ice formation was also observed by a rapid reduction of  $MI$  and water distribution variation with time in the case where pore pressure was reduced below the quadruple point of methane hydrates (Fan et al., 2017).

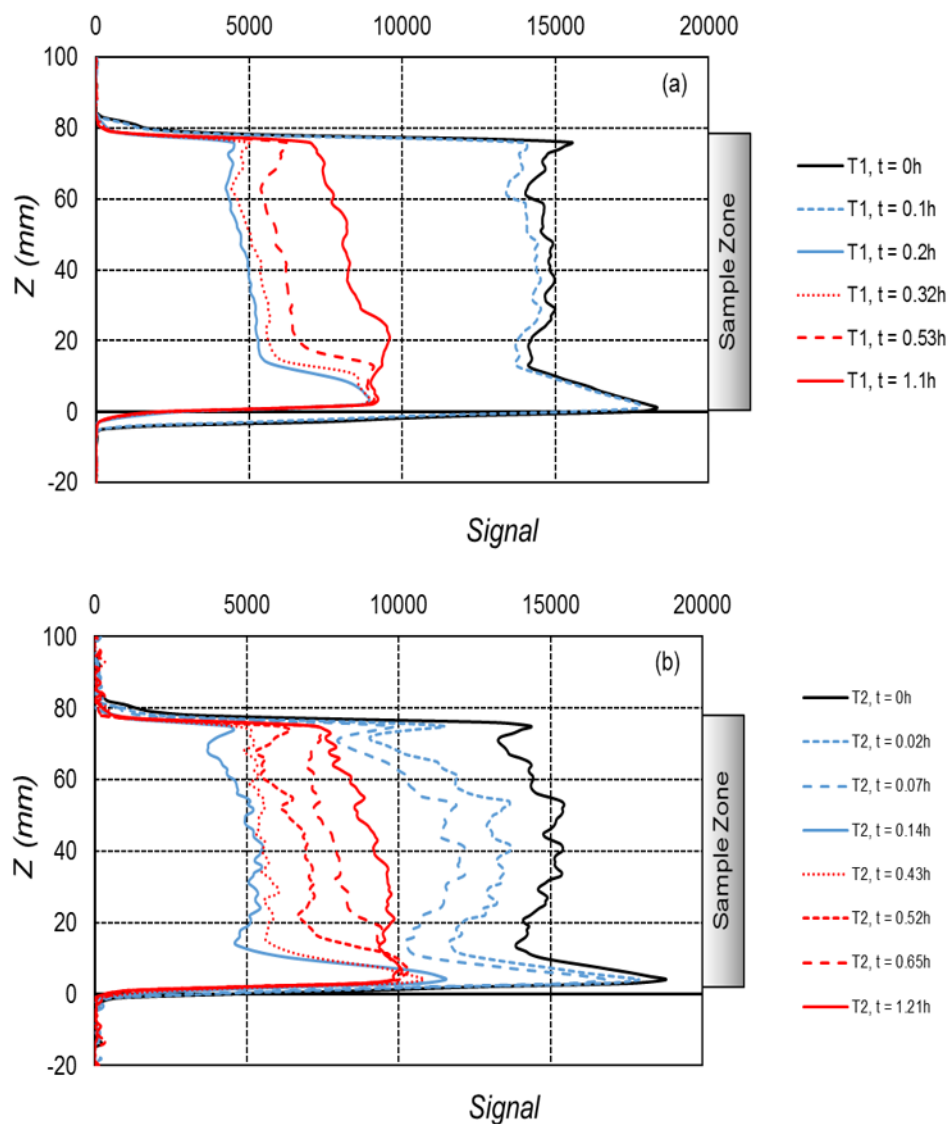


Figure 4.14: Signal versus the sample height for two tests during the MH dissociation.

## 4.4 Conclusions

MHBS were firstly created by pressurizing methane gas (at 7 MPa) into already chilled moistened packed sandy samples (after the excess-gas method). Following the MH formation, water was injected into the sample and the remaining gas was bled out simultaneously. A subsequent heating/cooling cycle was applied in order to completely dissociate MHs and then recreate them inside the sample. Methane hydrate dissociation following the depressurization method was also investigated after the whole MH formation process. From MRI measurements, the following conclusions can be drawn:

- Pressurizing methane gas into already chilled moistened packed sandy sample created MHs in the sample. The formation was fast at the beginning, slowed down after some hours and then stabilized after some ten hours. The formation of MHs was uniform along the sample height;
- Subsequent water saturation redistributed MHs in the sample.  $S_h$  at the water inlet was smaller than that in the other parts (due to MH dissociation) while  $S_h$  at the opposite end could be higher (due to an additional MH formation);
- Undrained heating/cooling cycle made MHs distributed more homogeneously in the sample;
- The ice formation in MHBS under excess-water conditions due to the depressurization-induced MH dissociation below the quadruple point of methane hydrates was observed, and induced heterogeneous MRI profiles before ice was completely melted.



# 5 XRCT MH observation technical developments

## 5.1 Introduction

This chapter is divided into two parts. The first one describes the development of three experimental setups, which aim at creating methane hydrates inside sandy sediment, adapted to XRCT/SXRCT observations. Furthermore, a new method, served to determine more accurately the volume fractions of three-phase media from XRCT images will be presented in the second part. This method combines a full use of the gray levels of a XRCT image with information on the morphology of the constitutive phases. It incorporates the physics of image noise and partial volume effects. This method has been applied to determine methane hydrate saturation of MHBS under excess-gas conditions.

The first part of this chapter is included in the publications:

- T.X. Le, P. Aïmedieu, M. Bornert, B. Chabot, A.M. Tang (2019) Experimental development to investigate the grain-scale morphology and pore habit of methane hydrate-bearing sandy sediment by X-ray computed tomography. Submitted to Geotechnical Testing Journal.
- T.X. Le, M. Bornert, P. Aïmedieu, B. Chabot, A.M. Tang (2019) Segmentation-insensitive accurate determination of volume fractions in unsaturated sand from X-ray computed tomography (XRCT). In preparation.

## 5.2 Part I: Experimental setups for XRCT/SXRCT observations

### 5.2.1 Introduction

It is challenging to investigate synthetic methane hydrate-bearing sand via XRCT/SXRCT because of the constraint to maintain the sample with high pressure and low temperature while it is scanned, as well as of the poor image contrast between methane hydrate and water. For XRCT images, spatial resolution depends mainly on the distances between the X-ray source, the object and the detector. Complex experimental setups for MHBS studies might limit the image spatial resolution because of the geometry of the sample environment. The image spatial resolution can be well improved by using SXRCT, for which this constraint is less critical compared to XRCT. However, SXRCT scans are costly and the access is limited. By using other gases ([Kerkar et al., 2009](#); [Ta et al., 2015](#);

Chaouachi et al., 2015; Chen and Espinoza, 2018), experimental setups were less complicated. For instance, there is no need of pressure control for observations of THF hydrates (THF hydrates can be formed at atmospheric pressure) while lower pressure and/or higher temperature are sufficient for the study of CO<sub>2</sub> or Xe hydrates. Note however that gas hydrate morphologies and pore habits depend on the type of gas used. Furthermore, XRCT/SXRCT image contrast can be improved either by using another gas/fluid (e.g. THF, Xe) or using saline water (e.g. BaCl<sub>2</sub>, KI). However, methane hydrate formation from saline solution can increase salt concentration and inhibit further MH formation.

XRCT scans have been usually conducted at the end of gas hydrate formation in sandy sediments as the scanning time is long (several hours). With the higher temporal resolution of SXRCT (few minutes), the dynamic process of gas hydrate growth/formation in sandy sediments could be captured.

Three experimental setups have been developed in the objective of investigating pore-scale morphologies and pore habits of MHs in sandy sediments via XRCT as well as SXRCT. Improvements in not only image contrast but also in image spatial resolution have been taken into account. As CT images alone cannot differentiate methane hydrate from water, saline water (i.e. KI) is used to better distinguish between the liquid phase and methane hydrate. Furthermore, efforts have been made to enhance the image spatial resolution in order to distinguish methane hydrates from the liquid phase (for both tap water and saline water cases) based on their morphology.

In the following parts, optimization of XRCT scan conditions for MHBS is first described. Afterward, the three experimental setups are presented and the corresponding advantages and drawbacks are discussed.

## 5.2.2 Optimization of image contrast

Absorption XRCT and SXRCT consist in exposing an object to X-rays from multiple orientations (by rotating the sample in this study) and measuring the intensity decrease for all source-detector paths generated this way. Gray levels of the obtained radiographic images, after the calibration, quantify the attenuation of the sample, i.e. reflect the proportion of X-ray absorbed/scattered as they pass through the object. More precisely, X-ray attenuation follows a Beer-Lambert type law (Swinehart, 1962), which involves the linear attenuation coefficient ( $\mu$ ). Different phases in the object can be well distinguished if their attenuation coefficients are significantly different from each other. Indeed, the coefficient  $\mu$  is a function of the energy of X-ray and in a polychromatic setups (as for XRCT), the gray levels of the image result from a complex average of the linear attenuation coefficients, relative to the used energy range, which may be optimized.

In this study, theoretical ratios of linear attenuation coefficient of different phases (methane gas, pure water, methane hydrate, saline water, quartz) are first calculated in order to quantify the induced contrast between phases on the image gray scale (see Figure 5.1). For the considered materials, sand grains are the most absorbing objects while methane gas is the least absorbing. We thus plot the absorption of the other phases (water, MHs and saline water) in a scale where 1 corresponds to grains and 0 corresponds to gaz. In the XCOM

program established by National Institute of Standards and Technology (<https://physics.nist.gov/PhysRefData/Xcom/Text/ref.html>)

the mass attenuation coefficient ( $\mu/\rho$ ) of various compounds are provided for various values of photon energy. These data allowed plotting the curves corresponding to the attenuation ratio of water/quartz and methane hydrate/quartz shown in Figure 5.1. For the saline solutions (i.e. KI), the value of mass attenuation coefficient of the solution is obtained according to a simple addition:

$$\mu/\rho = \sum_i w_i(\mu/\rho)_i \quad (5.1)$$

where  $w_i$  is mass proportion of the component  $i$  (water or salt),  $\rho$  is the unit mass, equal to 1 and 3.12 ( $\text{g}/\text{cm}^3$ ) for water and KI respectively. The results obtained for KI solution of 2, 3.5 and 5 % by weight are also plotted in the Figure 5.1. Note that density of quartz, methane gas, methane hydrate and water are 2.65, 0.0007, 0.9 and 1 ( $\text{g}/\text{cm}^3$ ) respectively.

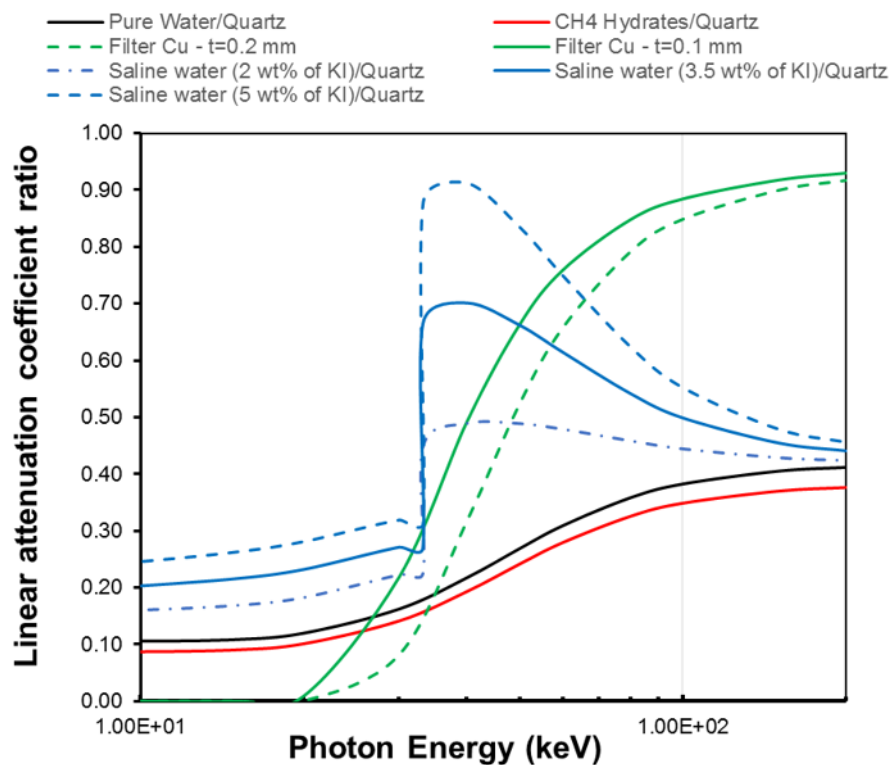


Figure 5.1: Linear attenuation coefficient ratio between phases versus photon energy.

Figure 5.1 shows that, for the whole energy range available in our laboratory setup (10-200 keV), there is almost no difference between the ratio of water/quartz and that of methane hydrate/quartz. The difference in gray level of these two phases is in the order of image noise (typically 2 to 10 % of gray level range). That is why it is difficult to distinguish methane hydrates from water in a XRCT image. For the case of KI solutions, their ratios are significantly different from that of methane hydrate in the range of photon energy higher than 33 keV where an absorption edge is observed. At 5 wt% of KI, the maximum ratio is really close to 1 (i.e. saline solution absorbs almost as quartz) while at 2



%, enhancement by using KI solution is moderate. Therefore, saline water of 3.5 wt% of KI by weight was chosen in this study so that saline water can be distinguished from both methane hydrate and sand grain. More precisely, for energies between 33 and 60 keV, the gray level of saline solution would be at optimal distance from quartz and MH, optimizing the image contrast. Note that, the XRCT source is a polychromatic source with a wide energy spectrum with a maximal energy corresponding to the prescribed electron beam acceleration voltage. However, its maximum intensity, due to the Bremsstrahlung effect, is somewhat below that maximum. Furthermore, to avoid beam hardening artifacts in XRCT scans and more specifically to reduce X-rays below 33 keV, a copper filter (Cu) was used to eliminate low energy X-rays. The fraction decrease of X-ray intensity  $\exp(-\mu_{Cu} \times t_{Cu} - \mu_{Al} \times t_{Al})$  of two cases of copper thickness ( $t_{Cu}$ ), rescaled as aforementioned, is shown in Figure 5.1 (Aluminum tube thickness,  $t_{Al}$  is  $2 \times 0.89$  mm). In this study, a Cu filter of 0.1 mm of thickness was used to conserve more X-ray energy in the range of 30 – 100 keV where the linear attenuation coefficient ratio of KI solution of 3.5 wt% is well separated from that of methane hydrates.

Preliminary scans at aforementioned optimized conditions (prescribed voltage of 80-100 keV; Cu filter of 0.1 mm of thickness) were done. Images obtained on mixtures of dry sand with either pure water or saline water compacted in an aluminum tube (exterior diameter,  $d_{ext.} = 6.45$  mm; thickness,  $t = 0.89$  mm) are shown in Figure 5.2. For the case of sand wetted with pure water, Figure 5.2a, the mean gray values of each phase were determined from the gray value profiles (Figure 5.2c):  $G_a = 21100$  (for air);  $G_q = 22700$  (for quartz);  $G_w = 21600$  (for pure water). Similarly, for the case of sand wetted with saline water (Figure 5.2b), Figure 5.2d shows:  $G_a = 12400$ ;  $G_q = 14150$ ;  $G_{sw} = 13400$  (for saline water). The ratios of water,  $R_{w/q}$  and of saline water,  $R_{sw/q}$  were calculated as follows:

$$R_{w/q} = (G_w - G_a)/(G_q - G_a) \quad (5.2)$$

$$R_{sw/q} = (G_{sw} - G_a)/(G_q - G_a) \quad (5.3)$$

After the results shown in Figure 5.2,  $R_{w/q}$  equals to 0.3 while  $R_{sw/q}$  equals to 0.6. Furthermore, it is expected that the ratio of methane hydrate/quartz is close to that of water/quartz. These scan conditions, based on the use of KI solution, would be then appropriate for MHBS scans, with an optimal contrast between air, MH, saline water and quartz (relative gray levels [0, 0.3, 0.6, 1]).

Different from XRCT, SXRCT so called “pink beam” uses a narrower energy spectrum (more concentrated around a mean energy). Preliminary SXRCT scans (shown in Figure 5.3) were performed at the Psiche at the French synchrotron SOLEIL (mean energy: 44 keV).  $R_{w/q}$  and  $R_{sw/q}$  are 0.25 and 0.6 respectively. These values are close to their theoretical ratios at 44 keV (see Figure 5.1). Note that the Paganin filter (Paganin et al., 2002), designed to account for and partly correct phase contrast artifacts, has been used during the image reconstruction.

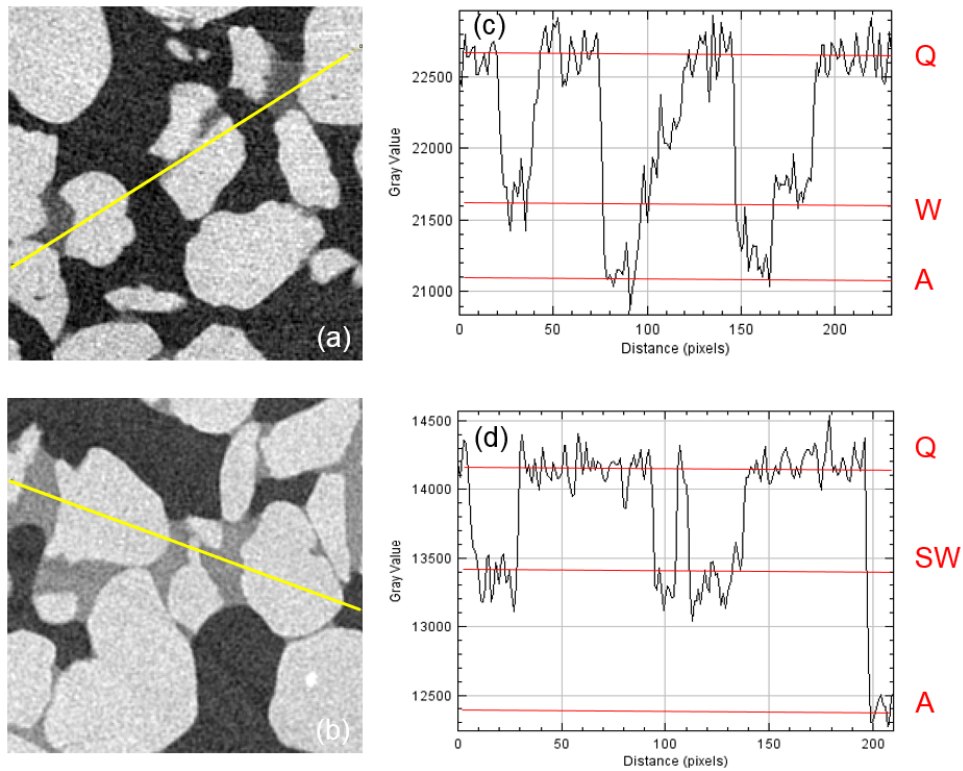


Figure 5.2: XRCT images of unsaturated sand with (a) pure water; and (b) saline water. Gray value profiles to determine ratios of water/quartz (c); and saline water/quartz (d).

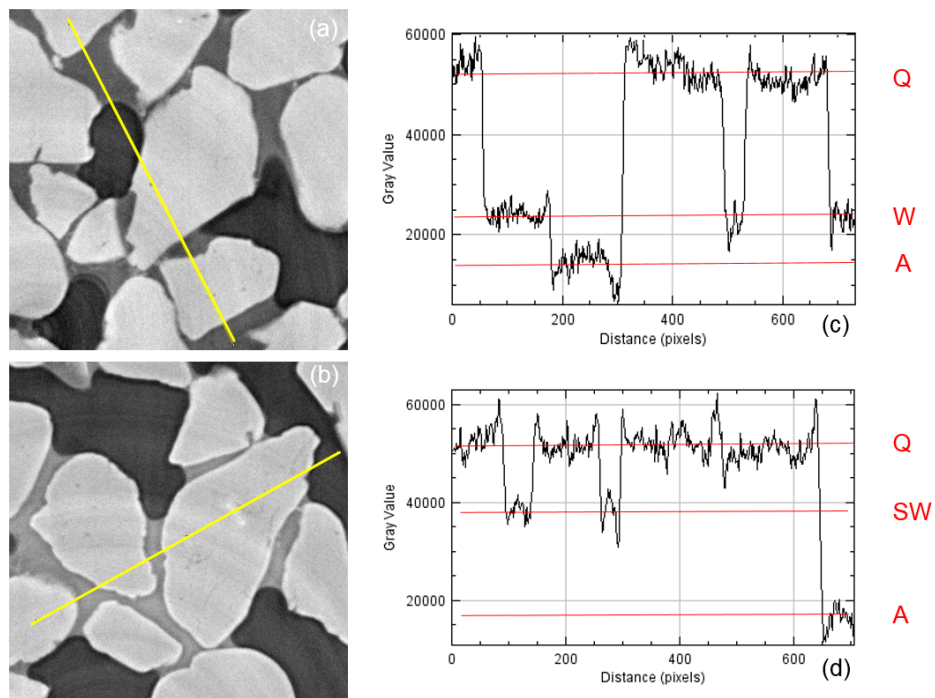


Figure 5.3: SXRCT images of unsaturated sand with (a) pure water; and (b) saline water. Gray value profiles to determine ratios of water/quartz (c); and saline water/quartz (d).

## 5.2.3 Experimental setup investigations

### 5.2.3.1 Materials and methodology

Moist Fontainebleau sand (with either tap water or saline solution of 3.5 wt% of KI) was first compacted into an aluminum tube (exterior diameter,  $d_{ext.} = 6.45$  mm; thickness,  $t = 0.89$  mm). Both high pressure and low temperature (7 MPa; 2-3 °C) need to be maintained for the MH formation.

To maintain low temperature, cooled air was circulated around the aluminum tube. Compressed air was cooled by a combination of chilled water (controlled by a cryostat) and an air/water heat exchanger. Cooled air temperature as well as sample temperature, both measured with thermocouples, were controlled via the compressed air flow rate. Note that air was chosen instead of other fluids for the temperature control to avoid additional X-ray absorption. In addition, preliminary experiment with wet sand showed an identical temperature in the air outside of the aluminum tube and at the center of the aluminum tube (wet sand) at the same height.

Methane gas was injected into the sample to maintain high methane gas pressure. It is supposed that methane gas pressure is constant in a closed system once the MH formation is finished (no need of any further methane gas for further MH formation). Therefore, at the end of MH formation where the medium is supposed to be stable, there is no need of methane gas pressure control for XRCT scans. However, to continuously follow MH formation over time by SXRCT scans, methane gas pressure should be maintained during the whole process.

The above conditions were maintained during the scans (about 12 hours for each XRCT scan) to avoid MH dissociation. Schematic view of the experimental setups is shown in Figure 5.4. The sample was fixed on a turntable for scans. An Ultratom scanner from RX Solutions, combining either a Hamamatsu L10801 Micro-focus reflection (230 keV) or a Hamamatsu L10712 Nano-focus (160 keV) X-ray sources and a Paxscan Varian 2520V flat-panel imager (1920x1560 pix<sup>2</sup>, pixel size: 127  $\mu$ m), was used for the XRCT scans. At an optimized Source Detector Distance (*SDD*), governed by the divergence of the X-Ray cone-beam, the smaller Source Object Distance (*SOD*) is, the higher the spatial resolution (smaller voxel size) is.

Furthermore, SXRCT scans were performed at the Psiche beamline at the French synchrotron SOLEIL (mean energy: 44 keV). The voxel size was 0.9  $\mu$ m and the scan time was 12-15 minutes. Paganin filter was optimized to limit phase contrast so that gray value of each phase in SXRCT images remains homogeneous.

Three experimental setups have been developed. The details of each one and the obtained results are presented in the following parts.

### 5.2.3.2 Experimental setup No. 1

Figure 5.5 shows the first setup for XRCT scans of MHBS. A Poly-methyl-methacrylate tube (PMMA tube; exterior diameter,  $d_{ext.} = 24$  mm; thickness,  $t = 3.5$  mm) was fixed

around the aluminum tube for cooled-air circulation from its bottom to its top. A manometer was fixed at the top of the aluminum tube to monitor methane gas pressure in the tube. The aluminum tube height was chosen to avoid collision between the manometer and the X-ray source during the scan (430 mm from the turntable to the top of the aluminum tube, see Figure 5.5). Note that the aluminum tube height could have been reduced and both available XRCT sources can be used. A thermocouple was installed between the aluminum tube and the PMMA one at the middle of its height. Methane gas at 7 MPa was injected during the MH formation by using a pressure controller, which was connected to a gas flowmeter. These conditions were maintained during 2 days for the MH formation. At the end of the MH formation, pressure controller and gas flowmeter were removed, and all the valves were closed prior to the transportation of the whole system to the X-ray tomography room.

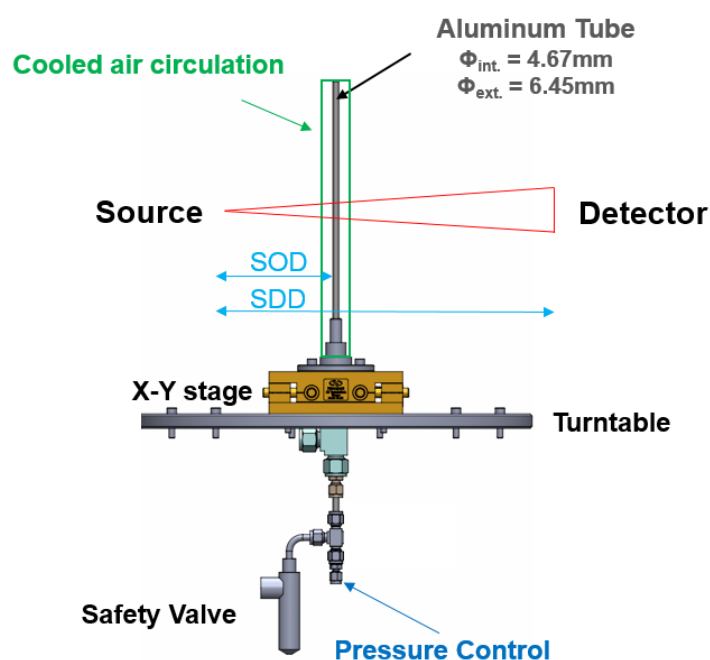


Figure 5.4: Experimental setup principles for XRCT scans of MHBS. SOD: Source Object Distance; SDD: Source Detector Distance.

A cooling gel was wrapped around the PMMA tube during the cell transportation (few minutes while cooled air was cut off) to avoid MH dissociation. Cooled-air circulation around the aluminum tube was reset as quickly as possible once the cell was installed inside the X-ray tomography room. Sample pressure and temperature were verified before the scan. The Source Object Distance was limited by the exterior diameter of the PMMA tube ( $SOD \geq 20\text{ mm}$  to maintain 8 mm of security gap). Dry compressed-air flow was shifted towards the PMMA tube to avoid water condensation during scans (anti-condensation system). Note that to maintain sample temperature during the scan (both aluminum and PMMA tube rotated together), the soft tube bringing cooled air from the heat exchanger to the PMMA tube needed to be long enough to rotate with.

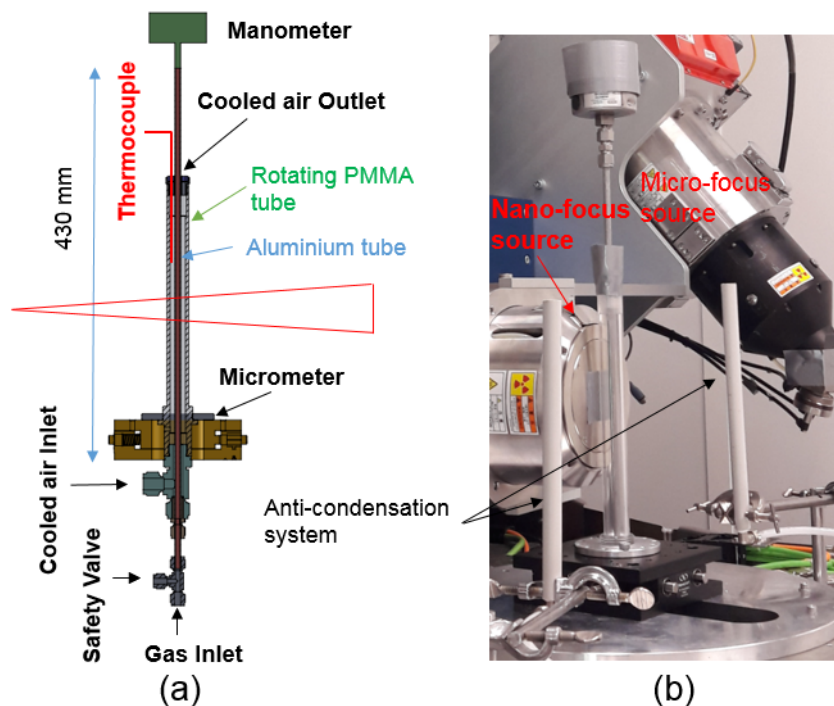


Figure 5.5: Experimental setup No. 1: (a) Schematic view; (b) picture.

Several tests have been run but only a few provided images with good quality (about 40 %). Actually, the cell vibrated slightly during the scan because of the cooled-air flow. That caused blurred images with edges that were not clear-cut (an example is shown in Figure 5.6). Gray value of each phase (e.g. grain) was not homogeneous. MH morphology observation was then impossible.

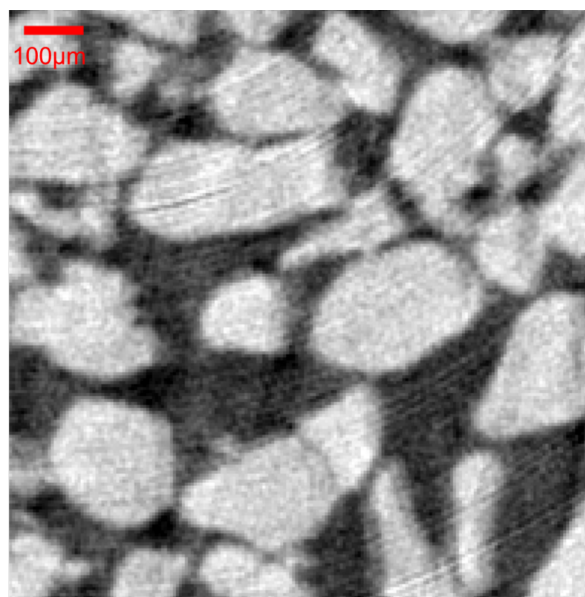


Figure 5.6: Example of image of an unsuccessful scan due to the cell vibration, obtained by the experimental setup No. 1.

An example of more successful scan is shown in Figure 5.7 (voxel size was  $5 \mu\text{m}$ ). The image shows an assembly of sand grains (light gray), the pore space filled with methane gas (black) and methane hydrates (gray). MHs can be observed at grain contacts and also on grain surfaces.

The mean gray values for each phase were determined from the gray value profiles (Figure 5.8):  $G_a = 22500$ ;  $G_q = 33000$  and  $G_{mh} = 26500$  (for methane hydrate).  $R_{mh/q}$  equals to 0.38, similar to the expected ratio. Furthermore, standard deviations of gray levels in the quartz and methane gas phase are close (700). The signal noise ratio (SNR) equals to  $(33000 - 22500)/700 = 1/0.067$ .

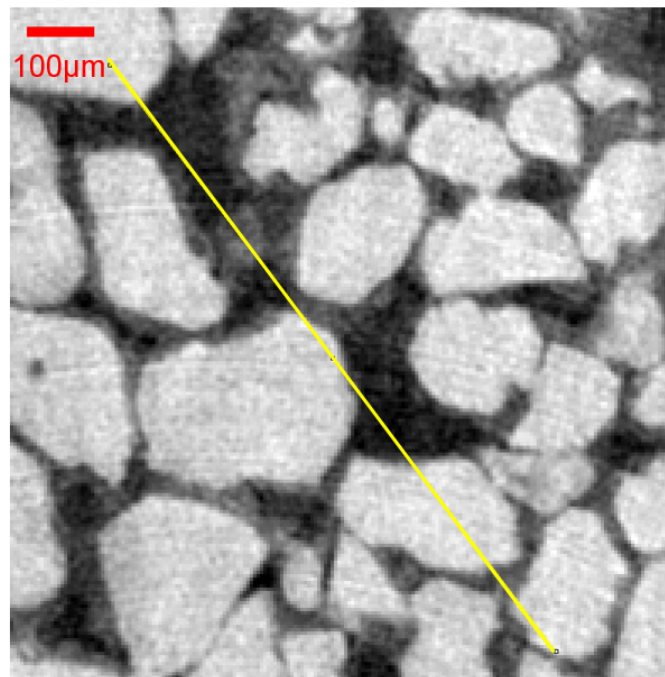


Figure 5.7: Example of image of MHBS obtained by the setup No. 1.

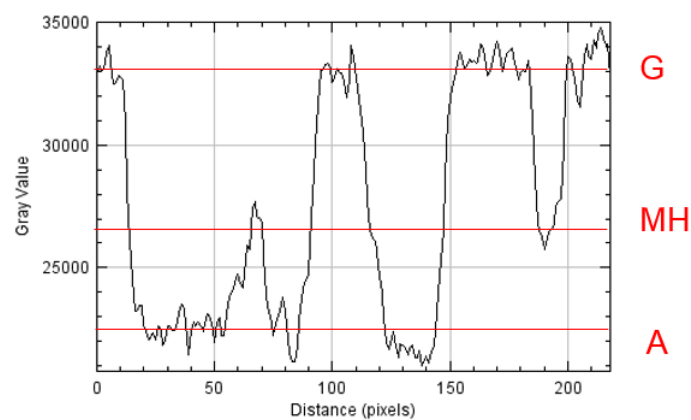


Figure 5.8: Gray value profiles to determine the ratio of MH/quartz of MHBS in Figure 5.7.

### 5.2.3.3 Experimental setup No. 2

In order to improve the image spatial resolution, the setup No. 2 (shown in Figure 5.9) has been developed for scans with the Nano-focus source. First, to reduce the *SOD*, the PMMA tube was removed. The Nano-focus source was placed close to the aluminum cell during the scans (with a *SOD* equals to 8 mm). A Polyvinyl Chloride (PVC) support was fixed to the source and enveloped the aluminum tube. Temperature control was ensured by a circulation of cooled air inside the PVC support (again from bottom to top). A thin Kapton film was used to thermally isolate the source and in particular its brittle Beryllium window and protect it from the cooled air. Within this system, the aluminum tube was rotated during the scans while the PVC support was fixed. Compared to the setup No. 1, a smaller air flow rate was needed to maintain similar sample temperature thanks to lower heat loss between the heat exchange and the cooled-air inlet (shorter soft tube length). Secondly, the manometer was fixed at the bottom of the cell. Thus, the aluminum tube height was reduced to 320 mm, constrained by the Nano-focus source size. These modifications allowed reducing the vibration of the aluminum tube during scans.

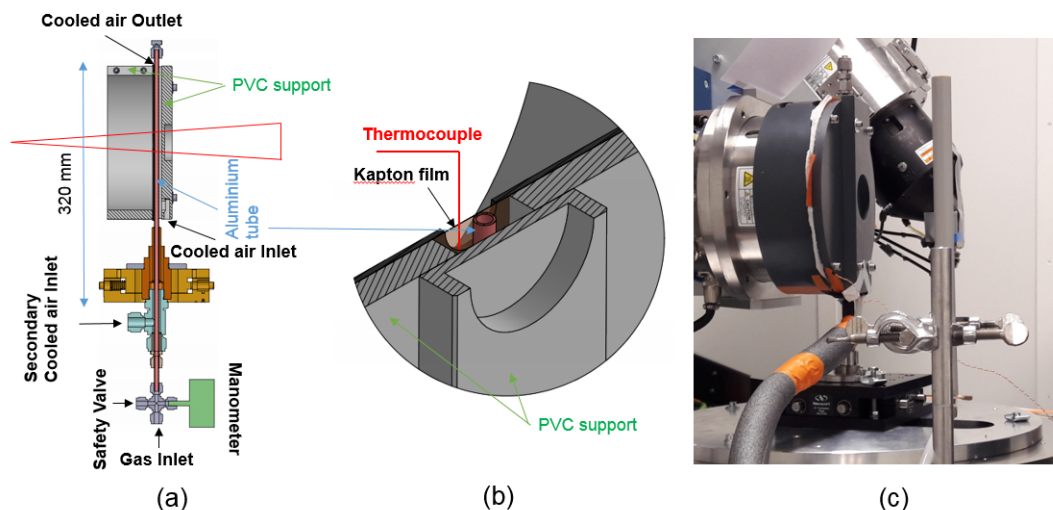


Figure 5.9: Experimental setup No. 2: (a), (b) Schematic view; (c) picture.

Methane hydrates were equally formed in sandy sediments in the laboratory then transported to the tomography room for scans. The PMMA tube (used for the setup No. 1) was placed around the aluminum tube to initially form MHs. Compared to the first case, the installation of the cell in the tomography room was more complicated as cooled air can only be circulated when the aluminum tube was enveloped by the PVC support. Sample temperature was maintained by a cooling gel wrapped directly around the aluminum tube during its installation. A thermocouple, fixed on the PVC support (see Figure 5.9), was used to measure sample temperature at the scanned zone.

Similarly to the first setup, among scans run with the second setup, only few have given images with good quality (about 40 %), again because of cell vibrations. An example of successful results is shown in Figure 5.10 (voxel size:  $3.5 \mu\text{m}$ ). MHs were distinguished more difficultly from methane gas even with a better image spatial resolution compared

to the first case.  $R_{mh/q}$  and  $SNR$  are one third and  $1/0.085$  respectively (Figure 5.11).

The reason why the gray values of each phase were not homogeneous was supposed due to the heterogeneous porous structure of PVC. X-rays passed through a thin PVC layer serving for thermal insulation before being captured by the detector. That caused problems for XRCT scan calibration (projection images without the sample and without X-rays) when the thin PVC layer was not at the same position for the scan and the calibration.

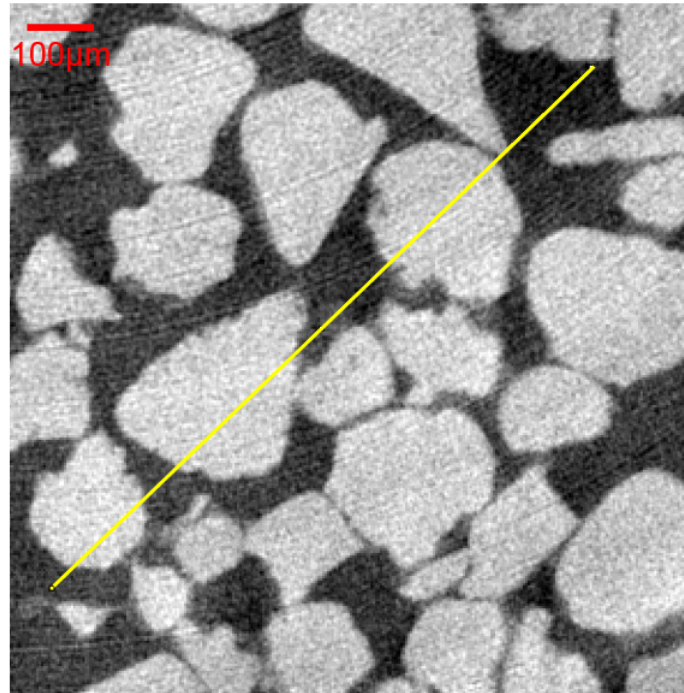


Figure 5.10: Example of image of MHBS obtained by the setup No. 2.

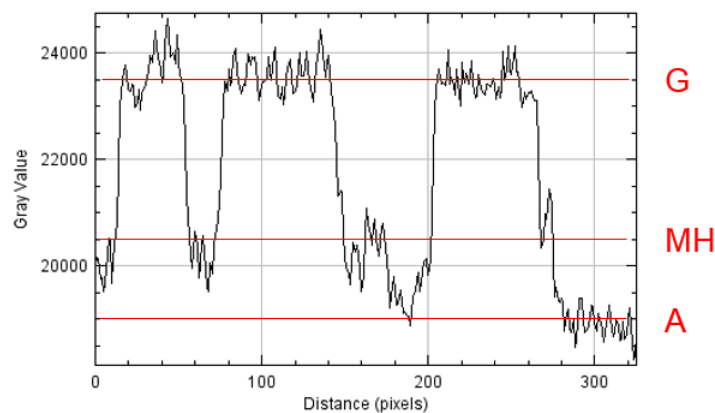


Figure 5.11: Gray value profiles to determine the ratio of MH/quartz of MHBS in Figure 5.10.



### 5.2.3.4 Experimental setup No. 3

Within the two first setups, methane hydrates were first formed outside the tomography room and XRCT scans were performed only when the MH formation was stabilized. During the scans, the cell was closed (at a constant pressure) and the temperature was maintained. The setup No. 3 was developed principally for SXRCT scans where MH formation can be followed continuously. For this reason, methane gas should be supplied during the scans.

Figure 5.12 shows the schematic view and a picture of the setup No. 3. A small methane gas bottle (volume of 40 ml) was connected to the methane gas inlet of the cell via a pressure reducer (which reduces the methane gas pressure from 13 MPa inside the bottle to 7 MPa at the gas inlet). This system was used to maintain methane gas pressure in the sample constant at 7 MPa ( $\pm 0.1$  MPa) during the MH formation and scans.

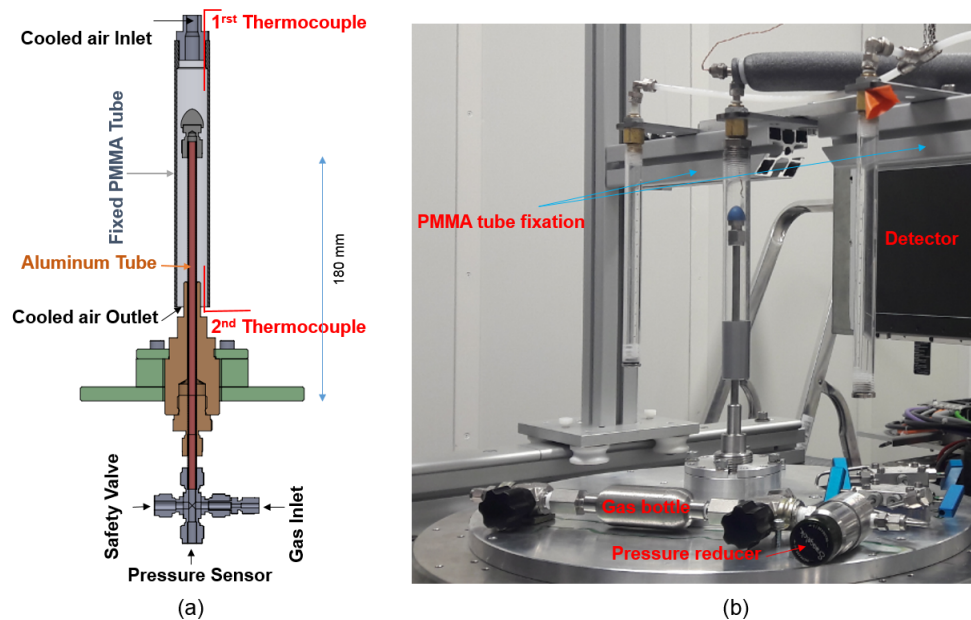


Figure 5.12: Experimental setup No. 3: (a) Schematic view; (b) picture.

Cooled air was circulated between the rotating aluminum and a fixed PMMA tube (slightly smaller than that used in the setup No. 1: exterior diameter,  $d_{ext.} = 23$  mm; thickness,  $t = 2$  mm) for the temperature control. The cooled-air inlet was now at the top of the PMMA tube. The PMMA tube was fixed at its top. In addition, the aluminum tube height was reduced to 180 mm. Two thermocouples, inserted into the PMMA tube to measure the air temperatures close to the air inlet and outlet, showed a temperature difference of 1.5 – 2.0 °C during the scans.

For the SXRCT scans, wet sand (with either tap water or saline water) was compacted in the aluminum tube to reach an average porosity of 0.40. After the installation of the system on the beamline, vacuum pump was applied in order to remove residual air prior to the application of methane gas at 7 MPa of pressure to the sample. Afterward, cooled

air was circulated to reduce the temperature inside the PMMA tube to form methane hydrates. Several scans were performed during the tests.

Figure 5.13 shows a preliminary result obtained by XRCT (the micro-focus source, voxel size:  $4 \mu\text{m}$ ). This image was recorded over 15 hours of scan performed after 28 hours of MH formation. MH morphologies (crystals/layers) were clearly observed over grain surfaces. Furthermore,  $R_{mh/q}$  and  $SNR$  are 0.3 and 1/0.095 respectively (Figure 5.14). It can be seen that the  $R_{mh/q}$  and  $SNR$  are in the same order for the three experimental setups when used in the laboratory XRCT. The difference was that successful scan ratios were lower for the two first cases due to cell vibration while this problem was well resolved by using the third one.

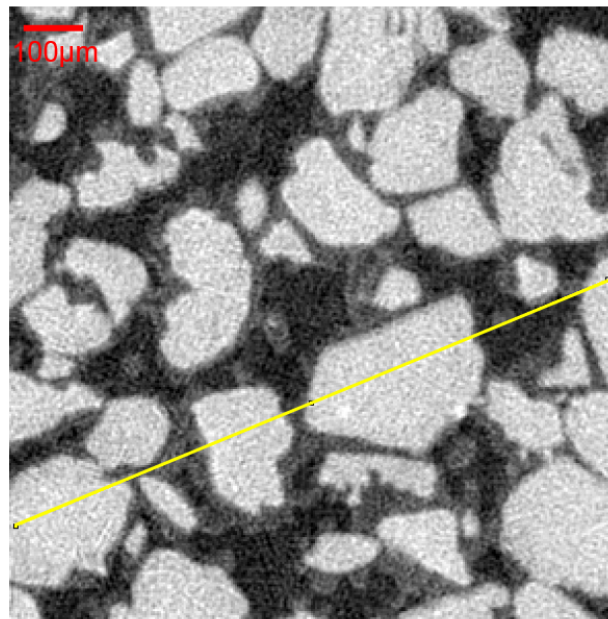


Figure 5.13: Example of XRCT image of MHBS obtained by the setup No. 3.

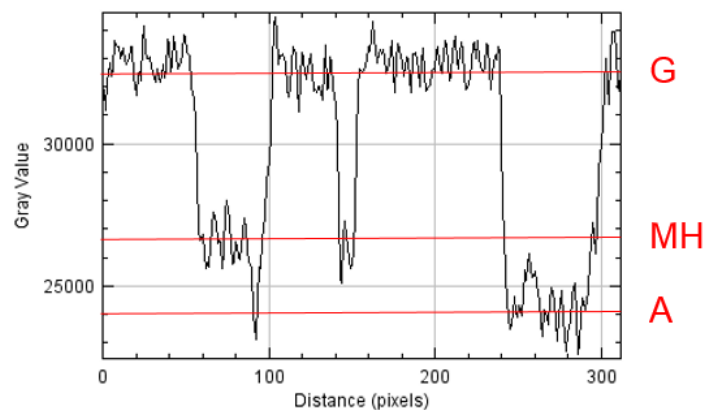


Figure 5.14: Gray value profiles to determine the ratio of MH/quartz of MHBS in Figure 5.13.

The experimental setup No. 3 was equally used to perform SXRCT scans (at the Psiche beamline at the Synchrotron Soleil). An example of MHBS scanned by SXRCT is shown in Figure 5.15 (voxel size was  $0.9 \mu\text{m}$ ). Even really small hydrates (in form of spikes) were clearly distinguished from saline water (KI, 3.5 wt%).  $R_{mh/q}$ ,  $R_{sw/q}$  and  $SNR$  are 0.27, 0.73 and 1/0.080, respectively (Figure 5.16). The ratios ( $R_{mh/q}$ ,  $R_{sw/q}$ ) calculated on the image are close to the theoretical ones. A small increase of salt concentration in the remaining saline water during the MH formation caused a slightly higher  $R_{sw/q}$  value.

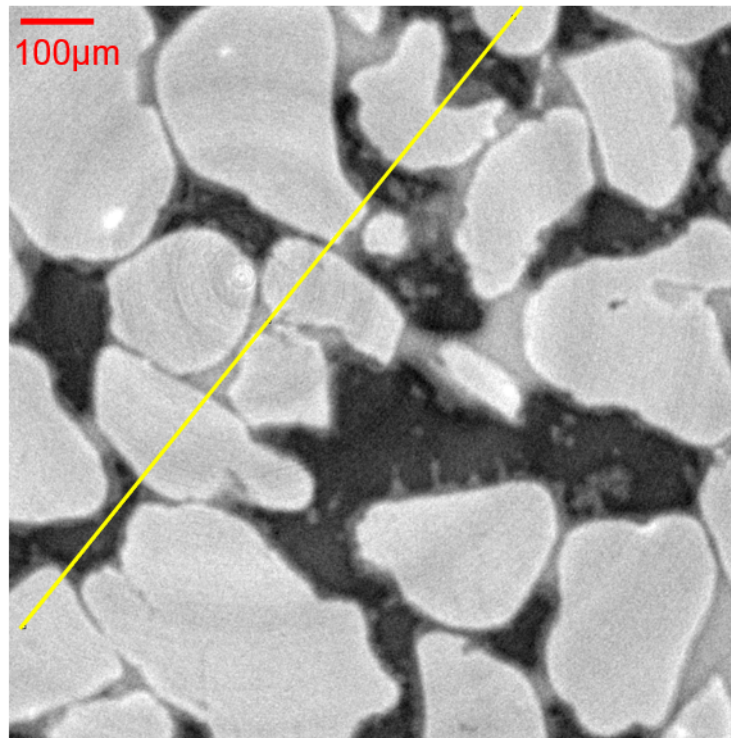


Figure 5.15: Example of SXRCT image of MHBS obtained by the setup No. 3.

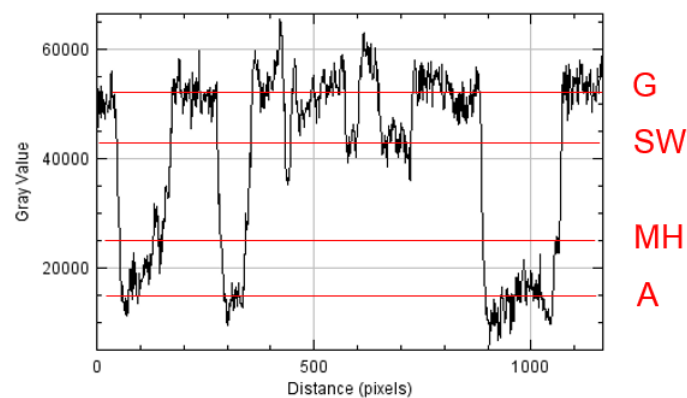


Figure 5.16: Gray value profiles to determine the ratio of MH/quartz of MHBS in Figure 5.15.

## 5.2.4 Discussions and recommendations

These above results show three experimental setups developed for pore-scale morphology and pore-habit investigations of MHs in sandy sediments via XRCT and SXRCT. The image spatial resolution was well improved by using SXRCT instead of XRCT. However, SXRCT scans are costly and its access is limited.

In some previous studies where gas hydrate morphology in sediments were investigated, THF or Xenon was used to facilitate the gas hydrate formation because only temperature control (Kerkar et al., 2009; Chaouachi et al., 2015) or pressure control (Chen and Espinoza, 2018) was required. In the present work, as methane hydrates were investigated, both low temperature and high pressure were required. Furthermore, in order to maintain low temperature, cooled water was usually used (Chaouachi et al., 2015; Ta et al., 2015; Zhao et al., 2015b; Le et al., 2018b; Le et al., 2019). That would avoid the system vibration induced by air flow, as observed in the present work. However, X-ray absorption of water would decrease the image quality significantly. Besides, Lei et al., 2019b used a Peltier plate for temperature control. Yet, a temperature gradient of 4 °C was measured between the top and bottom of the sample (about 54 mm height), i.e. 0.08 °C/mm. By using cooled air in this study, the temperature gradient over 150 mm of the tube height was about 2 °C, i.e. 0.013 °C/mm.

In several previous studies, investigating the morphology of MHs in sediments (sand or glass beads), voxel size in XRCT images was quite high, in a range of 20-30  $\mu\text{m}$  due to complex experimental setups (needing both temperature and pressure controls) (Ta et al., 2015; Yang et al., 2015; Zhao et al., 2015b). Within such resolution, small particles of MHs could not be observed. Furthermore, the partial volume effect was important. In the present work, a voxel size of 4  $\mu\text{m}$  was obtained by using the setup No. 3 in the laboratory with a very good image's quality. MH morphologies (crystals, layers) were thus clearly observed.

Among the three experimental setups developed in the present study, the third one was the most optimized. Actually, the aluminum tube height was shortened to minimize the cell vibration induced by the air flow. The setup No. 2 has the best spatial resolution for XRCT scans (voxel size equals to 3.5  $\mu\text{m}$ ) but its experimental procedure is the most delicate and induces artifacts. Besides, the setup No. 2 is compatible only with the Nano-focus source while the two others can be used for all types of X-ray source.

Concerning the pressure control system, the sample can be disturbed during the system transportation to the tomography room in the case of the two firsts setups. However, it avoids occupying the tomography room during a long period. The setup No. 3 (using a small methane gas bottle) is the best choice for SXRCT scans.

## 5.2.5 Conclusions

This first part describes the scan condition optimizations and the developments of special experimental setups to investigate pore-scale morphologies and pore habits of MHBS via XRCT, and SXRCT.

Based on theoretical attenuation coefficient ratio between phases, XRCT scan conditions were chosen (scan energy, filter thickness and saline water solution). Preliminary XRCT and SXRCT scans performed on compacted sand wetted with pure water or saline water confirmed the theoretical estimations.

Afterward, three experimental setups were developed with the objective of improving the image spatial resolution for pore-scale morphology and pore-habit investigations of MHs in sandy sediments via XRCT and SXRCT. The details of temperature and methane gas pressure controls were presented. The results obtained for each experimental setup allowed evaluating its performance to observe morphologies and pore habits of MHBS. The experimental setup No. 3 turns out to be the most appropriate. Sample temperature was controlled by circulating cooled air between the aluminum and the PMMA tube which was fixed at its top. Attention was paid to minimize the cell vibration induced by the cooled air flux.

The choices of temperature and pressure controls presented can be useful to further studies (using XRCT/SRXCT) on MHBS as well as other geomaterials involving control of temperature and/or pressure during XRCT/SXRCT scans.

## 5.3 Part II: Methodology for accurate determination of volume fractions from XRCT images

### 5.3.1 Introduction

X-ray computed tomography has been widely used to investigate the pore geometry, water flow, water distribution at the microscopic scale in porous media as well as the water retention curve thanks to its high spatial resolution (Gao et al., 2017; Georgiadis et al., 2013; Wildenschild and Sheppard, 2013; Khaddour et al., 2018). However, in spite of recent technological developments, tomography artifacts (e.g. beam hardening, ring artifact) and more inherently image noise and the partial volume effect so-called “PVE” due to limited CT image spatial resolution are still major issues of this technique, that are to be carefully taken into account for its proper applications (Cnudde and Boone, 2013; Kaestner et al., 2008). The PVE is the averaging of attenuation coefficients of different materials with features whose characteristic length is below voxel length scale: a discrete voxel gray level may be encoding an edge between materials with very different attenuation properties (Roose et al., 2016). Quantitative determination of volume fractions, which is often based on voxel counts of three segmented phases in XRCT images of three-phase partially saturated porous media, would strongly depend on the choice of gray level thresholds used for segmentation.

Many classical image processing enhancement methods (e.g. median filter, anisotropic diffusion filter, edge enhancement. . .) and classification methods (e.g. histogram bias correction, global thresholding, local thresholding...) have been developed and well reviewed (Kaestner et al., 2008; Iassonov et al., 2009; Schlüter et al., 2014). Choosing a segmentation method – the most crucial step affecting all subsequent quantitative analysis based on

voxel counts and eventually simulation results, is not straight-forward, whereas choosing an image processing enhancement method, which is appropriate for case-by-case images, is more evident (Kaestner et al., 2008). Segmentation, with thresholds chosen based on the shape of global grayscale or linear attenuation coefficients, may introduce operator bias especially when phase contrast is low, but also when material geometric features are smaller than voxel size because of the PVE (Kulkarni et al., 2012). Specific image segmentation techniques have been adapted for granular media: mainly for two-phase media (Clausnitzer and Hopmans, 1999; Lindquist et al., 1996; Fonseca et al., 2009; Schlüter et al., 2010; Müter et al., 2012) and some for three-phase media (Kulkarni et al., 2012; Houston et al., 2013). Recently, Hashemi et al., 2014 proposed a segmentation method based on simultaneous region-growing method. A seeding of each of three phases was needed (an initial seeding from partial-thresholding plus a PVE removal for the seeding of the middle phase) and three phases were finally attributed to the media image. In spite of various improvements in segmentation methods, a voxel in a three-phase-media image, even if it corresponds to an interface between two phases of a XRCT image, would be finally segmented/attributed to one phase for the volume fraction calculation which would then be influenced by the PVE.

We propose here an alternative method to quantify more accurately the volume fractions of three-phase porous media (e.g. unsaturated sand, to calculate the porosity and water saturation) from XRCT images, considering the image noise and the PVE. The image is considered composed of voxels of three pure phases (solid-only, air-only and water-only) and that of three interface phases (air/solid, air/water, and water/solid). The number of voxels containing three-phase interfaces is usually limited and is considered to be negligible in the present work and checked to be so in specific application of the proposed method. Each voxel in the image is first attributed to one of these six families. Afterward, the volume fraction of each phase in two-phase voxels is quantified based on a linear interpolation of mean gray levels of the two corresponding pure phases. This reflects the physical formation of the gray levels on an ideal XRCT image. The total volume fraction of each phase is the addition of the volume fraction of this phase in its one-phase voxels and that of its two-phase voxels associated with the interfaces with the two other phases.

Details of the method are first presented. Afterward, the results obtained on two samples, one with unsaturated glass beads and one with an unsaturated sand, for which the volume fractions were known from global physical measurements, are shown to validate the method. Finally, the method has been applied to evaluate methane hydrate saturation of MHBS under excess-gas conditions.

### 5.3.2 Method

Note that if a three-phase media image was free of any noise and artifacts and the image spatial resolution was high enough so that the number of voxels close to the interface of two phases would be negligible with respect to the total number of the sample voxels, the gray value of almost all voxels (proportion to linear attenuation coefficient) would be one of three values ( $\mu_{P1}, \mu_{P2}, \mu_{P3}$ ) corresponding to a unique gray value of each of three phases (Phase 1 – P1, Phase 2 – P2, Phase 3 – P3; ordered corresponding to an increase in absorption). However, due to the image noise caused by the random nature of both photon

emission and attenuation and the high number of photons used to obtain gray levels, the histogram of a pure phase in a real image is Gaussian (Clausnitzer and Hopmans, 1999) with a mean gray value ( $\mu$ ) and a standard variation ( $\sigma$ ). Furthermore, due to the limited image spatial resolution, inducing the PVE, some intermediate values occur for voxels located near the interface between phases. More precisely, P1/P2 interface voxels have gray value in a range of  $[\mu_{P1}, \mu_{P2}]$ , P2/P3 interface voxels have gray value in a range of  $[\mu_{P2}, \mu_{P3}]$ , while P1/P3 interface voxels have gray value in a range of  $[\mu_{P1}, \mu_{P3}]$ . In addition, these voxels are also influenced by image noise.

On the basis of these aforementioned assumptions, a new method has been proposed in this study. Based on the morphology of porous media, two-phase interfaces are determined by intersecting the dilated surfaces of two corresponding pure phases which are first found based on strict segmentations and some morphological operations. Finally, three pure-phase voxels and three two-phase voxels are attributed to a three-phase media image. Three-phase interface voxels are ignored.

The spatial domain of interest here contains three miscible phases (Phase 1 – Air, Phase 2 – Water, Phase 3 – Solid). Each previous phase is represented in a XRCT image by a pure phase part and another part being interfaces with two other phases. Two pure zones (air-only and solid-only zones) are first identified by strict segmentations (partial-thresholdings) together with some morphological operations. The interfaces of these two zones (air/solid interfaces) are then found by intersecting the dilated surfaces of these two pure zones. The two other interface zones (air/water, water/solid interfaces) are preliminarily determined (by intersecting the remaining domain with the corresponding dilated domain of the two found pure phases) in order to get the last pure zone (water-only) based on the histogram of the remaining part via partial-thresholding. Finally, the two interface zones (air/water, water/solid interfaces) and the water-only zone are adjusted by adding appropriate voxels of the remaining part (which has not been assigned). Besides, some additional corrections for pure phases, based on regional voxels, can be used in the objective of considering the remaining image noise and/or especially some beam hardening effects. Note that the histogram of such a selected pure phase is supposed to be Gaussian and is checked to be so.

Once all voxels in the image are classified, the volume fractions of two corresponding phases in the interface phases are calculated based on a linear interpolation of mean gray levels of these two corresponding pure phases (Hsieh et al., 1998). The total volume fraction of any phase in a three-phase media image is its volume fraction in the pure phase voxels plus that in the two corresponding interface voxels.

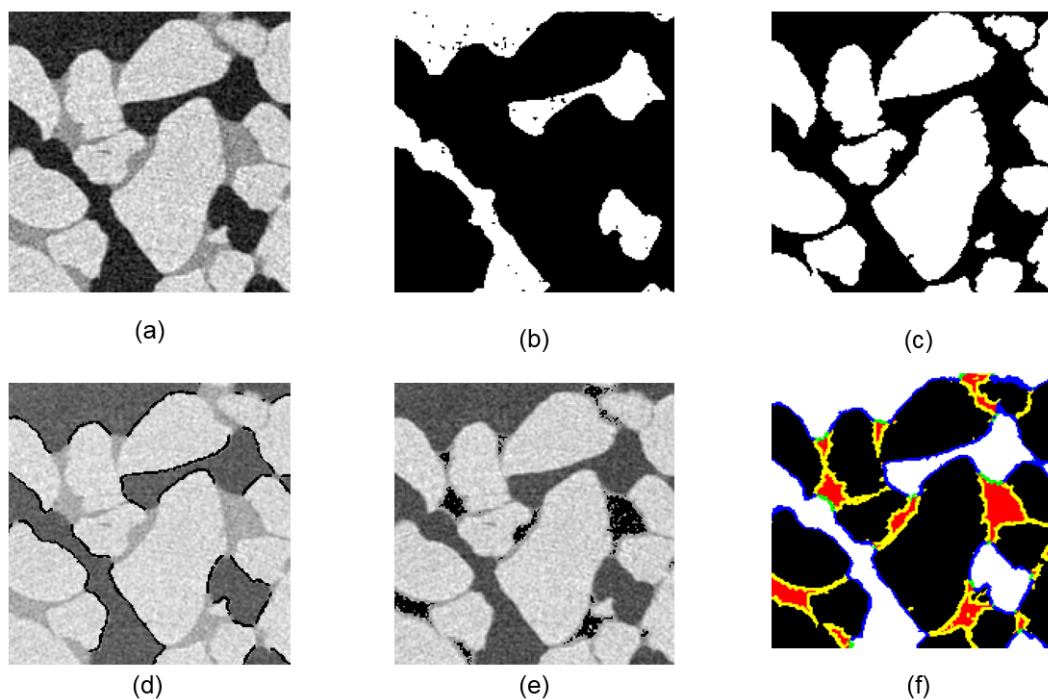
### 5.3.2.1 Phase attribution procedure

Figure 5.17a shows an example of a XRCT image obtained from an unsaturated sand sample (voxel size:  $4 \mu\text{m}$ ) containing air, Fontainebleau sand and water doped at 3.5 wt% of KI which was used to improve the image contrast compared to an image with pure water. Its histogram is shown in Figure 5.18.

In order to assign each voxel of the image to one of the six families (air-only, water-only,

solid-only, air/water, water/solid, and air/solid), the following steps were used:

- Step 1: Two zones strictly corresponding to solid and air pure phases were first identified from the image histogram. The image was first filtered with a standard median filter, which affects moderately the contours. Two thresholds which correspond to two gray values having a count value equal to 30 % of the peak value (see Figure 5.18) were used. This allows determining voxels containing air-only and voxels containing solid-only from the filtered image. Morphological operations (an erosion followed by a dilation operation of only one pixel) can be used to eliminate dispersed voxels (Note that these operations are optional). As each grain (solid phase) is continuous and simply convex, small holes (if exist) inside each grain were filled with a hole filling algorithm. Air-only and solid-only zones are shown in white voxels in Figure 5.17b and Figure 5.17c respectively. Note that 2D or 3D calculations can be used but 3D calculations were used here. For the following steps, *the original image* (i.e. image before median filtering, 180 x 180 x 180 voxels) with the center image shown in Figure 5.17a was used.



*Figure 5.17: Classification of voxels: (a) XRCT image of unsaturated sand; (b) Voxels containing air-only shown in white; (c) Voxels containing solid-only shown in white; (d) Voxels containing air/solid are shown in black; (e) Voxel containing water-only shown in black; (f) Final results: air-only (white), solid-only (black), water-only (red), air/solid (blue), water/solid (yellow), air/water (green). Image dimensions: 0.720 mm x 0.720 mm. Voxel size: 4  $\mu$ m.*

- Step 2: Voxels corresponding to air/solid interfaces were determined by dilating the identified air and solid pure zones by  $n$  voxels and finding their intersections (voxels belonging already to air-only/grain-only were withdrawn). Note that due



to the image blur, the spatial range of intermediate voxels (i.e. the PVE) usually extends over several voxels in the direction normal to the interface (Clausnitzer and Hopmans, 1999). Therefore, the number of voxels used for the dilation ( $n$ ) depends on the sharpness of the individual projections, i.e., geometric factors such as the size of X-ray source and detector. If the air-only and grain-only zones are well determined, this value can be detected directly from the original image without the voxels corresponding to these two pure phases. These interface voxels are shown in black in Figure 5.17d.

- Step 3: Pre-determine voxels corresponding to water-only zone, air/water interfaces and water/solid interfaces by using morphological operations and partial-thresholding. The predetermined air/water interfaces were the intersections of the remaining part after the second step and the air-only zone dilated by  $n$  voxels. Similarly, the predetermined water/grain interfaces were the intersections of the remaining voxels after the second step and the grain-only zone dilated by  $n$  voxels. Similarly to Step 1, the water-only zone was determined from the histogram of the actual remaining part (i.e. the remaining voxels after the second step, from which the predetermined air/water and water/grain interface voxels were removed), shown in Figure 5.19.

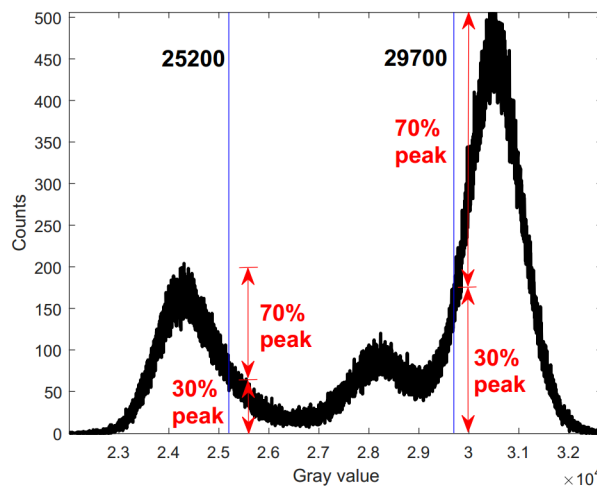


Figure 5.18: Histogram of the example image shown in Figure 5.17a (median filter, radius of 2 pixels) containing respectively air, saline water (KI 3.5 wt%) and grains corresponding to gray value increase.

- Step 4: Determine voxels corresponding to the water-only zone, air/water interfaces and water/solid interfaces based on morphological operations (the Step 3) and on grayscale of the remaining voxels, not assigned after the Step 3. Mean gray value and standard deviation of the predetermined water-only zone were calculated and denoted  $\mu_{pre}$ ,  $\sigma_{pre}$  respectively. The final water-only zone was found by combining voxels in the remaining voxels having gray level in the range of  $[\mu_{pre} - \sigma_{pre}, \mu_{pre} + \sigma_{pre}]$  with the predetermined water-only voxels. These voxels are shown in black in Figure 5.17e. The final air/water interface zone was found by combining voxels in the remaining part having gray level smaller than  $\mu_{pre} - \sigma_{pre}$  with the predetermined

air/water interface zone. On the contrary, the final water/grain interface zone was voxels in the remaining part having gray level greater than  $\mu_{pre} + \sigma_{pre}$  plus the predetermined water/grain interface zone.

Three pure phases (air-only, solid-only, and water-only) and three interface phases (air/solid, air/water, and water/solid) were assigned to the original image after all these above steps. The final results are shown in Figure 5.17f where all voxels have been attributed to the corresponding phases.

For real unsaturated granular media image, some additional corrections based on regional voxels could be performed in the objective of taking into account the noise of pure phases and/or especially a limited beam hardening effect:

- In Step 1, watershed transform can be applied to eliminate voxels representing contacts between grains in the attributed grain-only phase;
- Some air-only voxels influenced by the remaining image noise and/or the beam hardening effect could be attributed to air/water interfaces (some dispersed black voxels being in the white voxel zones in Figure 5.17b). To correct this, voxels in the air/water interface zone (which did not have any voxels within a radius of  $n$  voxels being the water-only phase or grain/water interfaces) were re-attributed to the air-only phase. This correction is similar to the filling small holes inside the air-only phase (see Figure 5.17b and white voxels in Figure 5.17f);
- Similarly to the air-only phase, for the water-only phase, additional corrections could be performed. Voxels in the air/water interface zone which did not have any voxels within a radius of  $n$  voxels being in the air-only phase were re-attributed to the water-only phase. For the water/grain interface zone, some voxels were re-attributed to the water-only phase if they were within a radius of 2 voxels of the water-only phase but not within the radius of  $(n + 1)$  voxels of the grain-only phase (see Figure 5.17e and red voxels in Figure 5.17f).

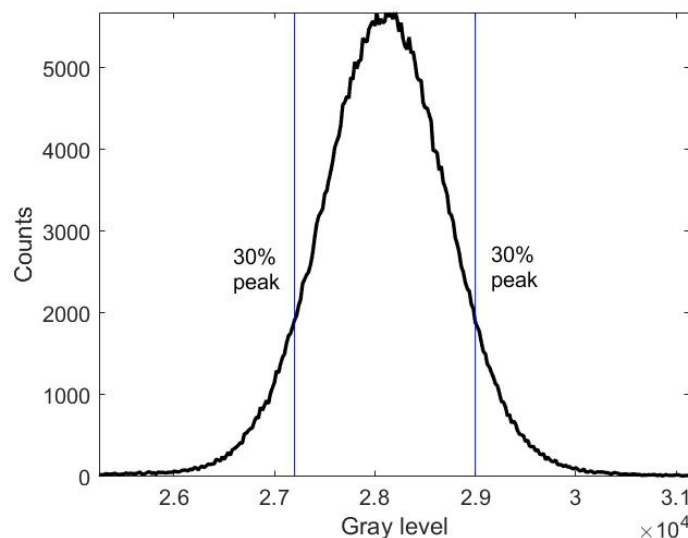


Figure 5.19: Histogram of the remaining voxels to pre-determine the water-only voxels.

Figure 5.20 shows the histograms and the corresponding Gaussian fits of air-only and solid-only zones on *the original image*. As both histograms were Gaussian, the two threshold values were considered to be well chosen.

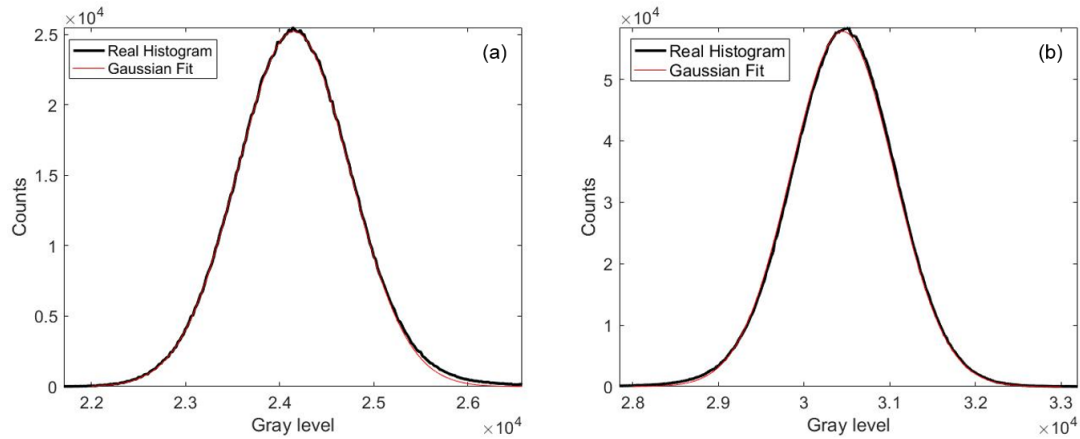


Figure 5.20: Histogram of air-only (a) and grain-only (b) in the original image.

The histogram and the Gaussian fit of the final water-only phase on *the original image* are shown in Figure 5.21. The histogram of the water-only phase was less perfectly Gaussian compared to that of the air-only and grain-only phases (see Figure 5.20) as some voxels of the water-only phase were attributed to water/grain interface voxels. It is well known that the “middle” phase of three-phase media is the most difficult to identify from XRCT images (Hashemi et al., 2014). For the proposed method, this small mis-classification (between water/grain interfaces and water-only) can be neglected as the volumetric fraction in interface phases is calculated based on mean gray values of two corresponding pure phases (the quantitative calculations will be presented in details in subsection 5.3.2.2). Note that Gaussian fits of the three pure phases have the same standard deviation, which shows that the image noise is uniformly distributed in the pure phase voxels.

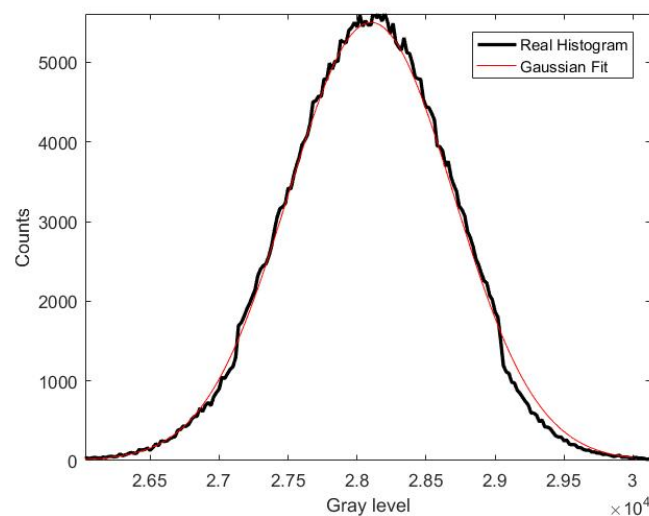


Figure 5.21: Histogram of the water-only phase.

### 5.3.2.2 Quantitative estimation of volume fractions

As aforementioned, the volume fraction, with respect to the whole domain of investigation, of the two corresponding phases in an interface phase is calculated based on a linear interpolation of their mean gray levels (Hsieh et al., 1998). We thus have:

$$\begin{cases} \theta_{I,J} + \theta_{I,K} = \theta_I \\ \theta_{I,J}E_J + \theta_{I,K}E_K = \theta_I E_I \end{cases} \quad (5.4)$$

Where capital letter I refers to interface phase of two J, K phases;  $\theta_I$ ,  $E_I$  are respectively volume fraction and mean gray level of the interface phase I on the whole image;  $\theta_{I,J}$ ,  $\theta_{I,K}$  are volume fraction of pure J, K phases in the interface I, respectively;  $E_J$ ,  $E_K$  are mean gray level of pure J, K phases, respectively, calculated from the two corresponding pure phase zones.

In three-phase media, any phase denoted P has two interfaces, with the two other phases denoted respectively M, N. The total volume fraction of any phase, denoted  $\theta_P$  is then given by:

$$\theta_P = \theta_{P,P} + \theta_{P,M} + \theta_{P,N} \quad (5.5)$$

Where  $\theta_{P,P}$ ,  $\theta_{P,M}$ ,  $\theta_{P,N}$  are volume fraction of P in the P-only zone and in the two interfaces M and N, respectively.

The volume fraction of Air, Water and Grain ( $\theta_{Air}$ ,  $\theta_{Water}$ ,  $\theta_{Grain}$ ) are thus:

$$\begin{cases} \theta_{air,air} + \theta_{air,air/water} + \theta_{air,air/grain} = \theta_{Air} \\ \theta_{water,water} + \theta_{water,air/water} + \theta_{water,water/grain} = \theta_{Water} \\ \theta_{grain,grain} + \theta_{grain,air/grain} + \theta_{grain,water/grain} = \theta_{Grain} \end{cases} \quad (5.6)$$

Consequently, porosity and water saturation can be calculated as follows:

$$\begin{cases} Porosity = \theta_{Air} + \theta_{Water} \\ Watersaturation = \frac{\theta_{Water}}{\theta_{Air} + \theta_{Water}} \end{cases} \quad (5.7)$$

## 5.3.3 Validations

### 5.3.3.1 Experimental method

The granular material used in this study was made of glass beads (diameter range: 200  $\mu\text{m}$  to 300  $\mu\text{m}$ , density: 2.5  $\text{g}/\text{cm}^3$ ) or Fontainebleau silica sand (NE34, consisting of poor-graded sub-rounded grains having diameter ranging from 100 to 300 microns and density of 2.65  $\text{g}/\text{cm}^3$ ).

An Ultratom scanner from RX Solutions, combining either a Hamamatsu L10801 Micro-focus reflection (230 keV) or a Hamamatsu L10712 Nano-focus (160 keV) X-ray sources and a Paxscan Varian 2520V flat-panel imager (1920x1560  $\text{pix}^2$ , pixel size: 127  $\mu\text{m}$ ), was used for the XRCT scans. The scans were performed at 80 kV and 40  $\mu\text{A}$ . A copper filter of 0.1 mm of thickness was used to reduce beam hardening artifacts.

A quantity of dry granular materials mixed with water doped at 3.5 wt% of KI was compacted in an aluminum tube (Internal diameter: 5.0 mm; External diameter: 6.0 mm). The two open ends of the tube were closed by using Plexiglas. The aluminum tube and Plexiglas before the sand compaction together with the whole system, consisting of the aluminum tube, Plexiglas and unsaturated sand were weighted to determine the mass of used unsaturated sand. Heat-shrinks were put outside of the two ends of the aluminum tube, closed by Plexiglas, to avoid water evaporation. The whole sample was scanned by using some successive scans along the sample height (stack scan). After the scan, the whole system without heat-shrinks was placed into an oven to determine the mass as well as the volume of used dry granular materials. Combined with the mass of unsaturated granular materials, the volume of used water was determined. The sample volume was determined from the whole sample image. The porosity and degree of water saturation were then determined. Note that the precision of balance used was about  $\pm 2$  mg and 3D calculations were applied to the whole sample. Even a small part of unsaturated sand, attached to Plexiglas at the two ends, was taken into account.

### 5.3.3.2 Results

Figure 5.22a shows a XRCT image of unsaturated glass beads. Glass beads were compacted into the aluminum tube with an average porosity of 0.40 and an average degree of saturation of 35 %. The XRCT scans (4-stack scan) were performed with the X-ray source Hamamatsu L10801. Voxel size was  $5 \mu\text{m}$ . Histogram of the whole original image of the sample containing three phases (Air, Saline water and Glass beads) is shown in Figure 5.23. The image obtained after the classification of all the image voxels shown in Figure 5.22a is shown in Figure 5.22b. From the quantitative analyses, the average porosity and the average degree of saturation of the sample were 0.39 and 35 % respectively. These values are similar to the measured values mentioned above.

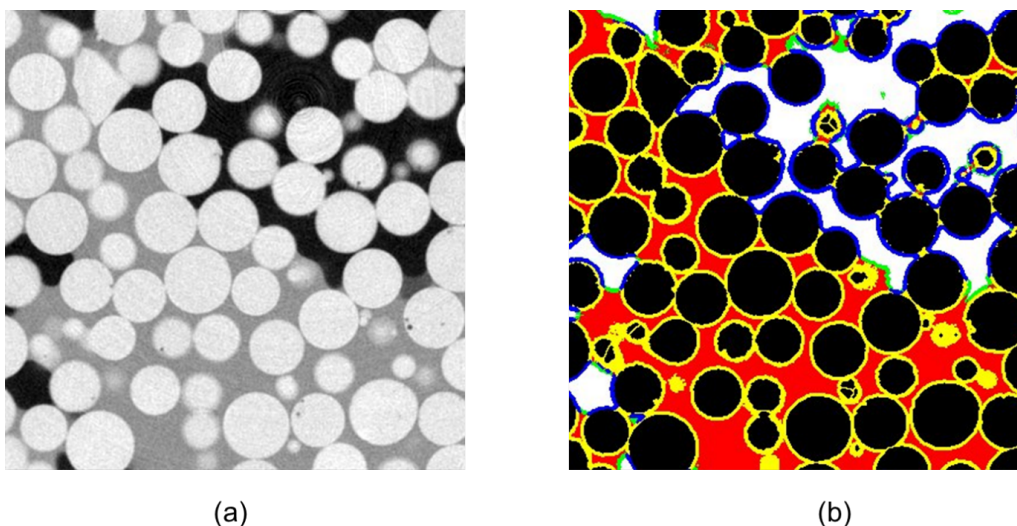


Figure 5.22: Test with unsaturated glass beads: (a) original image; (b) image obtained after the classification of voxels – solid-only (black), air-only (white), water-only (red), air/solid (blue), water/solid (yellow), air/water (green). Image dimensions: 2.000 mm  $\times$  2.000 mm.

For the test on an unsaturated sand, the X-ray source Hamamatsu L10712 was used. The voxel size was  $3.5 \mu\text{m}$ . An image obtained by XRCT scans (5-stack scan) is shown in Figure 5.24a. Note that the same source and scan duration were used for this XRCT scan as well as that used to explain the procedure (Figure 5.17a). However, the image resolution here was slightly higher (voxel size:  $3.5 \mu\text{m}$  compared to  $4 \mu\text{m}$ ). Fontainebleau sand grains were compacted at an average porosity of 0.40 and an average degree of saturation of 28 %. The corresponding image of the image shown in Figure 5.24a, obtained after the voxel classification is shown in Figure 5.24b. The average porosity of the sample was estimated at 0.41 and the average degree of saturation was at 29.5 %. These values are close to the aforementioned measured values. The range of error is between 2 and 5 %.

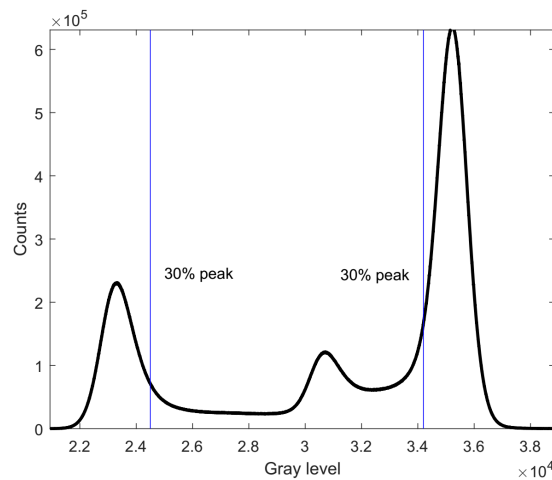


Figure 5.23: Histogram of the image obtained on unsaturated glass beads.

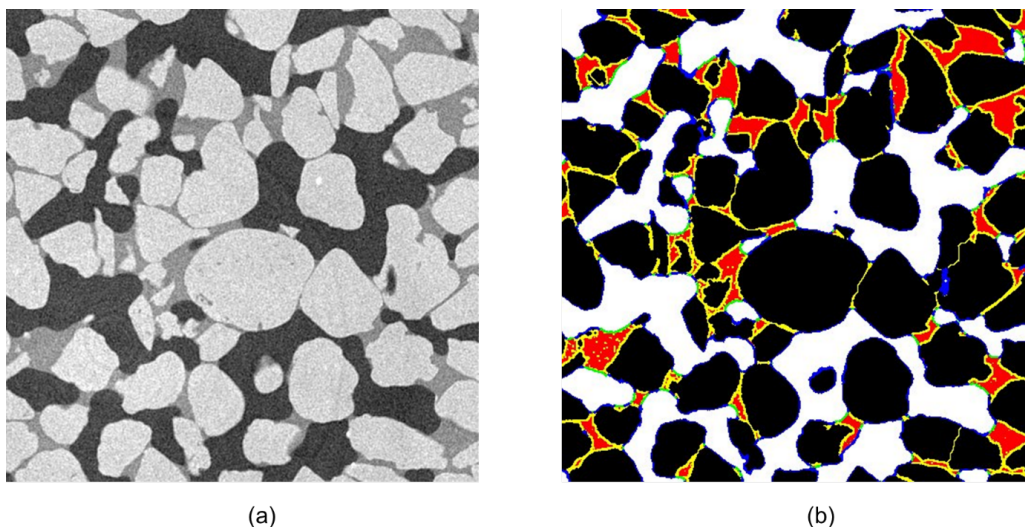


Figure 5.24: Test with an unsaturated sand: (a) original image; (b) image obtained after the voxel classification – solid-only (black), air-only (white), water-only (red), air/solid (blue), water/solid (yellow), air/water (green). Image dimensions:  $1.750 \text{ mm} \times 1.750 \text{ mm}$ .

Three-phase interface voxels (which can not belong to the three pure phases) were found by dilating the three two-phase interfaces by  $n$  voxels then finding their intersections. Their total volume fraction in the whole image calculated was about 2 % (1.8). Furthermore, they were all attributed to the nearest two-phases. That is why the three-phase interfaces can be neglected as aforementioned.

### 5.3.4 Discussions on accuracy

#### 5.3.4.1 Parameter sensitivity

The proposed method involves some parameters as:

- Thresholds used for preliminary segmentation of the three pure phases;
- $n$  used for dilation operations to determine interface phases.

As aforementioned,  $n$  depends mainly on the sharpness of the individual projections, i.e., geometric factors such as the size of X-ray source and detectors as well as the image spatial resolution and the scan duration. In this study, with the same scan conditions (the same source, image spatial resolution and scan duration), the same  $n$  value (3) worked well for both the demonstrative case (Figure 5.17a) and the unsaturated sand test (Figure 5.24a) while  $n = 4$  was a better choice for the test with unsaturated glass beads (Figure 5.22a scanned with another X-ray source).

Therefore, the main parameter are the thresholds used for the preliminary segmentation of the three pure phases. Image (180 x 180 x 180 voxels) of the procedure demonstration case (Figure 5.17a) was used to study the effect of threshold levels used for segmentation of three pure phases of the proposed method on the final results (porosity and degree of saturation). We recall that the gray levels corresponding to 30 % of the peak count values were used in the analysis shown above. If the threshold is too far from the peak, it would involve two-phase voxels in the pure phase. Inversely, if the threshold is too close to the peak, it would increase unnecessarily the number of two-phase voxels and reduce the accuracy of the determination of the average gray level of the pure phase. Table 5.1 and Figure 5.25 present the results obtained from a sampling image (180 x 180 x 180 voxels) where various thresholds corresponding to 20 %, 30 %, 40 %, and 50 % of the peak count values were used. These values were proposed to make sure that almost pure phases were chosen without any voxels of other phases (other pure phases or interfaces). When these thresholds were varied in this range, the porosity and the degree of saturation remained almost constant. The results of degree of water saturation were fluctuated more compared to that of porosity because of the difficulty to identify the “middle” phase, i.e. water. 30 % was chosen to make sure that grain boundaries were well separated and voxels being interior of grains were considered as grain-only phase even if their gray value was smaller due to the image noise (see Figure 5.25). Note that the final histograms of pure phases (i.e. air-only, grain-only and water-only) were verified to be Gaussian as shown in Figure 5.20 and Figure 5.21.

3D view of the resulting image, where 6 phases were well attributed, is shown in Figure 5.26.

Table 5.1: Effects of threshold choices used for the proposed method on the final results.

Ratio to peak value (%)	Porosity (-)	Degree of saturation (%)
50	0.3988	31.00
40	0.3962	30.43
30	0.3932	29.73
20	0.3896	28.80

### 5.3.4.2 Comparison with Otsu's method

A comparison between a well-known traditional segmentation method – Otsu's method (Otsu, 1979) and the proposed method is shown in Figure 5.27. A median filter (radius of 2 pixels) was used before applying Otsu's segmentation method. Porosity and water saturation were slightly higher according to the Otsu's method than that determined by the proposed method. It can be seen that some voxels at the interfaces of air and grain (which were well determined after the proposed method), having gray value in a range of that of water due to the PVE, were considered as water by the Otsu's method. In addition, some grain pixels having lower gray values than normal values due to artifacts were considered as water following the Otsu's method while they were attributed to grain-only or water/grain interfaces after the proposed method.

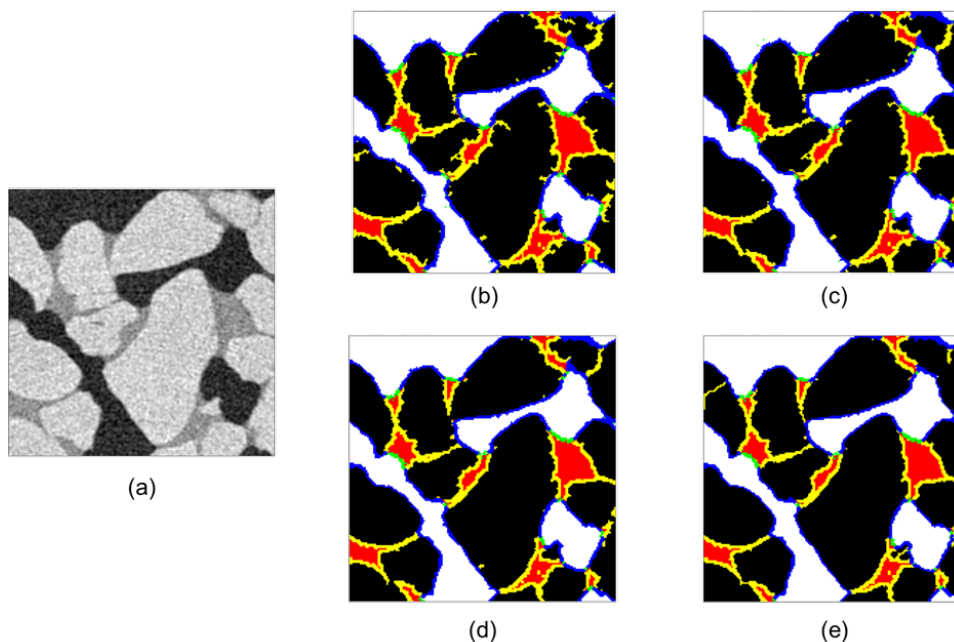


Figure 5.25: Effects of threshold choices on the resulting image: (a) original image; (b) ratio to peak value = 50 %; (c) ratio to peak value = 40 %; (d) ratio to peak value = 30 %; (e) ratio to peak value = 20 %. Image dimensions: 0.720 mm x 0.720 mm.



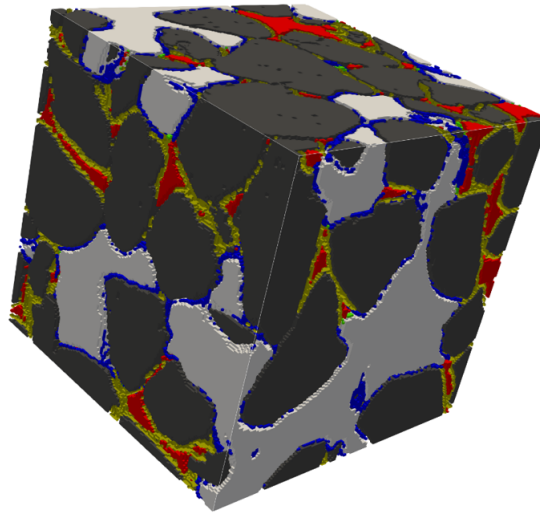


Figure 5.26: 3D view of the resulting image. Image dimensions: 0.720 mm x 0.720 mm x 0.72 mm.

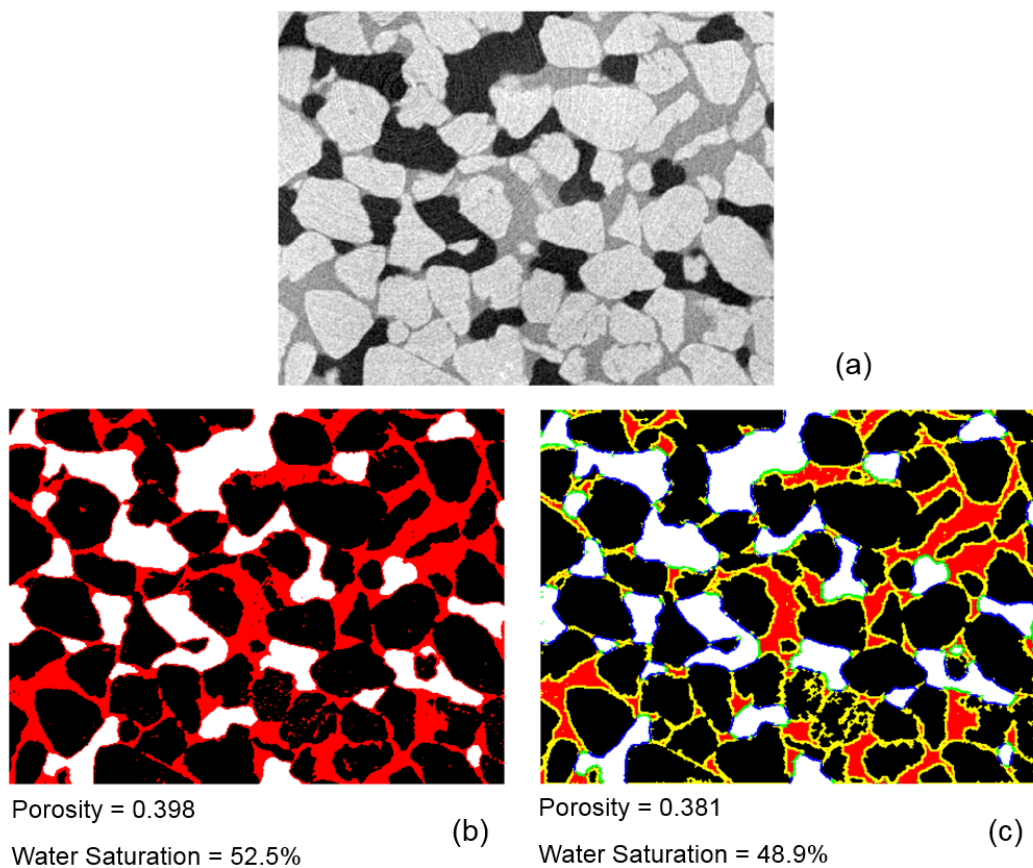


Figure 5.27: Comparison between the proposed method and Otsu's method: (a) original image; (b) resulting image following the Otsu's method; (c) resulting image following the proposed method. Image dimensions: 1.500 mm x 1.200 mm.

Effects of threshold values used for a global threshold method on the final results are shown in Table 5.2. The thresholds found following the Otsu's method are:  $T_{01}$  and  $T_{02}$ . The threshold values used for the segmentation of three phases ( $T_1, T_2$ ) are varied in ranges: ( $[T'_1, T_{01}]$  and  $[T'_2, T_{02}]$ ) respectively, shown in Figure 5.28. Note that the count values corresponding to  $T_{01}$  and  $T_{02}$  are equal to that corresponding to  $T'_1$  and  $T'_2$  respectively. The values of porosity and degree of saturation vary significantly (see Table 5.2). These results demonstrate that the global threshold method is more sensitive to the choice of threshold values than the proposed method.

Table 5.2: Effects of threshold choices for a global threshold method on the final results.  $T_{01}$  and  $T_{02}$  are values found following the Otsu's method.

First Threshold, T1	Second Threshold, T2	Porosity (-)	Degree of saturation (%)
$T_{01}$	$T_{02}$	0.43	34.0
$T'_1$	$T_{02}$	0.43	39.5
$T'_1$	$T'_2$	0.40	35.5
$T_{01}$	$T'_2$	0.40	29.7

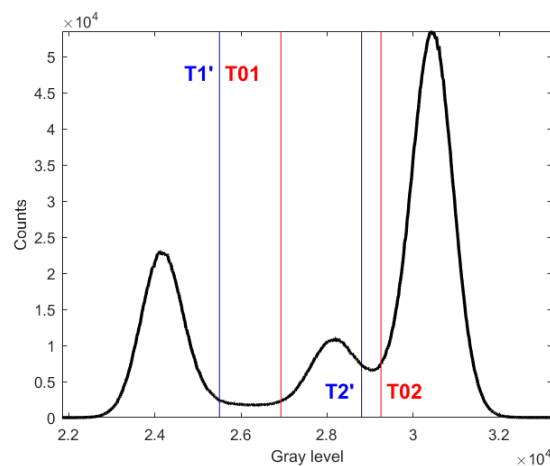


Figure 5.28: Histogram of filtered image ( $180 \times 180 \times 180$  voxels, median filter of 2 voxels) and threshold choices.  $T_{01}$  and  $T_{02}$  are values found following the Otsu's method.

### 5.3.5 Application to MHBS

Figure 5.29 shows an example of an image (obtained at the Psiche beamline at the Synchrotron Soleil, voxel size:  $0.9 \mu\text{m}$ , filtered by using a median filter with a radius of 2 pixels) of MHBS under excess-gas conditions (consists of methane gas, methane hydrate and sand grains) and its histogram. To the naked eyes, methane hydrates are found all around sand grain surfaces. Furthermore, it can be seen from the histogram that methane gas and methane hydrate have similar gray values while sand grains have much higher gray values. That explains why sand grains can be well identified on the image while it is not evident to distinguish between methane gas and methane hydrate. The proposed method needs to be adapted to the MHBS image as the partial-thresholding of the pure

methane gas phase is not obvious. It should be noted that despite the use of the Paganin filter, a slight phase contrast can still present (i.e. gray values at the interface voxels can fluctuate remarkably). Therefore, it is of essence to identify the interface phases as the determination of volume fractions on the three-phase media image, involving the phase contrast, by segmenting the image into three phases based on gray values, would induce a more important error.

### 5.3.5.1 Phase attribution

It can be seen from Figure 5.29 that almost all grain surfaces are covered by methane hydrates so methane gas/grain interfaces can be neglected in a first approach. That means that all voxels corresponding to the interfaces of sand grains are methane hydrate/grain interfaces. The MHBS image was thus decomposed into three pure phases (grain-only, methane gas-only and methane hydrate-only) and two interface phases only (methane gas/methane hydrate and methane hydrate/grain) voxels following the steps below:

- Step 1: Identify the pure grain voxels from the image histogram. The threshold which corresponds to gray value having a count value equal to 30 % of the peak value was used (see Figure 5.30). The histogram of the grain-only phase was the image histogram part on the right of the threshold chosen.
- Step 2: Determine the voxels corresponding to the methane hydrate/grain interfaces by dilating the grain-only phase by 12 voxels. The blue line in Figure 5.30 represents the histogram of the grain-only phase dilated by 12 voxels.

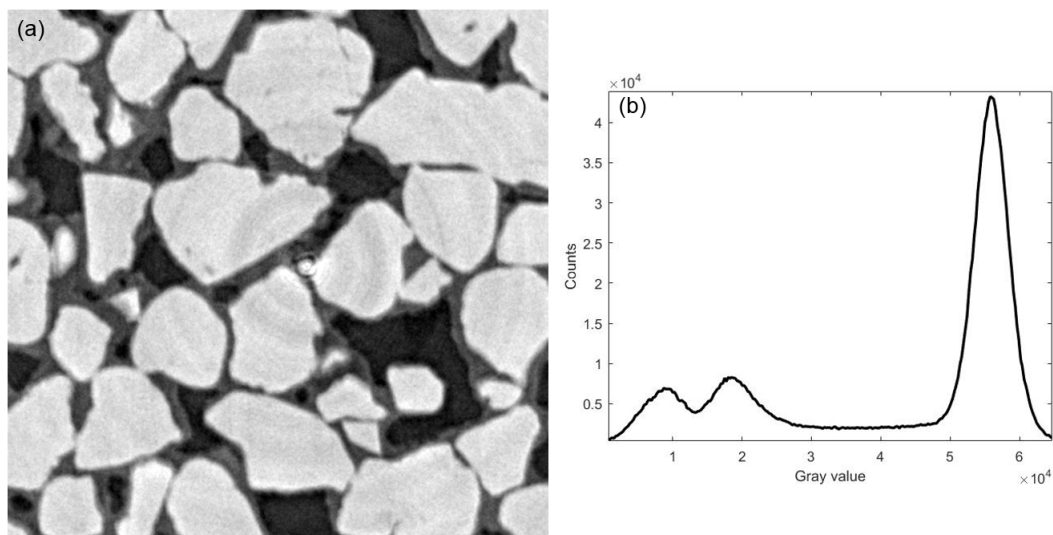


Figure 5.29: MHBS under excess-gas conditions: (a) SXRCT image, 1.200 mm x 1.200 mm; (b) its histogram.

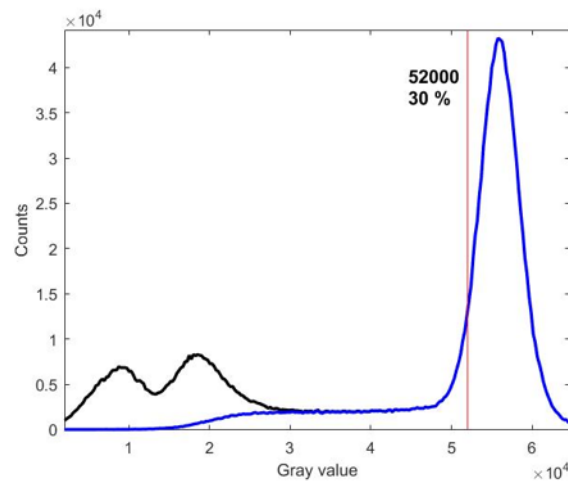


Figure 5.30: Histograms of the grain-only phase and grain interfaces.

The remaining part is now composed of methane gas-only, methane hydrate-only and methane gas/methane hydrate interface voxels. Its histogram is shown in Figure 5.31 (Real histogram).

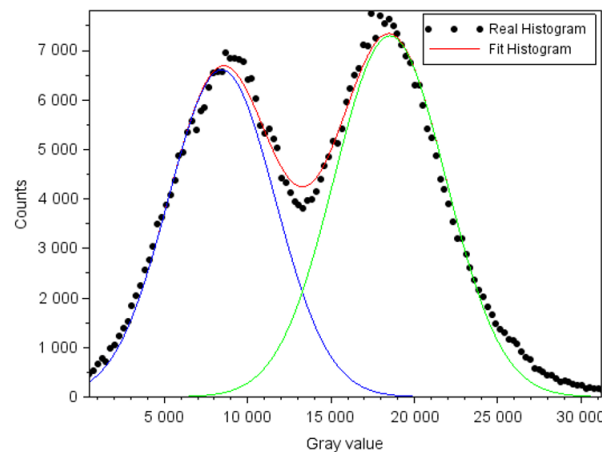


Figure 5.31: Histograms of the rest and two fitted Gaussian curves.

- Step 3: Divide the remaining part preliminarily into two parts. The histogram of the remaining part was fitted with a combination of two Gaussian curves (the fit histogram - the red line is the sum of the blue and the green lines). The gray value at the intersection of both Gaussian curves ( $T = 13300$ ) was used to classify the remaining part into two parts. It is supposed that the first part (having gray values smaller than  $T$ ) is composed of voxels of methane gas-only and that of methane gas/methane hydrate interfaces that are close to the methane gas phase voxels. On the contrary, the second part (having gray values greater than  $T$ ) consists of voxels of methane hydrate-only and that of methane gas/methane hydrate interfaces that are close to the methane hydrate phase voxels.

- Step 4: Determine the voxels corresponding to the methane gas/methane hydrate interfaces, methane gas-only and methane hydrate-only. The methane gas/methane hydrate interface voxels were found by dilating both parts (found in the step 3) by 6 ( $= 12/2$ ) voxels and finding their intersection. The methane gas-only voxels were that in the first part (found in the third step) without methane gas/methane hydrate interfaces. Furthermore, the methane hydrate-only voxels were that in the second part (found in the third step) without methane gas/methane hydrate interfaces.

Three pure phases (grain-only, methane gas-only and methane hydrate-only) and two interface phases (methane gas/methane hydrate and methane hydrate/grain) voxels were assigned to the original image after all the aforementioned steps. The final results is shown in Figure 5.32 where all voxels have been attributed to the corresponding phases.

It is observed that there are few pure methane gas and pure methane hydrate voxels while the numbers of methane hydrate/grain and especially methane gas/methane hydrate interface voxels are quite important. This is first related to the Paganin filter making the gray values in each phase on the SXRCT image less homogeneous. Furthermore, MH morphologies and pore habits are quite complex in geometry, and MHs could be porous. That is why it is better to classify these voxels as two-phase voxels. On the other hand, small holes inside grains were closed because grains are solid and convex.

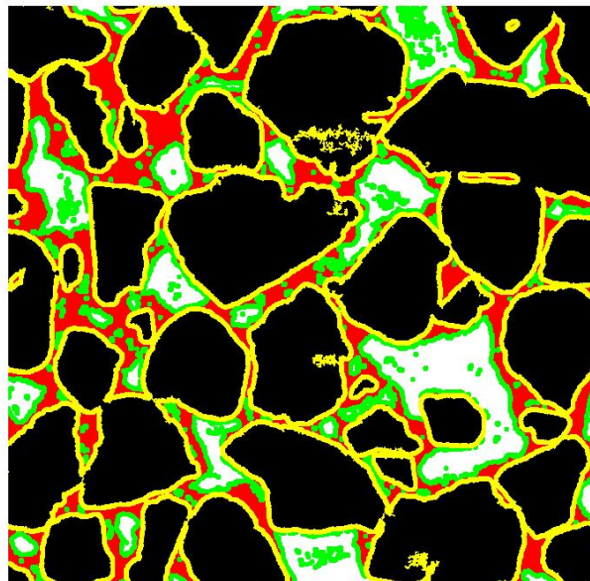


*Figure 5.32: Image obtained after the classification of all voxels into five families: grain-only (black), methane gas-only (white), methane hydrate-only (red), methane gas/methane hydrate interfaces (green), and methane hydrate/grain interfaces (yellow).*

### 5.3.5.2 Quantitative estimation

As aforementioned, the numbers of methane gas-only and methane hydrate-only voxels are small so that determining their mean gray values is delicate. Therefore, the mean gray value of the grain-only phase can be determined from the found grain-only voxels while the mean gray values of the methane gas-only and the methane hydrate-only phase

are determined from a line profile shown in Figure 5.33. Note that the gray value of the grain-only phase determined from the line profile is similar to that calculated from the grain-only voxels. Furthermore, determining the volume fraction of the two corresponding phases in an interface phase based on a linear interpolation of their mean gray value can induce an important error with the presence of the phase contrast. That is why in this study, first the Paganin filter was optimized to limit the phase contrast so that this quantitative determination can still be applied. Second, the interface phase voxels have been chosen to be thick ( $n = 12$ ) with the hope that the phase contrast effects would be compensated. It is believed that these artifacts result in an overestimated gray level in one side of an interface and an underestimation in another side.

Porosity and methane hydrate saturation calculated after the classification of all voxels into five families are 0.33 and 66.5 %.

In this first approach, methane gas/grain interface voxels were neglected. However, in some areas, it appears difficult to verify whether or not a thin MH layer exists around sand grain. Successive methane hydrate/grain and methane gas/methane hydrate interface voxels could be methane gas/grain interface voxels as shown in Figure 5.34 (the used algorithm is not detailed here). Porosity and methane hydrate saturation calculated after the classification of all voxels into six families are 0.33 and 62.7 %.

The comparison of these analysis provides a confidence zone. The porosity measurement is 0.33 for both ones while the methane hydrate saturation ranges from 62.7 to 66.5 % (i.e. a margin of error of approximatively 5 %). It is noteworthy that the image was influenced by ring artifacts (a proper problem of XRCT/SXRCT images), the quantification could be slightly influenced due not only to the possible mis-classification of different phases but also to the error of mean gray level calculation.

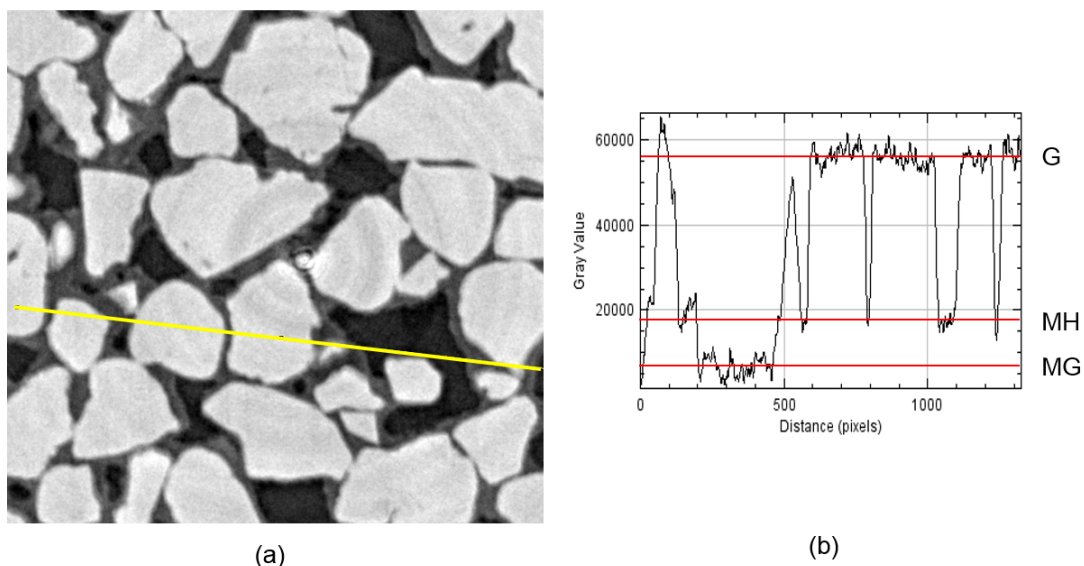
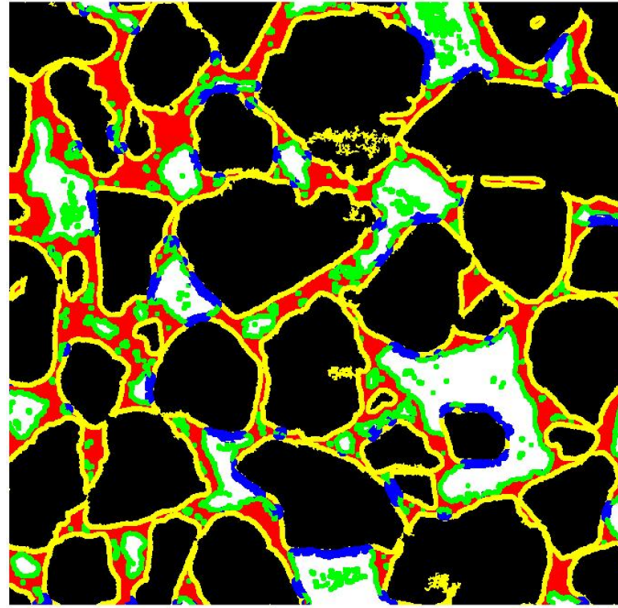


Figure 5.33: Line profile to determine the mean gray values of the methane gas-only and the methane hydrate-only phase: (a) Line profile on the original image; (b) Gray value profile.



*Figure 5.34: Image obtained after the classification of all voxels into six families: grain-only (black), methane gas-only (white), methane hydrate-only (red), methane gas/grain interfaces (blue), methane gas/methane hydrate interfaces (green), and methane hydrate/grain interfaces (yellow).*

### 5.3.6 Conclusions

A new method was proposed to determine more accurately the volume fractions of three phases (Air, Water, and Solid) in unsaturated porous media through XRCT images. The medium image was decomposed into not only three pure phases but also three interface phases (two-phase media) voxels in order to account more accurately for image noise and PVE. Two pure phases (air-only, solid-only) were first identified based on the image histogram together with some morphological operations while the pure water phase (the pure phase the most difficult to segment) was determined after determining the interface phases, found by intersecting dilated pure phases. The contrast of the three phases needs to be high enough so that they could be segmented based on the image histogram and the images should not be influenced strongly by tomography artifacts as beam hardening, ring artifacts for accurate quantizations. Once each voxel in the 3D image was classified, the volume fraction of each phase was calculated. Actually, volume fraction of each phase in two-phase voxels was calculated based on a linear interpolation of mean gray levels of the two corresponding pure phases, which reflects the physical formation of gray levels in an ideal XRCT image. The total volume fraction of each phase was finally calculated by combining its volume fraction in pure phase voxels with that in the two corresponding interface phases. The proposed method was applied to two specimens (unsaturated glass beads and unsaturated sands). The calculated values (porosity and degree of saturation) are similar to those measured on both specimens. These results confirm that this method can determine accurately the volume fractions of three phases in unsaturated granular media from XRCT images. Note that the proposed method makes use of the media microstructure whereas other existing methods were mainly based on mathematics (Kulkarni et al., 2012; Houston et al., 2013).

The proposed method can be applied to not only unsaturated granular media but also to other three-phase porous media (i.e. MHBS under excess-gas conditions). It is evident that the method is based on the morphology of the media and, as a consequence, the method needs to be adapted to the media case-by-case.





# 6 MH morphologies and pore habits

## 6.1 Introduction

In this chapter, the growth of MHs generated with the excess-gas method, their spatial distribution and their various morphologies and pore habits at submicron/micron voxel size were investigated by using SXRCT, and optical microscopy which provide a good temporal resolution (some minutes and sub-second respectively), adopted to the kinetics of MH formation. Both water and saline water solutions were used. Changes of MH morphologies and pore habits at both pore and sample scales due to multiple water migrations were observed during the process. Furthermore, morphologies and pore habits of MHs under excess-gas and excess-saline-water conditions are discussed.

The main findings of this chapter are included in the publications:

- T.X. Le, M. Bornert, R. Brown, P. Aïmediou, D. Broseta, B. Chabot, A. King, A.M. Tang (2019) Grain-scale morphologies and distribution of methane hydrates formed in sandy sediment under excess gas conditions. In preparation.
- T.X. Le, M. Bornert, P. Aïmediou, B. Chabot, A. King, A.M. Tang (2019) An experimental investigation on the methane hydrate morphologies and pore-habits in sandy sediment by using Synchrotron X-ray Computed Tomography. In preparation.

## 6.2 Experimental method

### 6.2.1 Experimental setups

Figure 6.1 shows a schema of the experimental setup used for SXRCT scans (see the third experimental setup, presented in Chapter 5). As aforementioned, SXRCT scans were performed at the Psiche beamline at the French Synchrotron SOLEIL (proposal No. 20181629). X-ray beam was used with an energy spectrum centred at 44 keV. Two types of scan were used. For high resolution scans, the scan zones (Z0\_HR, Z1\_HR, Z2\_HR, Z3\_HR) are marked with green lines (1.75 mm in height and 1.75 mm in diameter). The voxel size and the scan time were 0.9  $\mu\text{m}$  and 0.2 hour respectively. The low resolution scans, marked with blue lines (3.47 mm in diameter and 1.75 mm in height), served to investigate methane hydrate distribution over the sample height. The voxel size in this case was 1.8  $\mu\text{m}$  and the scan time was 0.25 hour. Paganin's filter parameters for the reconstruction with the PyHst software were optimized to limit the phase contrast so that gray levels within each phase in the image remain almost homogeneous. Therefore,

contrast in a SXRCT image depends mainly on the difference of material attenuation. Figure 6.2 shows the Psiche instruments and the in-situ experimental setups.

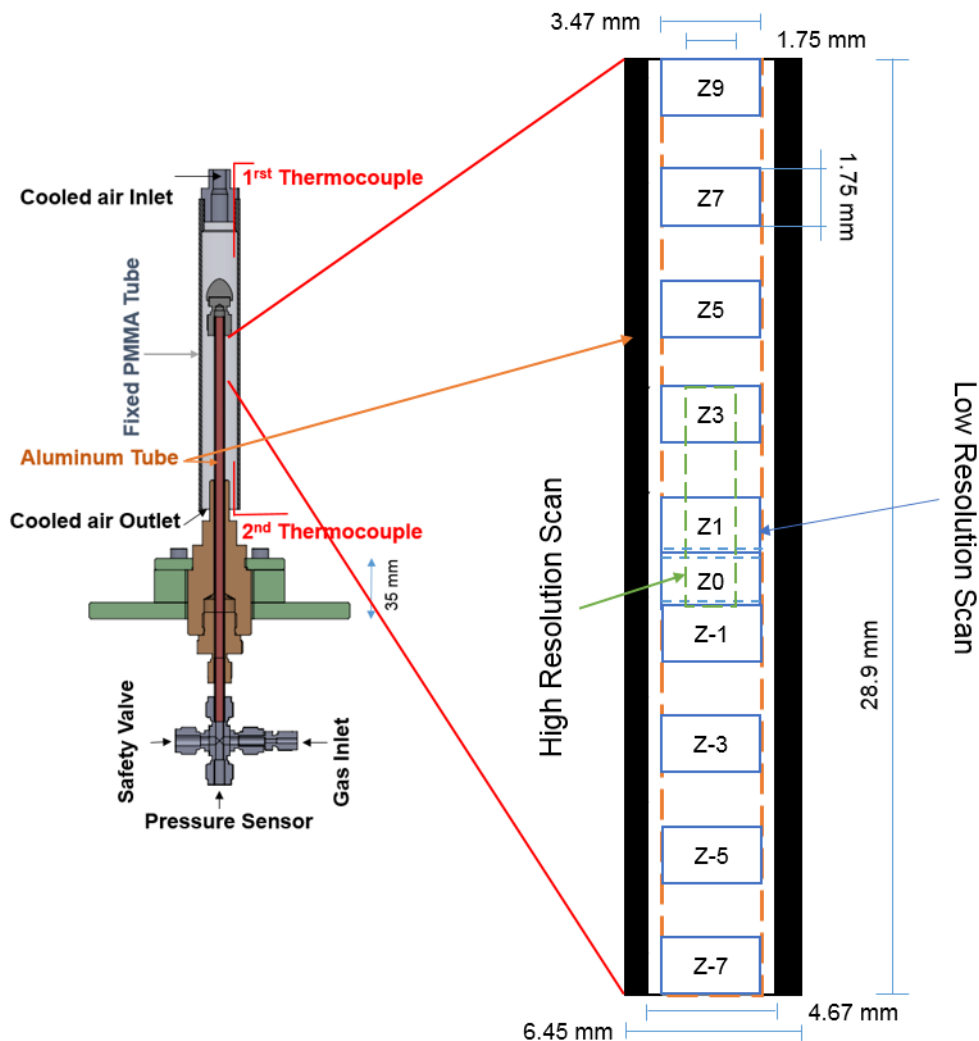


Figure 6.1: Schema of the experimental setup showing pressure/temperature controls for SXRCT tests and scan types/positions.

Moreover, a schematic view of the experimental setups used for optical microscopy tests is shown in Figure 6.3. Wet sand grains were contained in a quartz capillary tube closed at one end. The tube has a square cross-section (internal section:  $500 \times 500 \mu\text{m}^2$  and  $100 \mu\text{m}$  in thickness). The temperature of the capillary tube was controlled by an annular Peltier element (upper face of the tube was in contact with the Peltier element cooled itself by a water-cooled radiator). The whole system was setup horizontally on an inverted microscope (Nikon<sup>TM</sup>), equipped with an Orca 4 camera (Hamamatsu). A methane gas bottle or a vacuum pump was connected to the open end of the tube in the objective of controlling the gas pressure inside the tube. Figure 6.4 shows the in-situ experimental setup used for the optical microscopy tests at Institut des Sciences Analytiques et de Physico-Chimie pour l'Environnement et les Matériaux (IRREM, in cooperation with the university of Pau).

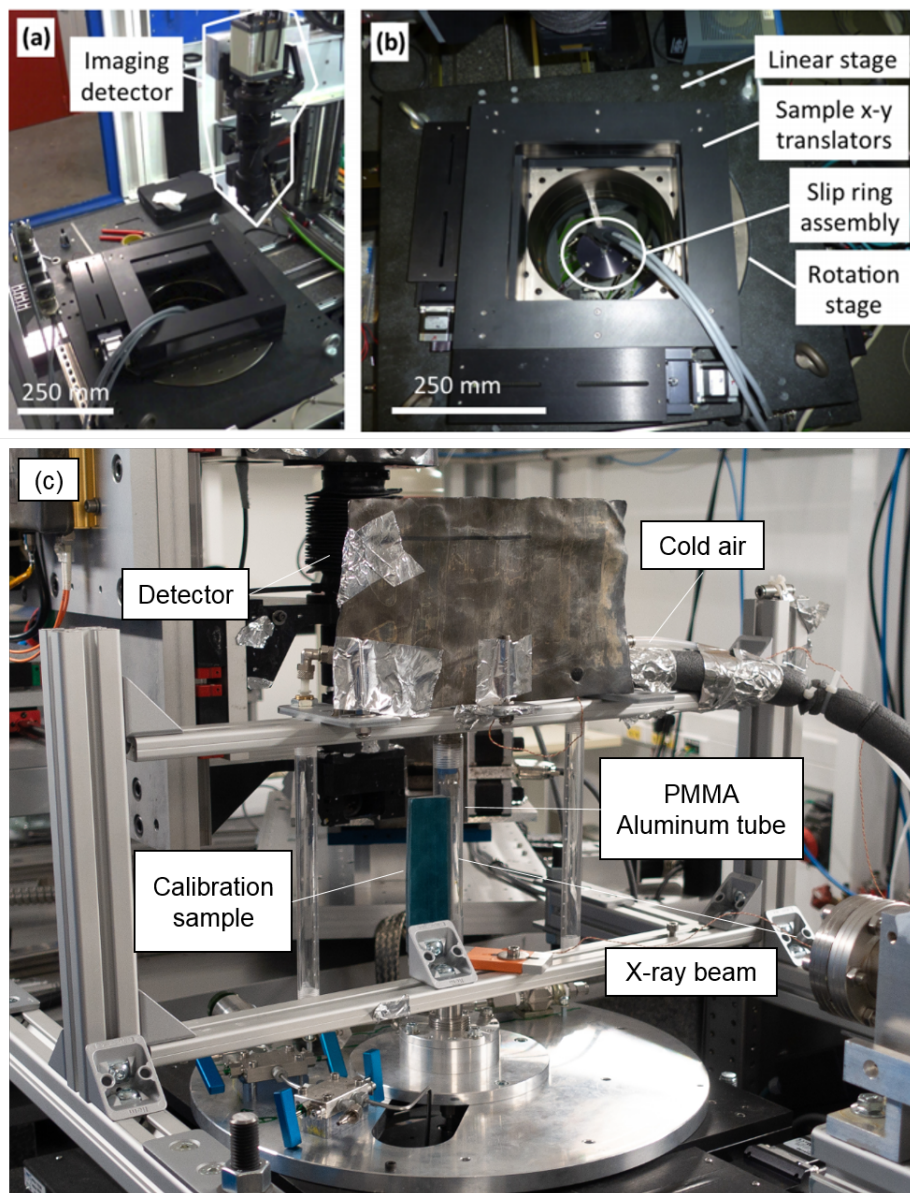


Figure 6.2: SXRCT experimental setups: (a) and (b) the Psiche tomography instruments; (c) In-situ MHBS experimental setups.

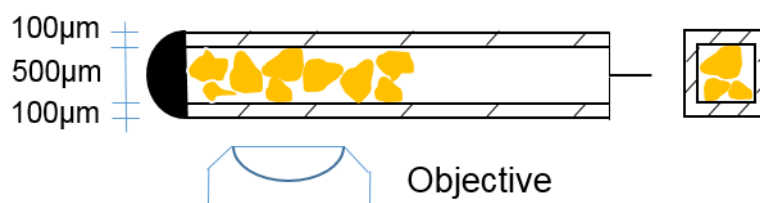


Figure 6.3: Schematic view of the experimental setup for optical microscopy tests. The capillary tube with square cross-section was inserted in a thermostated holder, installed on an inverted microscope.

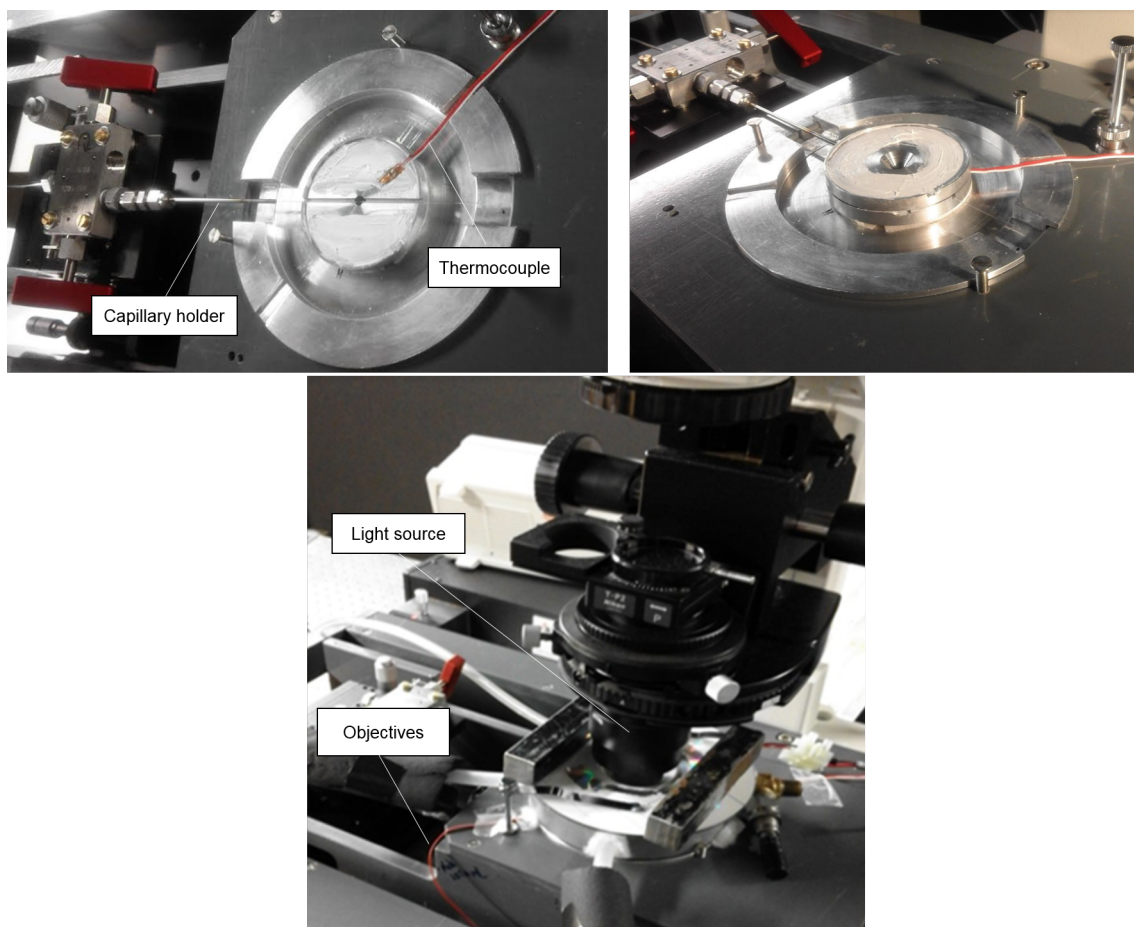


Figure 6.4: In-situ optical microscopy experimental setup.

## 6.2.2 Test procedure

For the SXRCT scans, wet Fontainebleau sand was compacted in the aluminum tube to reach an average porosity of about 0.4. After the installation of the system (Figure 6.1) on the beamline, vacuum was applied to the tube in order to remove residual air prior to the application of methane gas pressure at 7 MPa. Afterward, cooled air was circulated to reduce the sample temperature to form methane hydrates. Different scans were performed during the tests. Four tests were performed including three tests with tap water and one test with saline solution (3.5 wt% of KI), see Table 6.1. The initial moisture content was 10 % and 15 %. Figure 6.5 shows the type and position of SXRCT scans used to follow MH formation over time for the four tests ( $t = 0$  corresponds to moment when the temperature of the cell reached the target value at 7 MPa of pressure). Note that Test 1 was considered as a preliminary test, that is why just a limited numbers of scans have been performed (high resolution scans at positions Z0 and Z5; low resolution scans at position Z0). Test 3 was stopped after about 7 hours because of the end of the beamline operating time. Both high and low resolution scans were performed at positions Z0 and Z1. Only high resolution scans were performed over four continuous zones (Z0 to Z3) during Test 2. For Test 4, high resolutions scans were first done at positions Z0 and Z1, and the low resolution scans were performed over zones (Z-7, Z-5, Z-3, Z-1, Z0, Z1, Z3, Z5, Z7 and

Z9). Furthermore, due to some technical issues (vibration during scans, image acquisition errors), some scans (at the beginning of Test 2 for example) are not available.

At the end of the MH formation following the excess-gas method of Test 1, excess-gas was replaced by saline water (KI, 3.5 wt%) at 7 MPa in the objective of saturating the sample with saline water (similar procedure as “Step 4” in subsection 3.2.3). Saline water was used instead of pure water to better observe MHs in the medium.

Table 6.1: Test program of SXRCT and optical microscopy

Test No.	Type of test	Type of water used	Initial moisture content (%)	Temperature imposed (°C)
Test 1	SXRCT	Tap water	10	2-3
Test 2	SXRCT	Tap water	10	3-4
Test 3	SXRCT	Tap water	15	2-3
Test 4	SXRCT	Saline water, KI 3.5wt%	15	1-2
Test 5	optical microscopy	Deionized water	-	-16
Test 6	optical microscopy	Deionized water	-	2

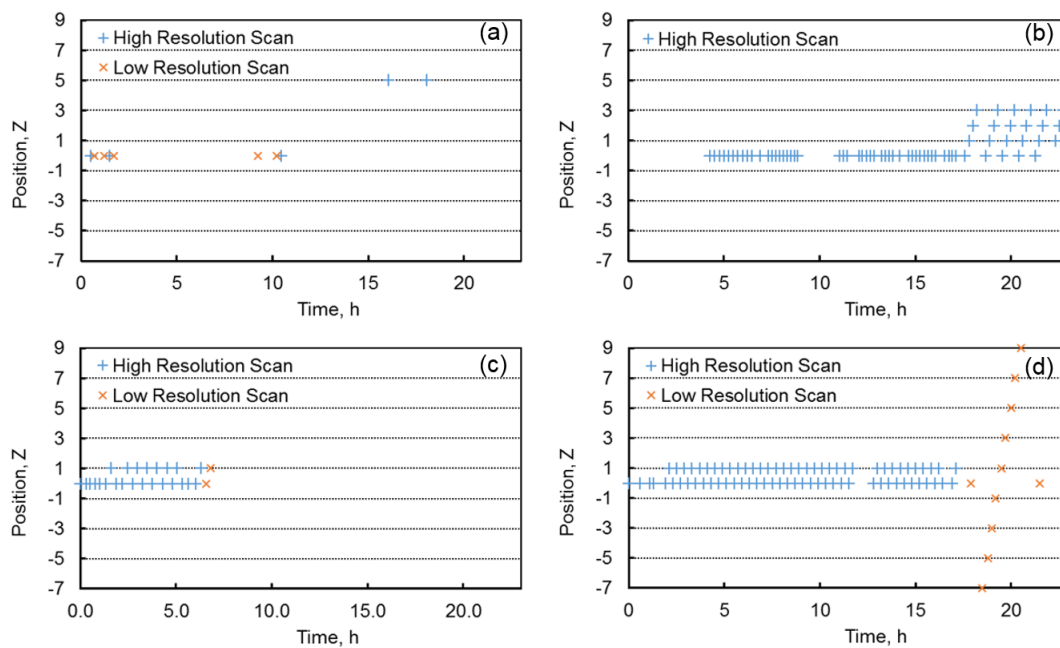


Figure 6.5: Scan type and position versus experiment time of: (a) Test 1; (b) Test 2; (c) Test 3; (d) Test 4.

For the optical microscopy observations, dry Fontainebleau sand grains were first introduced into the capillary tube. Afterward, deionized water was dropped on the sand grains. Once the experimental setup has been installed (Figure 6.3), vacuum was applied. Two tests were performed. For the first test, methane gas pressure was first applied at 8 MPa and then the temperature was decreased and stabilized at  $-16\text{ }^{\circ}\text{C}$  to form methane hydrates. For the second test, the temperature was first decreased to  $-25\text{ }^{\circ}\text{C}$  for ice formation then increased and stabilized at  $-5\text{ }^{\circ}\text{C}$ . Methane gas pressure was then applied at 8 MPa before temperature was raised to  $2\text{ }^{\circ}\text{C}$ .

Note that the mean initial moisture content of sample for the SXRCT tests was controlled via the quantity of water mixed with dry sand before compaction while the quantity of water injected into dry sand in the capillary tube for optical microscopy tests was not well controlled. The durations of the two optical microscopy tests (Test 5 and Test 6) are 3 and 5 hours respectively.

## 6.3 Experimental Results

### 6.3.1 MH growth

Figure 6.6 shows MH growth in zone Z0\_HR of Test 1 at various times after temperature was set. At  $t = 0.5$  h, water menisci were clearly found at grain contacts because of the capillary suction while MHs could not be found yet (Figure 6.6a). MH spikes were first observed at grain surfaces at  $t = 1$  h (Figure 6.6b) far away from water menisci. They became bigger at  $t = 1.5$  h (Figure 6.6c). MH layers/shells at water/methane gas interfaces and at grain surfaces were clearly evidenced in Figure 6.6d (at  $t = 10.5$  h) by the changes in the surface's roughness: smooth interfaces between liquid and gas due to interfacial tension are replaced by jagged ones. Furthermore, MH spikes (in Figure 6.6a and b) were transformed to more rounded objects called “crystals” at  $t = 10.5$  h (Figure 6.6d).

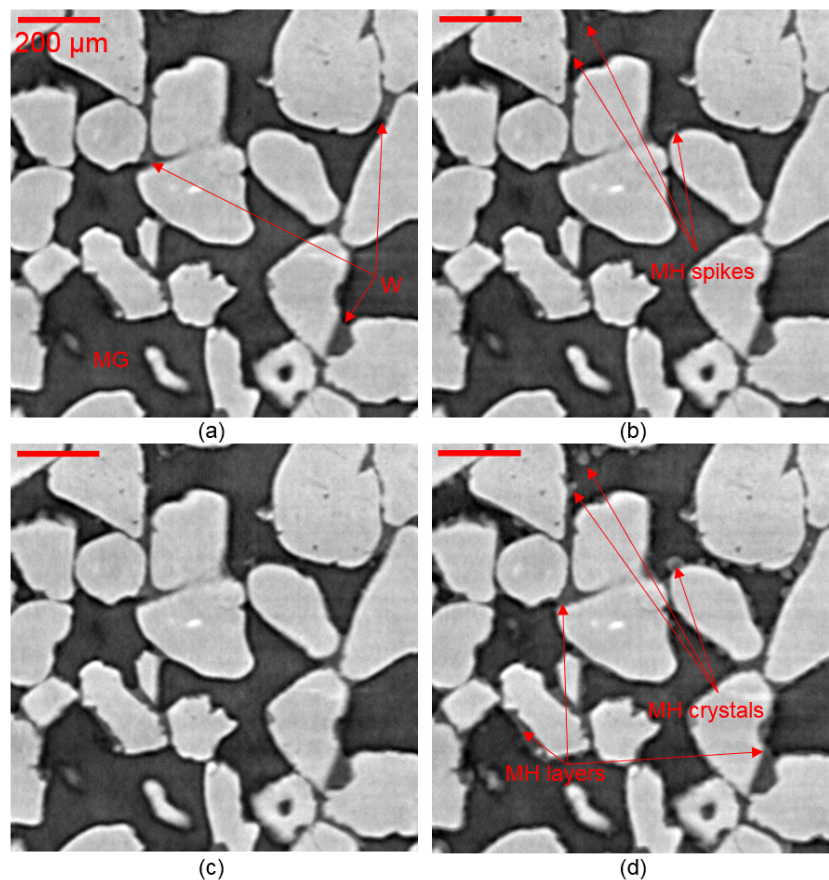


Figure 6.6: Test 1, transverse cross-section through Z0\_HR: (a)  $t = 0.5$  h; (b)  $t = 1$  h; (c)  $t = 1.5$  h; (d)  $t = 10.5$  h.

An example of MH growth at various times during the firsts six hours (in the zone Z0\_HR of Test 3) is shown in Figure 6.7. At  $t = 0.3$  h, water seems to fill the void zones heterogeneously and some water menisci were observed (Figure 6.7a). Note that mean initial water saturation of Test 3 was higher than that of Test 1. Water was moved out of the scanned zone between  $t = 0.3 - 0.8$  h (Figure 6.7b), supposed to form MHs outside of the scanned zone. MHs at grain surfaces and at methane gas/water interfaces (formed already at  $t = 0.8$  h, became more evident at  $t = 2.2$  h in Figure 6.7c) were observed clearly at  $t = 4.3$  h. MHs in form of spikes in Figure 6.7d (at  $t = 4.3$  h) became “crystals” at 6.0 h (Figure 6.7e). It seems that water in at grain contacts was moved for the formation of MHs (in different forms as spikes, “crystals” or layers) at the nearby grain surfaces. It should be noted that the scanned zone before the sample temperature set (at 7 MPa and ambient temperature) was slightly shifted compared to that at  $t = 0.3$  h: Figure 6.8 with similar zones shown in red box. Furthermore, the scan during progressive sample temperature decrease could not be reconstructed efficiently, probably because of sample motion. These phenomena suggest that the sample was slightly re-arranged during the temperature decrease.

MH layer/shell growth at methane gas/water interfaces and at grain surfaces in a local transverse cross-section in the zone Z0\_HR of Test 3 is shown in Figure 6.9. Some water was moved out of this area between  $t = 0.3 - 0.8$  h. MH layers/shells became thicker with time. Interestingly, no MH “crystals” were found in the zone shown here, contrary to what was shown in Figure 6.7. Water and methane hydrate have similar gray levels (brightness), they were again distinguished here on the basis of their morphology evolution thanks to SXRCT scans at high spatial resolution. Once again, it can be supposed that water at grain contacts nearby was moved for the formation of MH layers on grain surfaces.



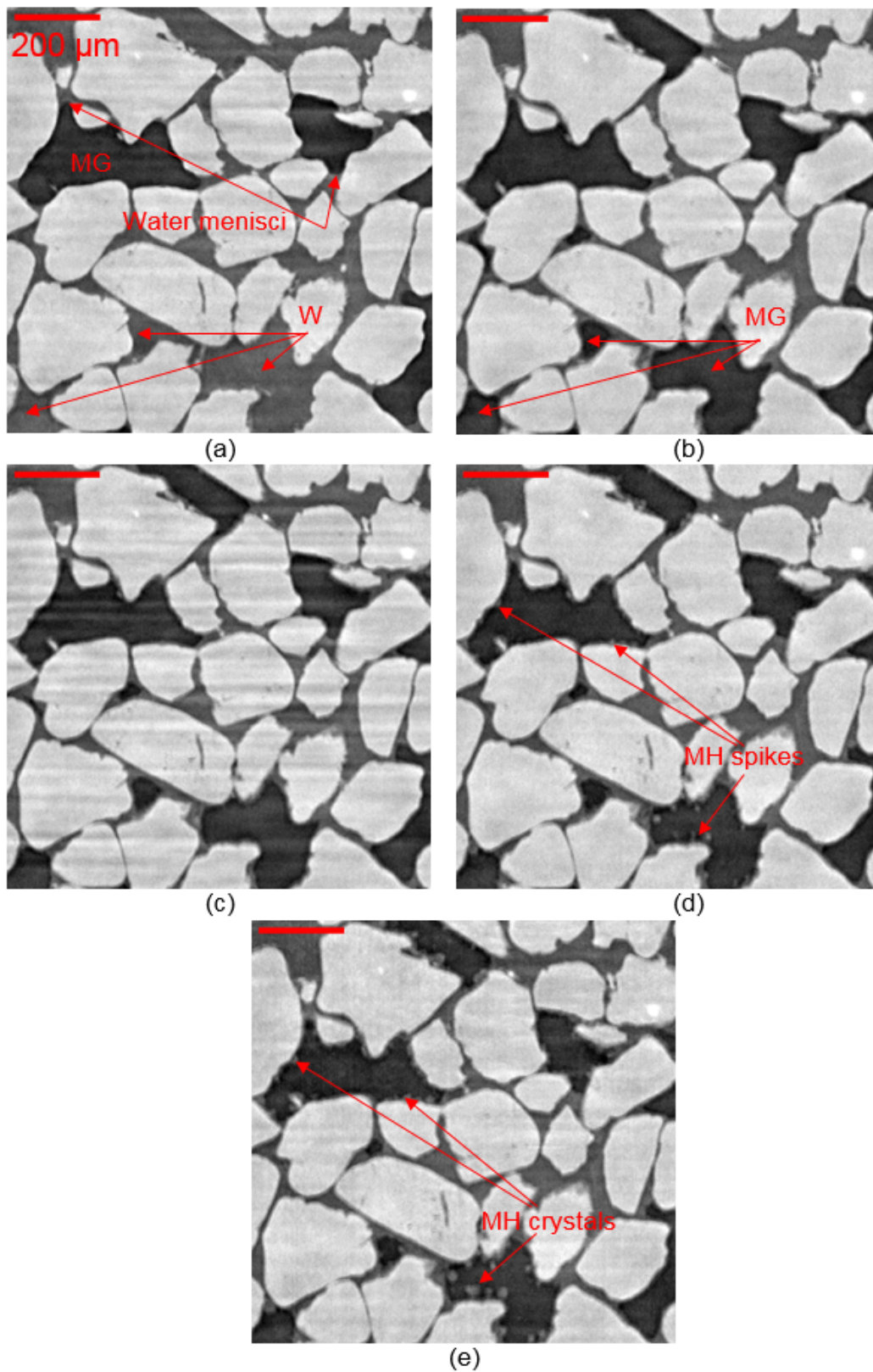


Figure 6.7: Test 3, transverse cross-section through ZO\_HR: (a)  $t = 0.3$  h; (b)  $t = 0.8$  h; (c)  $t = 2.2$  h; (d)  $t = 4.3$  h; (e)  $t = 6.0$  h.

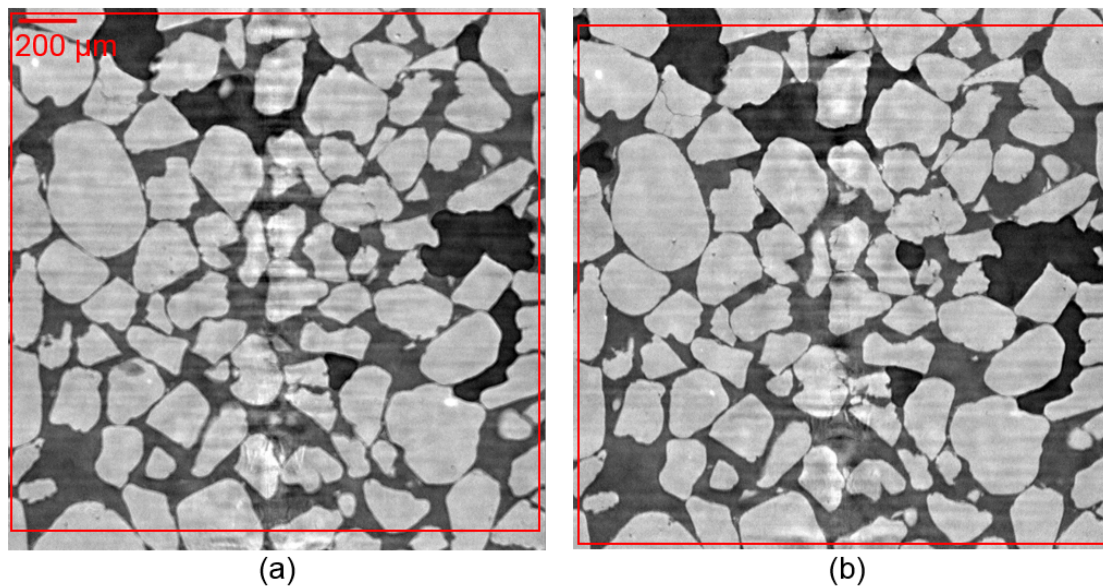


Figure 6.8: Test 3, vertical cross-section through Z0\_HR: (a) Before temperature decrease; (b)  $t = 0.3$  h.

Figure 6.10 shows an example of MH layer growth at grain surfaces and at methane gas/water interfaces in the zone Z1\_HR of Test 3. Some MH spikes could also be observed at grain surfaces (Figure 6.10b).

The kinetics of the MH formation in the zone Z0\_HR of Test 2 from 4 to 22 hours are shown in Figure 6.11. Initial water saturation was quite low in the scanned zone (Figure 6.11a) with some MHs found from  $t = 4.3$  h. Some additional small MH “crystals” and thin MH layers were found at the surfaces of sand grains at  $t = 7.7$  h (Figure 6.11b). At  $t = 11.2$  h, the SXRCT images started to be influenced by ring artifacts. Once the whole image was influenced by the ring artifacts, we checked the PMMA tube and noted that the tube zone subjected to the X-ray projection was damaged (the initially transparent PMMA had become a porous material). Note that in the present experiment, the PMMA tube was fixed during the scans (only the aluminum tube was rotated) so that the same PMMA area had been irradiated during all previous scans and the accumulated irradiation caused damage. The PMMA tube was then manually rotated to avoid that X-rays pass through the damaged zone during the subsequent scans. The image obtained at  $t = 14.6$  h (Figure 6.11d) shows no more ring artifacts. MH layers at methane gas/water interfaces and at grain surfaces were thicker in Figure 6.11e (at  $t = 17.6$  h). In addition, separated MH “crystals” on grain surfaces in Figure 6.11b seem to be connected by MH layers in Figure 6.11e. At  $t = 21.3$  h, the thickness of MH layers was quite homogeneous, in a range of 10 to 20  $\mu\text{m}$  in Figure 6.11f. Furthermore, in some zones, MHs tended to fill the pore space. Interestingly, methane hydrate saturation was much higher than the initial water saturation which evidenced that water was absorbed from other zones to form MHs in this zone. Note that in these 2D images, some MHs appear suspended in the pore space but in a 3D view they are all attached to either methane gas/water interfaces or sand grain surfaces.

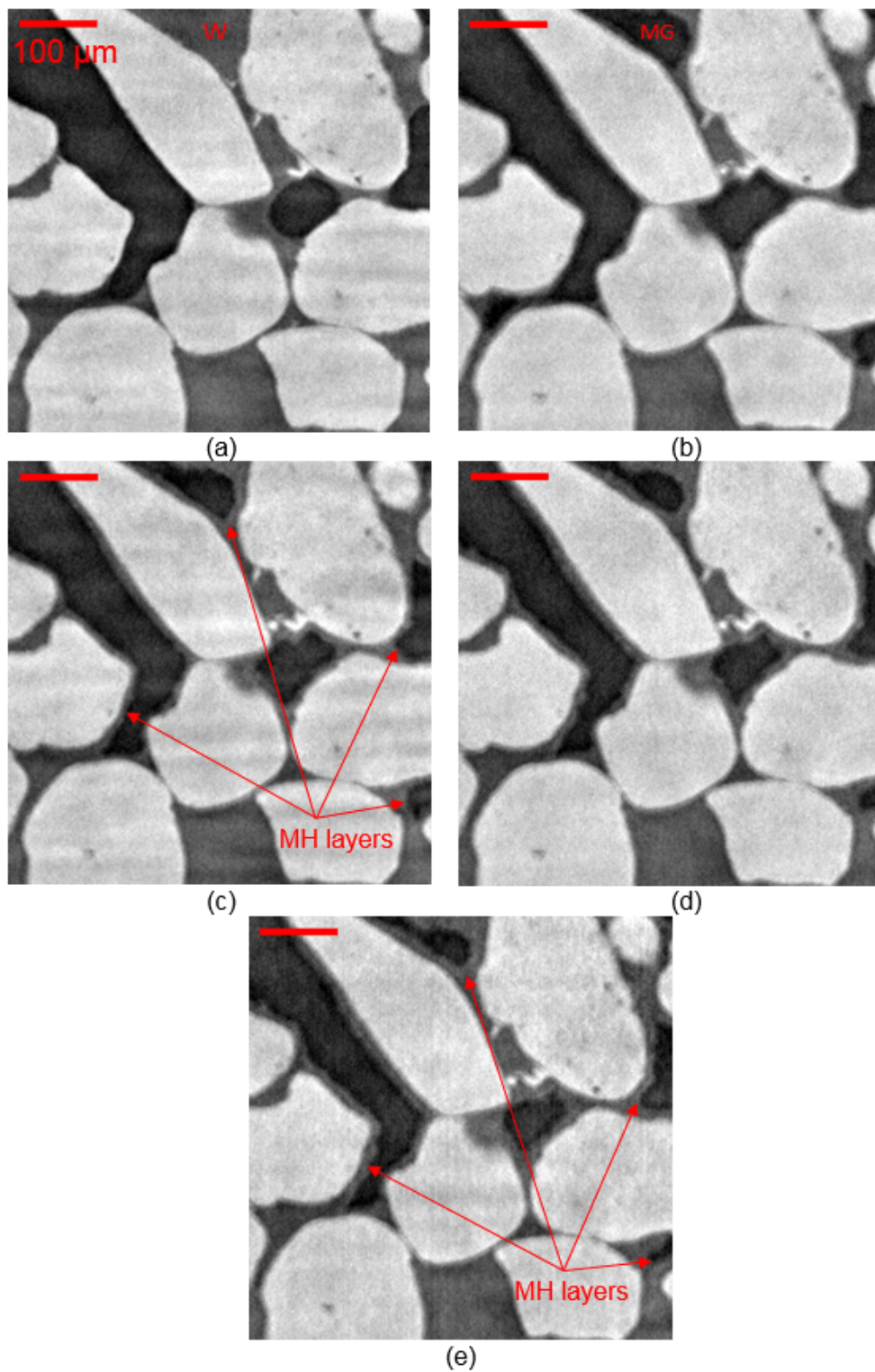


Figure 6.9: Test 3, transverse cross-section through ZO\_HR: (a)  $t = 0.3$  h; (b)  $t = 0.8$  h; (c)  $t = 2.2$  h; (d)  $t = 4.3$  h; (e)  $t = 6.0$  h.

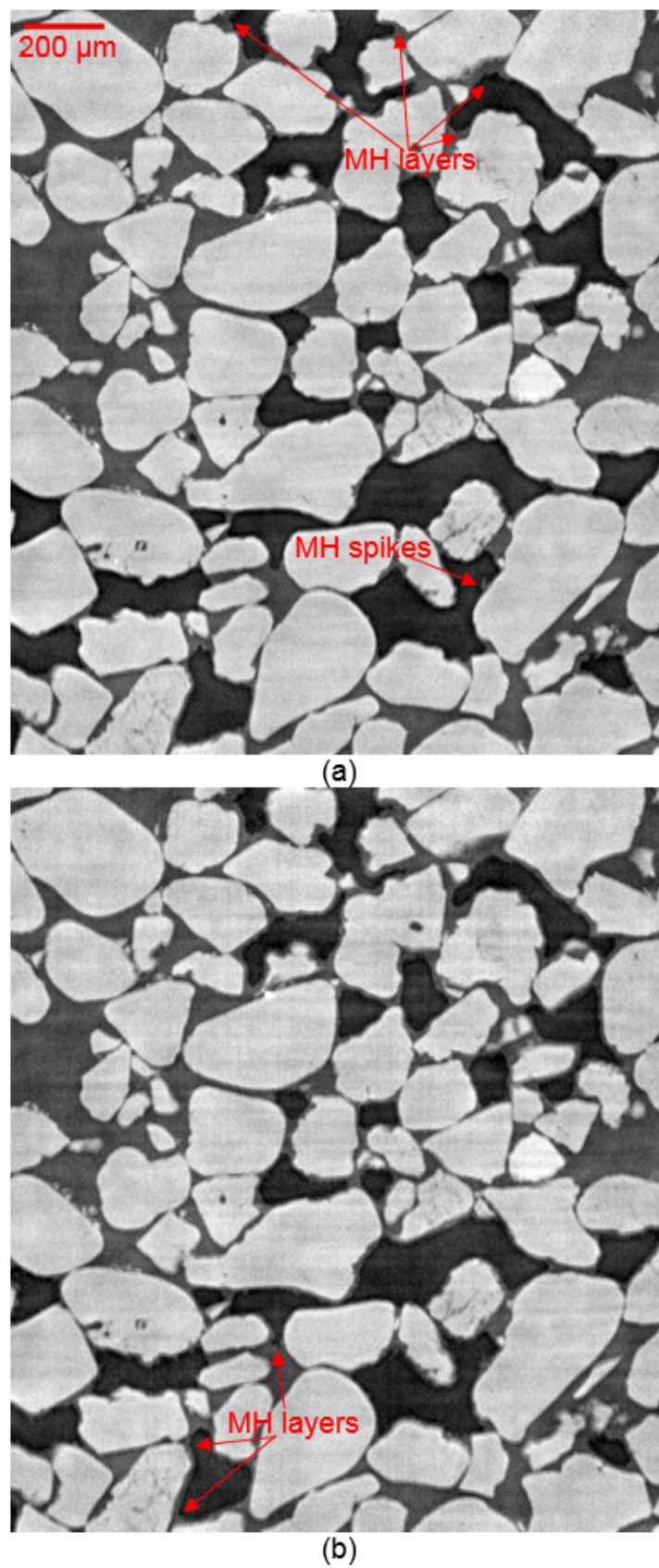


Figure 6.10: Test 3, vertical cross-section through Zl\_HR: (a)  $t = 1.6$  h; (b)  $t = 6.3$  h.

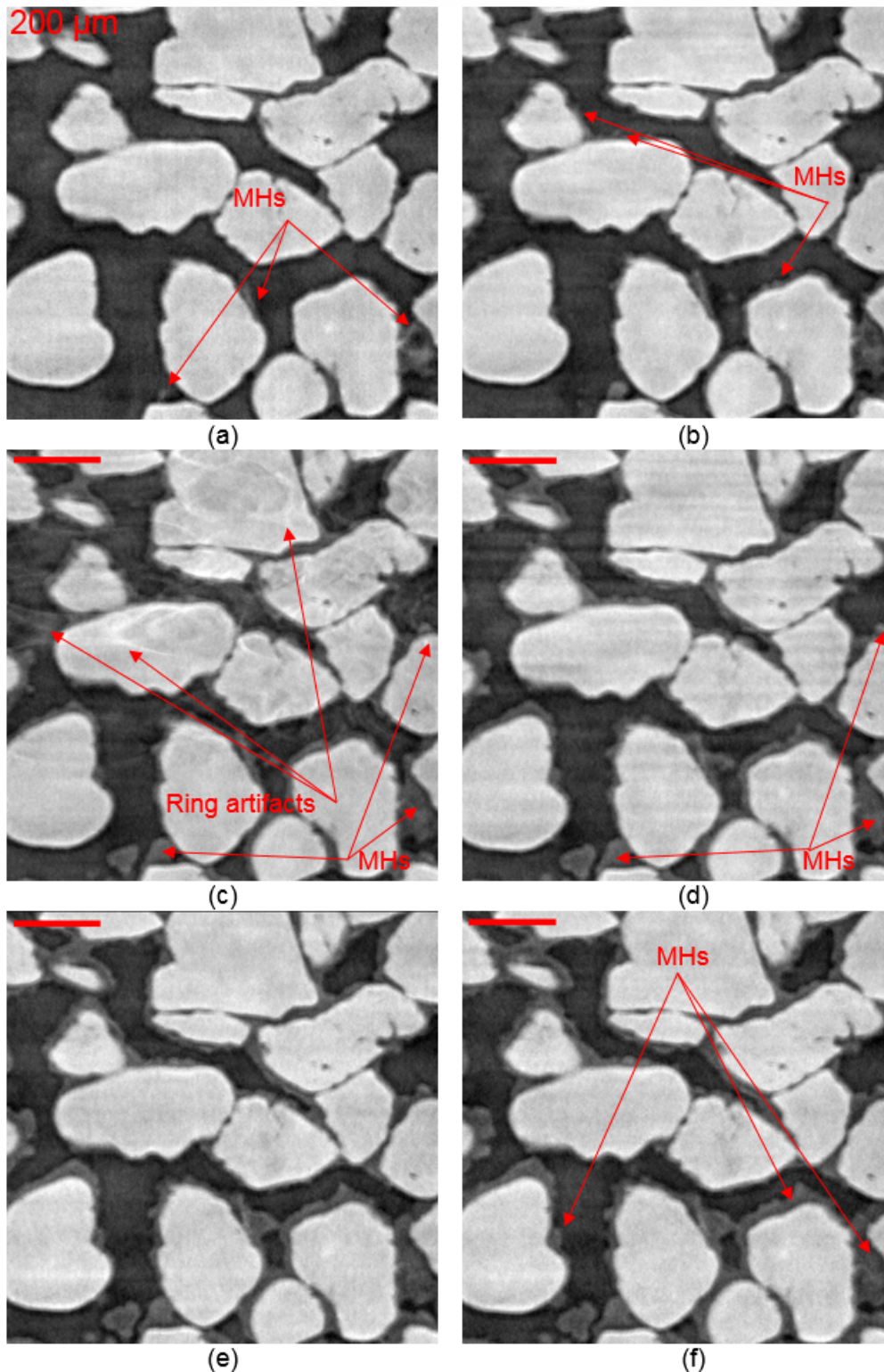
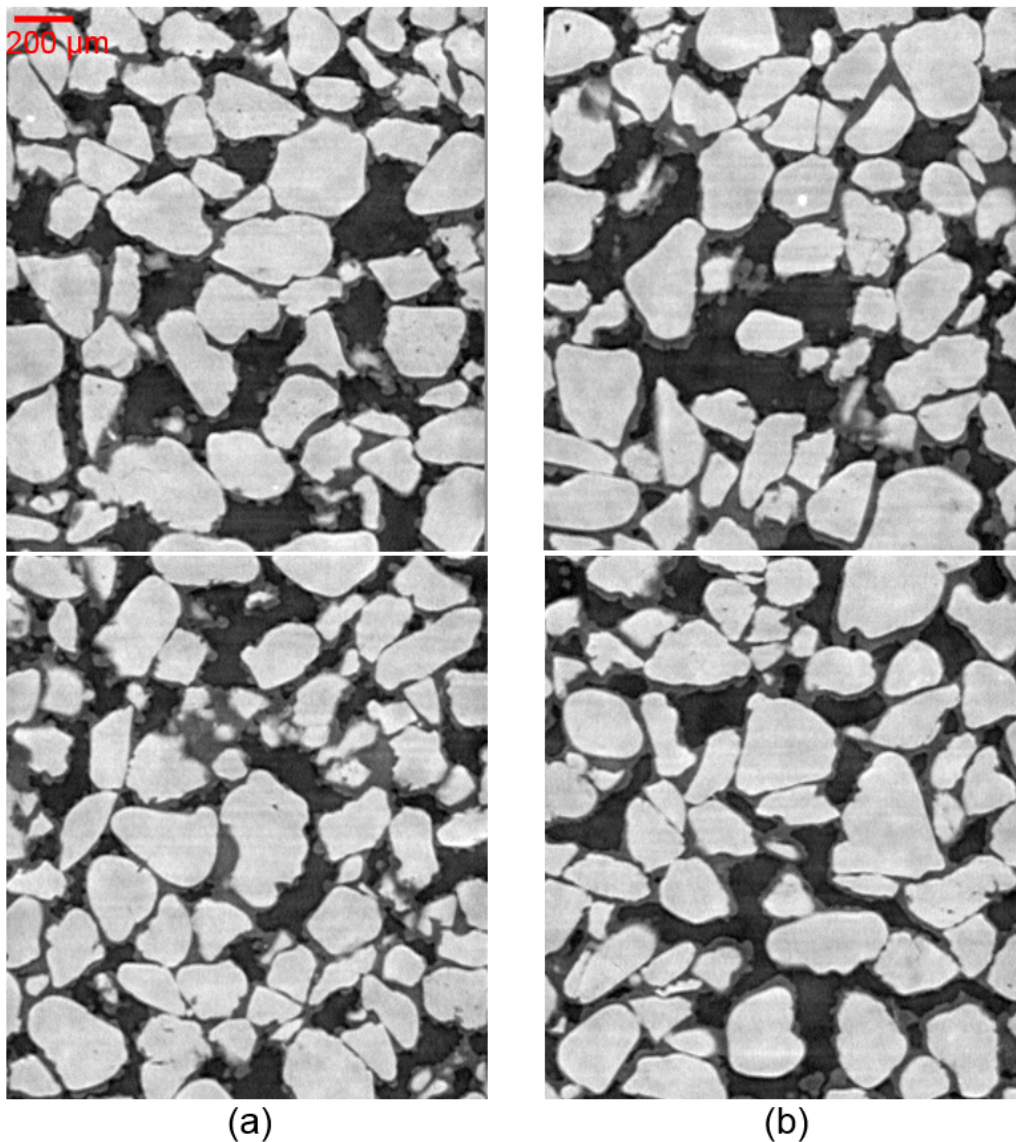


Figure 6.11: Test 2, transverse cross-section through ZO\_HR: (a)  $t = 4.3$  h; (b)  $t = 7.7$  h; (c)  $t = 11.2$  h; (d)  $t = 14.6$  h; (e)  $t = 17.6$  h; (f)  $t = 21.3$  h.

MH distribution along the sample height of Test 2 (zones: Z3\_HR, Z2\_HR, Z1\_HR, and ZO\_HR) is shown in Figure 6.12. Both MH “crystals” and layers were found at grain surfaces and at methane gas/water interfaces. In addition, no MH saturation gradients in

both vertical and horizontal directions were remarked.



*Figure 6.12: Test 2, vertical cross-section through: (a) Z3\_HR at  $t = 18.2$  h and Z2\_HR at  $t = 18.0$  h; (b) Z1\_HR at  $t = 17.8$  h and Z0\_HR at  $t = 17.6$  h.*

Images from the zone Z0\_HR of Test 4 during the firsts 4.5 hours are shown in Figure 6.13. At the beginning of the test (Figure 6.13a), the liquid phase (saline water) was located at the contacts of sand grains because of the capillary suction. Menisci at the interfaces between the liquid phase and the gas phase can be easily identified. At 0.6 h after the application of MH formation conditions, methane hydrates were already formed (Figure 6.13b). MH spikes at grain surfaces and methane gas/saline water interfaces can be well distinguished from saline water while MH layers (which might have been already formed at grain surfaces and at methane gas/saline water interfaces) could not be clearly observed due to both their thin thickness and the partial volume effect. Similar to Test 3 (shown in Figure 6.7), the volume of liquid at grain contacts in Figure 6.13b was significantly reduced compared to that shown in Figure 6.13a. On the one hand, that could be

explained by the MH formation in the other zones (outside of the observed one) which absorbed water of the observed zone. On the other hand, the small “crystals”/spikes of MHs found at grain surfaces and at the interfaces of methane gas/saline water could have taken a part of the water. Figure 6.13c and Figure 6.13d show MH morphologies and pore habits over the zone Z0\_HR at  $t = 4.0$  and  $4.5$  h, respectively. MH spikes and layers became bigger and thicker over time at grain surfaces and at methane gas/saline water interfaces (compared to the Z0\_HR zone at  $t = 0.6$  h).

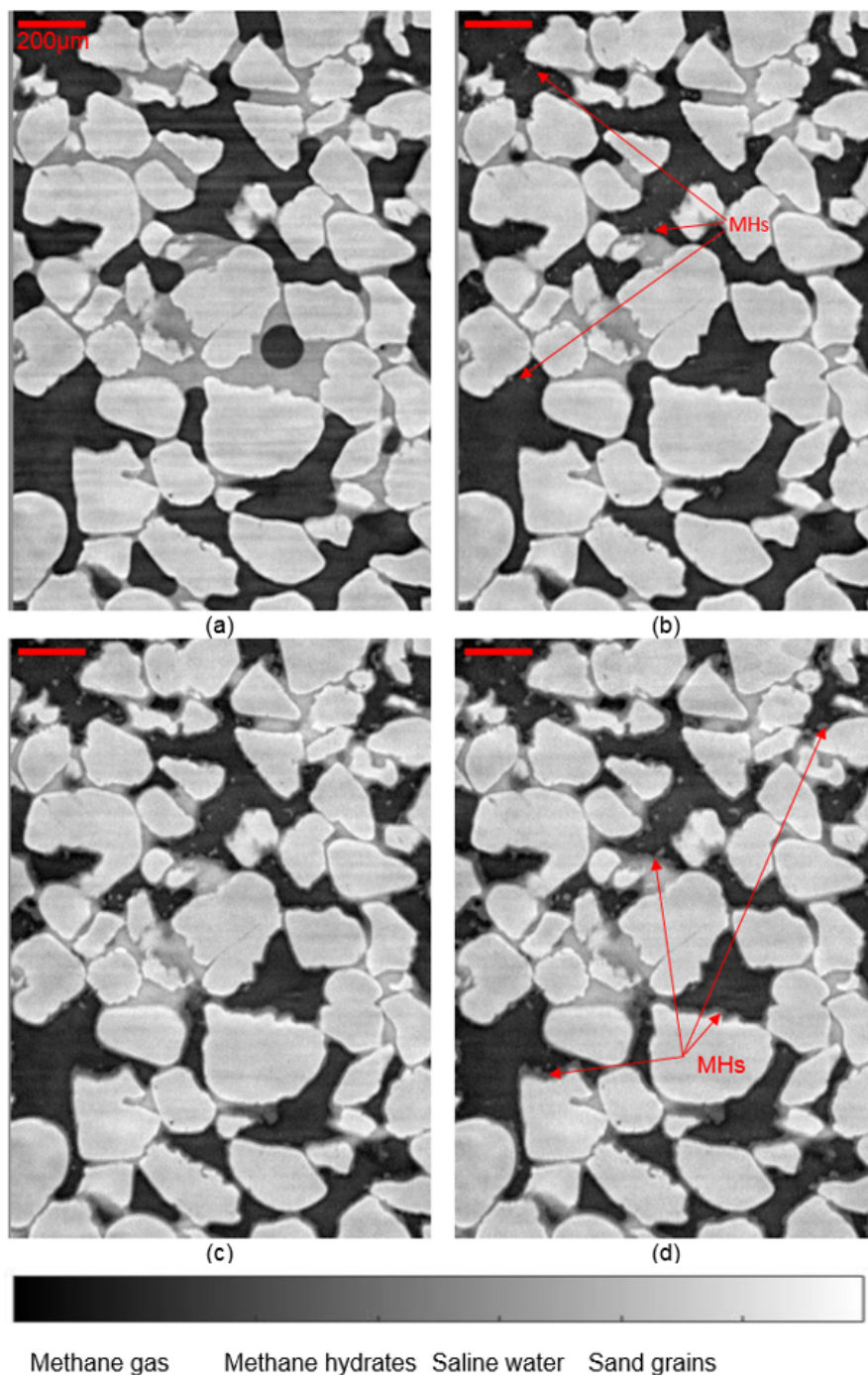


Figure 6.13: Test 4, vertical cross-section through Z0\_HR: (a)  $t = 0$  h; (b)  $t = 0.6$  h; (c)  $t = 4.0$  h; (d)  $t = 4.5$  h.

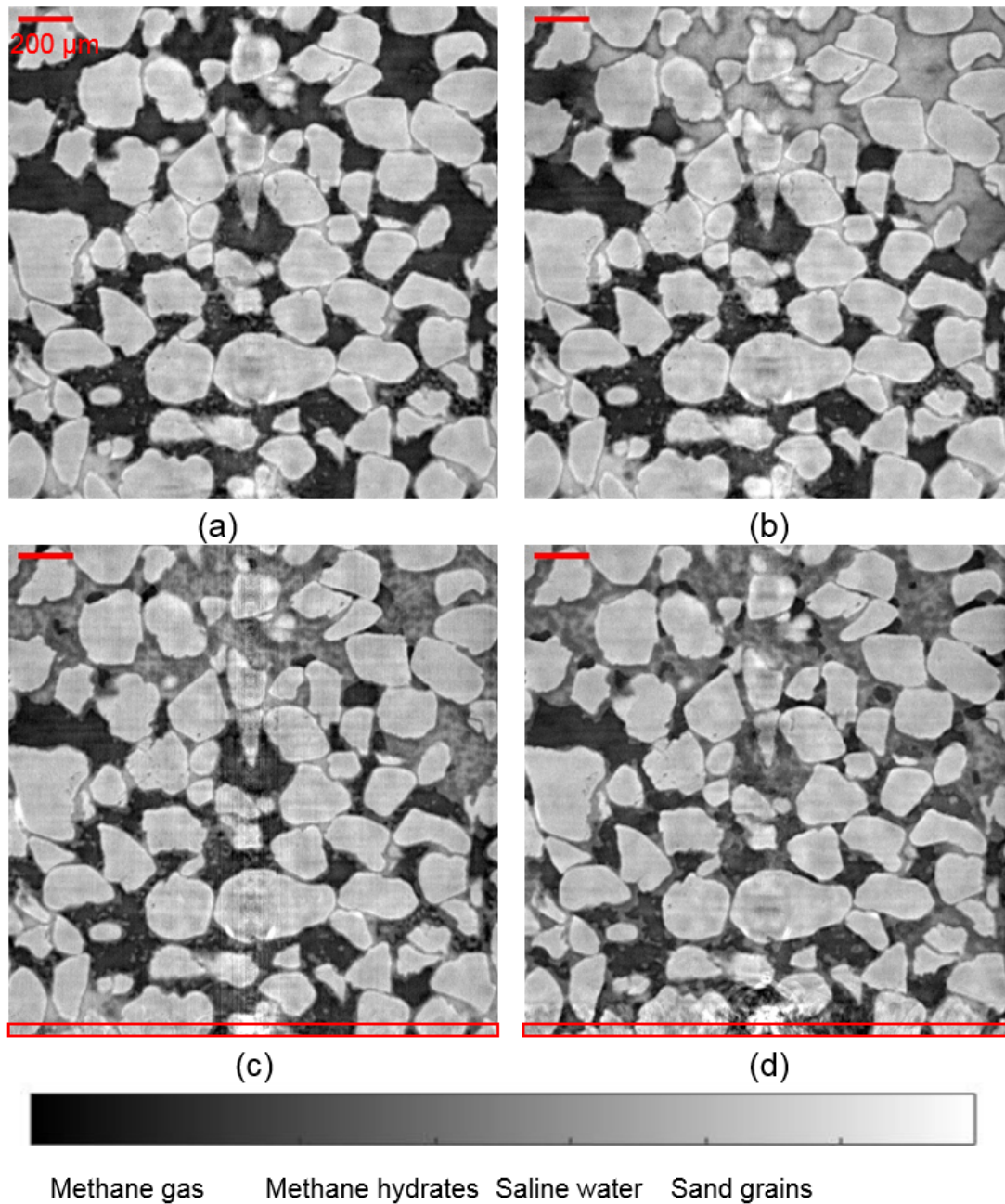


Figure 6.14: Test 4, vertical cross-section through Z1\_HR: (a)  $t = 3.8$  h; (b)  $t = 4.3$  h; (c)  $t = 8.0$  h; (d)  $t = 12.4$  h.

Images of the zone Z1\_HR of Test 4 (at  $t = 3.8, 4.3, 8.0$  and  $12.4$  h) are shown in Figure 6.14. At  $t = 3.8$  h (Figure 6.14a), MH “crystals”/spikes and layers can be observed at grain surfaces and at methane gas/saline water interfaces. However, it seems that water saturation was lower than the mean initial water saturation (i.e. 60 %). At  $t = 4.3$  h, saline water invaded the pore space on the top of the image while MHs in the other zones were not changed (Figure 6.14b). At  $t = 8.0$  h (Figure 6.14c), on the top of the image, MHs were formed inside the pore space filled with saline water (pore-filling habit). Actually, the gray level of these zones changed from a bright level (corresponding to saline water) to a darker gray level (corresponding to MH). In the other zones of the image where pore



spaces were filled with methane gas, MHs continued to grow (compared to the image at  $t = 4.3$  h, Figure 6.14b). It was observed that, from 8 h, the common zone of Z0\_HR and Z1\_HR (the red box in Figure 6.14c and Figure 6.14d) where the irradiation of the PMMA tube might be more intense, was influenced by ring artifacts. MHs continued to grow in the zone Z1\_HR from 8.0 to 12.4 h (Figure 6.14c and Figure 6.14d).

The growth of MH “crystals” and layers at grain surfaces and at methane gas/saline water interfaces over the zone Z0\_HR of Test 4 can be better observed with grain-scale images in Figure 6.15. Small MH spikes were formed at grain surfaces at  $t = 0.6$  h (Figure 6.15a). After being extended (Figure 6.15b), they were enlarged and became like-crystals (Figure 6.15e). MH layers, formed at methane gas/saline water interfaces and at grain surfaces, were clearly found in Figure 6.15b (at  $t = 2.3$  h) and became thicker over time (Figure 6.15c,d,e). The results show that MH layers were formed at the methane gas/saline water interfaces but saline water still existed at  $t = 10.3$  h (Figure 6.15e). The methane hydrate formation from KI water solution induces an increase in KI concentration in the remaining water so that the brightness of the remaining water in the image was increased during the methane hydrate formation. This concentration increase can also hinder further methane hydrate formation.

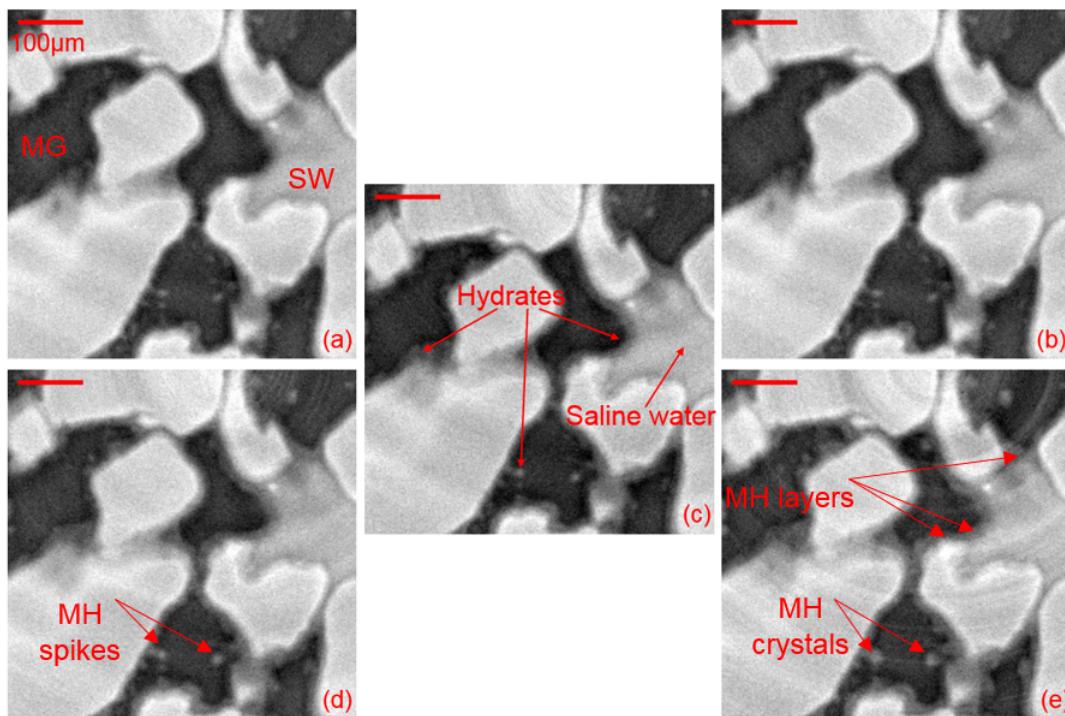


Figure 6.15: Test 4, detail transverse cross-section through Z0\_HR: (a)  $t = 0.6$  h; (b)  $t = 2.3$  h; (c)  $t = 4.3$  h; (d)  $t = 6.5$  h; (e)  $t = 10.3$  h.

Figure 6.16 shows images over the zone Z0\_HR of Test 4 at  $t = 12.2$ , 13.4 and 16.3 h. At  $t = 12.2$  h (Figure 6.16a), MHs can be observed but the whole image was influenced by the ring artifacts. Similarly to Test 2, the zone of the PMMA tube irradiated by the X-ray beam was damaged. The PMMA tube was manually rotated to avoid the crossing of X-rays through the damaged zone during the subsequent scans. The image obtained at

$t = 13.6$  h (Figure 6.16b) shows no more ring artifacts. However, the quantity of MHs and water was significantly reduced compared to that at  $t = 12.2$  h. This trend was confirmed by the image obtained at  $t = 16.3$  h (Figure 6.16c) where MHs can be no longer observed in this zone. Only a small quantity of water remained at grain contacts.

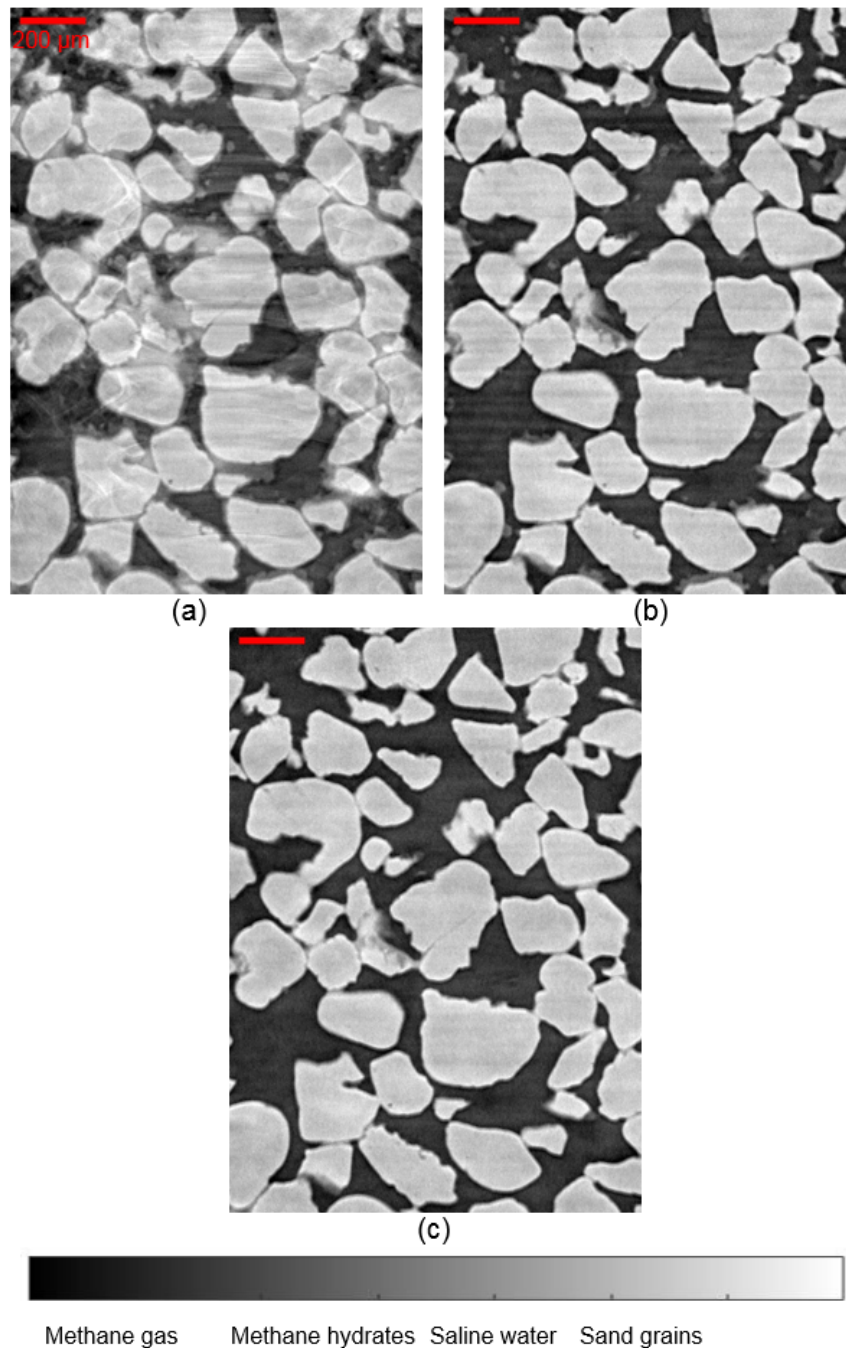


Figure 6.16: Test 4, vertical cross-section through Z0\_HR: (a)  $t = 12.2$  h; (b)  $t = 13.4$  h; (c)  $t = 16.3$  h.

The results obtained in the zone Z1\_HR at  $t = 13.6$  and  $16.5$  h of Test 4 are shown in Figure 6.17. The ring artifacts observed at  $t = 12.4$  h (Figure 6.14d) were no longer be present at  $t = 13.6$  h (Figure 6.17a). Furthermore, the quantity of MHs and water

seems to decrease at the zone bottom similarly to what was observed in the zone H0\_HR Figure 6.16. The reduction trend can be confirmed by the image obtained at  $t = 16.5$  h where MHs could no longer be observed in the lower half part of the image (Figure 6.17b). Furthermore, as in the Z0\_HR zone shown in Figure 6.16b, only a small quantity of saline water was found at grain contacts on the bottom of this zone. It seems that MHs under excess-water conditions at the top part of the image were more stable than MHs under excess-gas conditions at the bottom part of the image.

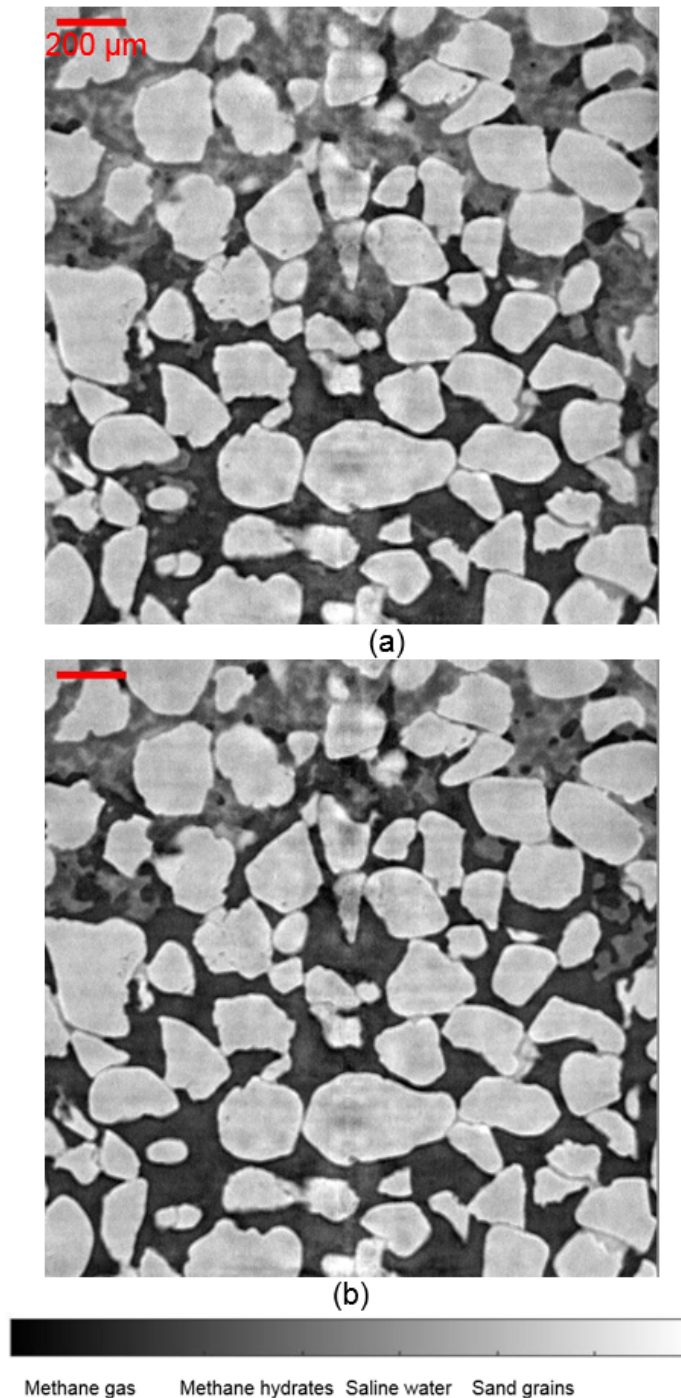


Figure 6.17: Test 4, vertical cross-section through Z1\_HR: (a)  $t = 13.6$  h; (b)  $t = 16.5$  h.

For a better understanding of the observed results, which suggest a strong macroscopic heterogeneity of MH volume fraction in the sample, scans at lower resolution (voxel size:  $1.8 \mu\text{m}$ ) were used to enlarge the size of the investigated area. Furthermore, due to the limited beamline time, the scanned zone was double in height by skipping scans of intermediate heights, shown in Figure 6.1. Larger scanned zone was 1.75 mm in height (limited by X-ray beam height) and 3.47 mm in diameter for each scan. These scans were performed along the sample (290 mm in height in total, from Z-7 to Z9, see Figure 6.1 and Figure 6.5).

Figure 6.18 shows the images (at low resolution) obtained in the zone Z-1 ( $t = 19.2$  h), Z0 ( $t = 21.5$  h) and Z1 ( $t = 19.5$  h). The results obtained in the common zone of the three scans showed that MHs and water did not change significantly during these scans. For this reason, the images were merged into a bigger image of 3.47 mm in width and 5.15 mm in height. The red box corresponds to the zones Z0\_HR and Z1\_HR scanned at high resolution previously. It is obvious that, in the center zone (i.e. the top of the zone Z-1\_HR, the whole zone Z0\_HR and the bottom of the zone Z1\_HR), no hydrates were present and saline water quantity was really small. Both MHs and saline water in larger amount were found in the periphery zone. Furthermore, it seems that the top of zone Z1 and the bottom of the zone Z-1 have similar pore space distribution (MHs were mixed with saline water with some methane gas pockets). However, MH quantity was higher on the top of the zone Z1 compared to that on the bottom of the zone Z-1 which contained more saline water. Note that a slight ring artifact was found in the center of the images.

Figure 6.19 shows the images obtained in the zones Z-3, Z-5 and Z-7. The medium was still under gas-saturated conditions. MHs were found in form of “crystals” and layers around sand surfaces and at interfaces of methane gas/saline water. In some areas saturated with saline water (in the zones Z-3 and Z-5), some round MH particles were found.

Images of the zones Z3, Z5, Z7 and Z9 are shown in Figure 6.20. It seems that methane gas, methane hydrates and saline water were mixed in the pore space of all these zones.

As aforementioned in subsection 6.2.2, in order to mimic natural methane hydrate-bearing sand in saline water saturated media, at the end of the MH formation of Test 1, excess-methane-gas was replaced by saline water (KI, 3.5 wt%) at 7 MPa. Figure 6.21 shows an example of image obtained after the injection of saline water. Unfortunately, it seems that all MHs were dissociated. It is supposed that the medium was composed of only sand grains and methane gas. Water released after the MH dissociation seems to move out of the scanned zones. Furthermore, saline water has not arrived to these zones yet. Note that the methane gas/saline water inlet was on the bottom of the cell (Figure 6.1) while the scanned zone was on the top of the aluminum tube. In addition, injected saline water was at ambient temperature.

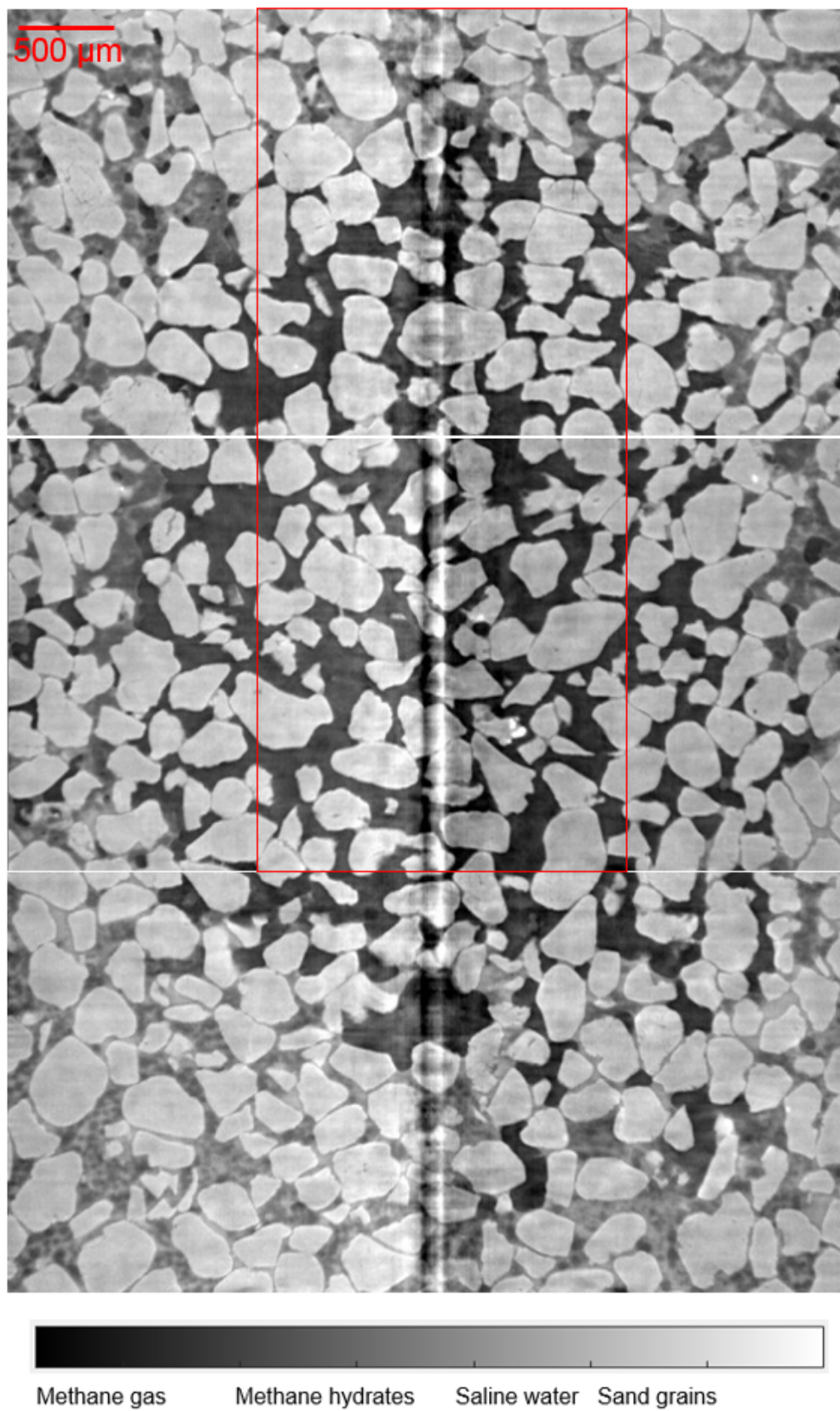


Figure 6.18: Test 4, vertical cross-section through: (a) Z1\_LR,  $t = 19.5$  h; (b) Z0\_LR,  $t = 19.5$  h; (c) Z-1\_LR,  $t = 19.2$  h.

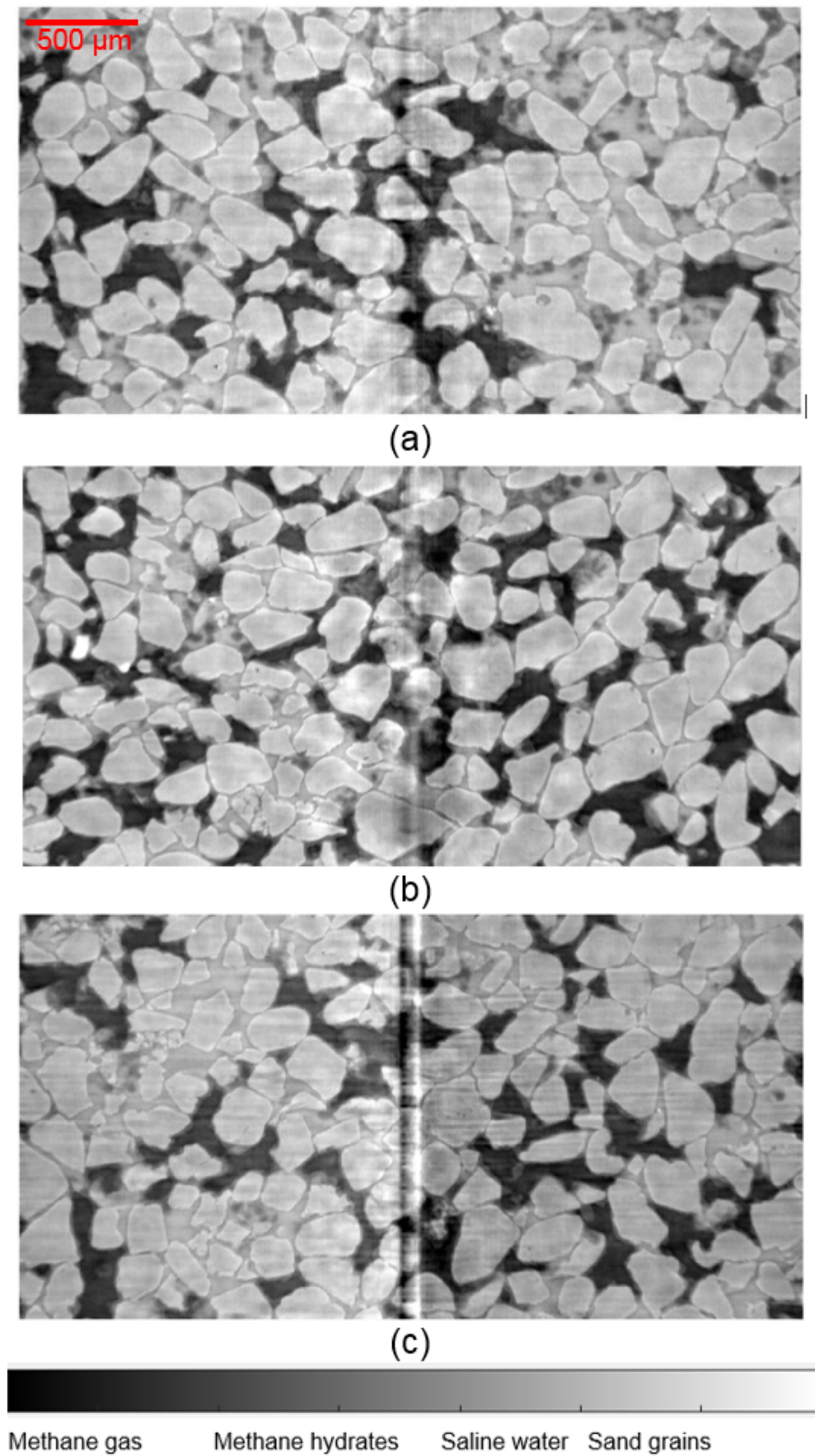


Figure 6.19: Test 4, vertical cross-section through: (a) Z-3 LR,  $t = 19.0$  h; (b) Z-5 LR,  $t = 18.8$  h; (c) Z-7 LR,  $t = 18.5$  h.

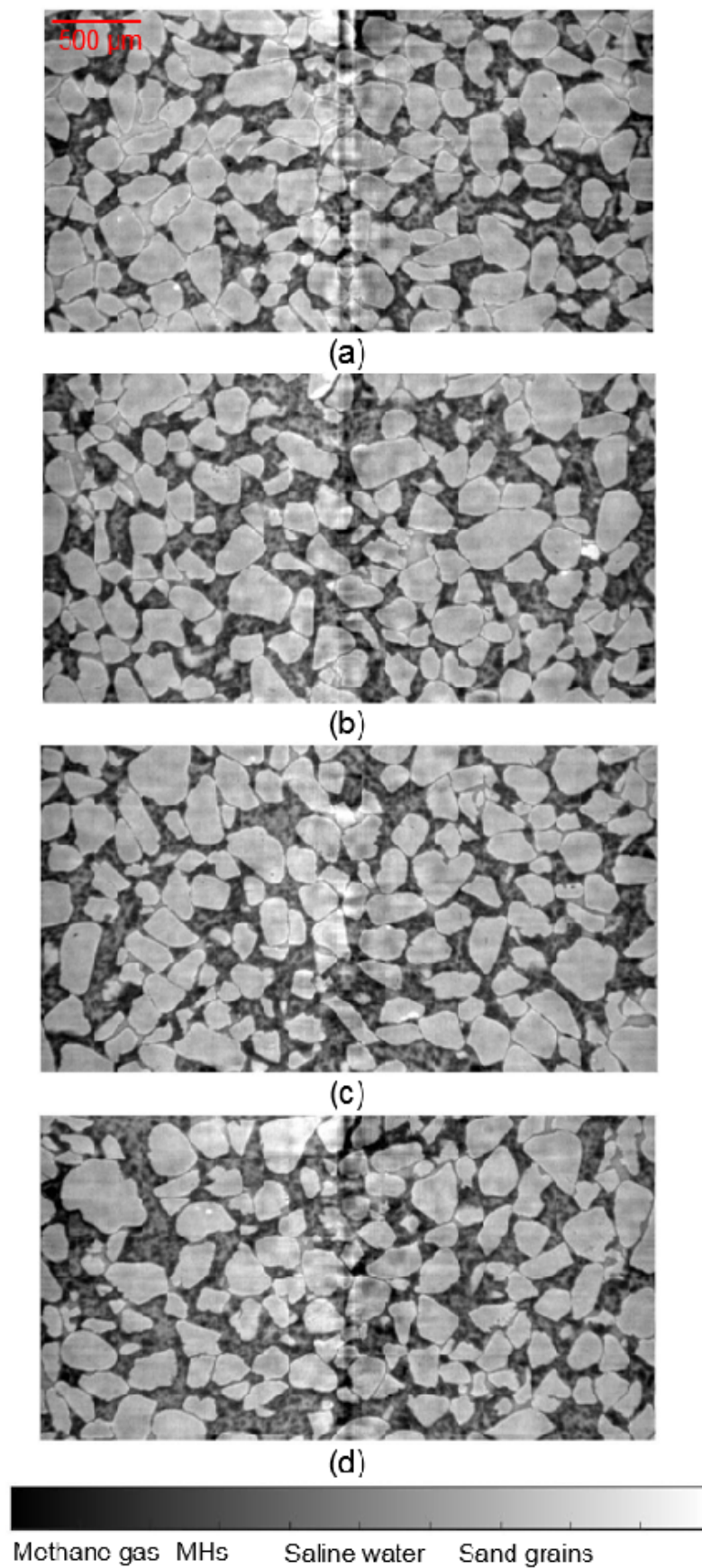
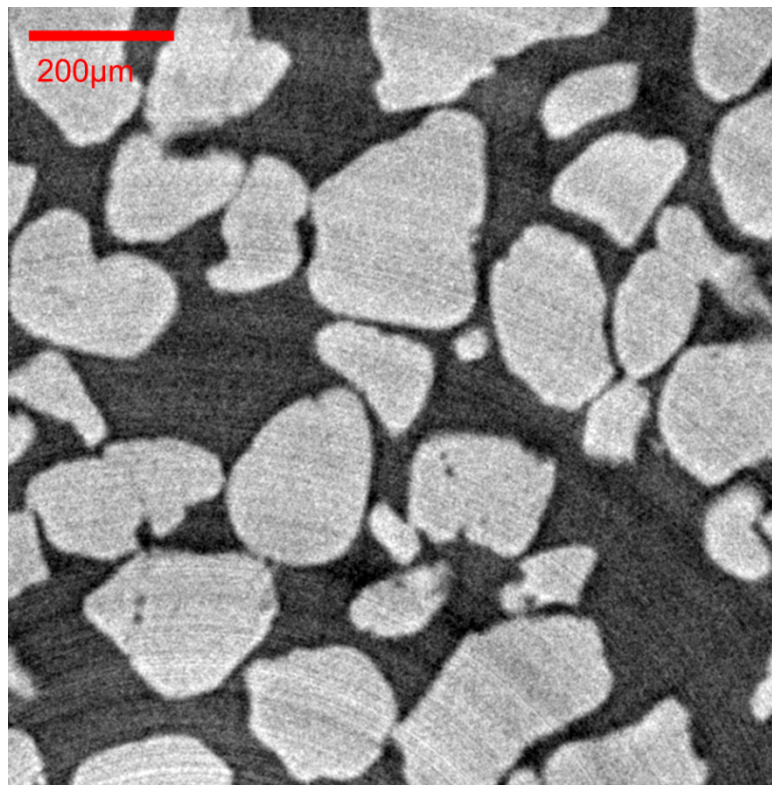


Figure 6.20: Test 4, vertical cross-section through: (a) Z9\_LR,  $t = 20.5$  h; (b) Z7\_LR,  $t = 20.2$  h; (c) Z5\_LR,  $t = 20$  h; (d) Z3\_LR,  $t = 19.7$  h.



*Figure 6.21: Test 1: a transverse cross-section obtained after the injection of saline water.*

### 6.3.2 MH morphologies and pore habits

Figure 6.22 shows MH morphologies and pore habits in sandy sediments under excess-gas conditions corresponding to various MH saturations of Test 1 and Test 2. Separated MH “crystals” or MH “crystals” connected via thin MH layers were found on sand grain surfaces and at contacts of grains at low methane hydrate saturation (Figure 6.22a,c). At higher methane hydrate saturation, MH “crystals” connected via MH layers and thicker MH layers were observed on almost all grain surfaces (Figure 6.22b, d). Interestingly, at high methane hydrate saturation, pore space seems to be filled with MHs. As aforementioned, CT images alone cannot differentiate water from methane hydrate therefore it is not guaranteed that all slight gray areas in Figure 6.22 are methane hydrates.

Different methane hydrate morphologies, formed at (8 MPa, -16 °C) and (8 MPa, 2 °C) respectively, observed by optical microscopy (Test 5 and 6), are shown in Figure 6.23, Figure 6.24 and Figure 6.25. MH spikes having similar diameter (of around 3  $\mu\text{m}$ ) can be clearly observed on grain surfaces at different sample zones of Test 5 (Figure 6.23). However, it seems that MH spikes in Figure 6.23b were longer than that shown in Figure 6.23a. Figure 6.24 confirms that MH spikes were formed at the methane gas side while at the water side they were in form of needles. Furthermore, MH “crystals”/spikes/layers were also observed at different sample zones of Test 6 (Figure 6.25). These results confirm the presence of MH spikes, “crystals”, layers observed by SXRCT at a lower spatial resolution.



Figure 6.26 shows some examples of images showing various MH morphologies and pore habits in saline water media (Test 4). Their corresponding gray level histograms are shown in Figure 6.27. Note that gray level ranges for the four phases in Figure 6.27 (real 32 bit images) overlap to take into account the partial volume effect and image noise. Furthermore, maximum grain count value of each image was normalized to 1. The images and their corresponding gray level histograms confirmed that MHs were in gas saturated media in Figure 6.26a; under saline-water-excess conditions with some methane gas bubbles in Figure 6.26b and in saline water saturated media in Figure 6.26c. MHs were found in form of angular “crystals” or layers at grain surfaces and at methane gas/saline water interfaces in gas saturated areas in Figure 6.26a. They mainly took form of round particles floating in saline water in excess-saline-water areas in Figure 6.26a, Figure 6.26b and in the whole Figure 6.26c. It seems that round MH particles of 20-30  $\mu\text{m}$  were found mixed heterogeneously with saline water to create saline water saturated zones (pore-filling/load-bearing habit).

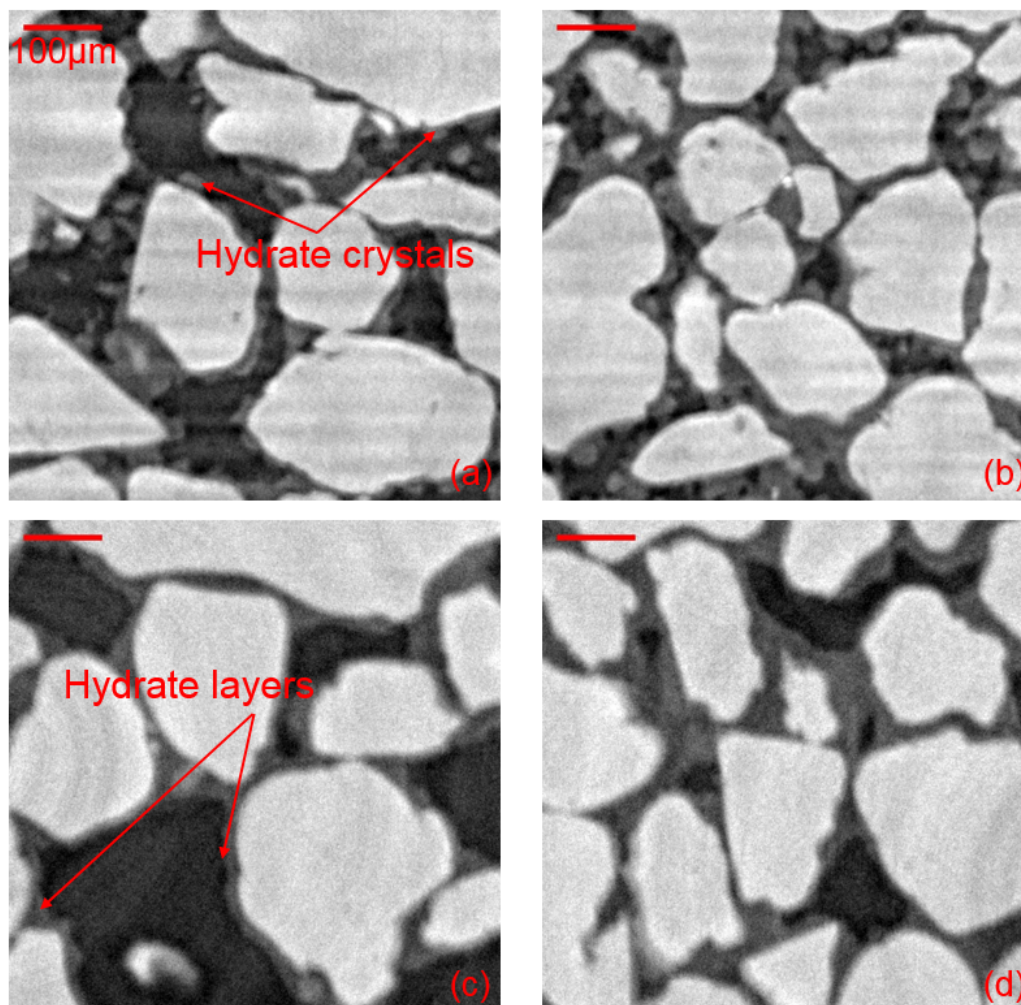
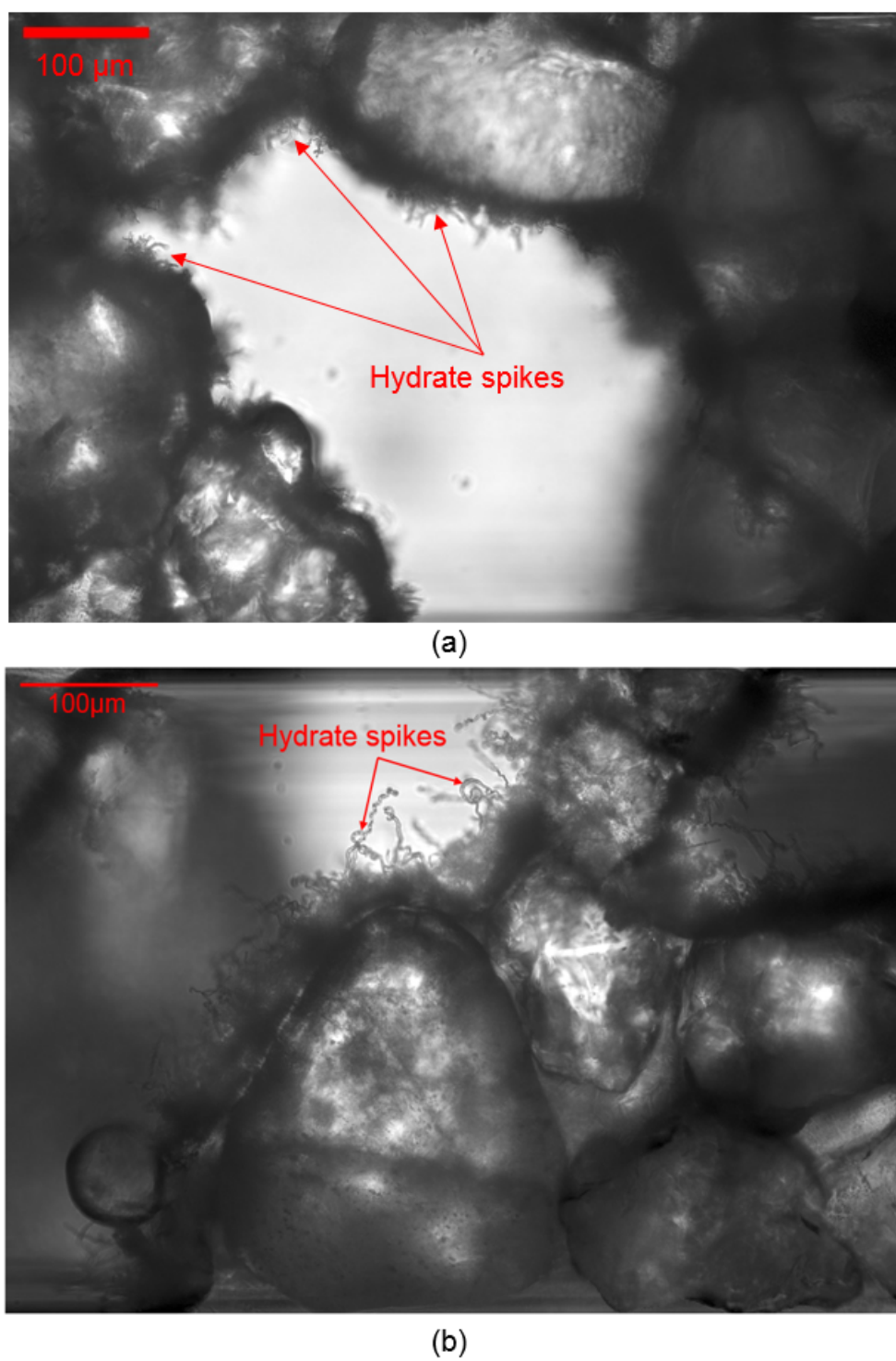


Figure 6.22: Test 1 and Test 2, MH morphologies and pore habits under excess-gas conditions: (a), (c) Test 1, Z5\_HR at 18.1 h; (a), (c) Test 2, Z0\_HR at 22.7 h.



*Figure 6.23: Test 5: Methane hydrate spike grow on the grain surfaces, observed by optical microscopy.*

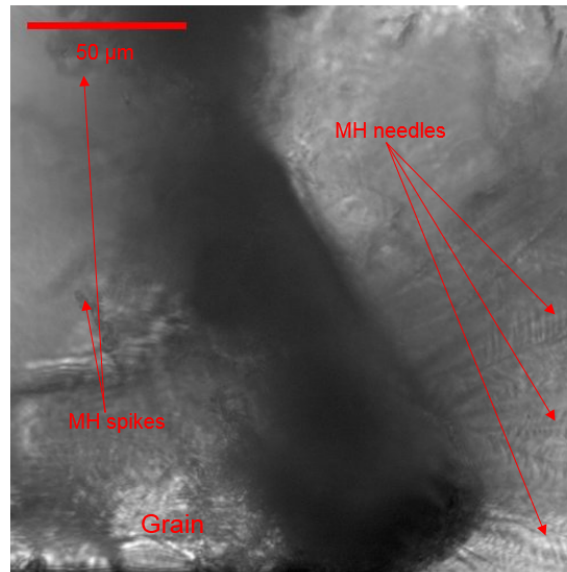


Figure 6.24: Test 5: Different MH morphologies in methane gas and water sides observed by optical microscopy.

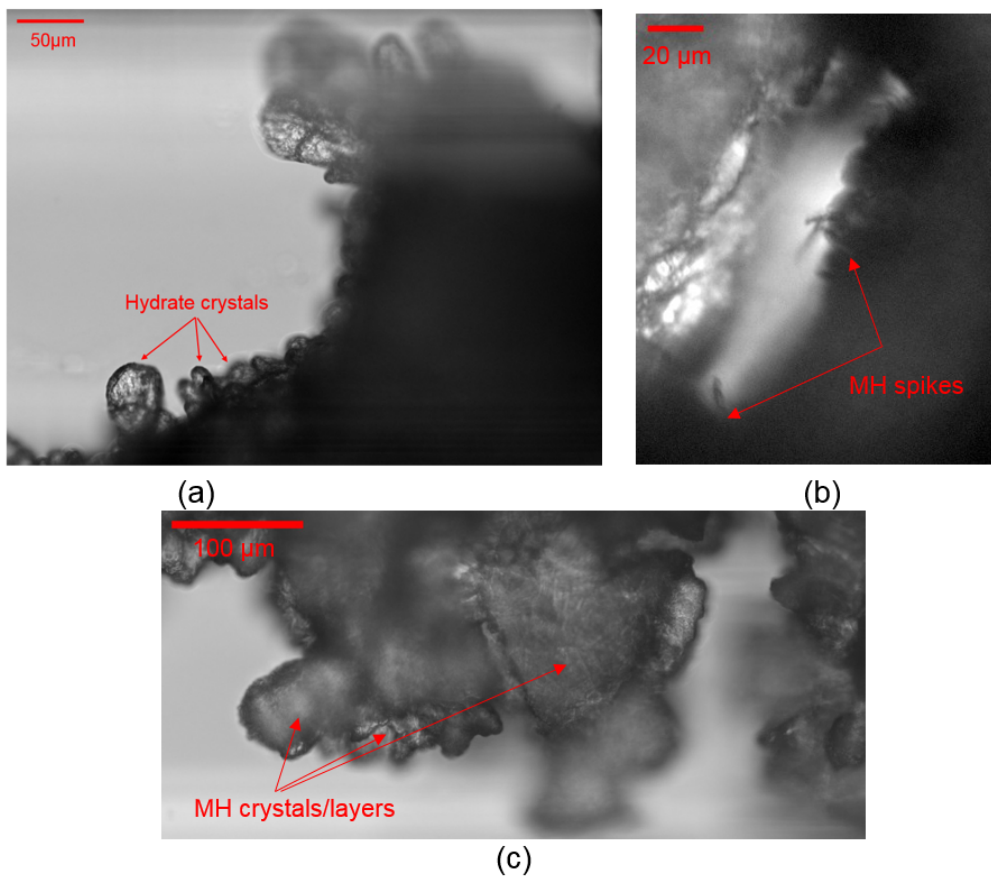
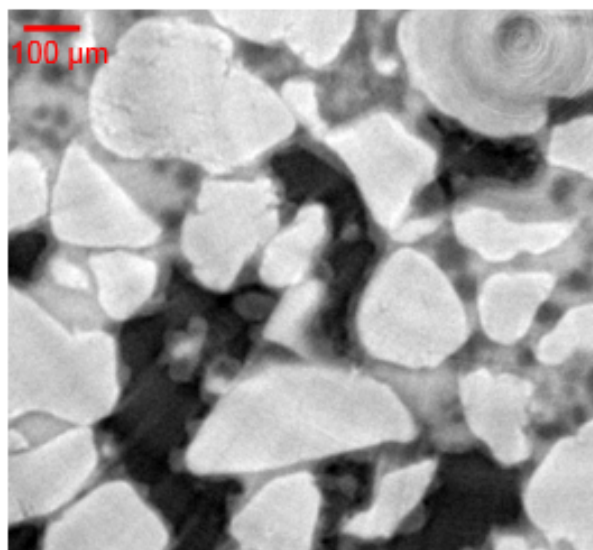
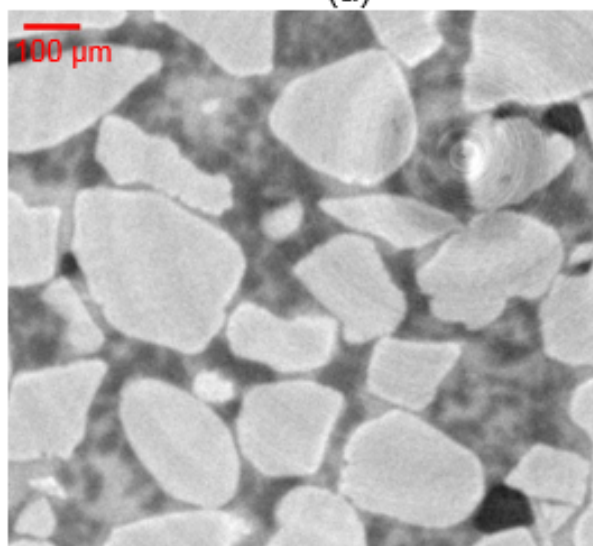


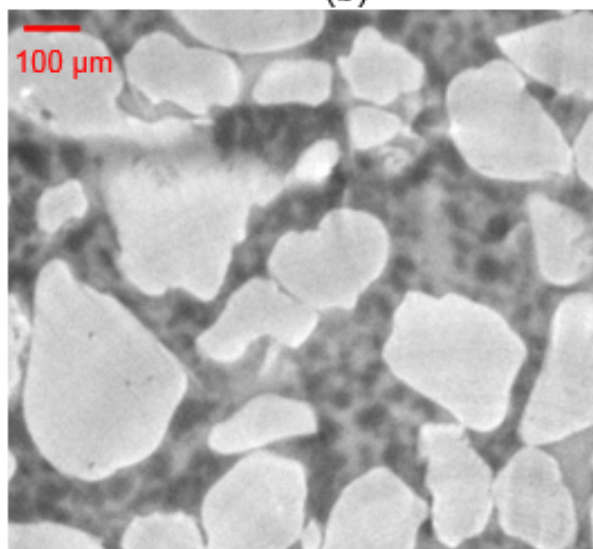
Figure 6.25: Test 6: Different MH morphologies: (a) “crystals”; (b) spikes; (c) layers, formed on grain surfaces, observed by optical microscopy.



(a)



(b)



(c)

Figure 6.26: Test 4, Possible MH morphologies and pore habits in saline water media:  
(a) Z-3 ( $t = 19$  h); (b) Z1 ( $t = 19.5$  h); (c) Z-1 ( $t = 19.2$  h).

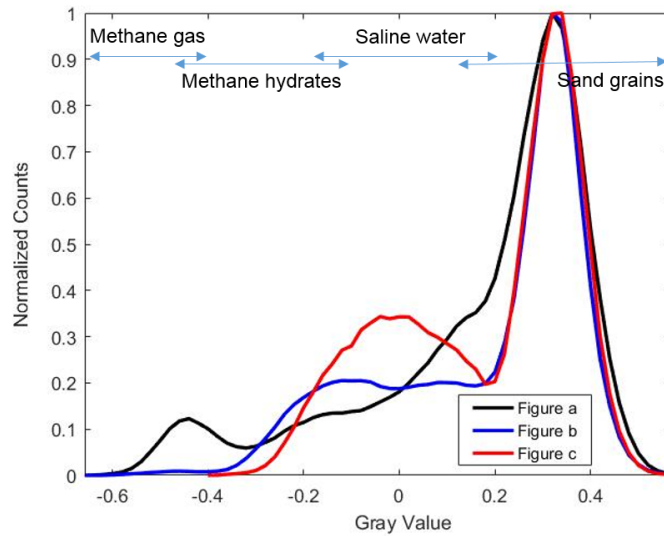


Figure 6.27: Test 4, Normalized Histogram of Figure 6.26 (a, b, c).

## 6.4 Conclusions

Methane hydrate-bearing sand was created first by pressurizing methane gas (at 7 MPa) then by decreasing sample temperature (following the excess-gas method). Four tests (three with tap water and one with saline water, KI 3.5 wt%) have been performed and followed by SXRCT scans. Furthermore, two MH formation tests at (8 MPa, -16 °C) and (8 MPa, 2 °C) were observed by optical microscopy. The following conclusions can be drawn:

- Water, found initially at menisci at grain contacts of unsaturated sand, was moved to form MHs on the nearby not wetted grain surfaces (local water migrations). Furthermore, water could be moved progressively or suddenly from one to another zone in the sample during MH formation (global water migrations);
- Under excess-gas conditions, different MH morphologies (e.g. spikes, “crystals”, layers/shells) could co-exist on grain surfaces and at contacts of grains (initially at methane gas/water interfaces). MHs tended to fill the pore space of areas with high MH saturation. In addition, MH spikes (at the methane gas side) could become “crystals” over time provided that water was supplied for further MH formation;
- Under excess-saline-water conditions, round MH particles were found floating in saline water in the pore space of the media;
- Multiple global water migrations could modify MH morphologies and pore habits in the pore space. The MH distribution was heterogeneous at the grain scale as well as at the sample scale.

# 7 Discussions

## 7.1 Introduction

In this chapter, we discuss about the MH formation and its effects on the mechanical properties of synthetic MHBS under both excess-gas and excess-water conditions. The MH formation following the excess-gas method is first discussed. Afterward, MH morphology and pore habit changes after the water saturation with or without an additional temperature cycle and their corresponding effects on the mechanical properties of MHBS are debated.

## 7.2 MH formation under excess-gas conditions

Figure 2.4 shows the MH formation in gas-saturated media in the literature which was divided into 4 stages (nucleation, growth at high and low rate, and steady state) based on mole (quantity) of methane gas consumed with time.

The volumetric deformation of eight triaxial tests during the MH formation following the excess-gas method (see Chapter 3) is shown in Figure 7.1a. Figure 7.1b shows an almost linear increase of  $V_P$  (after the induction time) with the logarithm of time before its stabilization (see Chapter 3). Furthermore, by calculating MH saturation based on *FID Intensity*, Figure 7.1c shows a linear increase of MH saturation with the logarithm of time before the steady state (see Chapter 4). The MH formation (at 2-3 °C, 7 MPa) is considered to be composed of MH nucleation, MH growth and MH steady state in this study.

### 7.2.1 MH nucleation

Gas hydrate formation in bulk water is different from that in sediment matrix due to intermolecular interaction between the sediment and pore fluid (Everett, 1961). Furthermore, the presence of particles/sediments promotes gas hydrate formation and shortens the induction time due to enhanced gas hydrate nucleation (Heeschen et al., 2016). Note that an induction time is the time taken for crystal nuclei to be formed until their occurrence could be first detected via e.g. temperature rise (endothermic nature of gas hydrate formation) and/or pressure decrease (gas consumption for gas hydrate formation in a closed system). Increasing the driving force for gas hydrate formation (by applying higher pressure and/or lower temperature) reduced the induction time (Metaxas et al., 2019).

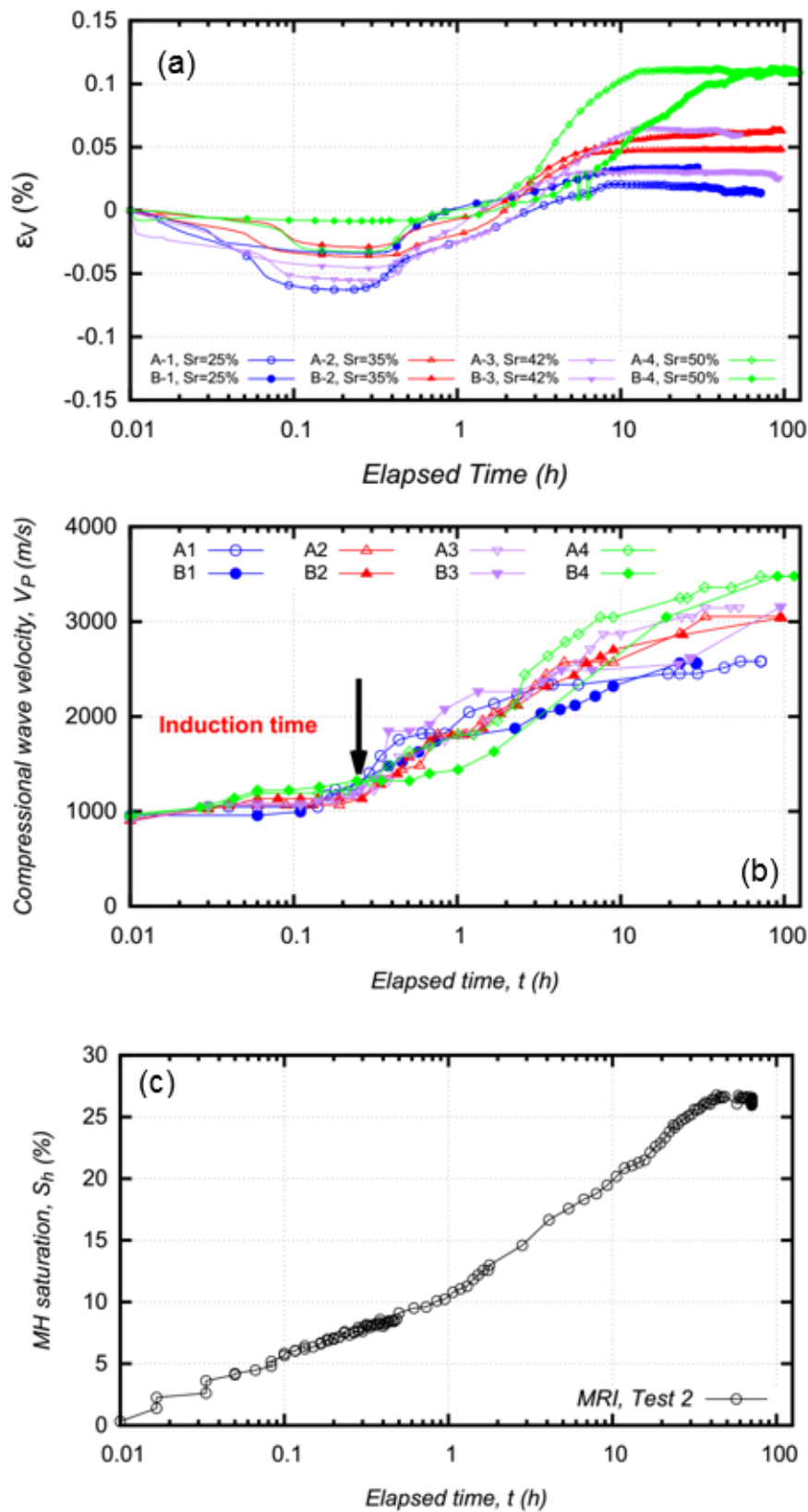


Figure 7.1: Kinetics of the MH formation following the excess-gas method. Triaxial tests: (a) Volumetric deformation versus elapsed time; (b)  $V_P$  versus elapsed time. MRI tests: (c) MH saturation versus elapsed time.

For our triaxial tests, when methane gas was injected into the sample to reach 7 MPa of pressure, the cell temperature (stable at 3 – 4 °C) just increased slightly from 0.1 to 0.3 h then stabilized (Figure 3.9b). Bagherzadeh et al., 2011 used MRI technique to investigate the formation of methane hydrates in an unconsolidated bed of silica sand and found that the MH formation was not uniform and that the nucleation of hydrate crystals occurred at different times and different positions inside the sample. Note that in this study, the thermocouple did not measure directly the sample temperature as shown in Figure 3.2 and methane gas consumption at the beginning could not be measured due to overcapacity of gas flowmeter. The induction time here was defined as the duration before an abrupt increase of  $V_P$  in Figure 7.1b. The observed induction time, approximately 0.3 h, was almost independent of the initial water saturation. This is in agreement with the results of Chong et al., 2016 who found an induction time of 0.1-0.8 h for fine sand (0.1 – 0.5 mm) prepared at 75 % of initial water saturation and (8 MPa, 4 °C). Similarly, the water movement together with the appearance of some MHs were observed for SXRCT tests (40-60 % of initial water saturation and at 7 MPa, 2-3 °C) from 0.3 to 0.6 h (Figure 6.7, Figure 6.13). Differently, for MRI tests (at 7 MPa, 2 °C), *FID Intensity* decreased directly once MH equilibrium conditions were reached (at 25 % of initial water saturation, shown in Figure 4.4a). MHs were formed directly with a very short induction time (Figure 7.1c). It is supposed that *FID Intensity* is the most appropriate parameter for the detection of created MH crystals as it is directly proportional to the quantity of water.

The MH formation boundary in (P,T) space was supposed to be shifted to higher pressure and lower temperature with an increase in salt concentration contained in water (Sloan Jr and Koh, 2007). MH formation involves local water salinity and salinity gradient between high salt concentration water pockets and surrounding water that can be equilibrated with time through film flow or ion diffusion in continuous water phase (Almenningen et al., 2018). On the other hand, lower methane gas solubility in saline solution can promote the MH formation in the MH stability zone (Zatsepina and Buffett, 1998; Davie et al., 2004). For our SXRCT tests (see Chapter 6), it seems that MHs were formed more quickly at the beginning of Test 4 (using saline water, KI 3.5 wt%) with earlier evidence of MH spikes compared to the three other tests with pure water (Test 1, Test 2, and Test 3). Higher initial rate of carbon dioxide hydrate formation in Toyoura sand for the firsts five hours in saltwater systems was observed compared to the case of pure water systems via gas consumption (Yang et al., 2016b). Furthermore, some salts (e.g. NaI, KI) were found to promote the MH formation at low salt concentration (below 1 mole or 16 wt% for the case of KI) (Sowa et al., 2014; Nguyen and Nguyen, 2015). This is in agreement with our observations as saline water solution was used at low KI concentration (only 3.5 wt%). Note that the sample temperature was slightly lower for the test with saline water (1-2 °C) compared to that of the three tests with pure water. It is noteworthy that tiny MHs (under the spatial resolution of SXRCT images) could have not been observed.

## 7.2.2 MH growth

The gas hydrate growth rate after the nucleation (quantified by the rate of gas consumption which was supposed to be proportional to the product of gas-water interfacial area and difference between gas hydrate equilibrium temperature and formation temperature - subcooling (Turner et al., 2005)), was stochastic and increased with subcooling (Metaxas



et al., 2019). Furthermore, Bagherzadeh et al., 2011 found that MH formation occurred faster in the sample with lower initial water saturation. In our study, the initial water saturation was fixed at 25 % for the both MRI tests while for triaxial tests the MH saturation varied in a small range (from 25 to 50 %). The rate of increase of  $V_P$  seems independent of water saturation within this range.

Our SXRCT and optical microscopy results (presented in Chapter 6) show at the grain scale not only methane hydrate morphologies and pore habits in sandy sediments but also the kinetics of methane hydrate formation following the excess-gas method. It should be noted that the excess-gas method is a common method used to create synthetic methane hydrate-bearing sandy sediments in laboratory for both macroscopic measurements (Choi et al., 2014; Waite et al., 2004; Le et al., 2018a) and observations via XRCT, SXRCT (Chaouachi et al., 2015; Ta et al., 2015; Yang et al., 2015). Several phenomena have been observed:

- First, the results showed that MH spikes formed at grain surfaces and/or methane gas/water interfaces and became thicker over time (Figure 6.6, Figure 6.7, Figure 6.15). MH spike formation after the excess-water method has been observed by Lei et al., 2019b. These authors supposed that MH spike formation was similar to ice spike formation (center of MH tube served as a water conduit for further MH growth into methane gas space). In this study, once MH spikes were formed at grain surfaces or methane gas/water interfaces under excess-gas conditions (like ice spike formation), they stopped extending in length and were clogged. They finally became like-crystals as observed in SXRCT experiments. For optical microscopy tests, they were still in form of spikes at the end of the experiment (Figure 6.23). Furthermore, MH spikes shown in Figure 6.23a (at low water saturation zone) seem to be shorter than those shown in Figure 6.23b (at high water saturation zone). Note that the experiment duration of optical microscopy test was shorter (about 5 hours compared to about one day for SXRCT tests). Furthermore, the sample temperature was lower (-16 °C compared to 2-3 °C for SXRCT tests).
- Second, thanks to high attenuation coefficient ratio between Xenon hydrate and water, thin water film between Xenon hydrate and sand surface was observed by Chaouachi et al., 2015 by using SXRCT. Lei et al., 2019b observed methane hydrates growing at sand surfaces in both excess-gas and excess-saline-water experiments and suggested that water migration driven via water film between sand grain and methane hydrate was likely to facilitate methane hydrate formation front over sand grains near the original water menisci (see Figure 2.26a). Furthermore, MH morphology evolved after the initial MH formation mainly via diffusion (water vapor, see Figure 2.26b). In the present study, with high temporal resolution of SXRCT, water was observed to move from grain contacts to form methane hydrates at nearby sand grain surfaces over time. However, due to the voxel size and scan time limit of SXRCT scans in this study (0.9  $\mu\text{m}$  and some ten minutes), the presence of water films could not be confirmed. The mechanism of MH layer formation at grain surfaces can be analyzed via the observations by optical microscopy. Figure 7.2 shows the propagation of methane hydrate layers on the quartz capillary tube surface during the methane hydrate reformation (Test 5 presented in Chapter 6, once the MH formation was finished, temperature was increased for the MH disso-

ciation then was decreased for the MH reformation). Halos (MH layers) absorbed quickly the nearby water droplets by forming a methane hydrate crust on the water droplet surface (Figure 7.2c). Similar phenomena were observed for cyclopentane hydrates by Martinez et al., 2016. Nano water film between the capillary tube surface and methane hydrate crust seems to attract the nearby water for further methane hydrate growth on the solid surface (substrate) due to cryogenic suction. Water migration via water film between substrate and methane hydrate for further methane hydrate formation on the substrate is highly likely. Hydrate spikes were formed on the substrate surface, orientated towards methane gas space once methane hydrates were spread over the substrate surface (Figure 7.2d). They allow to transform excess-water under the continuous layers on the quartz capillary tube surface into additional MHs.

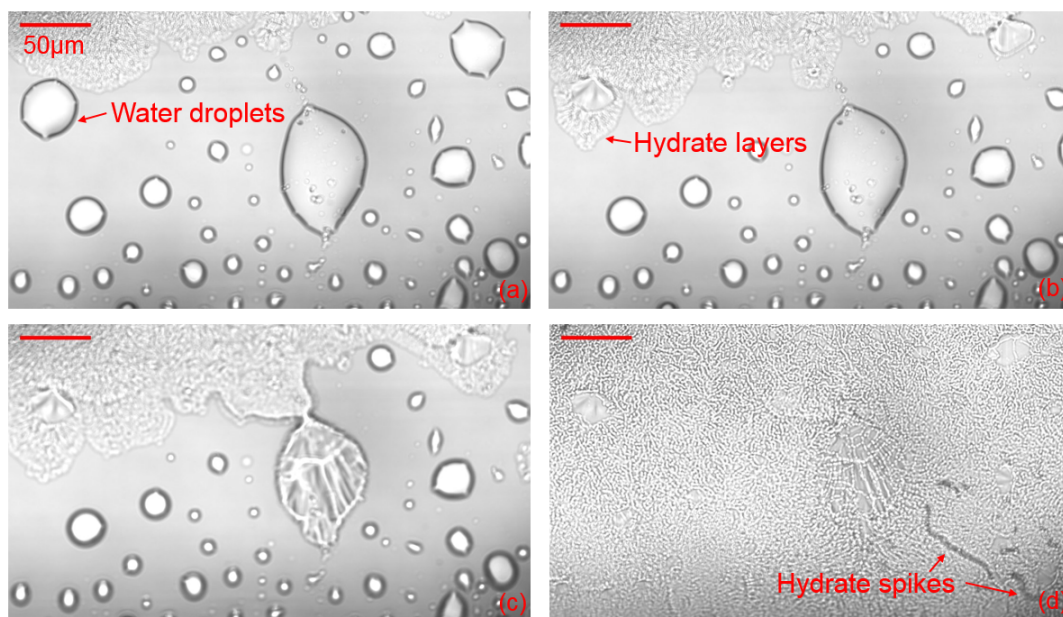


Figure 7.2: MH layer propagation on a solid surface (Chapter 6, Test 5): (a)  $t = 0$  s; (b)  $t = 1.3$  s; (c)  $t = 2.2$  s; (d)  $t = 18$  s.

Some mechanisms of the MH formation under excess-gas conditions have been proposed (see Figure 2.27, Figure 2.28, Figure 2.26a, b)). It is supposed here that methane hydrate crusts were first formed on sand-water-gas contact lines and at water-gas interfaces (Figure 7.3). Water under cryogenic suction in menisci was moved over grain surfaces for further methane hydrate formation. Lei et al., 2019b supposed that pore size, particle size, initial phase saturation (excess-gas or excess-water) and nearby mass supply affect the methane hydrate formation. In this study, methane hydrates in form of “crystals” and/or layers could be formed at sand surfaces or at contacts of grains (Figure 6.13). First, it seems that initial water saturation influences methane hydrate morphologies. At low initial water saturation, methane hydrates would be mainly in form of “crystals” while mainly methane hydrate layers would be formed at high initial water saturation. It is supposed that if initial water quantity in menisci is low, moved water could form small “crystals” at grains and become bigger over time. Thin water layer between sand grain

and methane hydrate could still exist due to the high cryogenic suction. If initial water quantity is high enough, once water is moved at sand surfaces, hydrate layers could form directly and be thicker over time. Water supply path could be via thin water layer between sand and methane hydrate. It could also migrate through the formed methane hydrate networks if methane hydrates are porous. Second, water could be absorbed progressively from other zones to form MHs in form of “crystals” and/or layers. Note that the remaining water at contacts of grains is supposed to be transformed gradually into MHs by means of methane gas and/or water diffusion via porous MHs, formed first at gas/liquid interfaces. Besides, thin water layers at grain surfaces are supposed to contribute to the formation of MHs in form spikes (as shown in Figure 7.4). Water could exist initially at surfaces of humid grains or was moved from nearby grain contacts.



Figure 7.3: Schematic of the first mechanism of MH formation under gas-excess conditions.

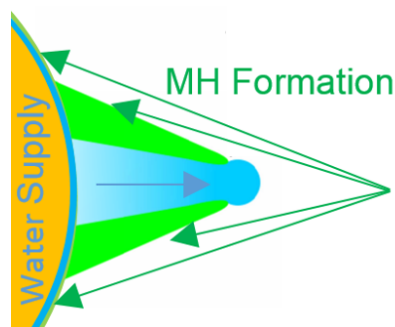


Figure 7.4: Schematic of the MH spike formation (Modified from Lei et al., 2019b).

MH growth was both affected by macro-property (initial water saturation) and micro-property (initial water distribution in the pore space) (Zhang et al., 2019). By using first saturated sand then injecting methane gas to displace free water in order to obtain desired initial water saturation for the MH formation, MHs were observed to be formed heterogeneously in the sample even at low initial water saturation by using MRI (Wang et al., 2018; Zhang et al., 2019) as the initial water distribution was not homogeneous.

Our homogeneous MRI profiles and vertical slices during the MH formation following the excess-gas method (Figure 4.5 and Figure 4.6) show homogeneous MH distribution at the sample scale (initial water saturation: 25 %). This is in agreement with the results shown by Bagherzadeh et al., 2011 when the sample was prepared following the same procedure (dry sand was mixed with desired water quantity before the compaction, initial water saturation was 25 %). However, MHs were found distributed heterogeneously for the samples with high initial water saturation (Bagherzadeh et al., 2011). It should be noted that the samples for our triaxial tests were prepared with an initial water saturation in a range of 25-50 %. It is then supposed that MHs were distributed homogeneously in these samples.

Our SXRCT results show multiple water migrations at the grain and sample scales during the MH formation in sandy sediment following the excess-gas method (Chapter 6). That results in heterogeneous MH distribution at both pore and sample scales. By using MRI, water was observed to migrate from the top to the bottom of the sample over time during the MH formation of the sample at 28 % of initial water saturation (Zhang et al., 2019). Furthermore, water and/or gas hydrate movement during gas hydrate formation at the pore scale were observed by XRCT/SXRCT (Chen and Espinoza, 2018; Lei et al., 2019a; Lei et al., 2019b; Nikitin et al., 2019). Chen et al., 2018 observed a gas hydrate coarsening over some ten days, which was explained by the reduction of the specific interfacial surfaces (Ostwald ripening). XRCT experiments were performed with Xenon hydrates while methane hydrate growth on water droplets was observed with optical microscopy. However, no water migration was observed. In the work of Lei et al., 2019b, water migration was found fast after MH nucleation, became slower after 24 h and water remained stable after 81 h. In addition, progressive methane hydrate migrations were observed by XRCT scans over the whole duration of the test. Lei et al., 2019a observed  $CO_2$  hydrates forming preferentially toward the periphery of the sample. In addition, sediment particles moved toward the sample center. These two phenomena were explained by cryogenic suction governed by temperature gradient generated during the gas hydrate formation. Furthermore, Nikitin et al., 2019 performed SXRCT scans to observe the MH formation in sandy sediment and found multiple fast water movements. That once again was explained by cryogenic suction.

In the present study (Chapter 6), pure water was observed to move out of the zone Z0\_HR between 0.3-0.8 h (Test 3, Figure 6.7) and saline water moved out of the zone Z0\_HR between 0-0.6 h (Test 4, Figure 6.13). However, saline water migrated into to the zone Z1\_HR at 3.8 h (Test 4, Figure 6.14). The two firsts events would be explained by the cryogenic suction governed by a local temperature gradient during the MH formation. Vertical temperature gradient was obvious (about  $0.013\text{ }^{\circ}\text{C}/\text{mm}$ ) while radial temperature gradient, which was negligible for an unsaturated sand case, could exist during the MH formation. The MH formation can increase sample temperature locally (an exothermic process) and it is supposed that this increase of temperature in the zones near the tube periphery could be compensated more easily by cooled-air circulation than in the center of the tube. The third event (saline water migration into the zone Z1\_HR) can be related to cryogenic suction and/or was a Haines jump when pressure-volume response was multi-value across pore throats due to the MH formation (Sun and Santamarina, 2019). Furthermore, both methane hydrates and saline water were moved out of the zone Z0\_HR at  $t = 13.4\text{ h}$  (Test

4, Figure 6.16) and the bottom of the zone Z1\_HR at  $t = 13.6$  h (Test 4, Figure 6.17). That can be explained by the Haines jump mechanism and/or the energy supplied by X-rays that locally heated the sample. This X-ray-induced heating has been evidenced by some theoretical models and experiments when studying biological molecules with macro-molecular crystallography (Helliwell, 1984; Kriminski et al., 2003; Wallander and Wallentin, 2017). These works showed that the increase of temperature depended not only on the absorbed energy but also on the heat transfer to the surrounding medium. In the present study, the zones Z0\_HR and Z1\_HR were exposed to X-rays continuously during the firsts twelve hours. That could explain the MH dissociation in these zones as shown in Figure 6.16. In addition, most water released after the MH dissociation was supposed to be moved to other zones for further MH formation. The Z0\_HR zone was more sensitive to beam-induced heating than the Z1\_HR zone because the Z0\_HR zone was exposed to X-rays 2 hours before the scans were switched between these two zones. Furthermore, the temperature in the zone Z1\_HR was slightly lower than that in the zone Z0\_HR due to the vertical temperature gradient. MHs still existed at the periphery of the zone Z0 (Figure 6.18) due to the radial temperature gradient as the tube periphery was in direct contact with cooled-air. In addition, X-rays irradiate continuously the central part of the sample, and only intermittently the periphery. Besides, it seems that the zones Z-3, Z-5 and Z-7 corresponded to the expected unsaturated gas media (Figure 6.19) while the zones Z3, Z5, Z7 and Z9 (situated at higher positions) were modified due to multiple water migrations during the MH formation (see Figure 6.20). That can be explained by the vertical temperature gradient which favored the MH formation on top of the sample. Note that no MH dissociation and movement were observed for Test 2 (Figure 6.12). That can be related to the stochastic nature of Haines jump, the unstable nature of the MH formation and/or a higher temperature increase induced by X-rays for the case of saline water (Test 4) compared to normal water case (Test 2). It should be noted that saline water absorbed more energy than normal water (see more details in Chapter 5). Furthermore, by using saline water, the MH equilibrium curve is shifted to higher pressure and lower temperature. At similar MH formation temperature and temperature increase, MHs are thus likely to be less stable in saline water media.

The MH formation is naturally an unstable and dynamic process. However, it seems that sample temperature gradient and X-ray-induced heating favored more water migrations. It should be noted that the ratio of sample height/diameter is generally close to two for macroscopic tests (e.g. triaxial tests) while it is much higher for XRCT/SXRCT studies. That involves important vertical temperature gradient. Temperature control shows an important role for the MH stabilization. Furthermore, studies on MHs should pay attention to the interaction of X-rays and the sample (beam-induced heating).

Figure 7.1a shows volumetric strain evolution during the MH formation once effective stress reached 3 MPa (pore pressure was at 7 MPa, see Chapter 3). It seems that the specimen exhibited dilation behavior during the MH nucleation then contraction behavior during the MH growth before being stable (at a constant effective stress). The conversion of water into MH increased sample volume (dilation). The contraction behavior is supposed due to the sample rearrangement (of mainly water and formed MHs) during the MH growth.

### 7.2.3 MH stabilization

For our triaxial tests, the stabilization of  $V_p$  at the end of the MH formation (Figure 3.11) suggested that almost the entire quantity of available water (25-50 %) has been transformed into methane hydrates. The final MH saturation increased with an increase in initial water in this range (Figure 2.6). Furthermore, two experiments at 25 % of initial water saturation, observed by MRI, showed that almost 100 % of water became methane hydrate in the end. Ten percent of volume increase was supposed for the water-methane hydrate conversion. However, in the work of Wang et al., 2018 and Zhang et al., 2019, 5 to 15 % of pore water was found to remain unconverted to methane hydrates at the end of the experiments with 25-50 % of initial water saturation. Actually, in these works, the signal of methane gas was not considered and that would induce errors in water content estimation in the specimen. In addition, the experiment duration was only a few hours for these works compared to several days for our triaxial and MRI tests (Wang et al., 2018; Zhang et al., 2019). For our SXRCT tests with tap water, it was not evident to confirm that all water was transformed into MHs at the end of the experiments due to close gray levels of water and methane hydrate. They were mainly distinguished based on their morphology so methane hydrate formation in some pockets initially filled with water could not be well investigated. Besides, saline water still existed at the end of the experiment with KI solution. That is supposed due to salt concentration increase during the MH formation. Note that these tests were observed during about one day only, the MH formation could still continue.

The injection of methane gas at a pressure of 7 MPa and a temperature of 3 – 4 °C induced the transformation of water into methane hydrates (eight triaxial tests). The results show that this methane hydrate formation in gas-saturated media increased  $V_p$  (see Figure 3.11), and this increase reached the stabilization state at the end of the MH formation. It was supposed that almost the entire quantity of available water has been transformed into methane hydrates and the distribution of methane hydrates were similar to that of water prior to their creation. Comparison between the experimental data and Dvorkin's model (Dvorkin et al., 2000) shown in Figure 3.17 suggests that at a low initial water saturation (methane hydrate saturation), methane hydrates were mainly distributed at grain surfaces (cementing - mineral coating), while at a high initial water saturation, the role of methane hydrates at grain contacts dominated (cementing - grain contacts). These macroscopic results are in agreement with that of Waite et al., 2004 by using similar approaches (velocity measurements and Dvorkin's model). Note that at high gas hydrate saturation, only (cementing - grain contacts) was considered (see Subsubsection 2.2.2.4).

At the pore scale, Zhao et al., 2015 observed MHs (formed following the excess-gas method) at gas-water interfaces, floated between sand grains without coating on grain surfaces (Figure 2.24). A thick water layer was found to envelop grain surfaces by using image segmentation. Besides, polyhedral crystals of Xe hydrates around grains and loosely connected aggregates of Xe hydrate crystals in the pore space (formed following the excess-gas method), were observed by SXRCT (see Figure 2.25) (Chaouachi et al., 2015). Furthermore, thin layers of water were observed to exist between sand grains and Xe hydrates. It should be noted that the Xe hydrate formation time was just some ten minutes, remaining water could still be transformed into MHs. Furthermore, the morphology of gas hydrates depends on the type of used gas.

Within spatial resolution of sub-micron voxel size of SXRCT images in this study, methane hydrate morphologies and pore habits were observed directly without the need of segmentation. They were later confirmed by observations via optical microscopy. That allows to discuss the four types of methane hydrate pore habits, proposed by Dvorkin et al., 2000: cementing (grain-grain contacts or mineral coating), load-bearing and pore-filling, usually used for predictions of physical/mechanical behaviors of methane hydrate-bearing sandy sediments (Waite et al., 2009; Pinkert and Grozic, 2014; Uchida et al., 2012; Sánchez et al., 2017). It is usually supposed that methane hydrates formed under excess-gas conditions in sandy sediments (following the excess-gas or ice-seeding method) have the shape of pendular water menisci (at grain-grain contacts) or thin uniform methane hydrate layers coating sand surfaces (cementing - mineral coating) (Waite et al., 2004; Priest et al., 2005). The present study and that of Lei et al., 2019b showed irregular shapes of methane hydrates at sand surfaces often accompanied by finger-like spreading patterns of methane hydrates at low methane hydrate saturation. It appears that methane hydrates were at grain-grain contacts and/or grains surfaces (cementing) at low hydrate saturation while they tended to fill the pore space at high hydrate saturation. Besides, methane hydrates could be porous if they were not totally clogged over time. It is clear that MH morphologies and pore habits in the sample are not only heterogeneous at the pore scale but also along the sample height (the sample scale) due to water migrations. Different types of MH morphologies and pore habits could exist in the sample (Figure 7.6). Not only MH pore habits but also MH morphologies in sandy sediments (which can only be observed at high image spatial resolution) are important for studies on physical/mechanical behaviors of methane hydrate-bearing sediments. At similar methane hydrate saturation, different MH morphologies (spikes, “crystals” or layers) at sand grain surfaces (cementing - mineral coating) or at contacts of grains (cementing - grain contacts) can play different roles in mechanical behaviors of methane hydrate-bearing sediments. We suppose here an intermediary model of MHs at the grain scale (see Figure 7.5) with complex geometry of MHs that could eventually be porous. MHs play more a role at grain contacts compared to the cementing, mineral coating model by forming bulk MHs. Furthermore, effects of thin water film (if exists) between sand grain and methane hydrate on physical/mechanical behaviors of sediments have not been well studied yet. It seems vital that numerical studies on mechanical behaviors of methane hydrates-bearing sediments, which have been based on four idealized methane hydrate pore habits, should take into account more realistic and less caricatural methane hydrate morphologies and pore habits.

Optical microscopy tests showed methane hydrates: only in form of spikes at low temperature (at  $-16\text{ }^{\circ}\text{C}$ , Figure 6.23), in form of spikes, layers or “crystals” at higher temperature (at  $2\text{ }^{\circ}\text{C}$ , Figure 6.25). It is in agreement with the findings of Ohmura et al., 2005 on the effects of gas hydrate formation temperature on the morphology of pure gas hydrates (Figure 2.22). SXRCT tests observed a conversion over time of MH morphology (spike into “crystals” shown in Figure 6.7, Figure 6.15). It is supposed that higher gas hydrate formation temperature facilitates the gas hydrate morphology conversion. Not only the resistance of pure methane hydrates but also methane hydrate morphologies in sediments could be changed with the methane hydrate formation temperature. However, few existing studies on mechanical behaviors of methane hydrate-bearing sediments have paid attention to temperature of the MH formation.

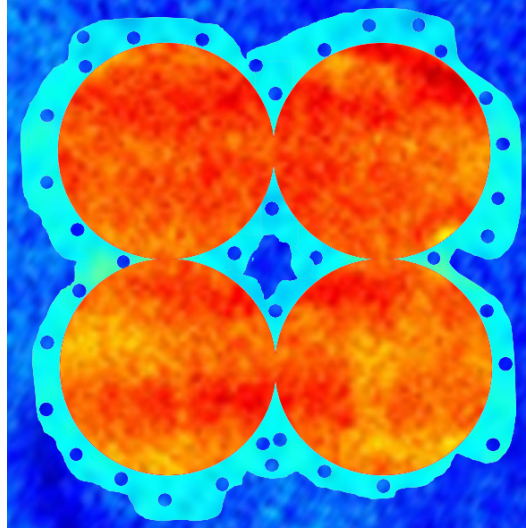


Figure 7.5: A new model of MH pore habits under excess-gas conditions (Blue: methane gas; Cyan: MHs; and Red: sand grains).

## 7.3 MH morphologies and pore habits under excess-water conditions

### 7.3.1 Water saturation

After the formation of methane hydrates under excess-gas conditions, the subsequent water saturation phase significantly decreased  $V_p$  during triaxial tests (Figure 7.7a). Ebinuma et al., 2008 and Kneafsey et al., 2010 observed a similar decrease in sonic velocities when saturating the gas-saturated MHBS with water. These results suggest that water saturation modified the MH distribution at the grain scale (Ebinuma et al., 2008; Kneafsey, 2011). MHs located at grain contacts and/or at grain surfaces would be progressively converted or/and redistributed into the pore space (Choi et al., 2014). In this study, the effects of water injection in gas-saturated methane hydrate-bearing sediments were investigated at different methane hydrate saturations. The results shown in Figure 7.7a and Figure 7.8a indicate that this process took longer time for higher methane hydrate saturation. For some specimens (B2, B4, A3, and A4), this transformation was not complete when the subsequent step (triaxial compression for the specimens A and heating/cooling cycle for the specimens B) was applied. This may explain the measured higher values of  $V_p$  after the water saturation than the predicted values of the load-bearing model. Besides, for the two tests following the procedure A at high methane hydrate saturation (A3 and A4), even after waiting long time for the water saturation (to make sure that MHBS was well saturated with water),  $V_p$  was still higher than the value predicted for the load-bearing model.



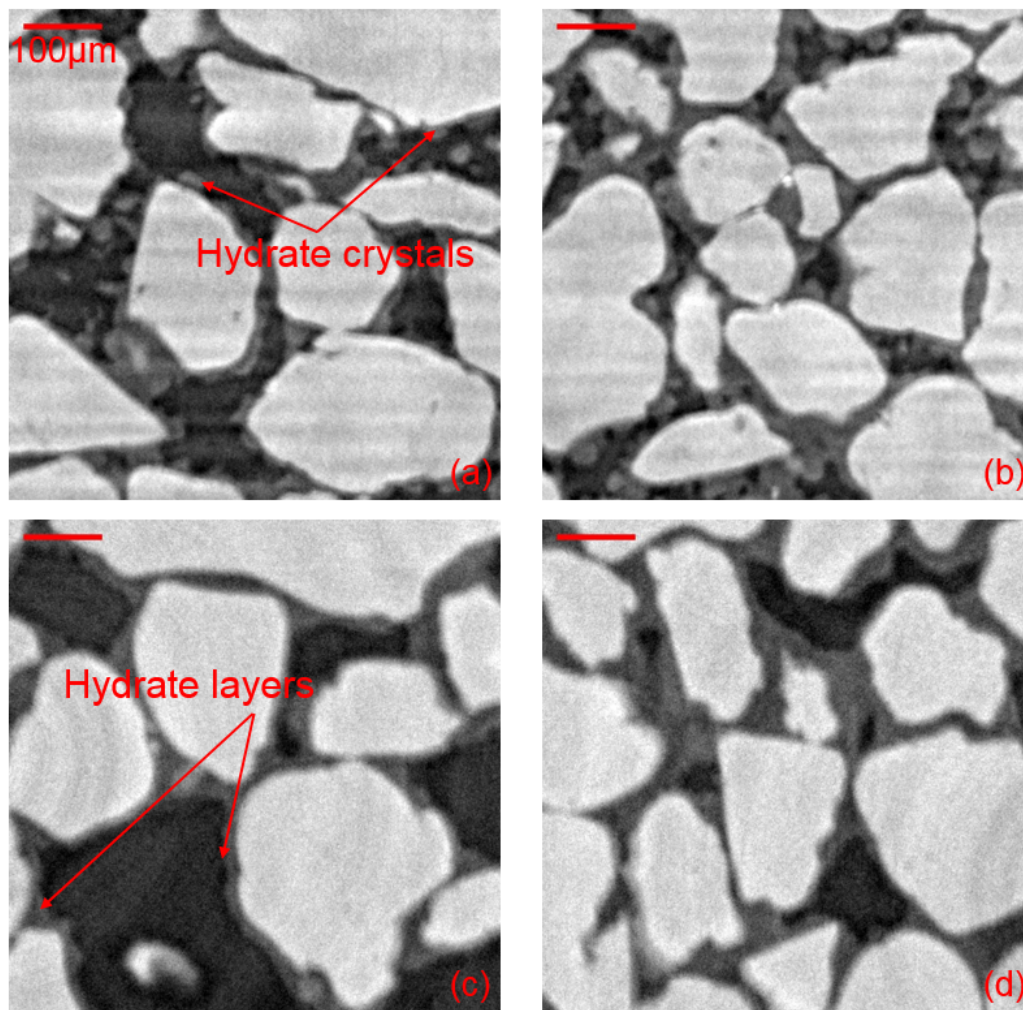


Figure 7.6: MH morphologies and pore habits under excess-gas conditions: (a), (c) Test 1, Z5\_HR at 18.1 h; (b), (d) Test 2, Z0\_HR at 22.7 h.

The results of MRI tests show heterogeneous water distribution along the sample height after the water saturation (Figure 7.7b). Similar water saturation procedure was applied for triaxial tests and MRI tests. However, for triaxial tests, water was injected from both top and bottom pore pressure transducers as they were connected by a T-valve while water was only injected from the bottom inlet for MRI tests. That explains why methane hydrate saturation was higher at the top of the sample compared to that at the bottom for MRI tests. Furthermore, the water injection time of MRI tests was longer than that of the triaxial tests. That could induce more MH dissociation during the water injection. MH distribution after the water saturation of triaxial tests is supposed to be more homogeneous.

For SXRCT tests, it is more difficult to saturate the media with water as the aluminum tube was so long while its diameter was small. Furthermore, water inlet was only on the cell bottom (similar to MRI tests). That explains why all MHs were dissociated before the arrival of saline water (Figure 6.21). It is not easy to saturate the whole sample with saline water (along the whole tube height).

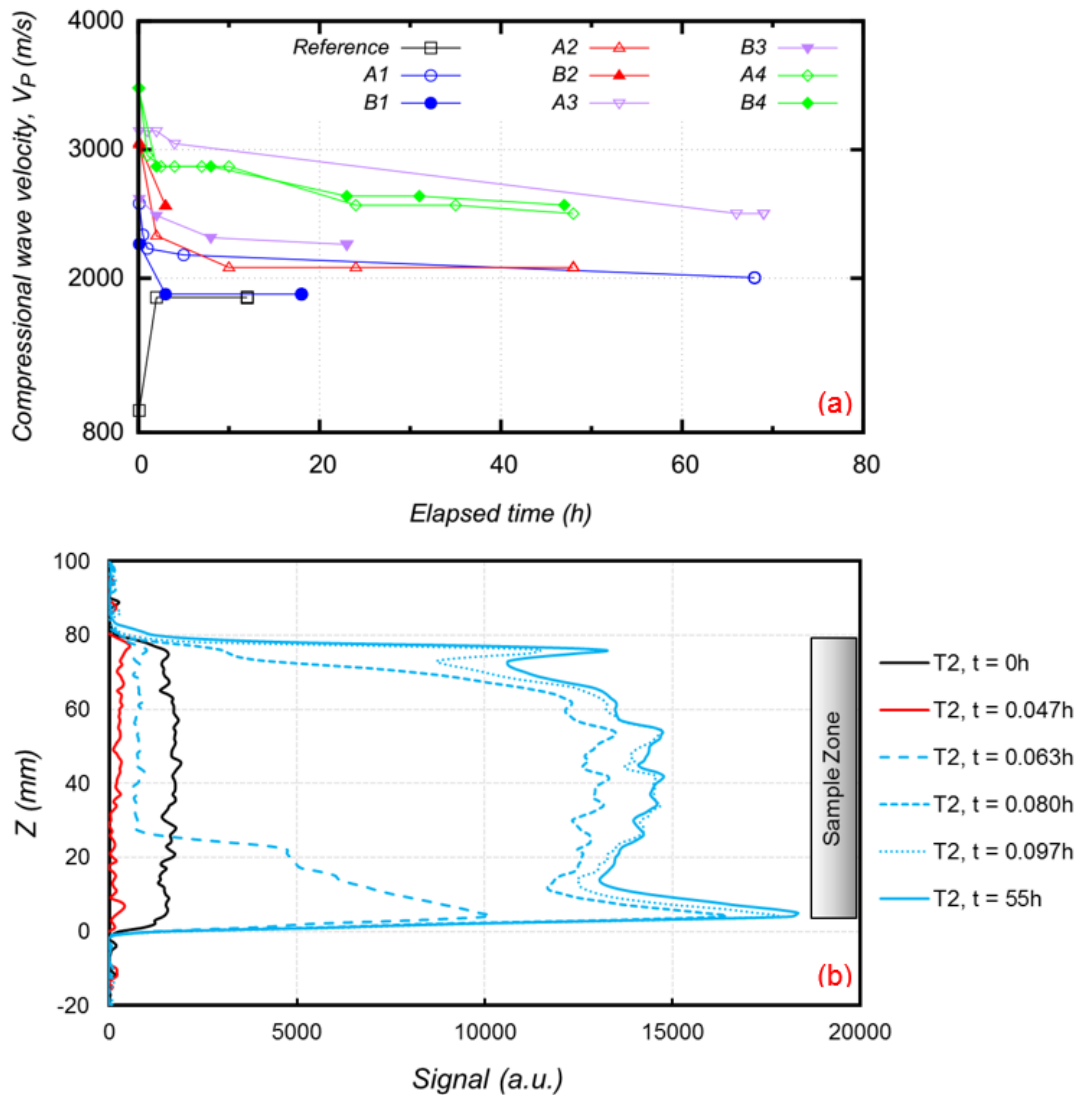


Figure 7.7: Water saturation: (a) Triaxial tests,  $V_P$  versus elapsed time; (b) MRI test,  $Z$  profile over time.

### 7.3.2 Temperature cycle

Choi et al., 2014 formed methane hydrates in unsaturated sand following first the excess-gas method, then injected saline water at conditions just outside of the MH stability zone for saline water and conducted a temperature cycle. It was concluded that slow saline water injection was a key to initiate the formation of non-cementing hydrates and that the temperature cycle ensured this formation.  $V_P$  after warming (the MH dissociation) was quite high while the sample was not saturated. The MH dissociation was perhaps not completed before the MH reformation. This could explain why the difference of  $V_p$  after the saline water injection and that after the temperature cycle was small. For our triaxial tests, normal water was injected to saturate the sample and MHs were completely dissociated before being reformed. The measurement of  $V_p$  at the end of the temperature

cycle was smaller than that obtained after the water saturation (see Figure 3.16 and Figure 7.8a). In addition,  $V_p$  at the end of the temperature cycle fitted with the pore-filling or the load-bearing model (Figure 7.8a). It can then be expected that in the range of 0-50 % of MH saturation, the heating/cooling cycle allows for the complete conversion of MHs with cementing pore habit into the non-cementing type either when the water saturation is not finished before the temperature cycle or when MH saturation is in a range of 40-50 % ( $V_p$  after the complete water saturation is still higher than the value predicted for the load-bearing model).

Figure 7.8b shows more homogeneous water distribution (MH distribution) along the sample height after the temperature cycle, which suggests that the temperature cycle can redistribute MHs at the grain scale as well as at the sample scale.

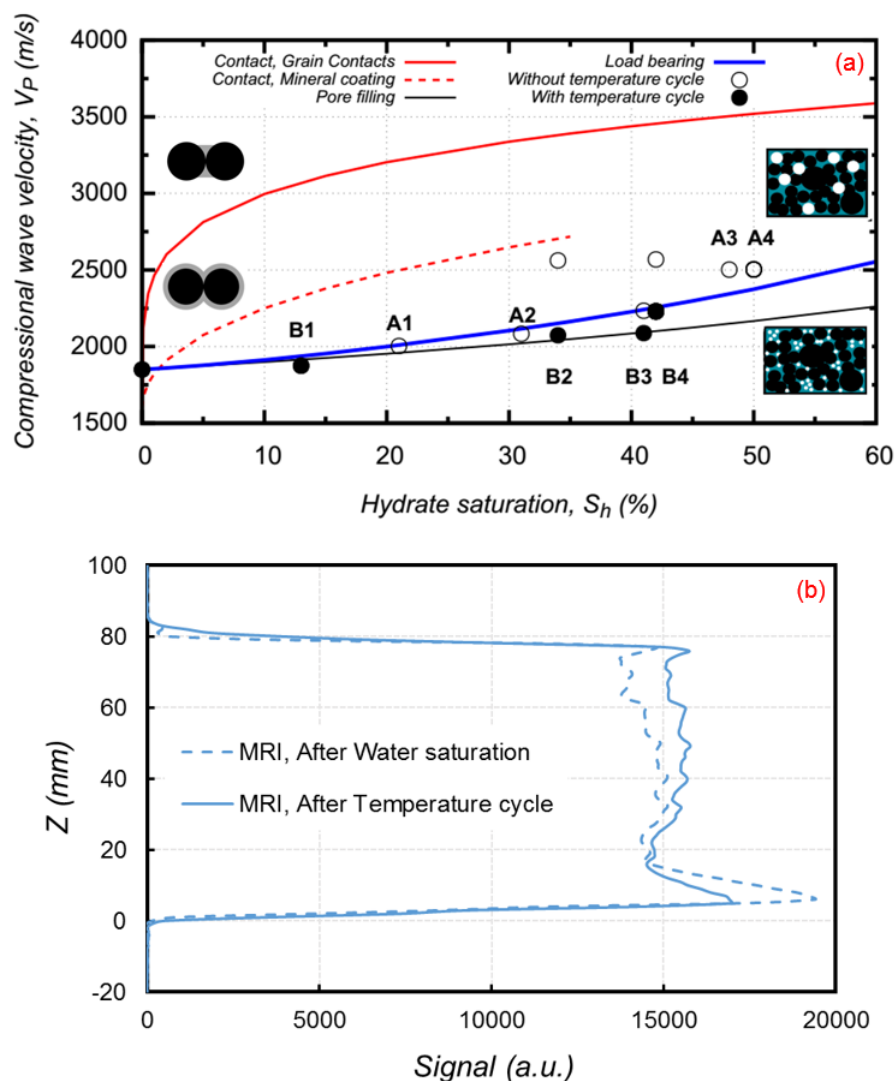
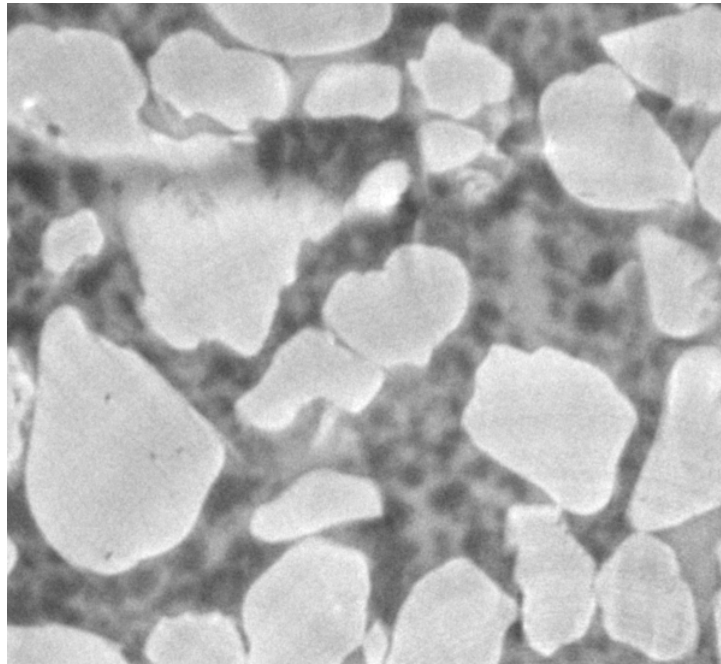


Figure 7.8: Temperature cycle: (a) Triaxial tests,  $V_p$  versus  $S_h$ ; (b) MRI test,  $Z$  profile.

### 7.3.3 MH morphologies and pore habits

To mimic natural methane hydrate-bearing marine sediments, the dissolved gas method is considered as the best method but it was time-consuming especially at high methane hydrate saturation due to the low solubility of methane gas in water (Spangenberg et al., 2005). The water-excess method, proposed by Priest et al., 2009, was suggested to create load-bearing MHs in sandy sediments at methane hydrate saturation lower than 40 % according to sonic wave velocity measurements. However, methane hydrates were observed to be formed heterogeneously inside their sample via XRCT (Kneafsey, 2011). Kerkar et al., 2014 confirmed patchy methane hydrate distribution and heterogeneous methane hydrate accumulation with XRCT at higher image spatial resolution. In the work of Lei et al., 2019b, the effect of saline water injection on the conversion/redistribution of MHs was confirmed by XRCT scans at high image spatial resolution. Furthermore, the obtained images showed round MH particles under excess-water conditions. In the present study, MHs were initially formed following the excess-gas method. However, after multiple water migrations, MHs in both excess-gas and excess-water media existed in the sample. MHs in excess-gas media were in cementing forms (mineral coating and/or grain contacts) while round MH particles were found mixed with saline water in the pore space under excess-water conditions (Figure 7.9). That confirmed the pore-filling/load-bearing distribution of MHs in excess-water media (round MH particles floating in saline water in the pore space of porous media). It is supposed that MH distribution at the grain scale of MHBS after the water saturation at low MH saturation and after the temperature cycle of Triaxial and MRI tests looks alike. Furthermore, the faster MH formation in gas saturated media together with the higher specific interfacial surfaces of MHs under excess-gas conditions could explain why they were less stable than MHs under excess-water conditions where MHs were formed slowly (mostly via methane gas diffusion).



*Figure 7.9: An example of MH morphologies and pore habits under excess-water conditions.*

## 7.4 Mechanical properties of MHBS

Figure 7.10 shows the deviator stress and volumetric strain versus axial strain for methane hydrate-bearing sandy sediments under excess-gas conditions according to the work of Hyodo et al., 2013. The water-saturated sand exhibited a strain hardening and shear contraction behavior while methane hydrate-bearing sediments showed a strain softening and a shear dilation behavior. The higher the methane hydrate saturation was, the higher the strength (maximum deviator stress during the test) and the more apparent the shear dilation behavior were. Furthermore, by comparing the mechanical properties of MHBS under excess-gas conditions with those under excess-water conditions (using the same sand, under the same stress conditions and at similar methane hydrate saturation) higher stiffness and higher failure strength were found for specimens under excess-gas conditions (see Figure 2.15).

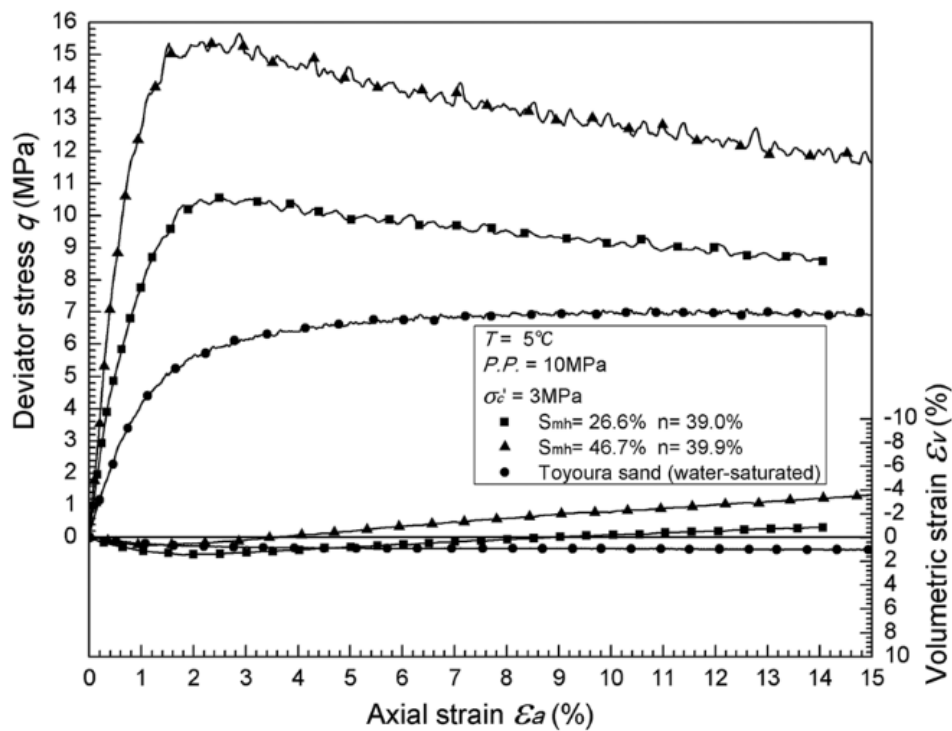


Figure 7.10: The influence of methane hydrate saturation,  $S_{mh}$  under excess-gas conditions (Hyodo et al., 2013).

The experimental results obtained from our triaxial tests showed higher values for the maximum deviator stress, secant Young's modulus, residual deviator stress, and dilation angle at a higher methane hydrate saturation (blue points in Figure 7.11) of MHBS under excess-water conditions. Hyodo et al., 2013 and Miyazaki et al., 2011 found similar effects of methane hydrate saturation on the maximum deviator stress and the secant Young's modulus while experimentally testing MHBS prepared following a procedure similar to the procedure A in the present work. The effects of methane hydrate saturation on the stiffness and the failure strength of MHBS were explained by particle bonding. However, the measurements of  $V_p$  in the present work suggest that cementing hydrates

have been significantly converted into non-cementing types at the end of the procedure A, as explained above. In addition, the results obtained by the procedure B (where the conversion has already been completed) showed similar effects of methane hydrate saturation on the stiffness and the failure strength of MHBS (red points in Figure 7.11). This indifference could be explained by the fact that these results were at high deformation when available MH-grain bonds were broken.

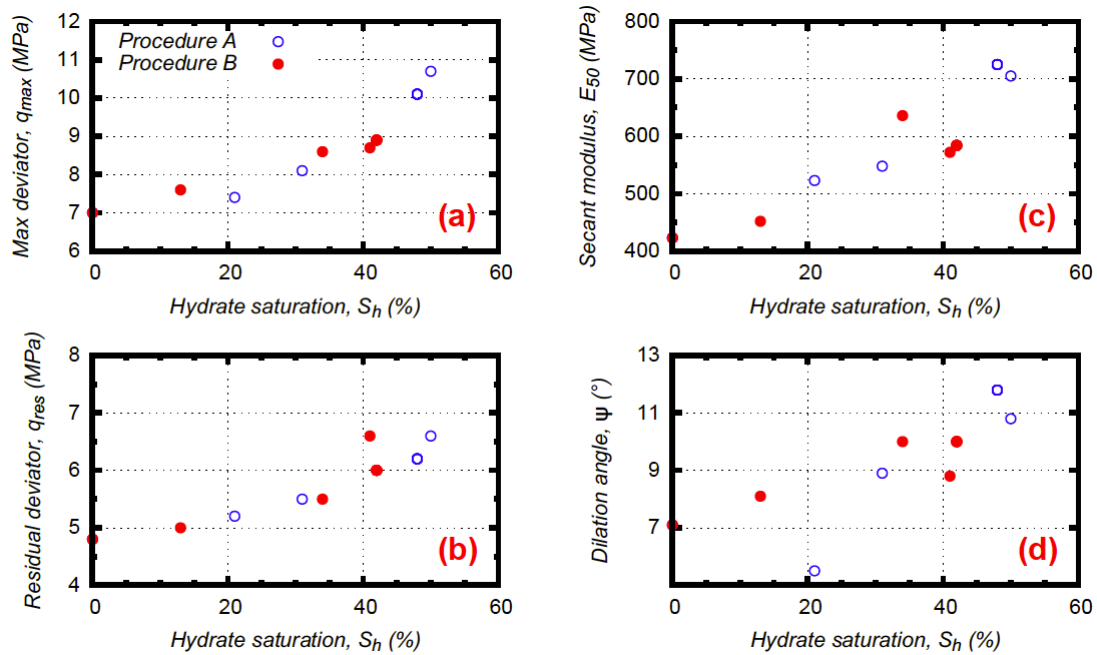


Figure 7.11: Dependence of mechanical properties of sand on methane hydrate saturation for all tests

When using the Rowe's stress-dilatancy analysis (axial deformations before the peak strength) (Pinkert, 2016) to analyze the data obtained in the present work (see Figure 3.21), the results from tests A3 and A4 were positioned above the other curves. These results corresponded then to a significant increase in degree of cohesion in the samples. This is also in agreement with the results shown in Figure 7.8a and the above comments in which it was expected that the conversion of methane hydrates at grain contacts and/or at grain surfaces to the pore space was not completed for these two cases (methane hydrate saturation higher than 40 %).

Soga et al., 2006 showed a similar increase in the dilation angle with an increase in methane hydrate saturation for natural samples and synthetic samples (using the excess-gas method for strong grain contacts and the ice-seeding method for weak grain contacts) at 1 MPa of confining pressure. An increase in methane hydrate saturation enhanced the dilative characteristics of sand, and this increase was more apparent when the methane hydrate saturation exceeded 30 %.

## 7.5 Conclusions

In this chapter, the MH formation under both excess-gas and excess-water conditions and the effects of formed MHs on the mechanical properties of methane hydrate-bearing sediments were discussed based on the literature and our own measurements at the macroscopic scale and observations of MH distribution via MRI and SXRCT. It can be seen that:

- The MH formation following the excess-gas method can be divided into three steps (MH nucleation, growth and stabilization). MH nucleation in porous media is almost spontaneous as the presence of sediments increases methane gas/water interfaces. MH growth is considered as a stochastic process and depends on driving force for the MH formation. At the macroscopic scale, methane hydrate saturation seems to increase linearly with the logarithm of time (Triaxial and MRI tests) while at the microscopic scale, many interesting phenomena have been observed by using SXRCT combined with optical microscopy. At the pore scale, water is observed to move from grain contacts to form MHs at nearby grain surfaces (via porous formed MHs and/or thin water layer between MH and grain surface). Thin water layers at grain surfaces contribute to the formation of MHs in form of spikes which could be prolonged, clogged and become finally like-crystals as long as water is provided. Furthermore, water is moved from one to another zone inside the sample during the MH formation (water migrations). That induces heterogeneous MH distribution in the sample at the pore scale as well as at the sample scale. Different MH morphologies and pore habits could co-exist in methane hydrate-bearing sandy sediments formed following the excess-gas method. It has been evidenced that MH formation is naturally an unstable and dynamic process. However, it seems that sample temperature gradient and X-ray-induced heating favor more water migrations during the MH formation observed by XRCT/SXRCT. MH morphologies and distribution at the grain scale of MHs under excess-gas conditions are much more complex than that described by the both cementing models (mineral coating and grain contacts) while for the media with MHs under excess-water conditions, the two idealized models (pore-filling and load-bearing) could be used to describe the MH distribution at the grain scale;
- Saturating MHBS by replacing excess methane gas by water is a delicate process that can dissociate a part of MHs and redistribute MHs at the sample scale (MRI tests). An additional temperature cycle (under undrained conditions) makes MHs distributed more homogeneously in the sample (compared to that after the water saturation). Furthermore, it is supposed that the water saturation converts (and/or redistributes) MHs in cementing form (grain contacts and/or mineral coating) to the pore space and the temperature cycle allowed for the completion of this conversion (and/or redistribution) for high methane hydrate saturation samples. The MH morphologies and distribution at the grain scale of formed MHBS are supposed to be similar to that of natural MHBS (pore-filling/ load-bearing habits);
- The higher the methane hydrate saturation was, the higher the mechanical properties of MHBS were. However, the mechanical properties of MHBS were higher under excess-gas conditions compared to that under excess-water conditions. The effects of the temperature cycle on the physical/mechanical properties of MHBS under

excess-water conditions could only be detected at high methane hydrate saturation. That is why to mimic natural methane hydrate-bearing sediments for the studies of their mechanical behaviors, with a range in MH saturation of 0-50 %, the procedure A (without a temperature cycle) could be used when methane hydrate saturation was smaller than 40 % to reduce the time of the MH formation, while at higher methane hydrate saturation (40-50 %), a temperature cycle should be added (the procedure B should be used) to complete the MH redistribution in the pore space.





# 8 Conclusions and Perspectives

## 8.1 General conclusions

Methane hydrates, formed naturally at high pressure and low temperature in marine and permafrost sediments, are nowadays being considered as an alternative energy source but also a considerable geo-hazard and climate change source. Knowledge of mechanical properties of sandy sediments containing MHs, which depend considerably on methane hydrate morphologies and pore habits i.e. their microstructure at the granular scale but also on their organization at a larger scale, is crucial for interpretations of geophysical data and reservoir-scale simulations in the scope of methane gas production. This study investigated the mechanical properties and the microstructure of synthetic MHBS at different scales, via different methods.

A new MH formation method was proposed for an initial water saturation in a range of 0-50 %. MHs were first formed by injecting methane gas into already chilled moistened packed sandy sample (the excess-gas method (Waite et al., 2004)). Ultrasonic compressional wave velocity,  $V_p$  increased significantly with MH formation and its final value depended on the initial water saturation. MHs were supposed to cement sand grains (cementing - grain contacts and/or mineral coating) by comparing measured ultrasonic wave velocities and that calculated based on rock physic models, assuming various idealized MH pore habits (Dvorkin et al., 2000). Furthermore, MHs were found to be formed homogeneously in the sample via MRI profiles (at 25 % of initial water saturation). Afterward, excess-methane gas was replaced by water to saturate the sample, involving a decrease in  $V_p$ . MHs could be redistributed completely in the pore space of the sample ( $S_h < 40\%$ ), and this process could take a long time at high methane hydrate saturation. An additional temperature cycle (modifying that of Choi et al., 2014 in the sense that MHs were completely dissociated before the reformation) could decrease  $V_p$  after the water saturation for the samples with higher methane hydrate saturation (40-50 %) to complete the redistribution of MHs in the pore space. Furthermore, MHs were distributed more homogeneously at the sample scale compared to the MH distribution after the water saturation (as shown by MRI profiles). Triaxial tests showed similar effects of methane hydrate saturation on the mechanical properties of MHBS formed following the both procedures (with or without an additional temperature cycle) except for the cases of high methane hydrate saturation ( $S_h > 40\%$ ). In general, all mechanical properties of MHBS increased with an increase in methane hydrate saturation. To mimic natural methane hydrate-bearing sediments (supposed to exhibit a pore-filling/load-bearing habit) for the studies of mechanical behaviors of MHBS, with methane hydrate saturation in a range of 0-50 %: the “procedure A” (without a temperature cycle) could be used for a MH saturation smaller than 40 %, while at higher MH saturation (40-50 %), a temperature cycle should be added

(the “procedure B” should be used). Furthermore, for samples at low MH saturation, the temperature cycle could be added to make MHs distributed more homogeneously in the sample.

Observations of MH morphologies and pore habits at the pore scale are challenging due to not only the need of special experimental setups (composed of both high pressure and low temperature controls) but also a low contrast between methane hydrate and water in XRCT/SXRCT images. XRCT scan conditions were optimized based on theoretical attenuation coefficients. Saline solution (*KI*, 3.5 wt%) was used to distinguish MHs from water. Furthermore, three experimental setups have been developed in the objective of improving the XRCT image spatial resolution and adapting to SXRCT scans so that MHs could be distinguished from pure water in sandy sediment based on their morphology.

By using the optimized experimental setup (among these three), SXRCT scans were conducted to follow the MH formation following the excess-gas method. Both pure and saline water were used. Furthermore, observations by optical microscopy (at higher image spatial resolution and higher temporal resolution) confirmed some SXRCT results. Water, found initially in the pores in between grains of unsaturated sand, was moved to form MHs around the nearby grain surfaces by cryogenic suction. Different MH morphologies (e.g. spikes, “crystals”, layers/shells) could co-exist around grain surfaces and/or at contacts of grains under excess-gas conditions. In some areas with high MH saturation, MHs seem to cover the full surface of grains and tend to fill the pore space. In addition, MH spikes could become “crystals” over time provided that water was supplied for further MH formation. Multiple water migrations could modify MH morphologies and pore habits in the pore space, at the grain scale as well as at the sample scale. Moreover, round MH particles were found floating in saline water in the pore space of the media under excess-saline-water conditions.

MH formation following the excess-gas method (the method the most actually used) can be divided into three steps (nucleation, growth and stabilization). It seems that the MH formation, which was more complex due to water migrations, needs more studies. MH morphologies and pore habits in the sample are heterogeneous not only at the pore scale but also at the sample scale, with strong gradient of saturation both along the sample height and radius, with fluctuations at millimeter scale smaller than MRI resolution. Not only MH pore habits (cementings, load-bearing, and pore-filling) but also MH morphologies in sandy sediments are important for studies on physical/mechanical behaviors of methane hydrate-bearing sediments. It is vital that numerical studies on mechanical behaviors of methane hydrates-bearing sediments, which have been based on four idealized methane hydrate pore habits (cementings, load-bearing and pore-filling), would take into consideration more realistic methane hydrate morphologies and pore habits. Furthermore, additional observations at the grain scale should be conducted in order to get more insights on MH distributions under excess-water conditions. Actually, pore-filling and load-bearing models could be used to describe MHs, at the grain scale, under excess-water conditions whereas more complex models are still needed to simulate MHs under excess-gas conditions (observed MH morphologies and pore habits were much more complex than the two idealized cementing models: mineral coating and grain contacts).

The dissociation of MHBS (under excess-water conditions) following the depressurization method was fast and involved ice formation as the pore pressure was reduced below the quadruple point of methane hydrates. Experimental scale turns then to be one of the important factors needed to be paid attention for future laboratory MH dissociation studies.

Besides, an alternative method has been developed to determine more accurately the volume fractions of three phases in an unsaturated-porous-media XRCT images based on image noise and partial volume effect considerations. This method was validated on partially saturated sand and then applied to determine methane hydrate saturation of MHBS under excess-gas conditions at the stabilization state (all water was supposed to be transformed into methane hydrates).

## 8.2 Perspectives

In this study, experiments at both macroscopic scale (triaxial tests and MRI) and microscopic scale (XRCT, SXRCT and optical microscopy) have been conducted in order to investigate the microstructure and the mechanical properties of MHBS. Further studies should be conducted to better link these two aspects as well as to better mimic natural methane hydrate-bearing sand in the context of methane gas exploitation from MHBS.

Macroscopic tests have been conducted at low initial water saturations (25-50 %) so that water was homogeneously distributed in the sample. It was then expected that MHs formed homogeneously under excess-gas conditions, that was confirmed by MRI tests only at low initial water saturation ( $S_h = 25\%$ ). However, SXRCT scans showed heterogeneous MH distribution along the sample height due to water migrations at millimeter scale. A more quantitative characterization of this sample heterogeneity is still to be done: the new methodology for accurate volume fraction determination would be extended to four-phase media and applied to the whole set of available 3D images. MRI experiments at higher initial water saturations should be conducted to verify the MH distribution at the sample scale while the effects of an additional temperature on the MH conversion/redistribution in the pore space should be verified by triaxial tests at higher methane hydrate saturation. Moreover, the kinetics of MH dissociation (following not only the depressurization method but also the thermal method or  $CO_2 - CH_4$  exchange) as well as its effects on the mechanical behaviors of formed MHBS should be investigated via MRI together with triaxial tests in the objective of minimizing the environmental impacts of future MH exploration.

Only qualitative SXRCT results were presented (MH morphologies, pore habits and MH distribution) through observations of 2D cross-sections of 3D SXRCT images. It is of importance to investigate directly the mechanical behaviors of MHBS from SXRCT images to take into account the real observed MH morphologies and pore habits and their evolution. Image based numerical simulations might be used to do so, using either virtually generated images or real SXRCT segmented images, with a specific methodology to account for partial volume effects and statistical fluctuations of phase distributions. The Finite Element Method (FEM) and the Discrete Element Method (DEM) have been simultaneously applied to solve, respectively, the structural problem at the macroscopic scale

and the material microstructure at the microscopic scale. FEMxDEM approach would be done in this case by using virtually generated images as the representative at the microscopic scale. Furthermore, in the work of Axelle Alavoine (another PhD thesis in the context of Hydre), FFT-based homogenization has implemented to study first the effects of MH pore habits and saturation on the mechanical behaviors of MHBS. A multi-scale FEM-FFT approach could make use of our numerous real SXRCT images (segmented). Moreover, methane hydrate saturation of MHBS during the MH formation should be determined precisely from SXRCT images. The medium is four-phase media consisting of methane gas, methane hydrate, sand grains as well as the remaining water/saline water which have not been transformed into MHs. An alternative methodology, to quantify precisely at a more local scale the formation of MHs, would use an image subtraction following a methodology similar to that used for crack detection (Nguyen et al., 2015). The application of discrete digital image correlation (Hall et al., 2010) would be useful to quantify grain motions due to MH formation and correct image subtractions.

Within the developed XRCT/SXRCT experimental setups, conducting a temperature cycle is not possible but investigating saline water injection after the MH formation following the excess-gas method which has been considered a dynamic process is necessary even if it is really delicate to perform. Saline water should be cooled before being injected into the sample.

The proposed method, applied to determine methane hydrate saturation of MHBS under excess-gas conditions, could be modified to adapt it to MHBS under excess-saline water conditions.

Few studies have been conducted to investigate the microstructural changes of gas hydrate-bearing sediments during macroscopic deformation due to limits on experimental apparatus. Compared to the experimental setups for observations of gas hydrate morphologies and pore habits which need the control of both high pressure and low temperature, XRCT based gas hydrate triaxial testing apparatus requires also the control of confining pressure and axial load as well. Li et al., 2019 developed a novel, low-temperature (-35 to 20 °C), high-pressure (>16 MPa of confining pressure and >95.4 MPa of vertical load) triaxial testing apparatus that is suitable for XRCT scans to capture the gas hydrate formation at the particle scale and measure the stress-strain responses of gas hydrate-bearing sediment at the core scale. Experiments were conducted for Xenon hydrate bearing-sediments (Li et al., 2019). Similar experiments on methane hydrate-bearing sediments (at higher spatial resolution), which are still challenging mainly due to low contrast between methane hydrate and water in XRCT images, can give better insights on the link between MH morphologies, pore habits and mechanical behaviors of MHBS. The combination of discrete digital image correlation and image subtractions aforementioned could be also useful for these studies.

The MH dissociation is a complex process involving not only changes in the mechanical behaviors of MHBS but also the phase changes, the water/methane gas flows and the thermal changes. Thermo-hydro-mechanical behaviors of MHBS during the MH dissociation should be studied both experimentally and numerically in order to not only optimize the method of methane gas extraction from MHBS but also to minimize the environmen-

tal impacts of future methane gas exploitation from deep-sea MHBS.

Besides, MHs in clayey sediments should also be investigated to minimize the environmental impacts due to natural MH dissociation, with the additional challenges of a much more complex and smaller scale of the microstructure of sediments.



# Bibliography

- Almenningen, S., Iden, E., Fernø, M. A., and Ersland, G. (2018). Salinity effects on pore-scale methane gas hydrate dissociation. *Journal of Geophysical Research: Solid Earth*, 123(7):5599–5608.
- Bagherzadeh, S. A., Moudrakovski, I. L., Ripmeester, J. A., and Englezos, P. (2011). Magnetic resonance imaging of gas hydrate formation in a bed of silica sand particles. *Energy & Fuels*, 25(7):3083–3092.
- Baldwin, B. A., Stevens, J., Howard, J. J., Graue, A., Kvamme, B., Aspnes, E., Ersland, G., Husebø, J., and Zornes, D. R. (2009). Using magnetic resonance imaging to monitor ch<sub>4</sub> hydrate formation and spontaneous conversion of ch<sub>4</sub> hydrate to co<sub>2</sub> hydrate in porous media. *Magnetic resonance imaging*, 27(5):720–726.
- Beaudoin, Y., Waite, W., Boswell, R., and Dallimore, S. (2014). Frozen heat: A global outlook on methane gas hydrates. *United Nations Environment Programme, GRID-Arendal*, 29.
- Beltrán, J. G. and Servio, P. (2010). Morphological investigations of methane- hydrate films formed on a glass surface. *Crystal Growth & Design*, 10(10):4339–4347.
- Boswell, R., Moridis, G., Reagan, M., and Collett, T. S. (2011). Gas hydrate accumulation types and their application to numerical simulation. *Manuscript*, 130:17–22.
- Boswell, R., Yamamoto, K., Lee, S.-R., Collett, T., Kumar, P., and Dallimore, S. (2014). Methane hydrates. In *Future energy*, pages 159–178. Elsevier.
- Brugada, J., Cheng, Y., Soga, K., and Santamarina, J. (2010). Discrete element modelling of geomechanical behaviour of methane hydrate soils with pore-filling hydrate distribution. *Granular Matter*, 12(5):517–525.
- Bybee, K. et al. (2009). Development of natural-gas supply chain by means of natural-gas hydrates. *Journal of Petroleum Technology*, 61(07):62–64.
- Carcione, J. M. and Tinivella, U. (2000). Bottom-simulating reflectors: Seismic velocities and avo effects. *Geophysics*, 65(1):54–67.
- Chaouachi, M., Falenty, A., Sell, K., Enzmann, F., Kersten, M., Haberthür, D., and Kuhs, W. F. (2015). Microstructural evolution of gas hydrates in sedimentary matrices observed with synchrotron x-ray computed tomographic microscopy. *Geochemistry, Geophysics, Geosystems*, 16(6):1711–1722.
- Chen, X. and Espinoza, D. N. (2018). Ostwald ripening changes the pore habit and spatial variability of clathrate hydrate. *Fuel*, 214:614–622.
- Choi, J.-H., Dai, S., Cha, J.-H., and Seol, Y. (2014). Laboratory formation of noncementing hydrates in sandy sediments. *Geochemistry, Geophysics, Geosystems*, 15(4):1648–1656.



- Circone, S., Kirby, S. H., and Stern, L. A. (2005). Direct measurement of methane hydrate composition along the hydrate equilibrium boundary. *The Journal of Physical Chemistry B*, 109(19):9468–9475.
- Clausnitzer, V. and Hopmans, J. W. (1999). Determination of phase-volume fractions from tomographic measurements in two-phase systems. *Advances in water resources*, 22(6):577–584.
- Clennell, M. B., Hovland, M., Booth, J. S., Henry, P., and Winters, W. J. (1999). Formation of natural gas hydrates in marine sediments: 1. conceptual model of gas hydrate growth conditioned by host sediment properties. *Journal of Geophysical Research: Solid Earth*, 104(B10):22985–23003.
- Cnudde, V. and Boone, M. N. (2013). High-resolution x-ray computed tomography in geosciences: A review of the current technology and applications. *Earth-Science Reviews*, 123:1–17.
- Collett, T., Bahk, J.-J., Baker, R., Boswell, R., Divins, D., Frye, M., Goldberg, D., Husebø, J., Koh, C., Malone, M., et al. (2014). Methane hydrates in nature - current knowledge and challenges. *Journal of chemical & engineering data*, 60(2):319–329.
- Collett, T. S. (2002). Energy resource potential of natural gas hydrates. *AAPG bulletin*, 86(11):1971–1992.
- Collett, T. S., Johnson, A., Knapp, C. C., Boswell, R., et al. (2010). *Natural Gas Hydrates: Energy Resource Potential and Associated Geologic Hazards*, AAPG Memoir 89, volume 89. AAPG.
- Cortes, D. D., Martin, A. I., Yun, T. S., Francisca, F. M., Santamarina, J. C., and Ruppel, C. (2009). Thermal conductivity of hydrate-bearing sediments. *Journal of Geophysical Research: Solid Earth*, 114(B11).
- Cox, J. L. (1983). Natural gas hydrates: Properties, occurrence and recovery.
- Dai, J., Xu, H., Snyder, F., and Dutta, N. (2004). Detection and estimation of gas hydrates using rock physics and seismic inversion: Examples from the northern deepwater gulf of mexico. *The leading edge*, 23(1):60–66.
- Dai, S., Santamarina, J. C., Waite, W. F., and Kneafsey, T. J. (2012). Hydrate morphology: Physical properties of sands with patchy hydrate saturation. *Journal of Geophysical Research: Solid Earth*, 117(B11).
- Dai, S. and Seol, Y. (2014). Water permeability in hydrate-bearing sediments: A pore-scale study. *Geophysical Research Letters*, 41(12):4176–4184.
- Dallimore, S., Uchida, T., Collett, T., et al. (1999). *Scientific results from JAPEX/JNOC/GSC Mallik 2L-38 gas hydrate research well, Mackenzie delta, Northwest Territories, Canada*, volume 544. Geological Survey of Canada Ottawa, Ontario, Canada.
- Davidson, D., Garg, S., Gough, S., Hawkins, R., and Ripmeester, J. (1977). Characterization of natural gas hydrates by nuclear magnetic resonance and dielectric relaxation. *Canadian Journal of Chemistry*, 55(20):3641–3650.
- Davie, M., Zatsepina, O. Y., and Buffett, B. (2004). Methane solubility in marine hydrate environments. *Marine geology*, 203(1-2):177–184.
- Dupla, J.-C., Pedro, L. S., Canou, J., and Dormieux, L. (2007). Comportement mécanique des sols grossiers de référence. *Bulletin des laboratoires des ponts et chaussées*, (268):31–58.

- Dvorkin, J., Helgerud, M. B., Waite, W. F., Kirby, S. H., and Nur, A. (2000). Introduction to physical properties and elasticity models. In *Natural Gas Hydrate*, pages 245–260. Springer.
- Dvorkin, J. and Nur, A. (1996). Elasticity of high-porosity sandstones: Theory for two north sea data sets. *Geophysics*, 61(5):1363–1370.
- Dvorkin, J., Nur, A., and Yin, H. (1994). Effective properties of cemented granular materials. *Mechanics of materials*, 18(4):351–366.
- Ebinuma, T., Kamata, Y., Minagawa, H., Ohmura, R., Nagao, J., and Narita, H. (2005). Mechanical properties of sandy sediment containing methane hydrate. In *Proceedings of Fifth International Conference on Gas Hydrates, Pap*, volume 3037, pages 958–961.
- Ebinuma, T., Suzuki, K., Nagao, J., Oyama, H., Narita, H., et al. (2008). Ultrasonic wave velocities associated with formation and dissociation of methane hydrate in artificial sandy sediments. In *Offshore Technology Conference*. Offshore Technology Conference.
- Ecker, C., Dvorkin, J., and Nur, A. (1998). Sediments with gas hydrates: Internal structure from seismic avo. *Geophysics*, 63(5):1659–1669.
- Ersland, G., Husebø, J., Graue, A., Baldwin, B., Howard, J., and Stevens, J. (2010). Measuring gas hydrate formation and exchange with co<sub>2</sub> in bentheim sandstone using mri tomography. *Chemical Engineering Journal*, 158(1):25–31.
- Everett, D. (1961). The thermodynamics of frost damage to porous solids. *Transactions of the Faraday society*, 57:1541–1551.
- Fan, Z., Sun, C., Kuang, Y., Wang, B., Zhao, J., and Song, Y. (2017). Mri analysis for methane hydrate dissociation by depressurization and the concomitant ice generation. *Energy Procedia*, 105:4763–4768.
- Feia, S., Dupla, J. C., Ghabezloo, S., Sulem, J., Canou, J., Onaisi, A., Lescanne, H., and Aubry, E. (2015). Experimental investigation of particle suspension injection and permeability impairment in porous media. *Geomechanics for Energy and the Environment*, 3:24–39.
- Feia, S., Sulem, J., Canou, J., Ghabezloo, S., and Clain, X. (2016). Changes in permeability of sand during triaxial loading: effect of fine particles production. *Acta Geotechnica*, 11(1):1–19.
- Fonseca, J., O’Sullivan, C., and Coop, M. (2009). Image segmentation techniques for granular materials. In *AIP Conference Proceedings*, volume 1145, pages 223–226. AIP.
- Freij-Ayoub, R., Tan, C., Clennell, B., Tohidi, B., and Yang, J. (2007). A wellbore stability model for hydrate bearing sediments. *Journal of Petroleum Science and Engineering*, 57(1-2):209–220.
- Gabitto, J. F. and Tsouris, C. (2010). Physical properties of gas hydrates: A review. *Journal of Thermodynamics*, 2010.
- Gao, Y., Lin, Q., Bijeljic, B., and Blunt, M. J. (2017). X-ray microtomography of intermittency in multiphase flow at steady state using a differential imaging method. *Water Resources Research*, 53(12):10274–10292.
- Garg, S. K., Pritchett, J. W., Katoh, A., Baba, K., and Fujii, T. (2008). A mathematical model for the formation and dissociation of methane hydrates in the marine environment. *Journal of Geophysical Research: Solid Earth*, 113(B1).

- Gassmann, F. (1951). Elastic waves through a packing of spheres. *Geophysics*, 16(4):673–685.
- Georgiadis, A., Berg, S., Makurat, A., Maitland, G., and Ott, H. (2013). Pore-scale micro-computed-tomography imaging: Nonwetting-phase cluster-size distribution during drainage and imbibition. *Physical Review E*, 88(3):033002.
- Gudmundsson, J., Hveding, F., Børrehaug, A., et al. (1995). Transport of natural gas as frozen hydrate. In *The Fifth International Offshore and Polar Engineering Conference*. International Society of Offshore and Polar Engineers.
- Haligva, C., Linga, P., Ripmeester, J. A., and Englezos, P. (2010). Recovery of methane from a variable-volume bed of silica sand/hydrate by depressurization. *Energy & Fuels*, 24(5):2947–2955.
- Hall, S. A., Bornert, M., Desrues, J., Pannier, Y., Lenoir, N., Viggiani, G., and Bésuelle, P. (2010). Discrete and continuum analysis of localised deformation in sand using x-ray  $\mu$  ct and volumetric digital image correlation. *Géotechnique*, 60(5):315.
- Han, G., Kwon, T.-H., Lee, J. Y., and Kneafsey, T. J. (2018). Depressurization-induced fines migration in sediments containing methane hydrate: X-ray computed tomography imaging experiments. *Journal of Geophysical Research: Solid Earth*, 123(4):2539–2558.
- Hashemi, M. A., Khaddour, G., François, B., Massart, T. J., and Salager, S. (2014). A tomographic imagery segmentation methodology for three-phase geomaterials based on simultaneous region growing. *Acta Geotechnica*, 9(5):831–846.
- Heeschen, K. U., Schicks, J. M., and Oeltzschner, G. (2016). The promoting effect of natural sand on methane hydrate formation: Grain sizes and mineral composition. *Fuel*, 181:139–147.
- Helgerud, M., Dvorkin, J., Nur, A., Sakai, A., and Collett, T. (1999). Elastic-wave velocity in marine sediments with gas hydrates: Effective medium modeling. *Geophysical Research Letters*, 26(13):2021–2024.
- Helliwell, J. (1984). Synchrotron x-radiation protein crystallography: instrumentation, methods and applications. *Reports on Progress in Physics*, 47(11):1403.
- Holland, M., Schultheiss, P., and Roberts, J. (2018). Gas hydrate saturation and morphology from analysis of pressure cores acquired in the bay of bengal during expedition ngbp-02, offshore india. *Marine and Petroleum Geology*.
- Holland, M., Schultheiss, P., Roberts, J., and Druce, M. (2008). Observed gas hydrate morphologies in marine sediments. In *6th International Conference on Gas Hydrates, Chevron, Vancouver, BC, Canada*, pages 6–10.
- Hong, H., Pooladi-Darvish, M., Bishnoi, P., et al. (2003). Analytical modelling of gas production from hydrates in porous media. *Journal of Canadian Petroleum Technology*, 42(11):45–56.
- Houston, A. N., Otten, W., Baveye, P. C., and Hapca, S. (2013). Adaptive-window indicator kriging: A thresholding method for computed tomography images of porous media. *Computers & geosciences*, 54:239–248.
- Hsieh, H., Brown, G. O., Stone, M. L., and Lucero, D. A. (1998). Measurement of porous media component content and heterogeneity using gamma ray tomography. *Water resources research*, 34(3):365–372.

- Hyodo, M., Li, Y., Yoneda, J., Nakata, Y., Yoshimoto, N., and Nishimura, A. (2014). Effects of dissociation on the shear strength and deformation behavior of methane hydrate-bearing sediments. *Marine and petroleum geology*, 51:52–62.
- Hyodo, M., Wu, Y., Nakashima, K., Kajiyama, S., and Nakata, Y. (2017). Influence of fines content on the mechanical behavior of methane hydrate-bearing sediments. *Journal of geophysical research: solid earth*, 122(10):7511–7524.
- Hyodo, M., Yoneda, J., Yoshimoto, N., and Nakata, Y. (2013). Mechanical and dissociation properties of methane hydrate-bearing sand in deep seabed. *Soils and foundations*, 53(2):299–314.
- Iassonov, P., Gebrenegus, T., and Tuller, M. (2009). Segmentation of x-ray computed tomography images of porous materials: A crucial step for characterization and quantitative analysis of pore structures. *Water Resources Research*, 45(9).
- Jakobsen, P. V. (2000). Focus on the cnn effect misses the point: The real media impact on conflict management is invisible and indirect. *Journal of Peace Research*, 37(2):131–143.
- Jiang, M., Chen, H., Tapias, M., Arroyo, M., and Fang, R. (2014). Study of mechanical behavior and strain localization of methane hydrate bearing sediments with different saturations by a new dem model. *Computers and Geotechnics*, 57:122–138.
- Jiang, M., Sun, Y., and Yang, Q. (2013). A simple distinct element modeling of the mechanical behavior of methane hydrate-bearing sediments in deep seabed. *Granular Matter*, 15(2):209–220.
- Jin, S., Nagao, J., Takeya, S., Jin, Y., Hayashi, J., Kamata, Y., Ebinuma, T., and Narita, H. (2006). Structural investigation of methane hydrate sediments by microfocus x-ray computed tomography technique under high-pressure conditions. *Japanese journal of applied physics*, 45(7L):L714.
- Jin, Y., Konno, Y., and Nagao, J. (2012). Growth of methane clathrate hydrates in porous media. *Energy & fuels*, 26(4):2242–2247.
- Johnson, A., Patil, S., and Dandekar, A. (2011). Experimental investigation of gas-water relative permeability for gas-hydrate-bearing sediments from the mount elbert gas hydrate stratigraphic test well, alaska north slope. *Marine and petroleum geology*, 28(2):419–426.
- Judge, A. (1982). Natural gas hydrates in canada. In *Proceedings of the 4th Canadian Permafrost Conference*, pages 320–328. Citeseer.
- Jung, J., Jang, J., Santamarina, J., Tsouris, C., Phelps, T., and Rawn, C. (2011). Gas production from hydrate-bearing sediments: the role of fine particles. *Energy & fuels*, 26(1):480–487.
- Jung, J.-W., Santamarina, J. C., and Soga, K. (2012). Stress-strain response of hydrate-bearing sands: Numerical study using discrete element method simulations. *Journal of geophysical research: solid earth*, 117(B4).
- Kaestner, A., Lehmann, E., and Stampanoni, M. (2008). Imaging and image processing in porous media research. *Advances in Water Resources*, 31(9):1174–1187.
- Kato, A., Nakata, Y., Hyodo, M., and Yoshimoto, N. (2016). Macro and micro behaviour of methane hydrate-bearing sand subjected to plane strain compression. *Soils and foundations*, 56(5):835–847.

- Kerkar, P., Jones, K. W., Kleinberg, R., Lindquist, W. B., Tomov, S., Feng, H., and Mahajan, D. (2009). Direct observations of three dimensional growth of hydrates hosted in porous media. *Applied physics letters*, 95(2):024102.
- Kerkar, P. B., Horvat, K., Jones, K. W., and Mahajan, D. (2014). Imaging methane hydrates growth dynamics in porous media using synchrotron x-ray computed microtomography. *Geochemistry, Geophysics, Geosystems*, 15(12):4759–4768.
- Khaddour, G., Riedel, I., Andò, E., Charrier, P., Bésuelle, P., Desrues, J., Viggiani, G., and Salager, S. (2018). Grain-scale characterization of water retention behaviour of sand using x-ray ct. *Acta Geotechnica*, 13(3):497–512.
- Kimoto, S., Oka, F., and Fushita, T. (2010). A chemo–thermo–mechanically coupled analysis of ground deformation induced by gas hydrate dissociation. *International Journal of Mechanical Sciences*, 52(2):365–376.
- Klar, A., Soga, K., and Ng, M. (2010). Coupled deformation–flow analysis for methane hydrate extraction. *Geotechnique*, 60(10):765–776.
- Klein, K. A. and Santamarina, J. C. (2003). Electrical conductivity in soils: Underlying phenomena. *Journal of Environmental & Engineering Geophysics*, 8(4):263–273.
- Kneafsey, T. J. (2011). Examination of hydrate formation methods: trying to create representative samples.
- Kneafsey, T. J., Tomutsa, L., Moridis, G. J., Seol, Y., Freifeld, B. M., Taylor, C. E., and Gupta, A. (2007). Methane hydrate formation and dissociation in a partially saturated core-scale sand sample. *Journal of Petroleum Science and Engineering*, 56(1-3):108–126.
- Konno, Y., Fujii, T., Sato, A., Akamine, K., Naiki, M., Masuda, Y., Yamamoto, K., and Nagao, J. (2017). Key findings of the world’s first offshore methane hydrate production test off the coast of japan: Toward future commercial production. *Energy & Fuels*, 31(3):2607–2616.
- Konno, Y., Uchiumi, T., Oyama, H., Jin, Y., Nagao, J., Masuda, Y., and Ouchi, H. (2012). Dissociation behavior of methane hydrate in sandy porous media below the quadruple point. *Energy & Fuels*, 26(7):4310–4320.
- Konno, Y., Yoneda, J., Egawa, K., Ito, T., Jin, Y., Kida, M., Suzuki, K., Fujii, T., and Nagao, J. (2015). Permeability of sediment cores from methane hydrate deposit in the eastern nankai trough. *Marine and petroleum geology*, 66:487–495.
- Kriminski, S., Kazmierczak, M., and Thorne, R. (2003). Heat transfer from protein crystals: implications for flash-cooling and x-ray beam heating. *Acta Crystallographica Section D: Biological Crystallography*, 59(4):697–708.
- Kulkarni, R., Tuller, M., Fink, W., and Wildenschild, D. (2012). Three-dimensional multiphase segmentation of x-ray ct data of porous materials using a bayesian markov random field framework. *Vadose Zone Journal*, 11(1):0–0.
- Kumar, A., Maini, B., Bishnoi, P., Clarke, M., Zatsepina, O., and Srinivasan, S. (2010). Experimental determination of permeability in the presence of hydrates and its effect on the dissociation characteristics of gas hydrates in porous media. *Journal of Petroleum Science and Engineering*, 70(1-2):114–122.
- Kwon, T.-H., Cho, G.-C., and Santamarina, J. C. (2008). Gas hydrate dissociation in sediments: Pressure-temperature evolution. *Geochemistry, Geophysics, Geosystems*, 9(3).

- Le, T. X., Aïmedieu, P., Bornert, M., Chabot, B., Rodts, S., and Tang, A. M. (2019). Effect of temperature cycle on mechanical properties of methane hydrate-bearing sediment. *Soils and Foundations*.
- Le, T. X., Rodts, S., Hautemayou, D., Aïmedieu, P., Bornert, M., Chabot, B., and Tang, A. M. (2018a). Kinetics of methane hydrate formation and dissociation in sand sediment. *Geomechanics for Energy and the Environment*.
- Le, T. X., Tang, A. M., Aïmedieu, P., Bornert, M., Chabot, B., and Rodts, S. (2018b). Methane hydrate-bearing sand-an energy resource? In *Vietnam Symposium on Advances in Offshore Engineering*, pages 158–163. Springer.
- Lee, M., Hutchinson, D., Collett, T., and Dillon, W. P. (1996). Seismic velocities for hydrate-bearing sediments using weighted equation. *Journal of Geophysical Research: Solid Earth*, 101(B9):20347–20358.
- Lee, M. W. and Collett, T. S. (2001). Elastic properties of gas hydrate-bearing sediments. *Geophysics*, 66(3):763–771.
- Lei, L., Liu, Z., Seol, Y., Boswell, R., and Dai, S. (2019a). An investigation of hydrate formation in unsaturated sediments using x-ray computed tomography. *Journal of Geophysical Research: Solid Earth*.
- Lei, L. and Santamarina, J. (2018). Laboratory strategies for hydrate formation in fine-grained sediments. *Journal of Geophysical Research: Solid Earth*, 123(4):2583–2596.
- Lei, L., Seol, Y., Choi, J.-H., and Kneafsey, T. J. (2019b). Pore habit of methane hydrate and its evolution in sediment matrix–laboratory visualization with phase-contrast micro-ct. *Marine and Petroleum Geology*, 104:451–467.
- Li, J.-f., Ye, J.-l., Qin, X.-w., Qiu, H.-j., Wu, N.-y., Lu, H.-l., Xie, W.-w., Lu, J.-a., Peng, F., Xu, Z.-q., et al. (2018). The first offshore natural gas hydrate production test in south china sea. *China Geology*, 1(1):5–16.
- Li, Y., Wu, P., Liu, W., Sun, X., Cui, Z., and Song, Y. (2019). A microfocus x-ray computed tomography based gas hydrate triaxial testing apparatus. *Review of Scientific Instruments*, 90(5):055106.
- Lindquist, W. B., Lee, S.-M., Coker, D. A., Jones, K. W., and Spanne, P. (1996). Medial axis analysis of void structure in three-dimensional tomographic images of porous media. *Journal of Geophysical Research: Solid Earth*, 101(B4):8297–8310.
- Liu, X. and Flemings, P. B. (2007). Dynamic multiphase flow model of hydrate formation in marine sediments. *Journal of Geophysical Research: Solid Earth*, 112(B3).
- Mak, T. C. and McMullan, R. K. (1965). Polyhedral clathrate hydrates. x. structure of the double hydrate of tetrahydrofuran and hydrogen sulfide. *The Journal of Chemical Physics*, 42(8):2732–2737.
- Malagar, B. R., Lijith, K., and Singh, D. (2019). Formation & dissociation of methane gas hydrates in sediments: A critical review. *Journal of Natural Gas Science and Engineering*.
- Masui, A., Haneda, H., Ogata, Y., and Aoki, K. (2005). The effect of saturation degree of methane hydrate on the shear strength of synthetic methane hydrate sediments. In *Proceedings of the 5th International Conference on Gas Hydrates, Trondheim, Norway*, volume 2037, pages 657–663.

- Masui, A., Haneda, H., Ogata, Y., and Aoki, K. (2006). Triaxial compression test on submarine sediment containing methane hydrate in deep sea off the coast off japan. In *Proceedings of the 41st Annual Conference, Japanese Geotechnical Society*.
- Merey, Ş. (2016). Drilling of gas hydrate reservoirs. *Journal of Natural Gas Science and Engineering*, 35:1167–1179.
- Metaxas, P. J., Lim, V. W., Booth, C., Zhen, J., Stanwix, P. L., Johns, M. L., Aman, Z. M., Haandrikman, G., Crosby, D., and May, E. F. (2019). Gas hydrate formation probability distributions: Induction times, rates of nucleation and growth. *Fuel*, 252:448–457.
- Minagawa, H., Nishikawa, Y., Ikeda, I., Miyazaki, K., Takahara, N., Sakamoto, Y., Komai, T., and Narita, H. (2008). Measurement of water permeability and pore-size distribution of methanehydrate-bearing sediments. In *6th International Conference on Gas Hydrates, Chevron, Vancouver, BC, Canada*, pages 6–10.
- Moridis, G. and Collett, T. (2003). Strategies for gas production from hydrate accumulations under various geologic conditions.
- Moridis, G., Silpngarmert, S., Reagan, M., Collett, T., and Zhang, K. (2011). Gas production from a cold, stratigraphically-bounded gas hydrate deposit at the mount elbert gas hydrate stratigraphic test well, alaska north slope: Implications of uncertainties. *Marine and petroleum geology*, 28(2):517–534.
- Moridis, G. J. (2008). Toward production from gas hydrates: current status, assessment of resources, and simulation-based evaluation of technology and potential.
- Moridis, G. J. and Reagan, M. T. (2007). Strategies for gas production from oceanic class 3 hydrate accumulations.
- Müter, D., Pedersen, S., Sørensen, H. O., Feidenhans, R., and Stipp, S. L. S. (2012). Improved segmentation of x-ray tomography data from porous rocks using a dual filtering approach. *Computers & geosciences*, 49:131–139.
- Natarajan, V., Bishnoi, P., and Kalogerakis, N. (1994). Induction phenomena in gas hydrate nucleation. *Chemical Engineering Science*, 49(13):2075–2087.
- Nguyen, N. N. and Nguyen, A. V. (2015). The dual effect of sodium halides on the formation of methane gas hydrate. *Fuel*, 156:87–95.
- Nguyen, T. T., Bornert, M., Chateau, C., Yvonnet, J., and Zhu, Q. (2015). 3d detection of damage evolution in porous brittle cement or plaster based materials.
- Nikitin, V. V., Dugarov, G. A., Duchkov, A. A., Fokin, M. I., Drobchik, A. A., Mokso, R., Shevchenko, P. D., and De Carlo, F. (2019). Study of methane hydrate formation and self-preservation using in-situ x-ray synchrotron tomography. *arXiv preprint arXiv:1907.03052*.
- Nur, A., Mavko, G., Dvorkin, J., and Galmudi, D. (1998). Critical porosity: A key to relating physical properties to porosity in rocks. *The Leading Edge*, 17(3):357–362.
- Ohmura, R., Matsuda, S., Uchida, T., Ebinuma, T., and Narita, H. (2005). Clathrate hydrate crystal growth in liquid water saturated with a guest substance: observations in a methane+ water system. *Crystal growth & design*, 5(3):953–957.
- Otsu, N. (1979). A threshold selection method from gray-level histograms. *IEEE transactions on systems, man, and cybernetics*, 9(1):62–66.

- Paganin, D., Mayo, S. C., Gureyev, T. E., Miller, P. R., and Wilkins, S. W. (2002). Simultaneous phase and amplitude extraction from a single defocused image of a homogeneous object. *Journal of microscopy*, 206(1):33–40.
- Pinkert, S. (2016). Rowe's stress-dilatancy theory for hydrate-bearing sand. *International Journal of Geomechanics*, 17(1):06016008.
- Pinkert, S. and Grozic, J. (2014). Prediction of the mechanical response of hydrate-bearing sands. *Journal of Geophysical Research: Solid Earth*, 119(6):4695–4707.
- Popenoe, P., Schmuck, E., Dillon, W., Schwab, W., Lee, H., and Twichell, D. (1993). The cape fear landslide: slope failure associated with salt diapirism and gas hydrate decomposition. *Submarine Landslides-Selected Studies in the US Exclusive Economic Zone*, pages 40–53.
- Priest, J. A., Best, A. I., and Clayton, C. R. (2005). A laboratory investigation into the seismic velocities of methane gas hydrate-bearing sand. *Journal of geophysical research: solid earth*, 110(B4).
- Priest, J. A., Rees, E. V., and Clayton, C. R. (2009). Influence of gas hydrate morphology on the seismic velocities of sands. *Journal of geophysical research: solid earth*, 114(B11).
- Reuss, A. (1929). Berechnung der fließgrenze von mischkristallen auf grund der plastizitätsbedingung für einkristalle. *ZAMM-Journal of Applied Mathematics and Mechanics/Zeitschrift für Angewandte Mathematik und Mechanik*, 9(1):49–58.
- Roose, T., Keyes, S. D., Daly, K., Carminati, A., Otten, W., Vetterlein, D., and Peth, S. (2016). Challenges in imaging and predictive modeling of rhizosphere processes. *Plant and Soil*, 407(1-2):9–38.
- Ruppel, C. (2007). Tapping methane hydrates for unconventional natural gas. *Elements*, 3(3):193–199.
- Ruppel, C. D. and Kessler, J. D. (2017). The interaction of climate change and methane hydrates. *Reviews of Geophysics*, 55(1):126–168.
- Rutqvist, J., Moridis, G., Grover, T., and Collett, T. (2009). Geomechanical response of permafrost-associated hydrate deposits to depressurization-induced gas production. *Journal of petroleum science and engineering*, 67(1-2):1–12.
- Rydzy, M. B. (2014). *The effect of hydrate formation on the elastic properties of unconsolidated sediment*. Colorado School of Mines.
- Rydzy, M. B. and Batzle, M. L. (2010). Ultrasonic velocities in laboratory-formed gas hydrate-bearing sediments. In *23rd EEGS Symposium on the Application of Geophysics to Engineering and Environmental Problems*.
- Sahoo, S. K., Marín-Moreno, H., North, L. J., Falcon-Suarez, I., Madhusudhan, B. N., Best, A. I., and Minshull, T. A. (2018). Presence and consequences of coexisting methane gas with hydrate under two phase water-hydrate stability conditions. *Journal of Geophysical Research: Solid Earth*, 123(5):3377–3390.
- Sánchez, M., Gai, X., and Santamarina, J. C. (2017). A constitutive mechanical model for gas hydrate bearing sediments incorporating inelastic mechanisms. *Computers and Geotechnics*, 84:28–46.



- Santamarina, J. C., Dai, S., Terzariol, M., Jang, J., Waite, W. F., Winters, W. J., Nagao, J., Yoneda, J., Konno, Y., Fujii, T., et al. (2015). Hydro-bio-geomechanical properties of hydrate-bearing sediments from nankai trough. *Marine and petroleum geology*, 66:434–450.
- Schlüter, S., Sheppard, A., Brown, K., and Wildenschild, D. (2014). Image processing of multiphase images obtained via x-ray microtomography: a review. *Water Resources Research*, 50(4):3615–3639.
- Schlüter, S., Weller, U., and Vogel, H.-J. (2010). Segmentation of x-ray microtomography images of soil using gradient masks. *Computers & Geosciences*, 36(10):1246–1251.
- Seol, Y. and Kneafsey, T. J. (2011). Methane hydrate induced permeability modification for multiphase flow in unsaturated porous media. *Journal of Geophysical Research: Solid Earth*, 116(B8).
- Servio, P. and Englezos, P. (2003). Morphology of methane and carbon dioxide hydrates formed from water droplets. *AIChE Journal*, 49(1):269–276.
- Shin, H. and Santamarina, J. C. (2009). Mineral dissolution and the evolution of  $k_0$ . *Journal of Geotechnical and Geoenvironmental Engineering*, 135(8):1141–1147.
- Sloan, E. D. (1998). Gas hydrates: review of physical/chemical properties. *Energy & Fuels*, 12(2):191–196.
- Sloan Jr, E. D. and Koh, C. A. (2007). *Clathrate hydrates of natural gases*. CRC press.
- Soga, K., Lee, S., Ng, M., and Klar, A. (2006). Characterisation and engineering properties of methane hydrate soils. *Characterisation and engineering properties of natural soils*, 4:2591–1642.
- Sowa, B., Zhang, X. H., Hartley, P. G., Dunstan, D. E., Kozielski, K. A., and Maeda, N. (2014). Formation of ice, tetrahydrofuran hydrate, and methane/propane mixed gas hydrates in strong monovalent salt solutions. *Energy & Fuels*, 28(11):6877–6888.
- Spangenberg, E., Kulenkampff, J., Naumann, R., and Erzinger, J. (2005). Pore space hydrate formation in a glass bead sample from methane dissolved in water. *Geophysical Research Letters*, 32(24).
- Sultan, N. and Garziglia, S. (2011). Geomechanical constitutive modelling of gas-hydrate-bearing sediments. In *Proceedings of the 7th International Conference on Gas Hydrates (ICGH 2011), Edinburgh, Scotland, United Kingdom, July*, pages 17–21.
- Sun, Z. and Santamarina, J. C. (2019). Haines jumps: Pore scale mechanisms. *Physical Review E*, 100(2):023115.
- Swinehart, D. (1962). The beer-lambert law. *Journal of chemical education*, 39(7):333.
- Ta, X. H., Yun, T. S., Muhunthan, B., and Kwon, T.-H. (2015). Observations of pore-scale growth patterns of carbon dioxide hydrate using x-ray computed microtomography. *Geochemistry, Geophysics, Geosystems*, 16(3):912–924.
- Tohidi, B., Anderson, R., Clennell, M. B., Burgass, R. W., and Biderkab, A. B. (2001). Visual observation of gas-hydrate formation and dissociation in synthetic porous media by means of glass micromodels. *Geology*, 29(9):867–870.

- Tohidi, B., Danesh, A., and Todd, A. (1997). On the mechanism of gas hydrate formation in subsea sediments. *Preprints of Papers - American Chemical Society, Division of Fuel Chemistry*, 42(2):485–487.
- Tonnet, N. and Herri, J.-M. (2009). Methane hydrates bearing synthetic sediments—experimental and numerical approaches of the dissociation. *Chemical Engineering Science*, 64(19):4089–4100.
- Tse, J. S. (1994). Dynamical properties and stability of clathrate hydrates. *Annals of the New York Academy of Sciences*, 715(1):187–206.
- Tse, J. S. and White, M. A. (1988). Origin of glassy crystalline behavior in the thermal properties of clathrate hydrates: a thermal conductivity study of tetrahydrofuran hydrate. *The Journal of Physical Chemistry*, 92(17):5006–5011.
- Turner, D., Boxall, J., Yang, S., Kleehammer, D., Koh, C., Miller, K., Sloan, E., Xu, Z., Matthews, P., and Talley, L. (2005). Development of a hydrate kinetic model and its incorporation into the olga2000® transient multiphase flow simulator. In *5th International Conference on Gas Hydrates, Trondheim, Norway*, pages 12–16.
- Uchida, S., Soga, K., and Yamamoto, K. (2012). Critical state soil constitutive model for methane hydrate soil. *Journal of Geophysical Research: Solid Earth*, 117(B3).
- Uchida, T., Ebinuma, T., Kawabata, J., and Narita, H. (1999). Microscopic observations of formation processes of clathrate-hydrate films at an interface between water and carbon dioxide. *Journal of crystal growth*, 204(3):348–356.
- Waite, W., Bratton, P. M., and Mason, D. H. (2011). Laboratory formation of non-cementing, methane hydrate-bearing sands. In *Proceedings of the 7th International Conference on Gas Hydrates*. Shell Edinburgh, Scotland, United Kingdom.
- Waite, W. F., Santamarina, J. C., Cortes, D. D., Dugan, B., Espinoza, D., Germaine, J., Jang, J., Jung, J., Kneafsey, T. J., Shin, H., et al. (2009). Physical properties of hydrate-bearing sediments. *Reviews of geophysics*, 47(4).
- Waite, W. F., Winters, W. J., and Mason, D. (2004). Methane hydrate formation in partially water-saturated ottawa sand. *American Mineralogist*, 89(8-9):1202–1207.
- Wallander, H. and Wallentin, J. (2017). Simulated sample heating from a nanofocused x-ray beam. *Journal of synchrotron radiation*, 24(5):925–933.
- Wang, S., Wang, P., Chen, B., Yang, M., and Li, Y. (2018). Velocity mapping of steady water flow through methane hydrate bearing samples. *Journal of Natural Gas Science and Engineering*, 53:385–393.
- Wildenschild, D. and Sheppard, A. P. (2013). X-ray imaging and analysis techniques for quantifying pore-scale structure and processes in subsurface porous medium systems. *Advances in Water Resources*, 51:217–246.
- Winters, W. (2000). 40. stress history and geotechnical properties of sediment from the cape fear diapir, blake ridge diapir, and blake ridge. In *Proceedings of the Ocean Drilling Program. Scientific Results*, pages 421–429.
- Xiong, L., Li, X., Wang, Y., and Xu, C. (2012). Experimental study on methane hydrate dissociation by depressurization in porous sediments. *Energies*, 5(2):518–530.

- Xu, C.-G. and Li, X.-S. (2015). Research progress on methane production from natural gas hydrates. *RSC Advances*, 5(67):54672–54699.
- Yamamoto, K. (2015). Overview and introduction: Pressure core-sampling and analyses in the 2012–2013 mh21 offshore test of gas production from methane hydrates in the eastern nankai trough. *Marine and Petroleum Geology*, 66:296–309.
- Yamamoto, K., Wang, X.-X., Tamaki, M., and Suzuki, K. (2019). The second offshore production of methane hydrate in the nankai trough and gas production behavior from a heterogeneous methane hydrate reservoir. *RSC Advances*, 9(45):25987–26013.
- Yang, L., Falenty, A., Chaouachi, M., Haberthür, D., and Kuhs, W. F. (2016a). Synchrotron x-ray computed microtomography study on gas hydrate decomposition in a sedimentary matrix. *Geochemistry, Geophysics, Geosystems*, 17(9):3717–3732.
- Yang, L., Zhao, J., Liu, W., Li, Y., Yang, M., and Song, Y. (2015). Microstructure observations of natural gas hydrate occurrence in porous media using microfocus x-ray computed tomography. *Energy & Fuels*, 29(8):4835–4841.
- Yang, S. H. B., Babu, P., Chua, S. F. S., and Linga, P. (2016b). Carbon dioxide hydrate kinetics in porous media with and without salts. *Applied energy*, 162:1131–1140.
- Yoneda, J., Jin, Y., Katagiri, J., and Tenma, N. (2016). Strengthening mechanism of cemented hydrate-bearing sand at microscales. *Geophysical Research Letters*, 43(14):7442–7450.
- Yoneda, J., Masui, A., Konno, Y., Jin, Y., Egawa, K., Kida, M., Ito, T., Nagao, J., and Tenma, N. (2015). Mechanical properties of hydrate-bearing turbidite reservoir in the first gas production test site of the eastern nankai trough. *Marine and Petroleum Geology*, 66:471–486.
- Yoneda, J., Masui, A., Konno, Y., Jin, Y., Kida, M., Katagiri, J., Nagao, J., and Tenma, N. (2017). Pressure-core-based reservoir characterization for geomechanics: Insights from gas hydrate drilling during 2012–2013 at the eastern nankai trough. *Marine and Petroleum Geology*, 86:1–16.
- Yousif, M., Abass, H., Selim, M., Sloan, E., et al. (1991). Experimental and theoretical investigation of methane-gas-hydrate dissociation in porous media. *SPE reservoir Engineering*, 6(01):69–76.
- Yun, T. S., Santamarina, J. C., and Ruppel, C. (2007). Mechanical properties of sand, silt, and clay containing tetrahydrofuran hydrate. *Journal of geophysical research: solid earth*, 112(B4).
- Zatsepina, O. Y. and Buffett, B. (1998). Thermodynamic conditions for the stability of gas hydrate in the seafloor. *Journal of Geophysical Research: Solid Earth*, 103(B10):24127–24139.
- Zhang, L., Sun, L., Sun, M., Lv, X., Dong, H., Miao, Y., Yang, L., Song, Y., and Zhao, J. (2019). Analyzing spatially and temporally visualized formation behavior of methane hydrate in unconsolidated porous media. *Magnetic resonance imaging*.
- Zhang, L., Zhao, J., Dong, H., Zhao, Y., Liu, Y., Zhang, Y., and Song, Y. (2016). Magnetic resonance imaging for in-situ observation of the effect of depressurizing range and rate on methane hydrate dissociation. *Chemical Engineering Science*, 144:135–143.
- Zhao, J., Lv, Q., Li, Y., Yang, M., Liu, W., Yao, L., Wang, S., Zhang, Y., and Song, Y. (2015a). In-situ visual observation for the formation and dissociation of methane hydrates in porous media by magnetic resonance imaging. *Magnetic resonance imaging*, 33(4):485–490.

- Zhao, J., Yang, L., Liu, Y., and Song, Y. (2015b). Microstructural characteristics of natural gas hydrates hosted in various sand sediments. *Physical Chemistry Chemical Physics*, 17(35):22632–22641.
- Zhao, J., Yang, L., Xue, K., Lam, W., Li, Y., and Song, Y. (2014). In situ observation of gas hydrates growth hosted in porous media. *Chemical Physics Letters*, 612:124–128.
- Zimmer, M. (2003). Seismic velocities in unconsolidated sands: Measurements of pressure, sorting, and compaction effects. *PhD thesis*.